The Dissertation Committee for William R. Lester Certifies that this is the approved version of the following dissertation:

From Rifting to Collision: The Evolution of the Taiwan Mountain Belt

Committee:

Kirk McIntosh, Supervisor

Luc Lavier, Co-Supervisor

Harm Van Avendonk

Brian Horton

Jaime Barnes

Char-Shine Liu

From Rifting to Collision: The Evolution of the Taiwan Mountain Belt

by

William R. Lester, B.S., M.S.

Dissertation

Presented to the Faculty of the Graduate School of

The University of Texas at Austin

in Partial Fulfillment

of the Requirements

for the Degree of

Doctor of Philosophy

The University of Texas at Austin

May 2013

Dedication

To my family, friends, and Winston

Acknowledgements

Many people have contributed to this dissertation in many different ways. I am extremely grateful to my advisor Kirk McIntosh for taking me on as a student and involving me in geophysical research in Taiwan. I have benefited greatly from his patient guidance, and will always be appreciative of the opportunities he afforded me during my time at UT. I would also like to thank Luc Lavier and Harm Van Avendonk, whom I also worked very close with. I have learned a great deal from Kirk, Luc and Harm through numerous discussions and our travels together. I would like to thank Char-Shine Liu for his involvement in this project and the manuscripts that came out of it, as well as for hosting me in Taipei during the summer of 2010. I am also grateful to Brian Horton and Jaime Barnes for lending their insight to much of this work.

I am forever indebted to my wonderful wife Beth, who constantly found new ways to put up with me as I completed this dissertation, and frequently was the glue holding our house together. I would also like to thank the Lesters and the Diesels for all the love, support, encouragement, and free meals they have offered over the last five years. There are too many friends, neighbors and colleagues to thank by name here, but I would like to mention my officemates Bobby Reece and Dan Eakin for keeping me on track and for their constant levity; and my neighbors Bobby and Melissa Rosas for the best fajitas I've never paid for. Finally, I would like to express my gratitude towards Winston, for the perspective and for keeping me human.

From Rifting to Collision: The Evolution of the Taiwan Mountain Belt

William R. Lester, PhD

The University of Texas at Austin, 2013

Supervisor: Kirk D. McIntosh

Co-supervisor: Luc L. Lavier

Arc-continent collisions are believed to be an important mechanism for the growth of continents. Taiwan is one of the modern day examples of this process, and as such, it is an ideal natural laboratories to investigate the uncertain behavior of continental crust during collision. The obliquity of collision between the northern South China Sea (SCS) rifted margin and Luzon arc in the Manila trench subduction zone allows for glimpses into different temporal stages of collision at different spatial locations, from the mature mountain-belt in central-northern Taiwan to the 'pre-collision' rifted margin and subduction zone south of Taiwan. Recently acquired seismic reflection and wide-angle seismic refraction data document the crustal-scale structure of the mountain belt through these different stages.

These data reveal a wide rifted margin near Taiwan with half-graben rift basins along the continental shelf and a broad distal margin consisting of highly-extended continental crust modified by post-rift magmatism. Magmatic features in the distal margin include sills in the post-rift sediments, intruded crust, and a high-velocity lower crustal layer that likely represents mafic magmatism. Post-rift magmatism may have been induced by thermal erosion of lithospheric mantle following breakup and the onset of seafloor spreading.

Geophysical profiles across the early-stage collision offshore southern Taiwan show evidence the thin crust of the distal margin is subducting at the Manila trench and structurally underplating the growing orogenic wedge ahead of the encroaching continental shelf. Subduction of the distal margin may induce a pre-collision flexural response along the continental shelf as suggested by a recently active major rift fault and a geodynamic model of collision. The weak rift faults may be inverted during the subsequent collision with the continental shelf. These findings support a multi-phase collision model where the early growth of the mountain belt is driven in part by underplating of the accretionary prism by crustal blocks from the distal margin. The wedge is subsequently uplift and deformed during a collision with the continental shelf that involves both thin-skinned and thick-skinned structural styles. This model highlights the importance of rifting styles on mountain-building.

Table of Contents

List of Tables

List of Figures

Chapter 1: Introduction and Overview

1-1: INTRODUCTION

Terrane accretion during collision is one of the primary mechanisms for growing the continents throughout geologic time (*Rapalini*, 2005; *Sengör et al.*, 1993; *Silver and Smith*, 1983). Many of these collisions are between continental margins and volcanic arcs. Despite the prevalence of arc-continent collisions in the geologic record, there are few modern-day examples to inform collisional models. Relict arc-continent collisions hold limited potential for exploring the collision process, as they may be deeply modified by erosion or subsequent tectonic events. Therefore it is necessary to examine an active arc-continent collision, such as Taiwan, to develop new insights into this fundamental geologic process.

Taiwan is the result of on-going collision between the Luzon arc of the Philippine Sea plate and the northern South China Sea rifted continental margin of the Eurasia plate (Figure 1-1). The oblique collision between the north-trending arc and northeast-trending rifted margin began first in central-northern Taiwan at ~4-7 Ma (Huang et al. 2006), and has been actively propagating southward (Byrne and Liu, 2002; Lee et al., 2006; Suppe, 1984). Because of the geometry, different spatial locations along the strike of the orogen may be viewed as different temporal stages in the evolution of the mountain belt (Suppe, 1981). This feature distinguishes Taiwan from other active arc-continent collisions (Huang et al., 2000), and makes it an ideal natural laboratory for investigating how a rifted margin develops into a mountain belt over the course of arc-continent collision.

1-2: GEOLOGIC BACKGROUND

The Taiwan arc-continent collision is the culmination of a Wilson cycle that opened and is now closing the South China Sea (SCS) marginal ocean basin (Figure 1-1). The Wilson cycle began by rifting of the South China block during the late Cretaceous – Oligocene (Ru and Pigott, 1986; Lee and Lawver, 1994; Holloway, 1982), forming the northern SCS rifted continental margin and the conjugate southern SCS margin. Rifting eventually lead to continental breakup and the seafloor spreading that opened the SCS during early Oligocene – middle Miocene (Briais et al., 1993; Taylor and Hayes, 1983; Barckhausen and Roeser, 2004).

Starting in the late Oligocene-early Miocene, the SCS ocean crust began subducting eastward beneath the Philippine Sea plate at the Manila trench (Yang et al., 1995; Yang et al., 1996; Hall, 2002). Subduction has built a doubly-vergent accretionary prism, forearc basin (Luzon Trough) and Luzon volcanic arc. Wadati-Benioff zone seismicity delineates the subducted slab to ~200 km depth dipping at a ~50-60° angle (Kao et al., 2000). Subduction continues present-day at the Manila trench west of the Philippines and south of Taiwan (Figure 1-1).

In the northeastern SCS, subduction at the Manila trench has consumed the ocean crust, bringing the northern SCS rifted margin into collision with the Luzon arc at Taiwan (Figure 1-2). The subduction zone features observed at the Manila trench in the oceanic subduction regime far south of Taiwan begin to grow into an incipient mountain belt at the earliest stages of collision offshore southern Taiwan. For example, the Manila trench becomes a less well-defined deformation front (Liu et al., 1997). The accretionary wedge broadens and thickens at the Hengchun Ridge (Figure 1-2) and its emergent equivalent, the Hengchun Peninsula (Huang et al., 1997). While forearc basin sequences are

relatively undeformed in the oceanic subduction regime, offshore southern Taiwan they are backthrust over the forearc to form the Huatung Ridge (Chi et al., 2003; Lundberg et al., 1997; Reed et al., 1992). The forearc block may also be deforming and subducting with the down-going Eurasia plate (Cheng, 2008; Malavieille et al., 2002; McIntosh et al., 2005).

The onshore collision in Taiwan is frequently discussed in terms of five distinct tectono-stratigraphic provinces (Figure 1-2, 1-3). The westernmost Coastal Plain is the flexural foreland basin filled with syn-orogenic Pliocene-Quaternary clastic sediments shed from the Taiwan mountain belt. The wedge-shaped basin reaches a maximum thickness of over 5 km along the west coast of Taiwan and thins into the Taiwan Strait to the west. Numerous flexural faults permeate the foreland basin strata, but occasionally penetrate into the passive margin sequences below (Chou and Yu, 2002). Simoes and Avouc (2006) document southward-shifting foreland basin depocenters that track the collision as it propagate to the south.

To the east is the Western Foothills foreland fold-and-thrust belt (Figure 1-2, 1-3). The Western Foothills in particular have been the focus of extensive study since the advent of critical taper theory (Davis et al., 1983). The Western Foothills primarily consist of thrust sheets of pre-orogenic Miocene passive margin sediments and Pliocene-Quaternary syn-orogenic sediments (Ho, 1986; Suppe, 1981). Thrust faults root in a shallow-dipping décollement within a thick succession of late Miocene shale in the Nanchuang Formation (Suppe and Wittke, 1977), though a number of studies have argued for a component of thick-skinned deformation in the Western Foothills as well (Mouthereau et al. 2001; Hung et al., 1999; Lee et al., 2002; Mouthereau et al., 2006). The Western Foothills accommodate ~3-5 cm/yr of shortening, and the northwest-

verging thrust faults and folds are generally consistent with the northwesterly direction of plate convergence (Cattin et al., 2004; Johnson et al., 2005; Simoes and Avouac, 2006; Mouthereau et al., 2001). However, a basement high of the northern SCS continental shelf (Peikang High) is indenting the Western Foothills, driving clockwise rotation and southwesterly escape of an upper crustal block in southwest Taiwan (Ching et al., 2007; Lacombe et al., 2001).

In northern Taiwan, the Western Foothills are bordered on the east by the Hsuehshan Range (Figure 1-2, 1-3). The Hsuehshan Range is an Eocene – Oligocene rift basin of the continental shelf inverted as a regional pop-up structure during collision (Clark et al. 1993; Tillman and Byrne, 1995; Fisher et al., 2002). The Hsuehshan Range constitutes the westernmost range of the slate belt in the metamorphic hinterland of Taiwan. Rocks of the Hsuehshan Range are lightly metamorphosed, with metamorphic grade generally increasing from unmetamorphosed or prehnite-pumpellyite facies in the west to lower greenschist facies in the east. However, the Hsuehshan Range may have upper greenschist facies rocks at its core, so the metamorphic gradient may not simply increase from east to west (Clark et al., 1993).

The eastern boundary of the Hsuehshan Range is the Lishan fault, a major morphologic and structural boundary (Figure 1-2). The Lishan fault has been a controversial structure, in large part because it is not easily mapped in the field and due to its poly-phase tectonic history (Lee et al., 1997). It is generally recognized by an abrupt decrease in metamorphic grade and age from the lower greenschist facies Eocene-Oligocene rocks in the Hsuehshan Range to the west to the prehnite-pumpellyite facies Miocene rocks in the Central Range to the east. Despite its controversial history, many

recent studies regard the Lishan fault as a reactivated rift fault of the northern SCS margin (Fisher et al., 2002; Simoes et al, 2007).

The Central Range to the east contains the highest elevations (~4 km) in Taiwan and comprises the bulk of the metamorphic hinterland (Figure 1-2, 1-3). Metamorphic grade resumes its easterly increase from prehnite-pumpellyite in the west to upper greenschist or lower amphibolite facies in the east (Ho, 1986; Ernst and Jahn, 1987; Beyssacs et al., 2007). The western Central Range (Backbone Range) comprises the eastern half of Taiwan's slate belt, and largely consists of Eocene – Miocene strata of the distal northern SCS margin that were subducted, incorporated into an accretionary prism and uplifted and deformed into the mountain belt (Ho, 1986; Ernst and Jahn, 1987; Huang et al., 1997).

Whereas the Western Foothills, Hsuehshan Range, and western Central Range represent the northern SCS passive margin and foreland basin sedimentary section deformed during collision, the eastern Central Range (Tananao Complex) consists of pre-Tertiary basement of the northern SCS continental margin (Figure 1-2, 1-3). These blocks include metamorphic basement rocks (schists and marbles) as well as ortho- and para-gneisses exposed in northern Taiwan (Ho, 1986; Ernst and Jahn, 1987). A small distribution of mafic material is scattered throughout the eastern Tananao Complex (Beyssacs et al. 2007; Ho, 1986), particularly in the Lichi mélange between the Central Range and the Coastal Range in southern Taiwan (Chung and Sun, 1992), and the Kenting mélange, a large shear zone in Hengchun Peninsula (Chang et al., 2003).

The easternmost province is the Coastal Range, the accreted Luzon arc complex (Figure 1-2, 1-3) (Lundberg and Dorsey, 1990). It is separated from the Central Range by the Longitudinal Valley plate suture. Thrust faults in the Longitudinal Valley

accommodate 2 – 3 cm/yr of shortening but also have a significant left-lateral component of motion as well (Angelier et al. 1996; Yu and Kuo, 2001). The Longitudinal Valley extends south to the South Longitudinal Trough offshore southern Taiwan and to the north where the Ryukyu trench encroaches on central-northern Taiwan (Lallemand et al., 2001).

East of Taiwan, the Philippine Sea plate subducts northward beneath the Eurasia plate at the Ryukyu trench (Lallemand et al., 2001; Kao et al., 1998). The Ryukyu trench extends north and east of Taiwan to Japan, where it pre-dates the Taiwan arc-continent collision (Figure 1-2). However, the lack of pre-Pliocene arc volcanism near Taiwan suggests that it did not extend towards Taiwan until after the onset of arc-continent collision (Shinjo, 1999). Subduction of the Philippine Sea plate generates the Ryukyu arc, Hoping and accretionary prism and forearc basins (Huang et al., 2000; Wang et al., 2004). These features are locally deformed by subduction of the north-trending Gagua Ridge, which is thought to be an Eocene fracture zone or transform boundary within the Philippine Sea plate (Deschamps et al., 1998; Font et al., 2000). Subduction here is also associated with the opening of the Okinawa Trough back-arc basin, which extends into northern Taiwan (Hsu et al., 2001; Lin et al., 2007). Whereas southern and central Taiwan is dominated by compression, northern Taiwan is in a state of tension due to some combination of post-orogenic collapse and the encroaching Okinawa trough and adjacent Ryukyu subduction zone (Kao et al., 1998; Suppe, 1984; Teng, 1996).

1-3: MODELS OF COLLISION FOR TAIWAN

The wealth of studies has prompted various models of mountain-building that propose a spectrum of behavior of converging crust and lithosphere. These studies are

often discussed as mutually exclusive hypotheses, though as discussed in the following sections, each was developed to explain disparate sets of observations that constrain different elements of the mountain-building process in Taiwan. It may be that facets of different models are true to some capacity, and other aspects may be incorrect or have limited applicability.

1-3-1: Thin-Skinned Critical Wedge

The most ubiquitous model for the Taiwan mountain belt is the thin-skinned critical wedge model (Figure 1-4) that describes mountain belts as a wedge of granular media everywhere on the verge of brittle failure (Dahlen et al., 1984; Davis et al. 1983). In this model, the mountain belt grows primarily by frontal accretion of material to a wedge that is deforming against a rigid backstop. The wedge-shape is defined by the slope of the surface topography and a basal décollement that decouples the deforming mountain belt above from passively subducting crust and lithosphere below. The shape of the wedge reflects a balance of strength within the wedge and shear stress on the basal décollement. With continued convergence, the wedge will thicken or propagate into the foreland to maintain its geometry.

The critical wedge model has been applied to numerous other fold-and-thrust belts and accretionary wedges throughout the world and geologic time. Subsequent studies in Taiwan and other mountain belts have expanded on this model by incorporating the coupled effects of erosion, sedimentation and climate (Morley, 2007; Whipple and Meade, 2004; Whipple, 2009; Willet, 1999b) as well as thermal effects and rheological heterogeneity (Willet, 1993; Willet, 1999a). As applied to Taiwan, the critical wedge model predicts the Luzon arc is behaving as the rigid backstop, while steady-state

subduction of the northern SCS continental margin delivers sediments to a constantly deforming sedimentary mountain belt (Figure 1-4).

The strongest support for this model comes from topographic profiles of Taiwan and the décollement identified in the post-rift sedimentary section beneath the Western Foothills foreland thrust belt (Suppe, 1981). The décollement occurs ~6-10 km deep in the foreland, and dips shallowly towards the hinterland (Suppe, 1980; Carena et al., 2002; Johnson and Segall, 2004). Major thrusts in the Western Foothills root into the décollement, suggesting it may function as the basal décollement described by the critical wedge model. More recent studies have sought to justify the critical wedge model beyond the foreland fold-and-thrust belt (Carena et al., 2002; Willet et al., 2003; Johnson et al., 2005), but the existence of such a thin-skinned décollement beneath the Hsuehshan and Central Ranges remains highly controversial.

1-3-2: Thick-Skinned Wedges

Despite the popularity of the thin-skinned model in Taiwan, there are a number of first-order observations that suggest the basement is involved to a significant degree in the mountain-building process in Taiwan. This is particularly evident in the Central Range where the pre-Tertiary basement of the northern SCS continental margin is exhumed and exposed at the surface (Ho, 1986). Additionally, rift faults in the northern SCS basement have been inverted in Taiwan's foreland beneath the thin-skinned structures exposed in the Western Foothills (Hung et al., 1999; Lee et al., 2002; Mouthereau et al., 2006). A number of studies have proposed thick-skinned wedge models for Taiwan to account for these observations (Figure 1-5).

One style of thick-skinned wedge model invokes a shallow-dipping, deeper mid-crustal décollement (Figure 1-5a) that is active contemporaneously with the shallow décollement of the thin-skinned wedge (Mouthereau et al, 2001; Lacombe and Mouthereau, 2002; Yamato et al., 2009). Such a deep décollement has been inferred at ~10-15 km depth from inversion structures, structural restorations and seismicity in Taiwan's foreland (Mouthereau et al., 2001; Mouthereau et al, 2002). These studies further suggest such a décollement may either be a pre-existing feature or develop from the inherited rheology of the northern SCS continental margin (Yamato et al., 2009; Mouthereau and Petit, 2003).

Other studies based on thermochronologic constraints and numerical modeling have emphasized underplating over frontal accretion (Figure 1-5b) as a possible mechanism for the development of both the Hsuehshan and Central Ranges (Beyssac et al.,2007; Fuller et al., 2006; Simoes et al., 2007). These models predict the shallow décollement observed in the foreland down-steps into thick, buoyant continental crust as it attempts to subduct beneath the Philippine Sea plate, shaving off slivers of the crust into the overlying orogenic wedge. Instead of two décollements at different structural levels, this thick-skinned wedge model requires a single décollement that down-steps towards the hinterland.

1-3-3: Forearc Subduction

Wedge models describe how convergence between the Eurasia plate and Philippine Sea plate may be accommodated by shortening in the northern SCS continental margin. However, convergence appears to be accommodated by shortening in the forearc as well, as the undeformed Luzon arc south of Taiwan is much wider than the

Luzon arc near Taiwan or the accreted arc in the Coastal Range. Marine geophysical studies have shown evidence of backthrusting throughout the forearc domain (Malavieille et al., 2002; McIntosh et al., 2005; Lundberg et al., 1997), which may be accommodating up to ~4 cm/yr of the plate convergence (Yu et al., 1997; Malavieille and Trullenque, 2009).

These observations indicate the Luzon arc may not behave as a simple rigid backstop as presupposed by the critical wedge models. Instead, these observations suggest the forearc block may be subducting as part of the collision process (Figure 1-6). The ramifications of this have been explored by analog and numerical modeling studies of Taiwan (Chemenda, et al. 1997; Tang et al., 2002; Malavieille and Trullenque, 2009). These studies suggest a model where the forearc breaks near the presumably weak volcanic arc and subducts at the early stage of collision. Forearc subduction induces rapid shortening and thickening of the rear of a critical wedge as it grows into the sub-aerial Central Range.

1-3-4: Lithospheric Collision

Wedge-based models assume that mountain-building is in one way or another driven by steady-state subduction of the northern SCS continental margin, a requirement not clearly supported by seismicity and regional tomography velocity models. Seismicity is generally diffuse but limited to the upper ~60 km of the lithosphere beneath Taiwan, so that no Wadati-Benioff zone may be discerned north of latitude ~22.5° N (Wu et al., 1997; Wu et al., 2004). Tomography models reveal Moho is depressed to ~60 km beneath the mountain ranges, suggestive of a deep crustal root (Kuo-Chen et al., 2012; Wu et al., 1997; Rau and Wu, 1995). Additionally, recent magnetotelluric data reveal the Lishan

fault to be a conductive body that penetrates deep into the crust beyond any proposed thin-skinned décollement (Bertrand et al., 2009).

Whereas the wedge models only involve the upper-middle crust in the collision, these observations support a model of collision that involves thickening of the crust and possibly lithosphere in both the Eurasia and Philippine Sea plates (Figure 1-7) (Wu et al., 1997). Although it predicts continuous deformation throughout a lithospheric-scale orogen, it does not necessarily preclude a detachment fault as observed in the Western Foothills. The lithospheric-scale collision model also appeals to an elevated geothermal gradient to explain a distinct lack of seismicity beneath the Central Range. In this model, the Central Range is deforming aseismically under ductile conditions.

1-4: VARIABILITY OF RIFTED CONTINENTAL MARGINS

A fundamental implication of any of these models is that Taiwan is a consequence of convergence between the subduction zone and thick, buoyant continental crust that would likely resist subduction. These models assume an impinging margin with crust ~30 km thick containing horst-and-graben rift basins typical of continental shelves. However, much work has been done on rifted continental margins around the world that reveal a wide-range of structural styles and compositional heterogeneities that may influence the collision process in different ways (Afonso and Zlotnik, 2011; Beltrando et al., 2010; Reston and Manatschal, 2011).

In the North Atlantic, relatively narrow magma-rich margins (Figure 1-8a) contain large volumes of intrusive and extrusive volcanic rocks (Hopper et al., 2003; White et al., 1987). These are manifest as flood basalts onshore or in the shallow-water continental shelf, seaward-dipping reflectors in seismic profiles from lava flows (White et

al., 1987), and high-velocity lower crustal layers attributed to magmatic underplating (Korenaga et al., 2000) or pervasive lower crustal intrusions (White et al., 2008). The excessive magmatism may be generated by rapid advection of warm asthenosphere during thinning or by the presence of a hot mantle plume. Vigorous magmatism during breakup and initial seafloor spreading may also generate atypically thick ocean crust in the distal margin of magma-poor rifted margins (Boutilier and Keen, 1999; Mutter et al., 1984).

In contrast to the magma-rich rifted margins, magma-poor rifted margins (Figure 1-8b) such as the Newfoundland-Iberia margins can be ~100 – 200 km wide and exhibit extreme crustal thinning with little associated magmatism (Whitmarsh et al., 2001; Pérez-Gussinyé et al., 2001). Magma-poor margins are characterized by wide tracts of hyper-extended continental crust that consists of faulted crustal blocks with listric faults that sole into low-angle detachment faults in the crust or upper mantle (Reston et al., 1996). Crust may be thinned to zero thickness, exposing serpentinized upper mantle at the continent-ocean transition in the distal margin (Whitmarsh et al., 2001).

The northern SCS continental margin is extremely wide (100s of km) and has been described as an 'intermediate' magmatic margin, since it exhibits characteristics of both magma-rich and magma-poor margins (Clift et al., 2001a). Marine geophysical studies have identified rotated crustal blocks typical of highly extended continental crust in magma-poor margins along a wide continental slope (Clift et al., 2001a; Huang et al, 2005; Zhu et al., 2012). However, they have also revealed numerous volcanic bodies interspersed throughout a wide continent-ocean transition, including a high-velocity lower crustal layer that may be indicative of mafic magmatism (Nissen et al., 1995b; Wang et al., 2006; Yan et al., 2001b; Zhao et al., 2010). Additionally, syn- and post-rift

volcanic rocks have been recovered in wells throughout rift basins of the continental shelf (Li and Rao, 1994; Yan et al., 2006; Wang et al., 2012). Despite the evidence for at least moderate syn-rift magmatism, there have been no observations of seaward-dipping reflectors or flood basalts typically associated with highly magmatic margins. As such, the relationship between rifting and magmatism in the northern SCS is poorly understood.

The nature of the northern SCS margin near Taiwan has been more controversial. Hsu et al. (2004) interpreted weak magnetic signals as possible ocean crust outboard of the continental shelf rather than the wide, highly extended margin documented in the central and western northern SCS margin. Subsequent gravity forward modeling suggested this crust was ~12 km thick (Yeh and Hsu, 2004) – much thicker than typical ocean crust, but perhaps suggestive of thick oceanic or volcanic crust of magma-rich margins. However, prior to the beginning of this dissertation, few high-resolution crustal-scale constraints have been available to study the rifted margin in the northeastern SCS near Taiwan.

1-5: DISSERTATION OUTLINE

The disparate models for the Taiwan collision highlight the uncertain behavior of the northern SCS margin during arc-continent collision. These models all suffer from a lack of consideration for the style of rifted margin colliding with the Luzon arc, which is likely to exert a strong influence on the collision process. Because of the southward propagation of the collision, Taiwan is an ideal location to test the existing models for collision, but also examine how the nature of the rifted margin impacts collisional dynamics. Since the rifted margin near Taiwan has previously been relatively

understudied, the new geophysical data used in this study also present an opportunity to investigate rifting and magmatism in the northern SCS margin. Ultimately, the goal of this dissertation is to apply crustal-scale geophysical methods to:

1) ascertain the crustal-scale structure and composition of the northeastern SCS rifted margin southwest of Taiwan as an analog for the pre-collision state of the Taiwan mountain belt
2) investigate rifting processes and magmatism in the northeastern SCS
3) document the early-stage collisional deformation of the northeastern SCS margin offshore southern Taiwan
4) relate these findings to mapped structures in the onshore mountain belt, if possible

The dissertation is organized into chapters consisting of published or publication-ready manuscripts that address these goals.

Chapter 2: Multiple Attenuation in Crustal-Scale Imaging: Examples from the TAIGER Marine Reflection Data Set (Lester and McIntosh, 2012 Marine Geophysical Research)

Chapter 2 documents the 2009 TAIGER (Taiwan Integrated Geodynamics Research) marine geophysical acquisition program. This program acquired over ~10,000 km of 2D marine seismic reflection profiles and wide-angle seismic data recorded by over ~270 ocean bottom seismometers (OBS) and onshore land seismometers with the goal of providing new constraints on the systems that impact the dynamics of the Taiwan arc-continent collision. Here I develop a processing flow for the seismic reflection data

with an emphasis on multiple attenuation. Effective treatment of multiples is necessary to achieve many of the deep-crustal imaging objectives of the TAIGER program.

The results of this chapter demonstrate how 2D surface-related multiple elimination (2D SRME), radon filtering and offset weighting are highly complementary techniques that can effectively attenuate multiples in a broad range of water depths, seafloor topographies, and lithologies. The success of these techniques are demonstrated on three seismic reflection profiles – two from the rifted margin southwest of Taiwan and one from the Ryukyu trench east of Taiwan. The processing flow discussed in detail in this chapter is also applied to the seismic reflection data that are the backbone of subsequent chapters of the thesis.

Chapter 3: Rifting and Magmatism in the Northeastern South China Sea from Wide-Angle Tomography and Seismic Reflection Imaging (Lester et al. in prep Journal of Geophysical Research)

In chapter 3 I discuss a new travel-time tomography velocity model and seismic reflection images that delineate the rift architecture and magmatic features of the rifted margin in the northeastern SCS. These data reveal moderately stretched continental crust along the continental shelf and a wide zone of highly thinned and magmatically intruded continental crust in the distal margin rather than oceanic crust as previously interpreted. The crust beneath the continental slope is as thin as ~4 km thick in a highly stretched rift basin that contains tilted fault blocks that sole into a low-angle detachment fault. Despite the extreme crustal thinning and strain localization in this basin, little to moderate syn-rift magmatism accompanied rifting here.

The ~12-15 km thick crust of the distal continent-ocean transition displays more evidence for magmatic modification. This includes a high-velocity lower crustal layer

that is likely formed by mafic magmatism, volcanic zones imaged in reflection data at the top of basement that disrupt and deform overlying post-rift strata, and sills intruded into the post-rift sedimentary section. Recently published dredged samples of post-rift Miocene basalts (Wang et al., 2012), coupled with these observations, suggest much of the inferred magmatism may be associated with post-rift seafloor spreading. A 1D thermal model of decompression melting during pure shear rifting (Bown and White, 1995) indicates magmatism in the distal margin is inconsistent with uniform thinning of the lithosphere. Recently published dredged samples of post-rift Miocene basalts (Wang et al., 2012), coupled with the new seismic observations, further suggest much of the magmatism may be associated with post-rift seafloor spreading. The post-rift magmatism may have been induced by convective removal of late refractory pre-rift continental lithosphere during breakup and subsequent seafloor spreading in the SCS.

Chapter 4: Crustal Accretion in the Manila Trench Accretionary Wedge at the Transition from Subduction to Mountain-Building in Taiwan (Lester et al., in submission Earth and Planetary Science Letters)

Chapter 4 introduces a new travel-time tomography velocity model and coincident seismic reflection image that illuminate the crustal structure of an incipient mountain belt offshore southern Taiwan. These data track the distal continental margin as it subducts eastward at the Manila trench subduction zone. The velocity model and seismic reflection image reveal similar features as described in chapter 3, including the high-velocity lower crustal layer, volcanic bodies and possible breakup unconformity and syn-rift strata. Beneath the lower slope of the Manila trench accretionary wedge, crust thins from ~10-14 km thick to ~6 km thick. The lower slope of the accretionary wedge consists of westward-verging imbricate thrusts and folded strata up to 10 km thick.

A sharp decrease in bathymetry marks the transition from the lower slope of the accretionary wedge to the upper slope (Hengchun Ridge) where the velocity model reveals a fast (> 6.0 km/s) seismic velocity anomaly at the base of the wedge. The anomaly may be indicative of highly extended crust that has been subducted and structurally underplated to the wedge. The upper slope of the prism is the morphological extension of the Central Range to the north, where pre-Tertiary basement blocks of the northern SCS rifted margin are exposed. These observations support a link between the Central Range and the wide zone of highly thinned continental crust that constitutes the distal continental margin.

Chapter 5: Active Extension in Taiwan's Pre-Collision Zone: A New Model of Plate-Bending in Continental Crust (Lester et al., 2012 Geology)

Chapter 5 presents a surprising observation from seismic reflection data across the continental shelf southwest of Taiwan. These data reveal active extension along a deep-seated rift fault near the continental shelf break. While ubiquitous minor flexural faulting may be observed throughout the Taiwan foreland, this fault is a listric rift basin-bounding normal fault that penetrates deep into the crust and forms a significant fault scarp with ~850 m of relief. These observations, along with a geodynamic model of collision between a subduction zone and young, weak passive margin suggests the recent extension may be the expression of plate bending in the continental crust as thin crust of the distal continental margin subducts at the Manila trench. A similar extensional episode prior to the onset of arc-continent collision at ~7 Ma has been identified in other rift basins of the northern SCS margin in Taiwan's foreland, further suggesting collision may be preceded by bending-related extension in the continental shelf.

There a number of similarities between the major rift fault imaged at the continental shelf edge southwest of Taiwan and the Lishan fault that suggest the Lishan fault may have been a similar fault that was inverted when the continental shelf collided with the subduction zone. In this scenario, the Lishan fault approximates the former continental shelf edge in Taiwan, dividing Taiwan into a western domain representing collision of the thick crust of the continental shelf and an eastern domain representing subduction and collision of thin crust along the distal margin with the Manila trench as suggested in chapter 4.

1-6: SUMMARY

This dissertation discusses the evolution of the northeastern SCS margin from rifting at the start of a Wilson cycle to mountain-building during arc-continent collision at the end of the Wilson cycle. In doing so, I seek to address outstanding issues regarding the behavior of colliding continental crust during collision. Chapter 2 functions as a methodology chapter that discusses in detail the seismic reflection data used in the dissertation. Chapter 3 identifies thick, moderately stretched continental crust along the continental shelf and a wide distal margin that contains highly thinned continental crust modified by Miocene post-rift magmatism. Chapter 4 tracks the thin crust of the distal margin into the Manila trench subduction zone, where there is evidence that the early growth of the mountain belt is driven by structural underplating of highly thinned continental crust in advance of the encroaching continental shelf. Chapter 5 focuses on a surprisingly active major rift fault and argues that collision in Taiwan was preceded by flexural-type extension in a weak continental shelf as the thin crust of the distal margin is subducted. This chapter concludes with arguments that such faults may be inverted once

the continental shelf becomes involved in the collision process and proposed the Lishan fault is an example of such a fault. The findings in this dissertation ultimately suggest a link between the rifting that formed the continental margin and the way that it deforms into a mountain belt during collision.

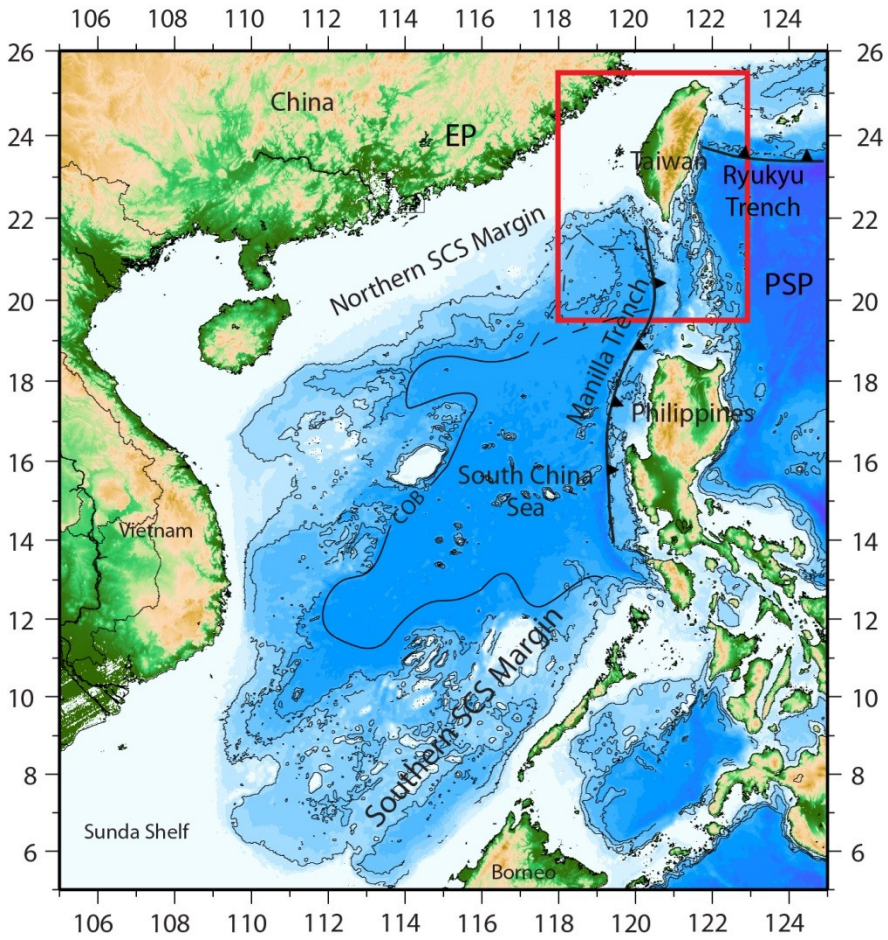

Figure 1-1: Regional map of the South China Sea marginal basin in Southeast Asia. Major tectonic features are labeled including the Eurasia Plate (EP), Philippine Sea Plate (PSP), Northern and southern SCS rifted margins, Manila trench and Ryukyu trench subduction zones. Red box is location of figure 1-2.

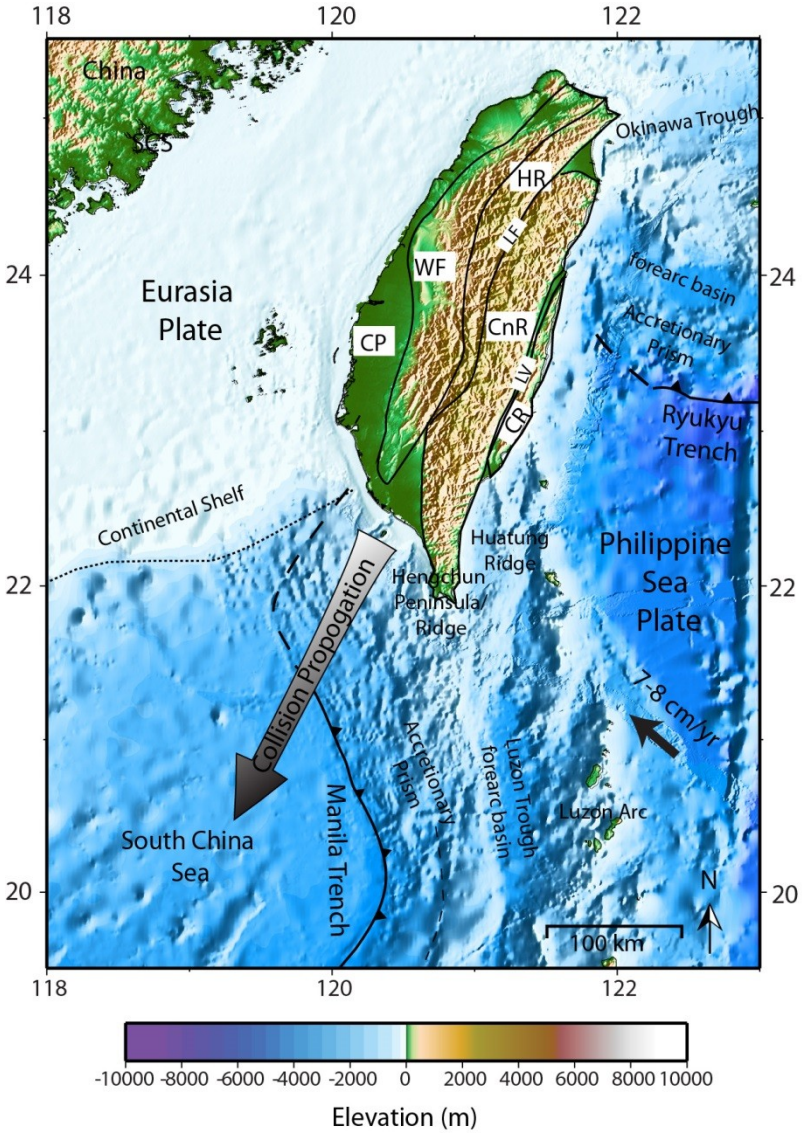

Figure 1-2: Elevation map of the Taiwan arc-continent collision. Onshore Taiwan consists of five tectonostratigraphic terranes: CP – Coastal Plain foreland basin; WF – Western Foothills fold-and-thrust belt; HR – Hsuehshan Range inverted Tertiary rift basin; CnR – Central Range metamorphic hinterland; CR – Coastal Range accreted arc complex. LF – Lishan fault; LV – Longitudinal Valley. Plate converge is NW-SE at 7-8 cm/yr, but the collision is propagating to the southwest due to the obliquely oriented continental margin and subduction zone. The collision is older in central-northern Taiwan, but just beginning offshore southern Taiwan.

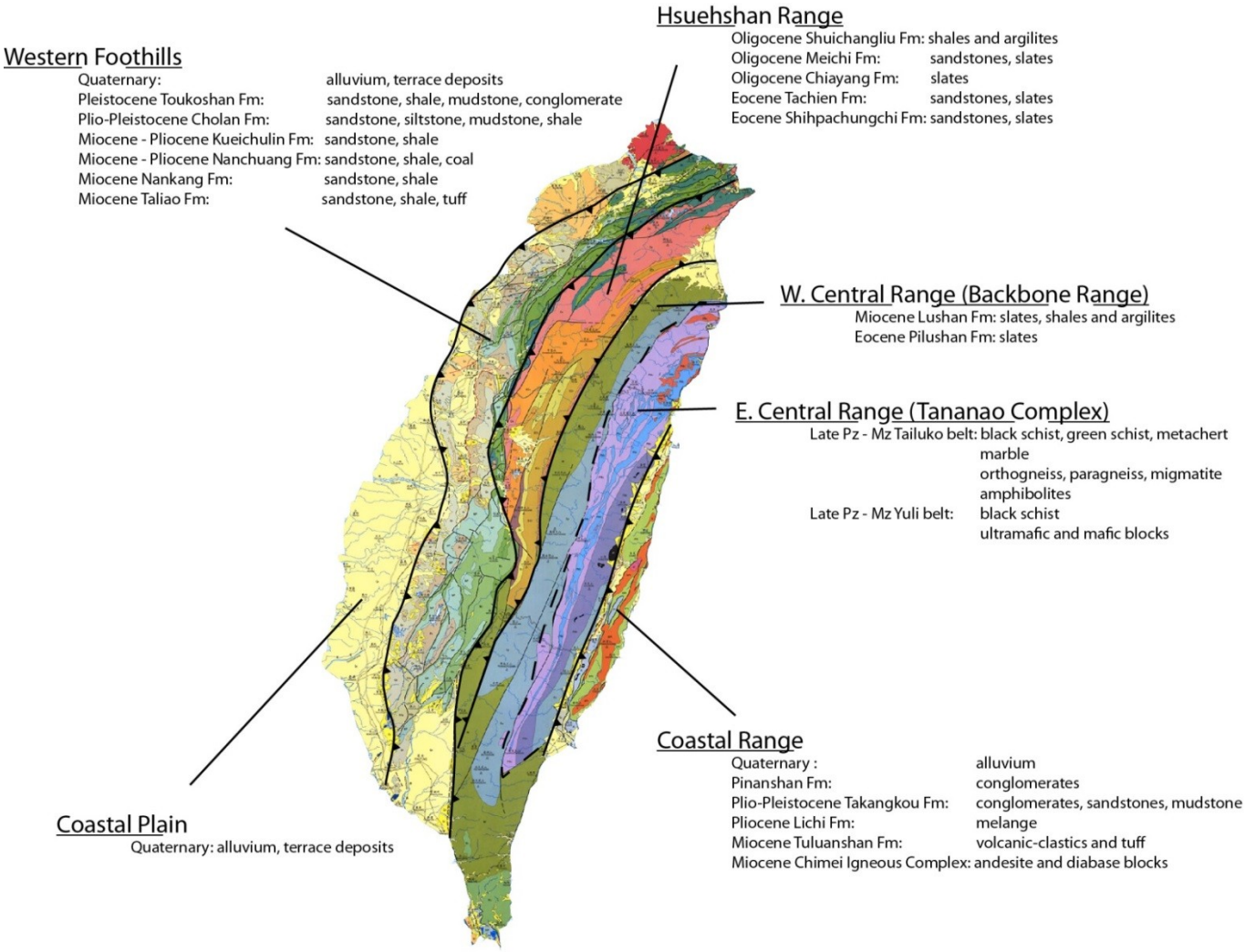

Figure 1-3: Geologic map of Taiwan (modified from Ho, 1988).

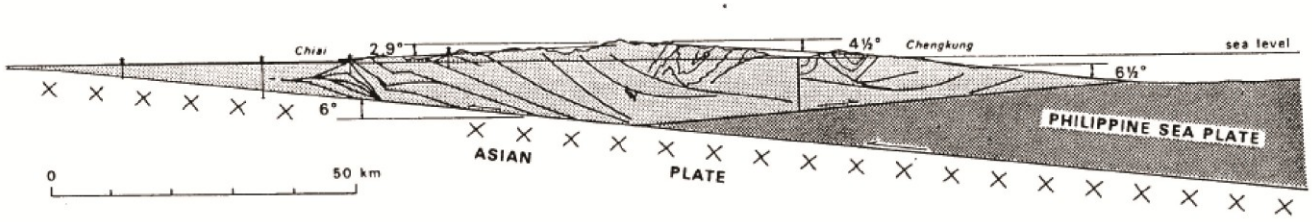

Figure 1-4: Thin-skinned critical wedge model (from Davis et al., 1983). In this model, the northern SCS continental margin of the Eurasia plate subducts beneath the Luzon arc of the Philippine Sea plate. The Luzon arc acts as a backstop scraping off incoming passive margin sediments into a deforming wedge. A shallow-dipping décollement decouples the orogenic wedge from the subducting crust below.

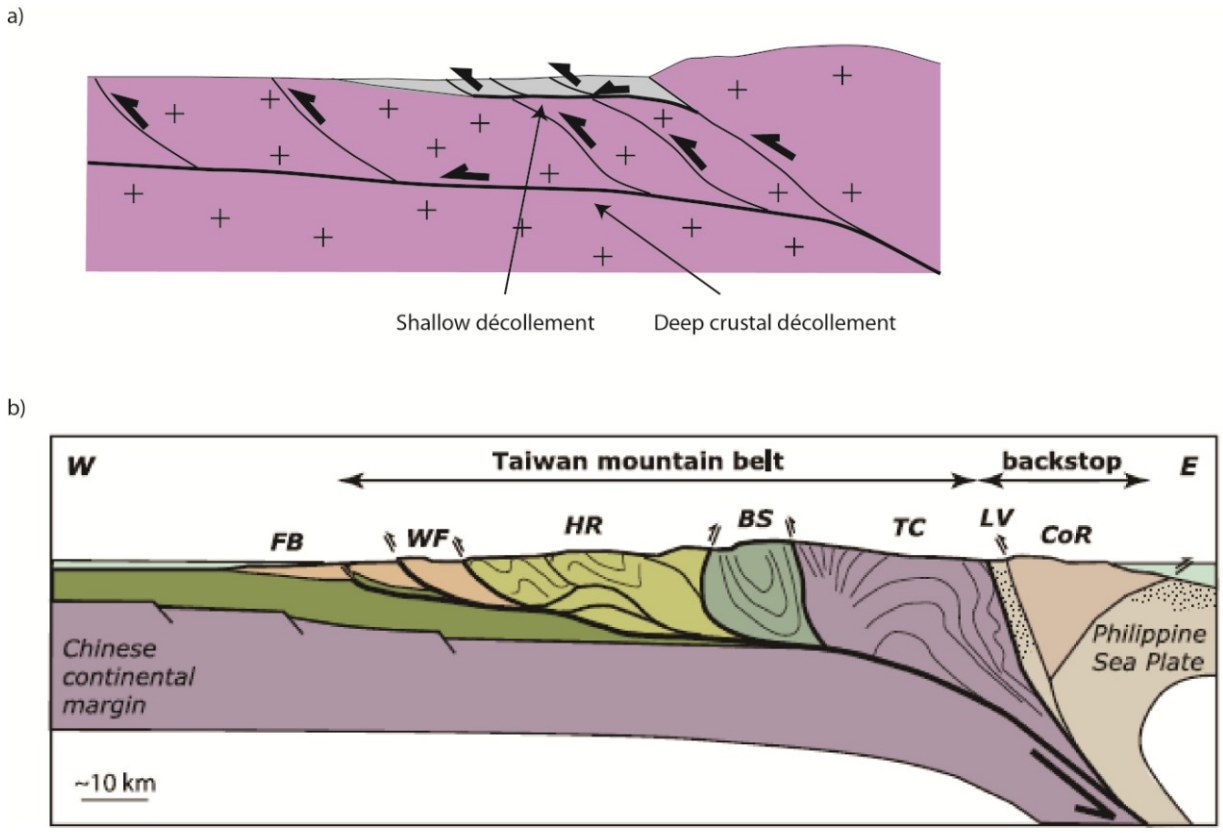

Figure 1-5: Thick-skinned critical wedge models invoking (a) simultaneous shallow and deep crustal décollements (after Lacombe and Mouthereau, 2002) or (b) a single décollement that steps down into subducting crust in the hinterland, thickening the crust by underplating (from Simoes et al. 2007).

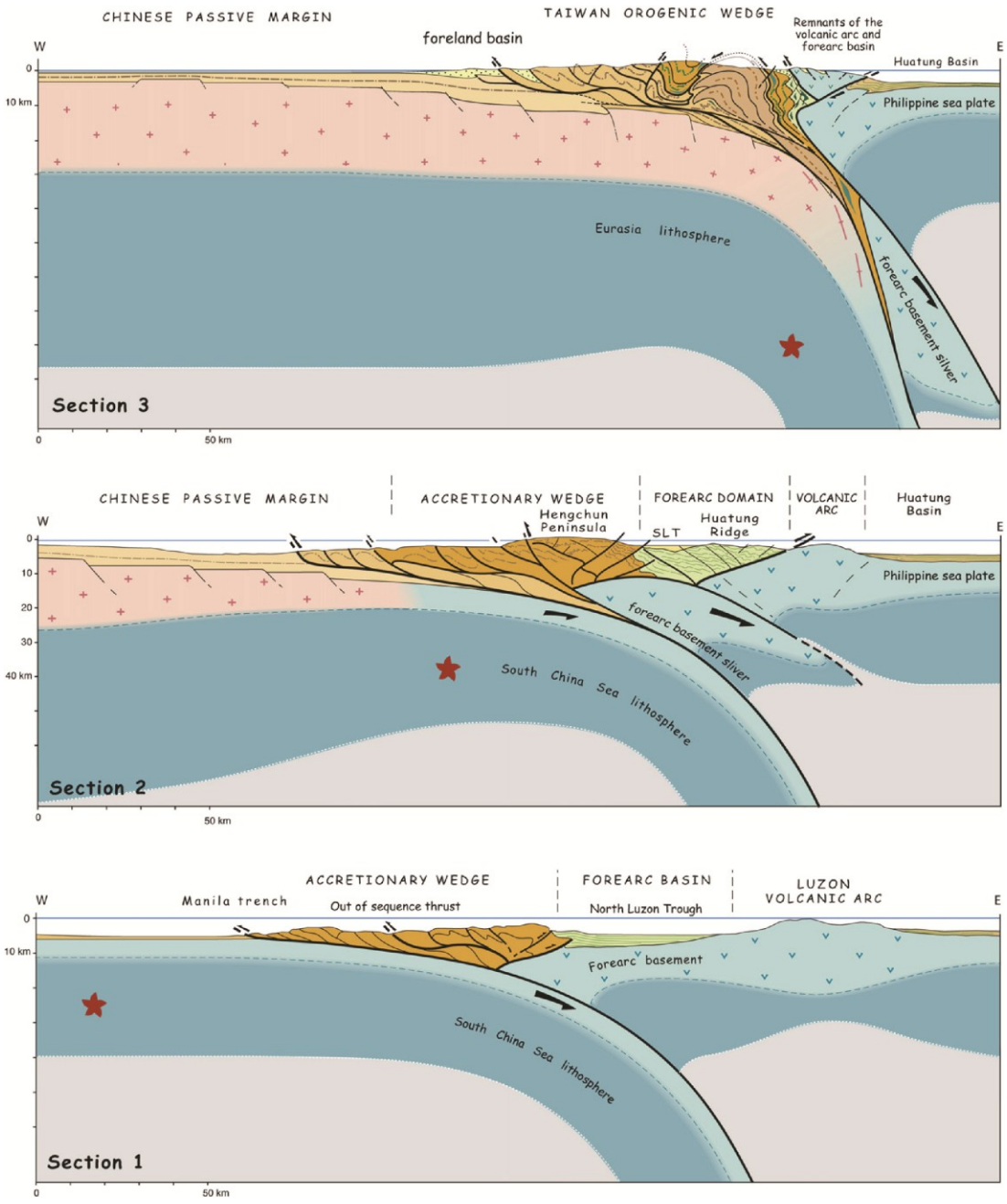

Figure 1-6: Forearc subduction variant of the critical wedge models (from Malavieille and Trullenque, 2009). Following subduction of the SCS lithosphere (section 1) the forearc block shortens at the early stages of collision, enhancing deformation of the incipient mountain belt (section 2) and eventually breaking off from the arc and subducting with the down-going Eurasia plate (section 3).

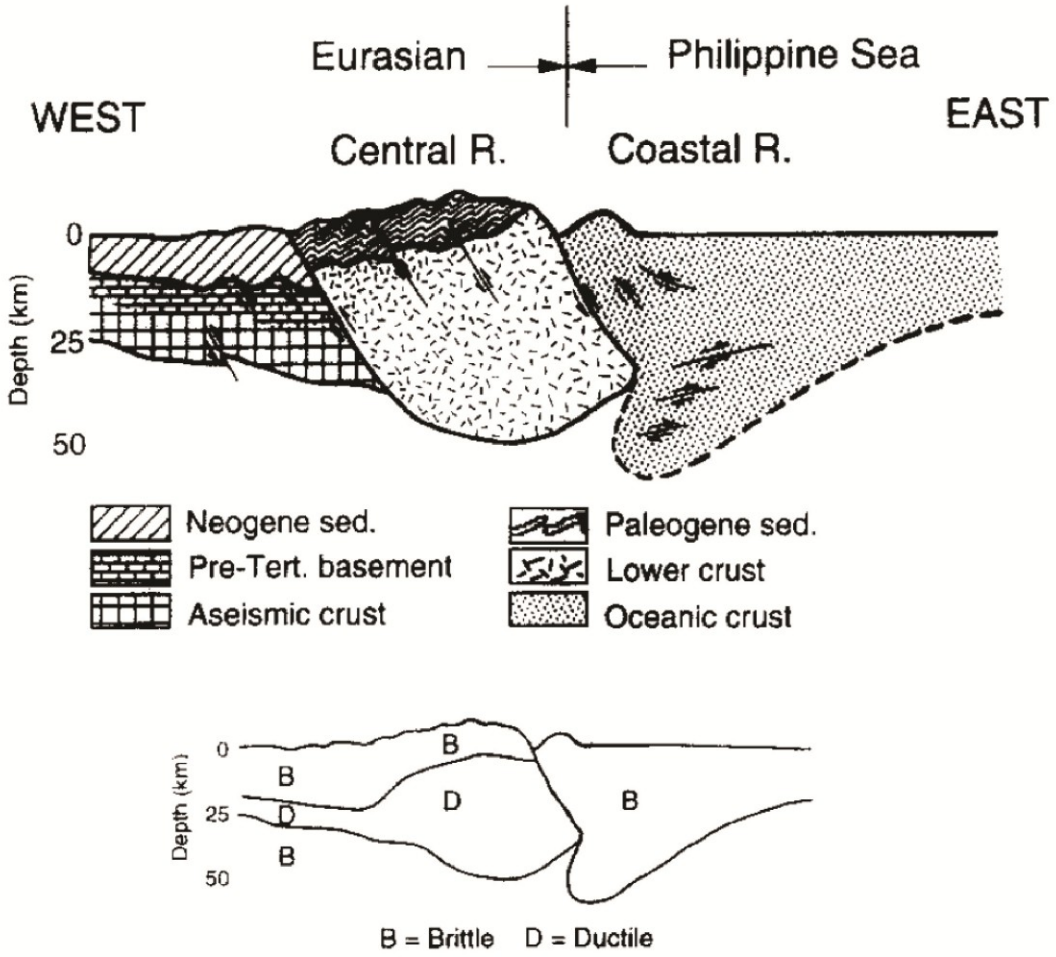

Figure 1-7: Lithospheric-scale collision model (from Wu et al., 1997) where the entire crust and lithosphere of the continental margin and arc are thickening in the collision. In this model, neither plate is actively subducting, but a ductile crustal root has developed under the Central Range.

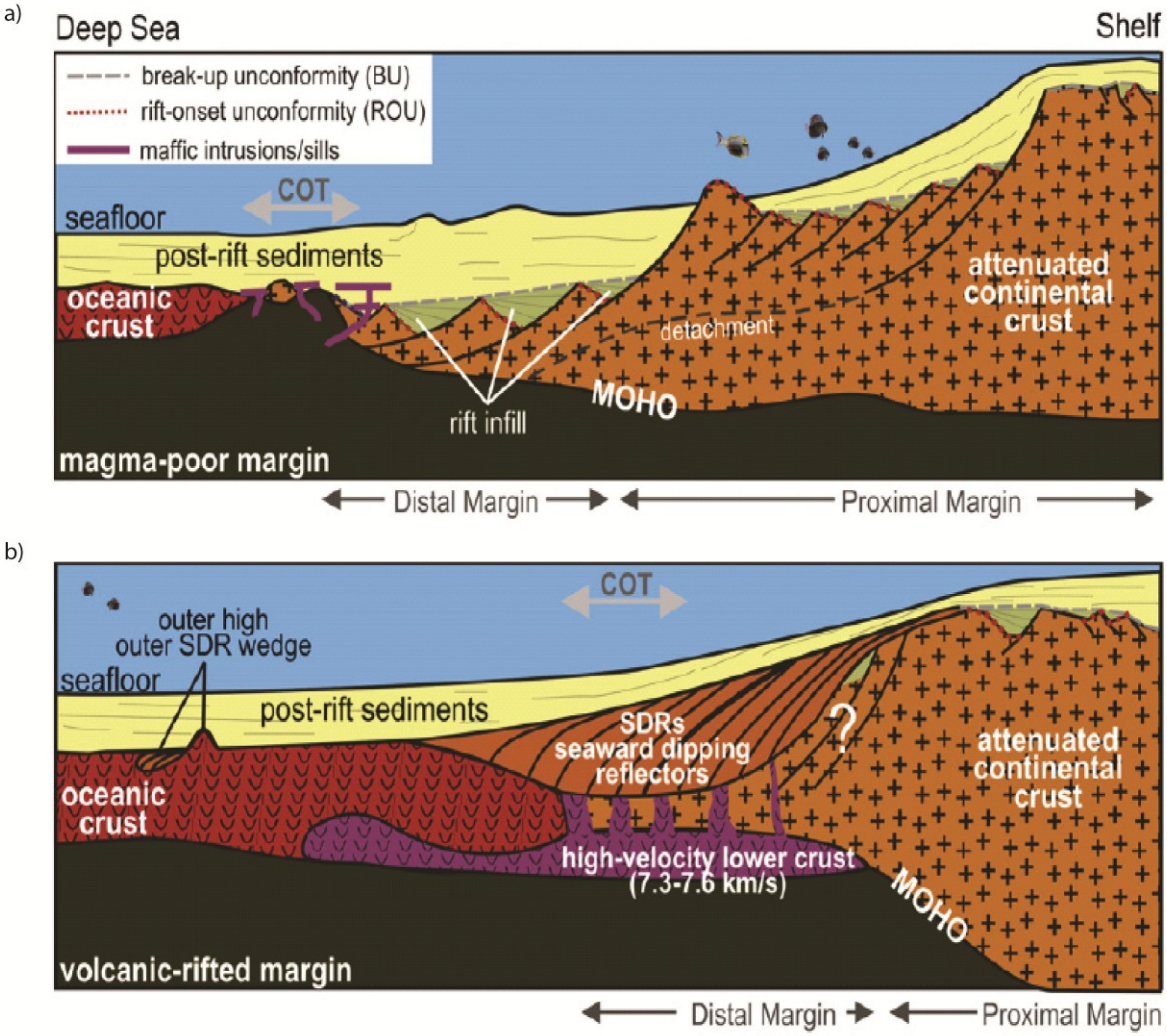

Figure 1-8: a) Magma-poor rifted margins are characterized by tilted fault blocks with normal faults that sole into a low-angle detachment fault. In the distal margin, brittle deformation may include the whole crust and potentially upper mantle. The continent-ocean transition (COT) may contain exhumed upper mantle at the seafloor. b) Magma-rich margins contain abundant intrusive and extrusive volcanic rocks. These include syn-rift volcanic flows manifest as seaward-dipping reflectors at the top of basement in seismic reflection data and a high-velocity lower crustal layer due to magmatic underplating or lower crustal intrusions. Ocean crust may be atypically thick at the distal end of the margin (from Frank, 2012).

Chapter 2: Multiple Attenuation in Crustal-Scale Imaging: Examples from the TAIGER Marine Reflection Data Set

2.1 INTRODUCTION

Taiwan was created when the northern South China Sea (SCS) continental margin of the Eurasia plate began colliding with the Luzon arc of Philippine Sea Plate in the late Miocene. As one of only a handful of young, active arc-continent collisions, Taiwan has been the subject of many geologic investigations aimed at understanding the dynamics of arc-continent collision. As a consequence, many models have been developed here that have been applied not only to Taiwan, but to other mountain belts around the world (Davis et al. 1983; Wu et al. 1997). These models propose a spectrum of crustal and lithospheric behaviors during collision that have not been tested due to a lack of high-resolution crustal-scale geophysical constraints.

During the summer of 2009, over 10,000 km of 2D marine seismic reflection data were acquired as part of the joint NSF and Taiwanese-funded TAIGER program with the goal of testing and refining hypothesized models of arc-continent collision (Figure 2-1). These data, along with wide-angle seismic data recorded by OBS and land instruments, were acquired in a wide range of marine imaging environments with the goal of constraining different aspects of the orogen, as well as northern SCS continental margin southwest of Taiwan, Manila subduction system south of Taiwan and Ryukyu subduction system east of Taiwan -systems that impact the dynamics of the Taiwan arc-continent collision.

The TAIGER active source seismic program was designed to acquire data along different spatial transects that may represent different stages of collision. In particular,

multi-channel seismic reflection data were acquired offshore southern Taiwan to image the incipient collision, as well as the northern SCS continental margin and Manila trench subduction system south of the collision. The goal of imaging the northern SCS margin and Manila subduction system (i.e. accretionary prism, Luzon arc, forearc basin) is to delineate the crustal structure and materials thought to be similar to those involved in the collision.

Similarly, multi-channel seismic reflection profiles were acquired east of Taiwan in the Philippine Sea to image the offshore extent of collision-related deformation and the Ryukyu subduction system, where the Philippine Sea plate is subducting northward adjacent to the Taiwan arc-continent collision. While the northern SCS margin, Manila and Ryukyu subduction systems merit study in their own right, the purpose of imaging these systems for the TAIGER project is to delineate the evolution of arc-continent collisions from the initial pre-collision stage, as represented by the northern SCS continental margin and Manila subduction system south of Taiwan, to the post-collision stage near the intersection of Taiwan and the Ryukyu trench.

There is a wide range of imaging targets within such an extensive dataset, including relatively flat strata of the northern SCS margin and abyssal plane, highly deformed sedimentary rocks of the Manila trench and Ryukyu trench accretionary prisms, and deep crystalline crustal structure, each with their own imaging challenges. Attenuation of multiples is one of the most ubiquitous of these challenges, and one of the primary challenges of any marine seismic reflection data set. Multiples are particularly problematic in crustal-scale imaging, as they often obscure reflections from deep imaging targets. The TAIGER reflection data span a variety of water depths, seafloor topographies, and lithologies, making the effective attenuation of all multiples an arduous

task. The purpose of this paper is to develop a consistent imaging strategy for TAIGER marine seismic reflection data, with particular focus on multiple attenuation. We present one profile from each of three acquisition legs (Figure 2-1) to demonstrate some of the challenges multiples impose in crustal-scale imaging, and a strategy for attenuating much of this unwanted energy.

2.2 GEOLOGIC BACKGROUND

The Taiwan arc-continent collision began 4–7 Ma when buoyant continental crust of the Eurasia plate encountered the Luzon arc of the Philippine Sea plate at the Manila trench (Liu et al. 2001; Suppe 1984; Huang et al. 1997; Lee et al. 2006; Wang 2001). Convergence between the Philippine Sea plate and the Eurasia plate is also accommodated by subduction of SCS lithosphere beneath the Philippine Sea plate at the Manila trench south of Taiwan, and by subduction of the Philippine Sea plate beneath the Eurasia plate at the Ryukyu trench east and north of Taiwan (Figure 2-1). A convergence rate of 7–8 cm/ year in a northwest direction has been well established from GPS data, earthquake focal mechanisms, and global plate models (Chamot-Rooke and Le Pichon 1999; Yu et al. 1997; Hall 2002; Lee and Lawver 1993; Seno et al. 1993). The convergence direction and orientations of the north-trending Luzon arc and northeast-trending northern SCS continental margin created an oblique arc-continent collision, which has led many to view the collision as propagating to the southwest, so that different spatial locations represent different temporal stages of collision (Byrne and Liu 2002; Lee et al. 2006; Suppe 1984).

Southwest of Taiwan, several reflection profiles were acquired in both dip and strike orientations across the northern SCS continental margin. These data extend from

the relatively shallow-water continental shelf to intermediate water depths of the distal continental margin. Geophysical and drilling observations of the northern SCS margin in the southwest and central SCS have revealed the margin to consist of passive margin sediments overlying moderately extended crust along the continental shelf and a wide distal margin consisting of highly thinned, volcanically intruded continental crust along the distal margin (Clift et al. 2001; Hayes et al. 1995; Nissen et al. 1995b; Nissen et al. 1995a; Yan et al. 2001; Wang et al. 2006). However, Hsu et al. (2004) interpreted magnetic anomalies that suggest crust of the distal margin in the vicinity of Taiwan may be volcanically thickened ocean crust, rather than thinned continental crust.

Following rifting of the south China block, the SCS opened by seafloor spreading during Oligocene - Miocene (Briais et al. 1993; Taylor and Hayes 1983). Subduction of the SCS oceanic lithosphere at the Manila trench beginning in the Miocene created a doubly-vergent accretionary prism, the North Luzon arc and North Luzon forearc basin (Figure 2-1). Several profiles were acquired to image these features away from Taiwan where they are not deformed by collision processes and likely represent the initial conditions prior to arc-continent collision.

The elements of the Manila trench subduction system are also associated with offshore morphologic features of the Taiwan collision. For example, Hengchun Ridge and its emergent equivalent, the Hengchun Peninsula, are the morphologic continuation of the accretionary wedge to the south of Taiwan and the Central Range to the north in Taiwan (Huang et al. 1997). While forearc basin sediments are relatively undeformed in the subduction regime, near Taiwan they are backthrust over the forearc to form the Huatung Ridge (Chi et al. 2003; Lundberg et al. 1997; McIntosh et al. 2005). Onshore, these sediments, as well as the Luzon arc, are further telescoped and obducted to form the

Coastal Range along Taiwan's east coast. The TAIGER profiles immediately south of Taiwan were acquired to constrain the deformation of the accretionary prism, Luzon arc, and forearc basin during the initial stages of collision.

While the Philippine Sea plate overrides the Eurasia plate south of Taiwan at the Manila trench, east of Taiwan the Philippine Sea plate subducts northward beneath the Eurasia plate at the Ryukyu trench, where it has generated the Yaeyaema accretionary prism, Hoping and Nanao forearc basins, Ryukyu arc, and Okinawa Trough back-arc basin (Figure 2-1). The Ryukyu trench extends north and east from Taiwan, where it predates the Taiwan arc-continent collision. However, the lack of pre-Miocene volcanism in the southwestern Ryukyu arc suggests that this subduction system was not established near Taiwan until the onset of arc-continent collision (Shinjo 1999).

Unlike southern and central Taiwan, northern Taiwan is in a state of tension, rather than collision-related compression (Yu et al. 1997; Kao et al. 1998). This has been attributed in varying measures to post-collisional gravitational collapse and the encroachment of the Okinawa Trough or Ryukyu trench (Teng 1996; Kao et al. 1998; Huang et al. 2000; Wang et al. 1999). Additionally, the Luzon arc accreted in the Coastal Range is no longer present north of the Ryukyu trench, suggesting it has been subducted with the Philippine Sea plate or subsided as part of the post-collisional relaxation process. TAIGER data east of Taiwan was acquired to document the accretion and eventual demise of the Luzon arc during arc-continent collision, as well as the complicated dynamic interplay between post-collisional processes, subduction at the Ryukyu trench and back-arc rifting in the Okinawa Trough.

The different seismic transects cover a wide range of water depths that gives rise to both short period and long period seafloor multiples that may require different

approaches to attenuate. Along the continental shelf, short-period multiples may be generated that required gapped deconvolution to effectively attenuate. Techniques such as radon or F–K filtering that rely on velocity discrimination may fail, as the multiples are likely coincident with primary reflections from shallow passive margin strata that may have similar move-out as the multiples. Additionally, shallow reflections typically have lower fold, further limiting the effectiveness of velocity-based methods.

However, multiples in deep water have too large of a period for gapped deconvolution to attenuate without damaging primary reflections. In these cases, velocity-based methods may be more effective, as there may be significant difference in move-out between seafloor multiples and the deep crustal reflections they obscure. 2D surface-related multiple elimination (SRME) should in principle attenuate much of the multiple energy regardless of water depth, seafloor relief or lithology. In practice, however, diffracted and out-of- plane multiples often require 3D SRME to attenuate. As seen in previous imaging efforts in the Taiwan region (Berndt and Moore 1999), more than one technique is likely required to effectively attenuate multiples in the TAIGER marine reflection data set.

2.3 DATA ACQUISITION AND PROCESSING

Data were acquired during the summer of 2009 with the R/ V Marcus G. Langseth using a 6-km streamer and 36 air gun source array. The source array consisted of 4 strings of 9 Bolt air guns with a nominal total volume of ~6,600 in^3. Shots were spaced every 50 m, with typical recording length of 15 s. Hydrophones were spaced every 12.5 m, and CDP spacing was 6.25 m. Sources were towed at a depth of 8 m to maximize low

frequencies of the source, without sacrificing significant bandwidth. Strong low frequencies in the source are important for imaging reflections from deep crustal structure, which may be low frequency due to the nature of reflecting interface, or because high-frequency energy may not penetrate to the depth of the reflecting interface.

2.3.1 Gapped Deconvolution

Standard deterministic gapped deconvolution uses the Weiner-Levinson algorithm (Yilmaz 2001) to design an inverse filter from autocorrelations (or in the multi-channel case, an average of some number of autocorrelations) that will remove the predictable part of the seismic trace (i.e. multiple energy). In practice, gapped deconvolution is used to attenuate short-period seafloor and intra-bed multiples, as well as collapse the source wavelet and sharpen the stacked image. It is often applied to either shot or CDP gathers, in the time–space or tau-p domain. An advantage of gapped deconvolution in tau-p space is that the periodicity of multiples is more consistent for all traces in the gather, as opposed to gathers in the time–space domain where it can vary with offset. An advantage of applying gapped deconvolution to shot gathers is that shot-consistent inverse filters are calculated for each source. In the case of TAIGER reflection data, gapped deconvolution was applied to shot gathers at an early stage in the processing flow, where the major goal is to collapse the source wavelet and gently whiten the amplitude spectrum.

Gapped deconvolution will design an operator from data within a designated window, and then apply that operator to data within another specified window. With the goal of crustal-scale imaging, deconvolution operators must be designed to handle a wavelet that changes with depth due to attenuation. To deconvolve arrivals from shallow sediments and lower-frequency arrivals from deeper crustal levels, a two-window

approach was used to compute separate operators for shallow sedimentary and deep crustal arrivals (Figures 2-2a, 2-2b). Design windows are generally at least 2–3 s long at the near offset, but this may be limited by sedimentary thickness at the window location. It is generally undesirable to include multiples in the design window, but doing so did not appear to significantly degrade the quality of result—likely because multiples contain the same source signature as primary reflections. Similarly, two different application windows must be chosen for the shallow and deep operator (Figures 2-2c, 2-2d). These are chosen in a similar fashion as the design windows, but with a 600 ms transition zone between the two operators to avoid artifacts.

Our preferred parameters for the shallow window are a 10 ms gap, 164 ms operator length and autocorrelations from 11 traces used to calculate an operator. Preferred parameters used in the deep window are a 32 ms gap, 164 ms operator length and autocorrelations from 11 traces used to calculate an operator. Figure 2-3 shows an example of gapped deconvolution using the two-window strategy and chosen parameters along the continental slope of the northern SCS margin. For most of the TAIGER data, the source array appears to be effectively tuned, so there is little contamination from a bubble pulse. Because of this, in the sedimentary section (Figures 2-3a, 2-3b), gapped deconvolution only provides mild whitening of the recorded spectrum. However, deeper crustal reflections (Figures 2-3c, 2-3d) generally exhibit more ringing. The two-window gapped deconvolution strategy effectively collapses the energy into a single event.

While this strategy is generally successful for most TAIGER reflection data, an exception occurs where strong low-frequency ringing obscures weakly reflective sediments beneath a high-amplitude seafloor reflection (Figure 2-4a). The low-frequency ringing may be a result of gun failure during shooting, resulting in a ringing source with

an unbalanced spectrum biased towards the low-frequency components. In these cases, deconvolution using any reasonable choice of gap and operator length introduces high-frequency, high-amplitude noise within a single operator length of the seafloor. Averaging over more autocorrelations largely mitigates this problem, though it somewhat dampens the effectiveness of the deconvolution. While the deconvolution is still generally successful at reducing the low-frequency oscillations without introducing any artifacts (Figures 2-4b, 2-4c), the strongest of these low-frequency oscillations occurs at nearly 0.5 s below the seafloor, and is beyond the ability of gapped deconvolution to reliably attenuate without damaging primary reflections. The reason for such a strong, late oscillation is not entirely clear, but it may be eliminated with a low-cut bandpass filter (Figure 2-4d).

2.3.2 2D Surface-Related Multiple Elimination (SRME)

2D SRME creates a multiple model based on a series of autoconvolutions of recorded traces (Verschuur et al. 1992). The obvious and oft-stated advantage of SRME is that it does not require any input beyond shot gathers (i.e. seafloor picks or velocities), but rather decomposes input traces into Taylor expansions where each term of the Taylor expansion corresponds to a higher order of multiples. Each Taylor expansion term is computed as convolution of input data with itself or lower-order Taylor term. The resultant multiple model may then be adaptively subtracted from the original shot gathers to produce records without multiples.

While 2D SRME does not require a velocity field, it does require a very general 1D RMS velocity to extrapolate from the nearest recorded offset back to true zero offset.

Different velocities seem to produce similar quality results, presumably because the difference in hyperbolic curvature from our nearest offset (162.5 m) to zero offset is negligible for different velocities for the frequencies of exploration to crustal scale data. To produce an accurate multiple model, particularly at farther offsets, 2D SRME also requires split-spread geometries, where ray paths are effectively reversed. For marine data, split-spread geometry is simulated by substituting traces from shots coinciding with receiver locations at negative offsets under the assumption of reciprocity. The use of reciprocal shots requires source and receiver spacing to be uniform, so that there exists a source for each receiver location—an unlikely condition for many reflection data sets. Reciprocal shots must then be generated by either interpolation, or simply copying shot records. This can greatly increase computation time, or potentially degrade the quality of result.

The accuracy of the multiple model generated by 2D SRME depends heavily on these reciprocal traces, particularly at far offsets (Figure 2-5). While multiples are attenuated at all offsets, 2D SRME appears to be most successful at the near offsets. For flat sedimentary strata, the strongest multiple energy is contained in the near offsets, so their multiples are effectively attenuated on stacked sections after application of 2D SRME (Figure 2-6). Unfortunately, 2D SRME is much less effective for attenuating multiples from more rugose, diffractive basement reflections and areas of high seafloor relief, such as a volcanic edifice or accretionary prism. (Figure 2-7).

2.3.3 Radon Transform Multiple Attenuation

Radon filtering, unlike 2D SRME, is based on velocity discrimination between primary and multiple reflections, and so requires an earth model. The radon

transformation maps seismic energy along specified parabolic trajectories (defined by an NMO velocity or slowness) from NMO-corrected CDP gathers into radon space. Primary events properly flattened with the correct NMO velocity will map along the 0 slowness contour, while multiples, with residual move-out, will map into the positive slowness domain and may be simply muted or filtered out. The ability to transform in and out of radon space with high fidelity, with the ability to separate multiples from primary events, has made radon a standard tool for multiple suppression and random noise attenuation for many years.

Often times, simply transforming into and out of radon space will eliminate much random noise. To attenuate multiples, multiples may be filtered out and the remnant signal transformed back into the time–space domain, or signal may be filtered out and the multiples subtracted from the original input gathers. In practice, the first approach can lead to some loss of seismic character that may be described as appearing ‘‘wormy’’ or ‘‘synthetic.’’ The latter approach often produces more desirable results as the signal is unfiltered by the radon process and so retains its original character. Radon filtering, like any velocity-based filter, may create spurious events from random noise. Subtracting multiples from input gathers prevents these artifacts from contaminating subsequent gathers and stacked sections. However, since multiples may have a wide range of move-out, this approach is more computationally expensive, as a large number of parabolas must be computed for each time sample to represent multiples in radon space.

While radon is generally effective at attenuating multiples, residual multiple energy may still be observed at all offsets (Figure 2-8). Figure 2-8b demonstrates that much of the residual multiple energy is contained at near offsets. This is one of the practical limitations of radon filtering. Energy at near offsets, near the apex of hyperbolic

events, will map into the same domain as flattened events (i.e. primary events). Therefore, even after filtering in radon space, multiple energy may not be attenuated at near offsets. This problem may be exacerbated for the low-frequency components of hyperbolic events, as the low frequencies are even less sensitive to velocity at near offsets. In some situations, this may lead to a low-frequency residual multiple deep in the crust that may be easily misinterpreted as a deep crust or Moho reflection. Fortunately, the respective limitations of 2D SRME and radon make them highly complementary techniques for attenuating multiples. While radon filtering is ineffective at near offsets but effective for far offsets, 2D SRME is most effective for near offsets and less effective for far offsets (Figures 2-8c–2-8f). In the example from MGL0908_03, 2D SRME and radon filtering have greatly attenuated seafloor multiples from flat sedimentary strata and revealed a strong Moho reflector.

2.3.4 Residual Multiple Attenuation

Any remaining multiple energy at this stage of processing is largely from diffractive, rugose basement or seafloor reflections not attenuated by 2D SRME or radon. For deep water depths where multiples with relatively high dominant frequencies obscure low frequency deep crustal or Moho reflections, an aggressive high-cut bandpass filter may eliminate much of the residual multiple energy (Figures 2-9a–2-9d). Additionally, since much of this energy is contained at near offsets, the residual multiple energy may be attenuated by either weighting traces with increasing offset or simply muting the near offsets at the onset of multiple energy. For many of the TAIGER reflection data, we use a simple linear weighting with increasing offset, though more sophisticated schemes may be implemented to optimize signal-to-noise ratio (i.e. Schoenberger 1996). While trace

weighting and inside muting are both computationally inexpensive and produce similar stacked responses (Figures 2-9e, 2-9f), inside muting has the advantage of being applied to pre-stack gathers at the onset of multiple energy, as opposed to trace weighting, which can potentially degrade the quality of shallower reflections in stacks by enhancing noise at far offsets. However, both techniques prevent multiple energy at near offsets from contaminating the stacked section.

2.4 Case Study and Discussion

Figure 2-10 shows our processing flow for TAIGER marine reflection data. Minor adjustments may be necessary on a case-by-case basis as data require. Following gapped deconvolution and multiple attenuation as discussed, CDP gathers are pre-stack time migrated using Kirchhoff time migration and then stacked to produce the final image. The stacking velocity field for each profile was transformed into an RMS velocity as an initial velocity field for pre-stack time migration, and refined using residual velocity analysis. In the case of MGL0905_22 and MGL0908_03, few iterations of migration and residual analysis were required. However, in the accretionary prism along MGL0906_18N, several iterations were necessary. These profiles are representative of many of the imaging challenges in the TAIGER crustal-scale marine reflection data, and are presented to demonstrate the general success of our processing strategy.

2.4.1 Profile MGL0905_22 – Northern SCS Proximal Margin

Figure 2-11 shows the pre-stack time migrated image of the northern SCS margin along MGL0905_22. This profile extends from water depths of ~150 m along the

continental shelf to ~3,000 m down the continental slope. Gapped deconvolution, 2D SRME, and radon filtering effectively suppress multiples along the continental shelf and much of the continental slope. Unfortunately, strong multiple energy persists beneath the upper slope at water depths of ~750–1,500 m. Here, 2D SRME has little effect on multiples, and radon filtering leaves significant multiple energy at near offsets. Multiples here also have similar bandwidth to the sedimentary reflections they obscure. Additionally, stretch muting after NMO-correction reduces the usable offset range at the onset of multiple energy so that offset weighting and inside muting are only marginally effective. While this creates problems in relating sediments of the continental shelf to those down the continental slope, the deeper crustal structure is still observable.

At the continental shelf, these data show about 3 s two-way time (~3–4 km) of foreland basin and post-rift sedimentary strata overlying thick pre-Tertiary basement (Figure 2-11a), as expected from extensive exploration seismic and drilling data sets from other sub-basins of the northern SCS margin near Taiwan (Lin et al. 2003; Liu et al. 1997). Extensive normal faulting is also observed that offsets shallow sedimentary strata near the seafloor, as well as the basement reflector at ~3–3.5 s two-way time. Similar normal faulting has been observed in other sub-basins near Taiwan that has been attributed to prior rifting or more recent collision-induced flexure (Lin and Watts 2002).

While these sedimentary packages and normal faults have been observed in many other data sets near Taiwan, the new TAIGER crustal-scale data reveals significant mid-crustal reflectivity (between ~5 and 7 s two-way time). Additional deep reflectivity may be observed near 10 s two-way time (~25–30 km) that likely represents the Moho discontinuity beneath the continental shelf. While residual multiple energy obscures the strata of the upper slope, this deep Moho reflector is observed to shoal across the upper

continental slope, where it is ultimately truncated by a large seaward-dipping normal fault. Unfortunately, the residual multiple energy along the upper slope also obscures the up-dip extent of this crustal-scale normal fault.

Across this normal fault, stratigraphic thickness increases to ~4 s two-way time (~5–6 km), and may be separated into an upper package and lower package separated by a relatively high-amplitude reflector interpreted as an unconformity (Yeh et al. 2010). Sediments are much thicker here than at the continental shelf, and our multiple attenuation efforts reveal thin, faulted crustal blocks seaward of the continental shelf (Figure 2-11b). While the Moho reflector is not obvious on the crustal block immediately on the down-thrown side of the crustal-scale normal fault, it may be observed rapidly shoaling from 8 to 8.5 s two-way time on the southernmost end of the profile. Locally, crust here is as thin as ~2 s or 5–6 km thick. These crustal blocks are each bounded by normal faults that appear to offset Moho and penetrate into the upper mantle.

2.4.2 Profile MGL0908_03 – Northern SCS Distal Margin

MGL0908_03 (Figure 2-12) continues southward from MGL0905_22 to image the crust beneath the lower continental slope and abyssal plane of the South China Sea near Taiwan. Due to the relatively smooth seafloor topography and intermediate water depths, 2D SRME and radon filtering are successful in attenuating multiples and reveal a strong Moho reflector along much of the profile. The north end of MGL0908_03 overlaps with the south end of MGL0905_22, and so the Moho reflector is observed at ~8 s two-way time, just as seen on the south end of MGL0905_22 (Figure 2-12a). The sedimentary section is also observed to be thickest at the north end of MGL0908_03, where crust is thinnest. Two isolated high-amplitude reflectors occur within these post-rift sediments

that we interpret as sills, possibly sourced by local magmatic activity associated with extreme crustal thinning observed here.

The Moho reflector deepens to ~10 s two-way time south of this zone, suggesting that the thinnest crust at the south end of MGL0905_22 and north end of MGL0908_03 is a local minimum in crustal thickness. Crust is ~4 s (~11–13 km) thick across the southern extent of MGL0908_03, consistent with regional forward gravity modeling (Yeh and Hsu 2004). While a number of faulted blocks are observed on this profile, they are separated by extensive zones of rugose crust that may be volcanic in nature. Post-rift sediments are much thinner (1–1.5 s two-way time or ~1–2 km thick) over the 11–13 km thick body of crust and generally flat-lying, except where locally disturbed over the crest of volcanic crust. This relationship, as well as the stratigraphic level of sills, would suggest a pulse of post-rift volcanic activity, similar to much of the volcanic activity observed elsewhere in the South China Sea (Yan et al. 2006).

A prominent seamount is imaged at the south end of MGL0908_03 (Figure 2-12b). However, just as in the case of the accretionary prism along MGL0906_18N, strong multiple energy still remains after attempts to attenuate this unwanted energy, although the seamount may not have any internal reflectivity to image. The seamount is apparently flanked by a rotated fault block, which may be pre- or syn-rift sediments deformed during emplacement of the seamount or volcaniclastics from the volcanic seamount. Deformation appears to be more concentrated on the seaward side, where early post-rift sediments are uplifted to the seafloor along the seaward flank of the seamount.

2.4.3 Profile MGL0906_18N – Ryukyu Subduction Zone

MGL0906_18N (Figure 2-13) illustrates the potential for crustal-scale imaging at subduction zones and the processing strategy described in Figure 2-10. Although the example is from the Ryukyu subduction zone, similar success is expected for data acquired across the Manila subduction zone. MGL0906_18N was acquired in the deep water (~6,000 m) of the Philippine Sea, so that south of the Ryukyu trench, multiples occur much later in the record than signal from the oceanic crust. South of the trench we observed 1–1.5 s two-way time (1–2 km) of sediments overlying thin oceanic crust (1.5 s two-way time, or ~5 km thick). This observation is consistent with crustal thicknesses previously observed throughout the Philippine Sea east of Gagua ridge (Louden 1980; Murauchi et al. 1968).

Across the Ryukyu trench, the accretionary prism is about 4–7 s (~6–14 km) thick (Figure 2-13a). Little internal reflectivity is observed in the accretionary prism away from the trench, either due to lack of significant impedance contrast, or due to strata dipping too steeply to be imaged with the given acquisition geometry. However, several discrete thrusts are imaged, each corresponding to local bathymetric lows within the accretionary prism. These thrusts extend down to the top of the subducting ocean crust at ~10 s two-way time. Despite some residual multiple energy, the top of the subducting crust is observable beneath much of the accretionary prism.

Along the north end of MGL0906_18N, we image at least four sedimentary packages within the forearc basin (Figure 2-13b). The most recent are weakly reflective, flat-lying strata at the basin center. Deeper sediment packages appear to have been folded and possibly faulted as the Philippine Sea Plate subducts below. Beneath the forearc basin and crust, multiple attenuation reveals two deep reflectors at 11.5–12 s and 13 s

two-way time that may correspond to the forearc Moho and top of subducted crust, respectively. Unfortunately, residual multiple energy makes correlation between these deep reflectors and the top of crust reflector beneath the prism uncertain. Residual multiple energy here also masks the geometry of the forearc backstop at the rear of the accretionary prism. However, reflections from the top of forearc crust, and potentially the forearc Moho, are observable beneath the forearc basin north of this zone of residual multiple energy, but not beneath the prism south of this zone. This suggests that the forearc backstop abruptly terminates within this narrow zone of residual multiples, consistent with previous observations of a steeply-dipping backstop in the southwestern Ryukyu subduction system (Klingelhoefer et al. in press; Font et al. 2000).

2.5 CONCLUSIONS

The three profiles presented illustrate some of the wide-range of imaging targets and associated challenges in crustal-scale imaging, particularly with respect to multiple contamination. The TAIGER marine reflection data set spans multiple tectonic environments and water depths, so that no one technique suppresses multiples in all environments. However, 2D SRME and radon filtering are highly complementary techniques that effectively suppress much of the multiple energy in these environments. Time-variant bandpass filtering and either offset-weighted stacking or inside muting may be used to eliminate much of the residual multiple energy left after 2D SRME and radon filtering.

Multiple attenuation was most successful at intermediate to deep water depths, such as MGL0908_03, where much of the multiple energy comes from relatively flat sediments and obscures a Moho reflector that is of lower-frequency and higher move-out

than the multiples. Multiple attenuation was least effective in areas of significant topography such as the accretionary prism along MGL0908_18 N or seamount observed on MGL0908_03. Here, only bandpass filtering and offset-weighting or inside muting attenuate multiple energy with any degree of success.

Although 2D SRME and radon filtering are computationally expensive, MGL0905_22, MGL0908_03, and MGL0906_18N demonstrate some of the potential deep crustal information that may be gained from these multiple attenuation techniques. The imaging strategy discussed reveals that a large, Moho-penetrating crustal-scale normal fault separates thick crust under the continental shelf from thin, normal fault-bound crustal blocks under thick slope deposits. Further to the south, crust is thicker and consists of faulted blocks and possible post-rift volcanic bodies. Across the Ryukyu trench east of Taiwan, our processing flow successfully images deep reflections (forearc Moho and subducting oceanic crust) beneath the accretionary prism. In each case, the presented imaging strategy, with emphasis on multiple attenuation, results in high-quality crustal-scale images that provide important constraints on the dynamic processes in the vicinity of Taiwan.

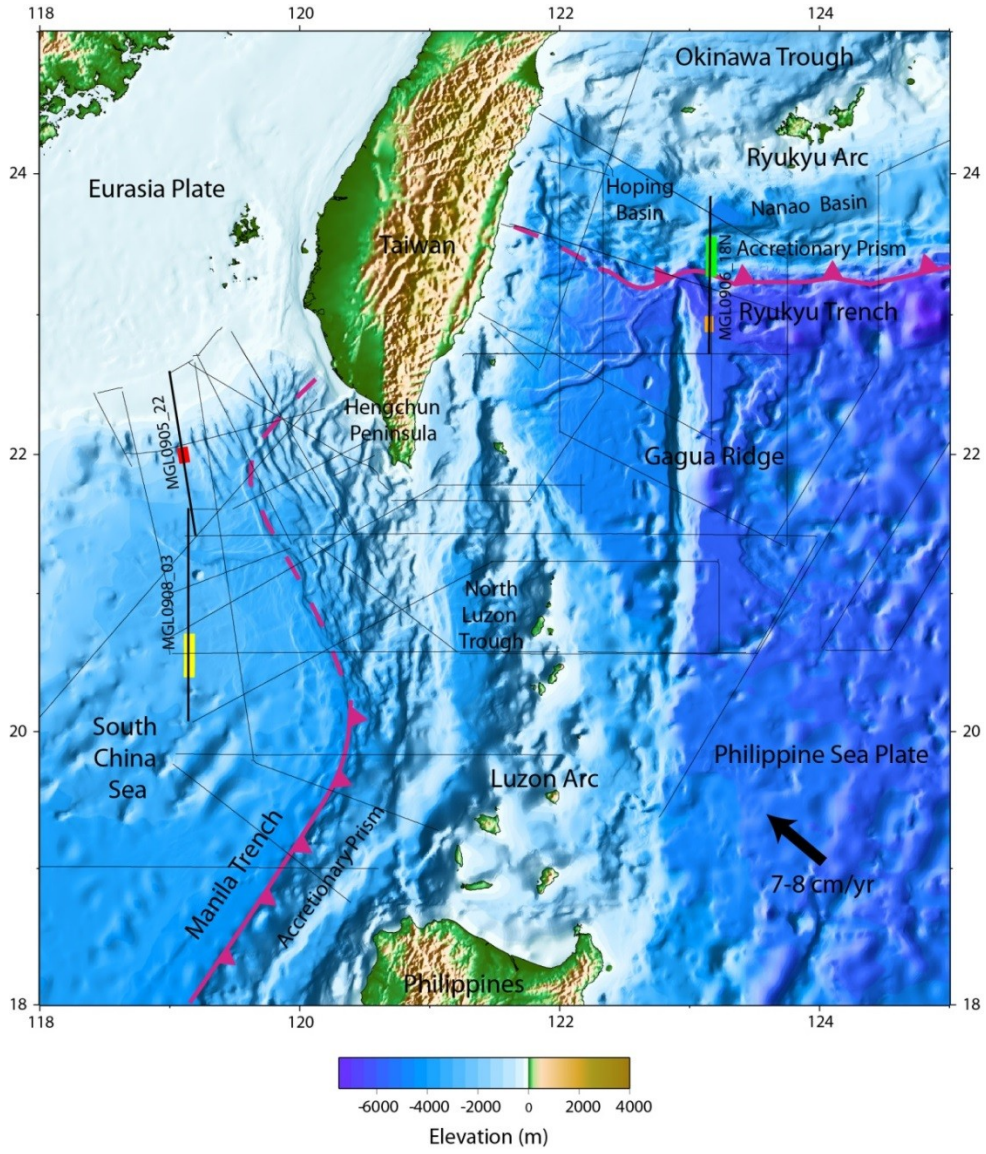

Figure 2-1: Bathymetry map of Taiwan region with major tectonic features labeled. Convergence rate between Philippine Sea plate and Eurasia plate is 7–8 cm/year in a northwesterly direction. Thin black lines indicate marine reflection profiles acquired during the 2009 TAIGER active source program. Thick black lines are seismic profiles MGL0905_22, MGL0908_03, and MGL0906_18N discussed in this study. Red box is the section in Figure 2-3, orange box is Figure 2-4, yellow box is Figures 2-6 and 2-8, and green box is Figures 2-7 and 2-9.

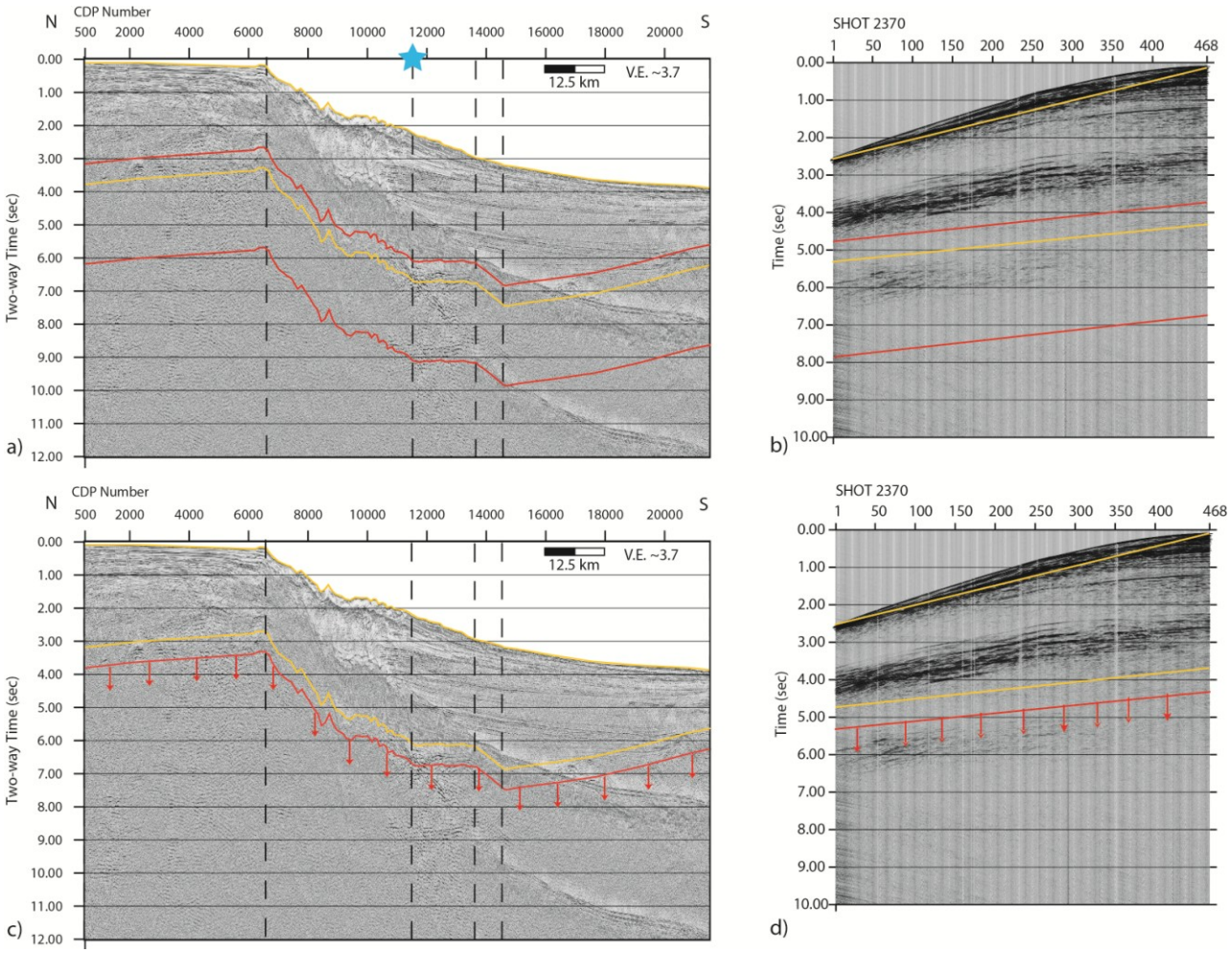

Figure 2-2: a) Profile MGL0905_22 stacked section (see Figure 2-1 for location) illustrating arrivals contained within the two design windows for gapped deconvolution. Yellow line is the shallow design window encompassing reflections from sedimentary strata, red line is the deep design window containing lower frequency, deeper crustal reflections. Dashed lines indicate location of window designs. b) Shot gather, with near offset shifted to the seafloor, illustrating two design windows. Shot location is near CDP 11500 (blue star) in (a). c) Stacked section illustrating arrivals shallow (yellow) and deep (red) operators are applied to. d) Shot gather, with near offset shifted to the seafloor, illustrating application windows

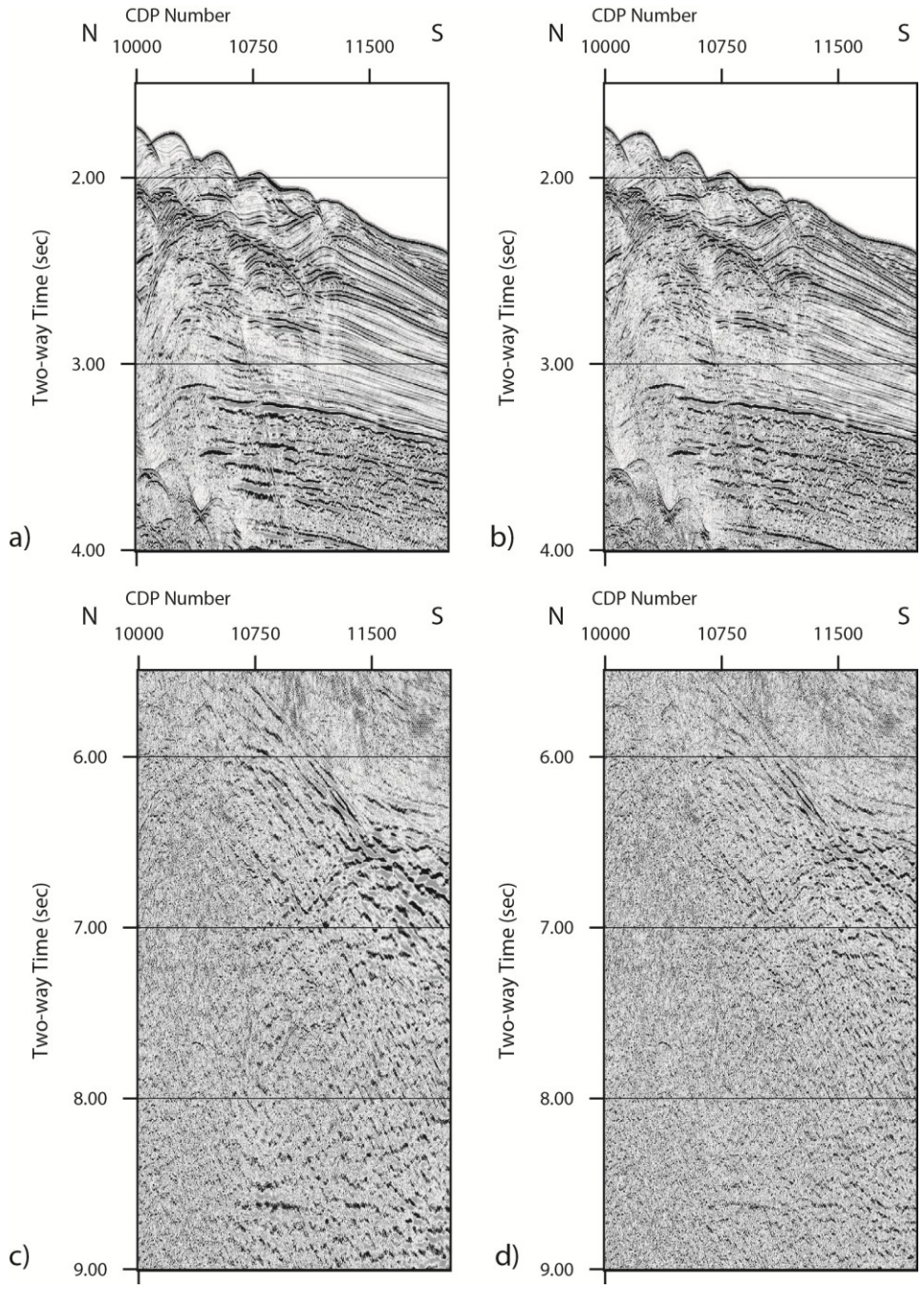

Figure 2-3: Stacked section from MGL0905_22 (see Figure 2-1 for location) showing continental slope (a) before and (b) after application of shallow gapped deconvolution operators to reflections from the sedimentary section; (c) before and (d) after application of deep gapped deconvolution operators to deep crustal reflections.

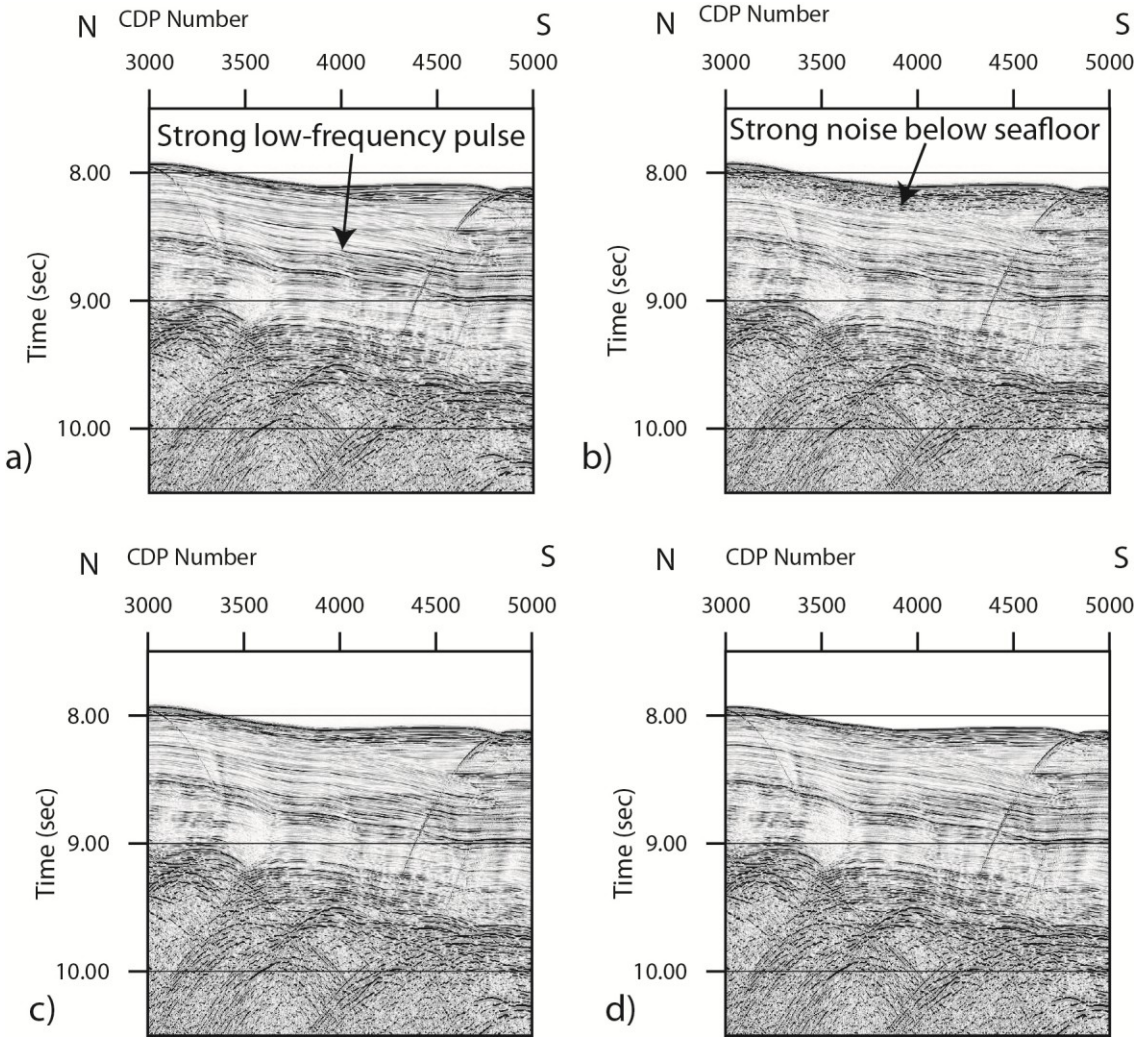

Figure 2-4: a) Stacked section from MGL0906_18N (see Figure. 2-1 for location) from the Philippine Sea exhibiting strong, low-frequency ringing. b) Gapped deconvolution with parameters used in Figure. 2-4 introduces strong noise within one operator length of the seafloor. c) The problem is mitigated by averaging over a large number of autocorrelations. d) Aggressive low-cut filtering is required to eliminate a strong, low-frequency pulse ~0.5 s below the seafloor.

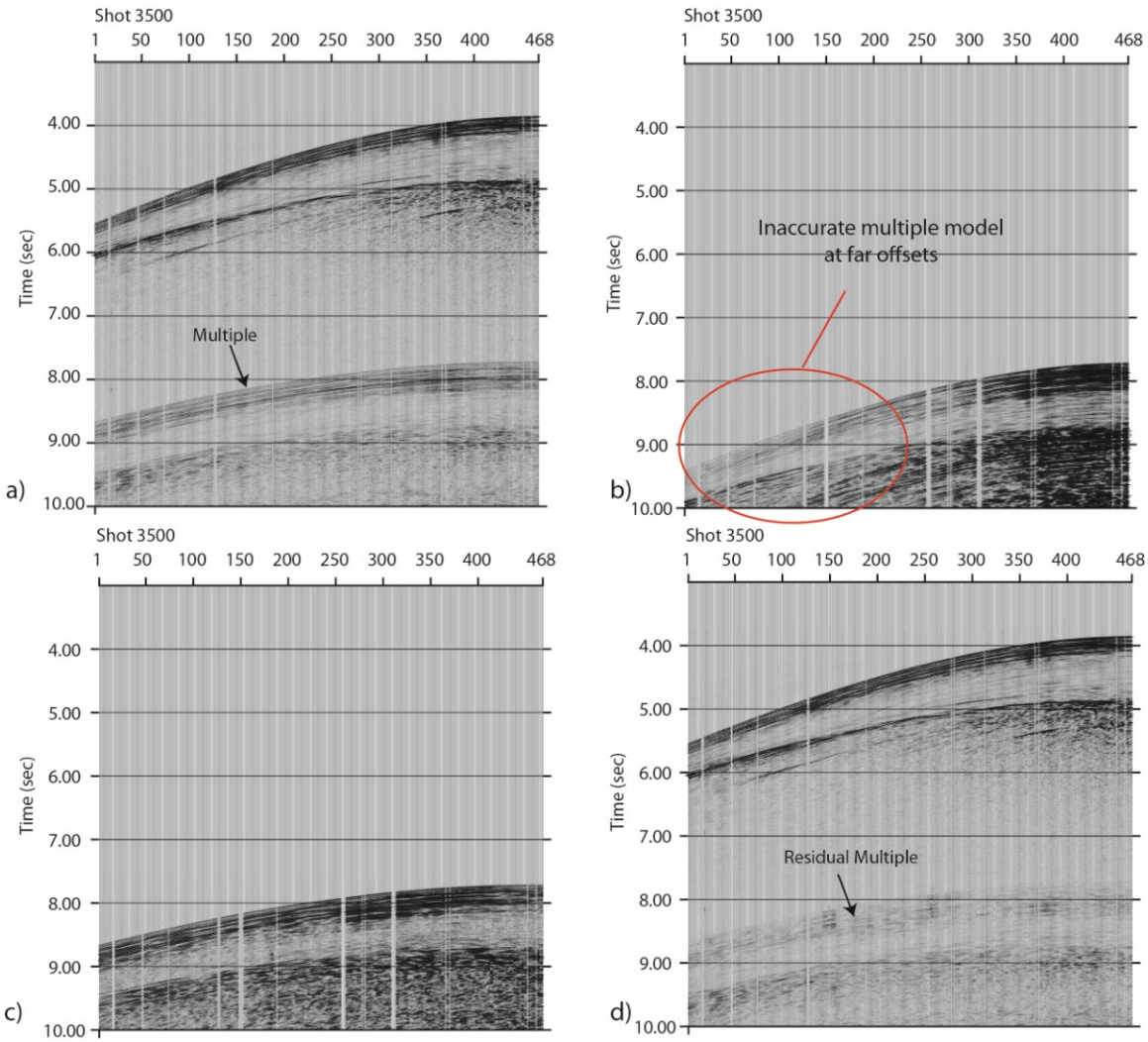

Figure 2-5: a) Shot gather from profile MGL0908_03 before 2D SRME (shot near CDP 20300— see Figure 2-1 for profile location, Figure 2-6 for location along stacked section) in area of low seafloor relief b) 2D SRME generates an inaccurate multiple model when only the single input shot gather is used c) 2D SRME produces a more accurate multiple model when reciprocal traces from adjacent shot gathers are used to simulate a split-spread geometry. Note that model amplitudes do not necessarily reflect those of original shot gathers. Adaptive subtraction or waveform matching is required to effectively attenuate multiples with the modeled multiples. d) Shot gather after adaptive subtraction of multiple model in (c). Multiple energy appears to be more effectively attenuated at near offsets than far offsets.

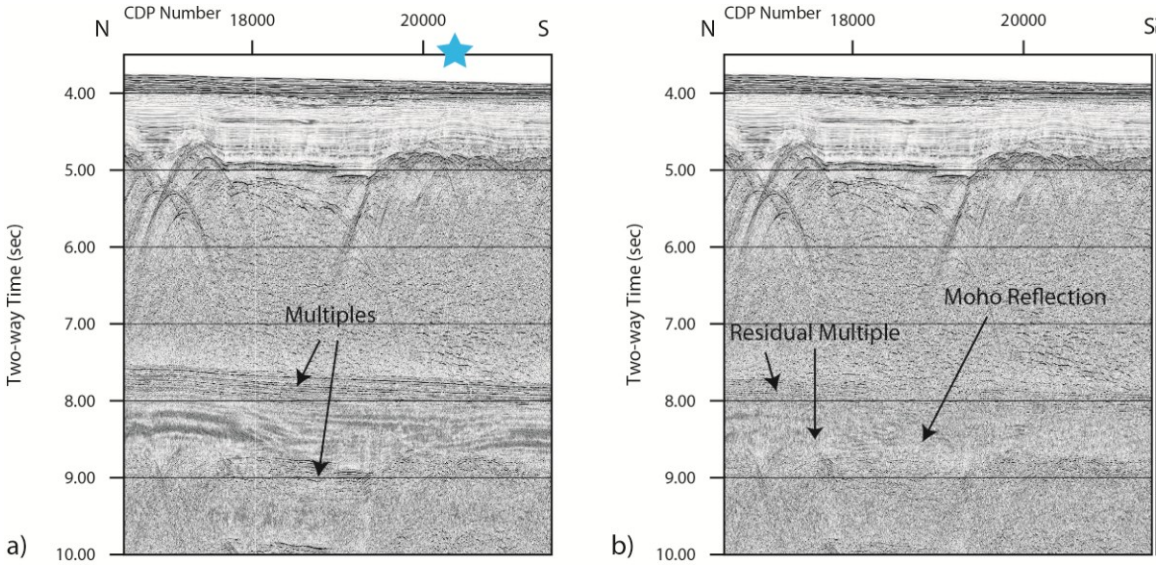

Figure 2-6: a) Stacked section from profile MGL0908_03 before 2D SRME in area of with low seafloor relief (see Figure 2-1 for location) b) Stacked section after 2D SRME. While much of the multiple energy is significantly attenuated, particularly from the flat sediments, significant residual multiple energy remains. Blue star is location of shot gather in Figure 2-5.

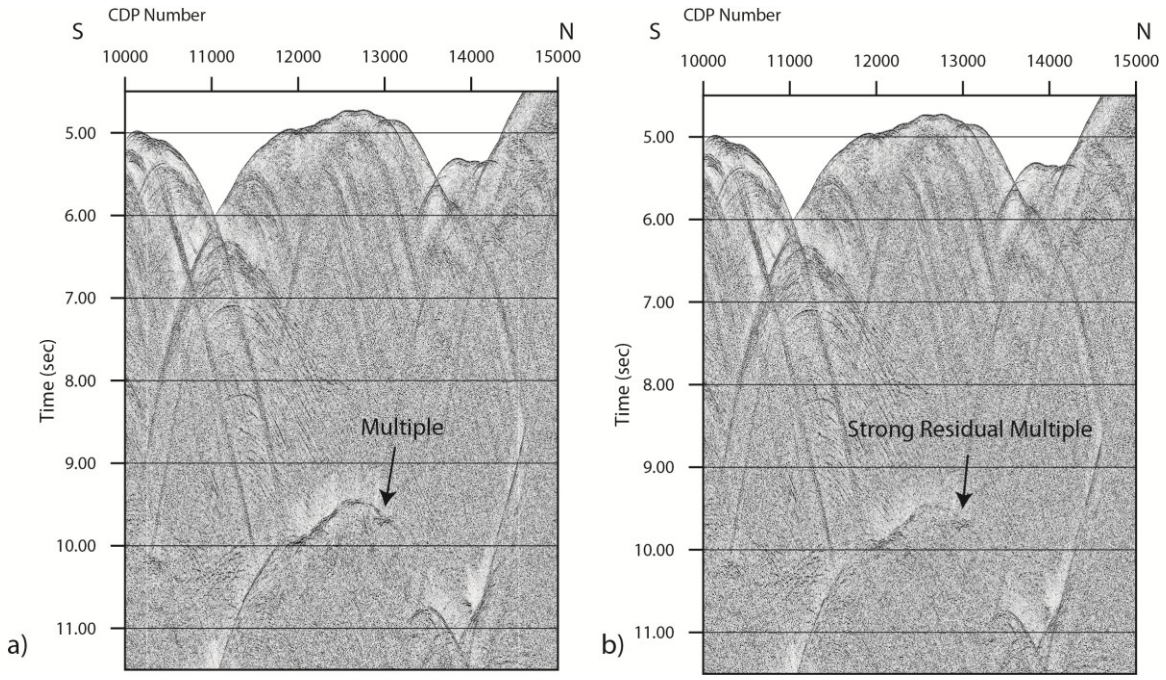

Figure 2-7: a) Stacked section from MGL0906_18N before 2D SRME in accretionary prism with significant seafloor relief (see Figure 2-1 for location). b) Stacked section after 2D SRME. 2D SRME attenuates some multiple energy, but strong residual multiple energy remains.

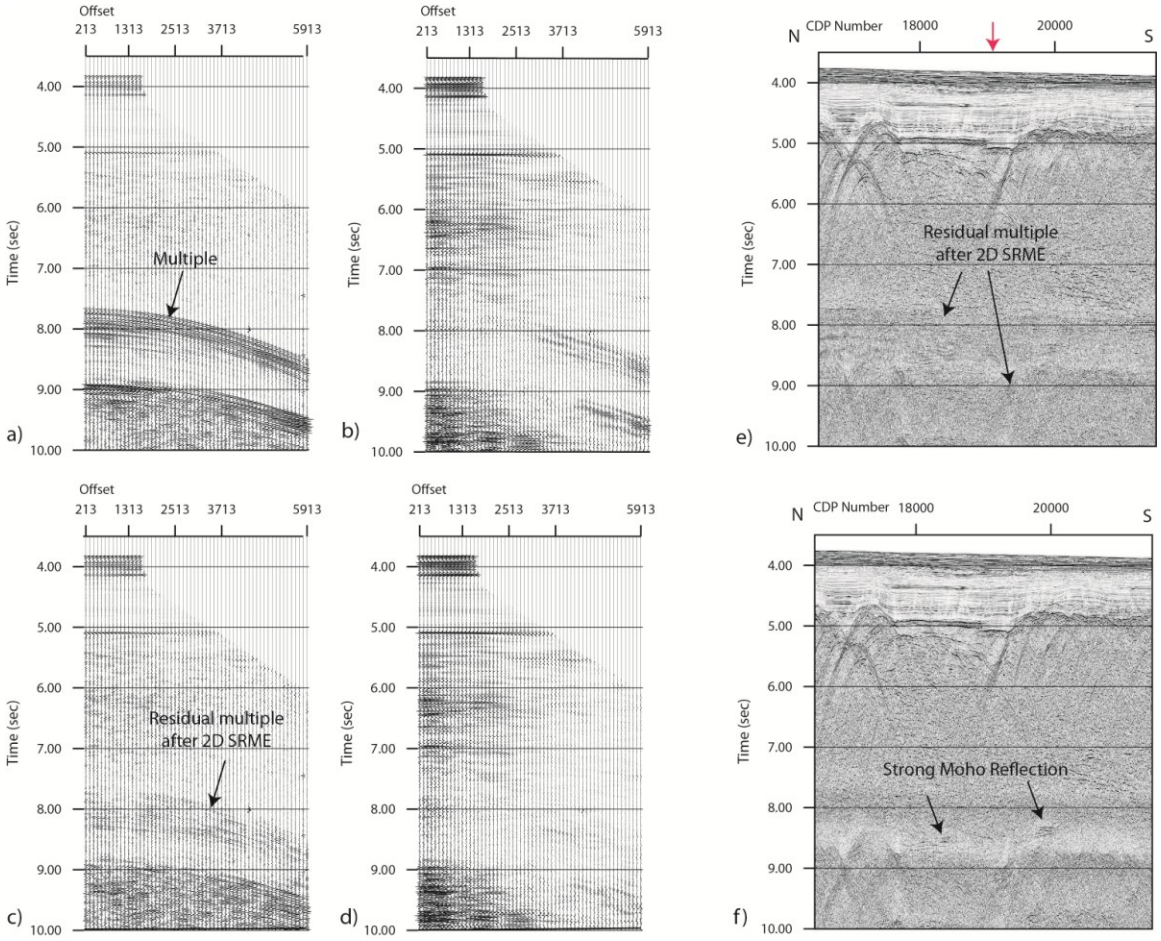

Figure 2-8: a) CDP 19000 from MGL0908_03 NMO-corrected without multiple attenuation. b) CDP after subtraction of multiples from radon filtering. While much of the multiple energy is attenuated, residual multiple energy remains at all offsets. c) NMO-corrected CDP with 2D SRME result used as input for radon filtering. d) CDP after both 2D SRME and radon. Multiples are more effectively attenuated at both near and far offsets. e) Stacked section (MGL0908_03) without radon multiple attenuation (same as Figures 2-6b). Red arrow is location of CDP in a–d. f) Stacked section after radon demultiple. Radon effectively eliminates the residual multiples from sedimentary reflections, but some residual multiple from basement reflections remain.

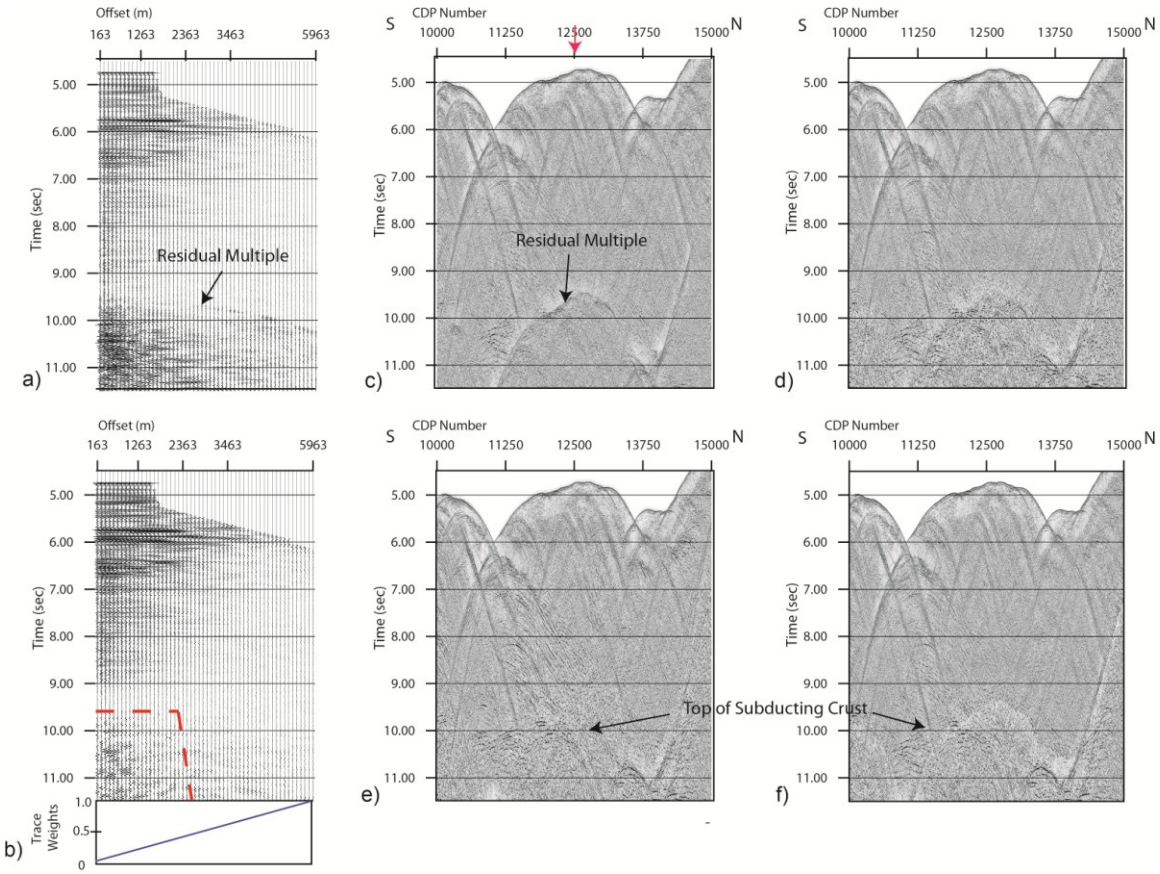

Figure 2-9: a) CDP gather 12500 and c) stacked section from MGL0906_18N (see Figure 2-1 for location) with 2D SRME and radon filtering along the Ryukyu accretionary prism with strong residual multiple energy. Red arrow in (c) is location of CDP 12500. b) CDP gather and d stacked section after application of bandpass filter with corners of 2, 5, 20 and 30 Hz. Aggressive bandpass filtering with inside muting (dashed line in b, stacked section in e) or offset-weighted stacking (weights in b, stacked section in f) attenuate much of the multiple energy 2D SRME and radon filtering do not.

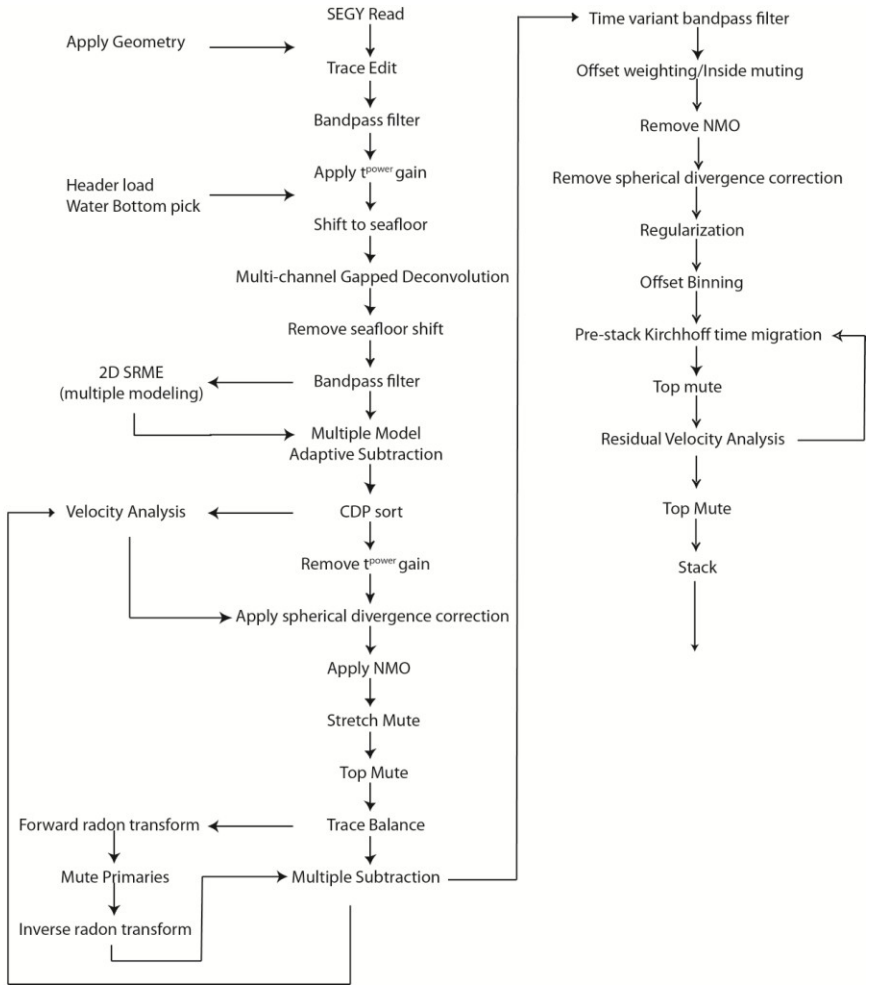

Figure 2-10: Processing flow chart for TAIGER marine reflection data through pre-stack time migration.

Figure 2-11: Profile MGL0905_22 final image of northern SCS margin using processing flow in Figure 2-10. a) These data show relatively flat-lying sediments overlying northward dipping strata along the continental shelf. Flexure-related normal faulting offsets basement and shallow strata. Mid-crustal reflectivity is also observed beneath the shelf. b) A large crustal-scale normal fault separates thick crust of the continental shelf from thin, normal fault-bound crustal blocks. These faults appear to offset Moho. Crustal thickness is at a minimum at the south end of the line.

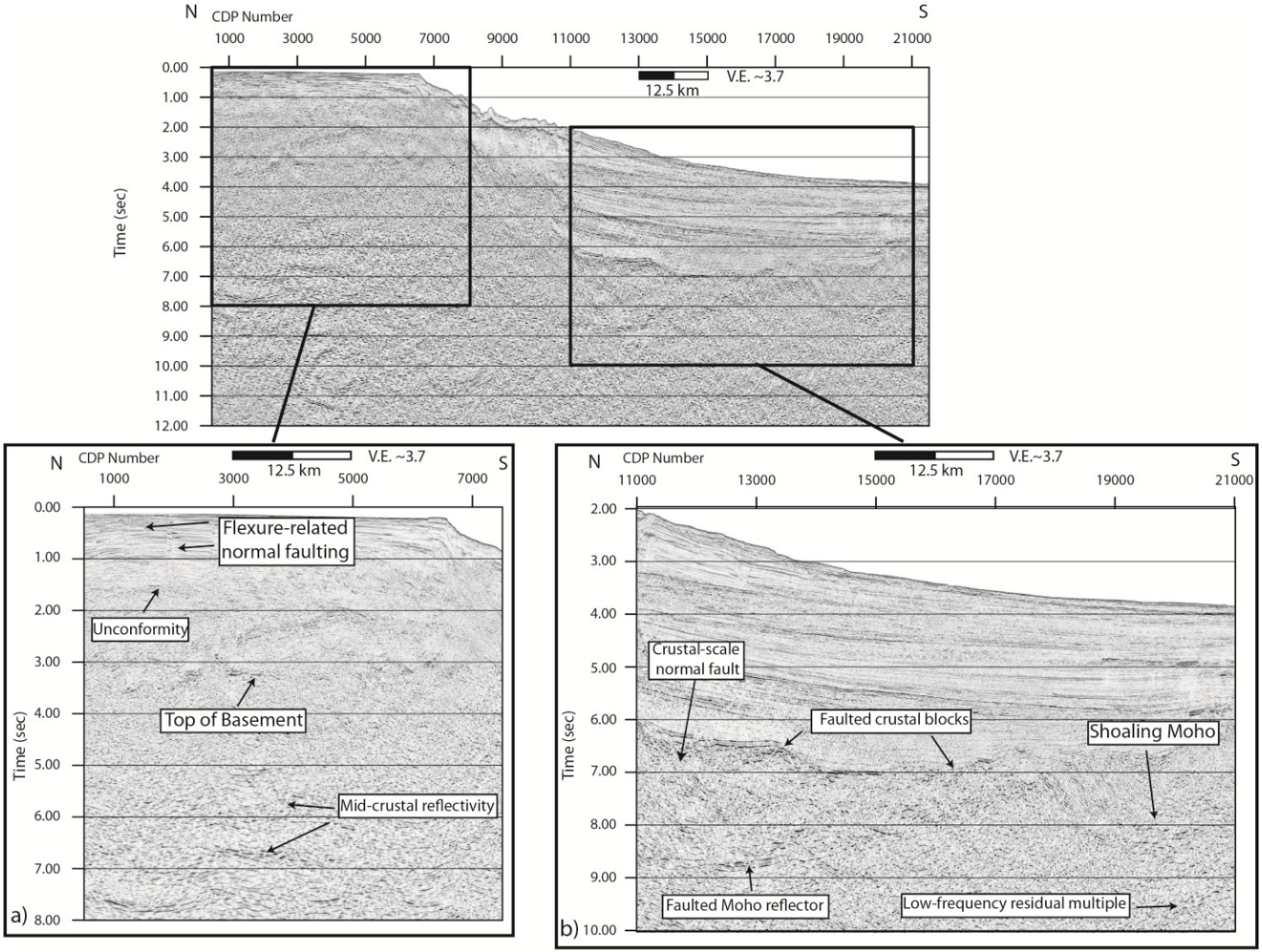

Figure 2-12: Profile MGL0908_03 final image in the South China Sea south of Taiwan using processing flow in Figure 2-10. a) Crustal thickness is a minimum at the north end of the line, overlapping with MGL0905_22. Crust is thicker south of this point, and may be characterized as a mix of faulted blocks and volcanic bodies. b) Crustal structure near prominent seamount south of Taiwan, near a zone of seamounts separating 10–12 km thick crust from normal South China Sea ocean crust to the south (Fig. 2-1). Seamount is bound by deformed sediment or volcaniclastics packages.

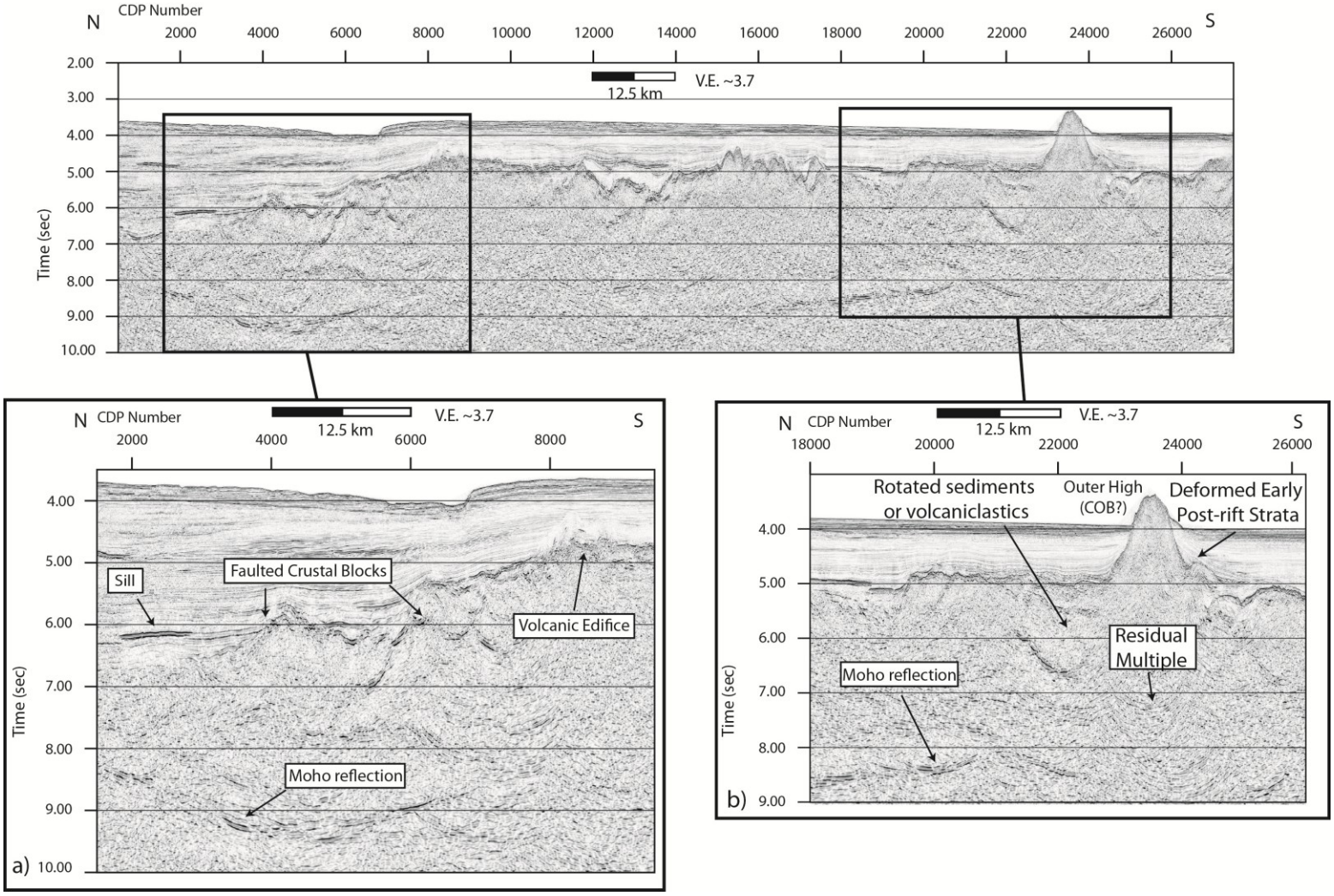

Figure 2-13: Profile MGL0906_18N final image across Ryukyu subduction zone using processing flow in Figure 2-10. a) Strata of accretionary prism are either too steep for imaging with these data or non-reflective. Several discrete thrusts are imaged down to the top of subducting ocean crust, which may be observed across much of the prism, despite residual multiple energy. b) Several distinct sediment packages are observed in the forearc basin, and two deep reflectors are observed beneath forearc crust.

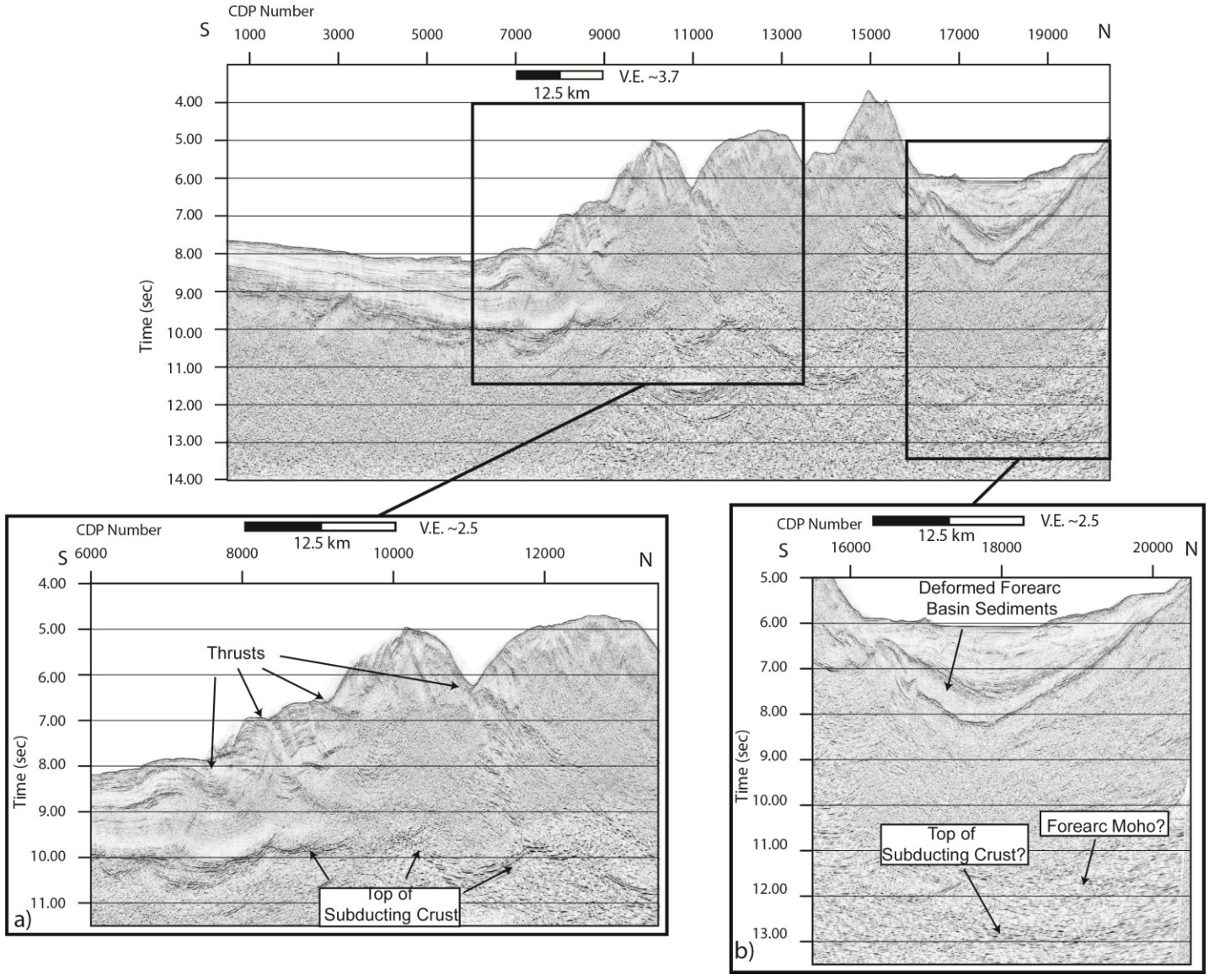

Chapter 3: Rifting and Magmatism in the Northeastern South China Sea from Wide-Angle Tomography and Seismic Reflection Imaging

3.1 INTRODUCTION

Rifted margins exhibit a wide range of structural styles and magmatic activity that may vary in space and time. Magmatism during rifting and continental breakup may be driven by the advection of warm asthenosphere during crustal thinning or the presence of a hot mantle plume, as observed in the magma-rich margins between East Greenland and the British Isles (Hopper et al., 2003; White et al., 1987). Magma-rich margins contain large volumes of intrusive and extrusive volcanic rocks in the continent-ocean transition (COT), manifest as seaward-dipping reflectors from volcanic flows (White et al., 1987) and a high-velocity lower crust (HVLC) commonly attributed to either magmatic underplating (Korenaga et al., 2000) or intrusions in the lower crust (White et al., 2008). Vigorous magmatism during breakup and early seafloor spreading may also form atypically thick ocean crust in the distal margin (Boutilier and Keen, 1999; Mutter et al., 1984).

At magma-poor margins like the Newfoundland-Iberia margins, initially cool lithosphere or conductive cooling at sufficiently slow extension rates can suppress partial melting and prevent significant magmatism during rifting (Pérez-Gussinyé et al., 2001; Whitmarsh et al., 2001). In contrast to magma-rich margins, magma-poor margins are characterized by wide tracts of hyper-extended continental crust and possibly unroofed mantle in the COT (Whitmarsh et al., 2001). The hyper-extended crust typically consists of tilted fault blocks with listric normal faults that sole into low-angle detachment faults in the brittle crust or upper mantle (Reston et al., 1996). In these cases, amagmatic

continental breakup may be facilitated by serpentinization of upper mantle and the low-angle detachment faults instead of intense magmatism (Pérez-Gussinyé and Reston, 2001).

Much progress has been made in unraveling the complex interaction between stress, strain, temperature and rheology that may influence rifting and continental breakup (Ruppel, 1995). However, much of this work has been accomplished in the context of North Atlantic Variscan mountain belts rifted during the breakup of Pangea. Rifted margins formed under different tectonic scenarios and initial conditions have the potential to deepen our understanding of the rifting and continental breakup process. The northern continental margin (Figure 3-1) in the South China Sea (SCS) is an example of a young, moderately magmatic rifted margin that may yield important new insights into the interplay between magmatism, rheology, and the structural evolution of rifted margins.

The northern SCS margin and its conjugate margin in the southeastern SCS (Figure 3-1) are over ~300 - 400 km wide and exhibit characteristics of both magma-rich and magma-poor margins (Clift et al., 2001a; Franke et al., 2011). Previous studies have found faulted crustal blocks typical of highly extended continental crust in magma-poor margins along a wide continental slope (Clift et al., 2001a; Huang et al., 2005; Shluter et al., 1996; Zhu et al., 2012). These studies have also revealed numerous volcanic bodies interspersed throughout the distal margin, including a HVLC (Nissen et al., 1995b; Wang et al., 2006) that may be indicative of mafic underplating (Yan et al., 2001b; Zhao et al., 2010) or pervasive lower crustal intrusions (Franke, 2012). Volcanic rocks have also been recovered from boreholes in rift basins of the continental shelf with a variety of lithologies and dates throughout the SCS syn-rift and post-rift history (Li and Rao, 1994; Wang et al., 2012; Yan et al., 2006). Despite the evidence for at least moderate syn-rift

magmatic activity, there have been no observations of seaward-dipping reflectors that are diagnostic of magma-rich margins. As such, the roles of magmatism and extension during rifting and continental breakup in the SCS are not well understood.

The nature of the crust in the northeastern SCS near Taiwan has been more controversial. Based on magnetic data, Hsu et al. (2004) interpreted the northeastern SCS to contain oceanic crust outboard the continental shelf edge rather than the wide distal margin documented in other areas of the northern SCS margin. Subsequent gravity forward modeling suggested this crust was ~8-12 km thick (Yeh and Hsu, 2004) – much thicker than typical ocean crust, but perhaps suggestive of thick oceanic or volcanic crust of magma-rich margins. These studies argue the continent-ocean boundary is near the base of the continental slope (Figure 3-2), as opposed to earlier studies of magnetic anomalies in the SCS that place the continent-ocean boundary much further to the south (Briais et al., 1993; Taylor and Hayes, 1983).

However, recent seismic reflection images revealed tilted fault blocks in the northeastern SCS typical of highly extended continental crust (McIntosh et al. 2013; Lester and McIntosh, 2012). New magnetic modeling has also suggested the magnetic anomalies interpreted as weak lineations in ocean crust may instead be indicative of magmatically intruded continental crust (Yeh et al., 2012). Here we present recently acquired multi-channel seismic (MCS) reflection and wide-angle data from ocean-bottom seismometers (OBS) in the vicinity of Taiwan that demonstrate the crust in the northeastern SCS contains highly extended continental crust with interspersed volcanic zones similar to the wide rifted margin observed throughout the rest of the northern SCS margin.

3.2 SCS TECTONIC BACKGROUND

The SCS is the largest marginal sea of the Western Pacific region (Figure 3-1). It is bound on the east by the Manila trench subduction system, where the SCS is subducting eastward beneath the Philippine Sea plate, and on the west by the Ailao Shan – Red River (ASRR) strike-slip fault system. The SCS is bound on the north by the northern SCS rifted margin and in the northeast by the Taiwan arc-continent collision, which is actively closing the SCS basin. The conjugate rifted margin is at the southern edge of the SCS, where it has collided at Borneo and Palawan in the southern Philippines.

The northern SCS margin formed by rifting during the late Cretaceous or early Paleocene through the Oligocene (Holloway, 1982; Lee and Lawver, 1994; Ru and Pigott, 1986) when extension began near the arc of an Andean-style Mesozoic subduction zone along the South China block (Hamilton, 1979; Li and Li, 2007). Continental breakup occurred ~30 Ma in the northeastern SCS (Lin et al., 2003) and propagated to the southwest, producing a diachronous unconformity that youngs from the northeast to the southwest (Franke, 2012). Magnetic anomalies also indicate a general northeast – southwest opening of the SCS during early Oligocene – Miocene (Briais et al., 1993; Taylor and Hayes, 1983), although the SCS opening involves at least one southward ridge jump at ~25 Ma and possibly a major transform fault between the southwest and eastern SCS sub-basins (Barckhausen and Roeser, 2004).

The mechanism that initiated rifting and seafloor spreading in the SCS is still controversial. The leading hypotheses suggest that the SCS opening may be driven by subduction forces in the western Pacific (Holloway, 1982; Taylor and Hayes, 1983) or extrusion from the India-Eurasia collision (Briais et al., 1993; Liu et al., 2004; Tapponnier et al., 1982). The extrusion hypothesis is strongly linked to the sense and

timing of motion along the ASRR fault. There is still much debate over the history of the ASRR fault, particularly its offshore extent, but many studies interpret potentially 100s of km of sinistral slip from the Oligocene to the mid-Miocene (Zhu et al., 2009), concurrent with SCS seafloor spreading. However, the timing of slip on the ASRR fault post-dates the onset of rifting and so does not account for the formation of the SCS rifted margins (Clift et al., 2008; Northrup et al., 1995; Pubellier et al., 2004). It is important to note, though, that these are not necessarily competing mechanisms, and that each may have contributed to formation of the SCS in different measures and at different stages.

The resultant northern SCS margin is over ~300-400 km wide and consists of a moderately stretched continental shelf and a broad continental slope and COT. Outboard of the continental shelf, previous studies revealed highly extended continental crust less than ~15 km thick with interspersed volcanic bodies (Nissen et al., 1995a; Nissen et al., 1995b; Wang et al., 2006; Yan et al., 2001b). Crust is locally less than ~6-8 km thick beneath thick sedimentary basins such as the Baiyun sag, a sub-basin of the Pearl River Mouth Basin (Hu et al., 2009; Huang et al., 2005), the Xisha trough near Hainan Island in the northwestern SCS (Qiu et al., 2001), and in other local minima in crustal thickness along the wide continental slope (Hayes et al., 1995).

Wide-angle profiles have also identified a HVLC of ~7.0-7.5 km/s in the lower crust of the distal margin attributed to mafic magmatism (Nissen et al., 1995b; Wang et al., 2006; Zhao et al., 2010). The HVLC has been documented in the vicinity of the Dongsha Rise, but it pinches out in the Pearl River Mouth Basin to the west near the Xisha trough (Qiu et al., 2001). The timing of emplacement for the HVLC is highly uncertain, but it is not generally regarded as a syn-rift feature. Instead, Nissen et al. (1995b) interpreted the HVLC as a pre-rift mafic lower crustal body, while others

associate the HVLC with possible post-spreading Pliocene-Holocene magmatism in Dongsha Rise (Franke, 2012; Yan et al., 2001a; Zhao et al., 2010).

No seaward-dipping reflectors have been found along the margin that would indicate extensive syn-rift magmatism, but a number of wells have encountered both syn-rift and post-rift volcanic rocks. Recovered syn-rift volcanic rocks are dated from latest Paleocene through the onset of seafloor spreading in the early Oligocene. Primarily felsic syn-rift volcanic rocks are reported from wells in the Pearl River Mouth Basin, though andesitic and basaltic samples have been recovered as well (Li and Rao, 1994; Yan et al., 2006). Near Taiwan, recovered syn-rift rocks are mainly basaltic (Wang et al., 2012).

Although the geological evidence demonstrates at least a moderate amount of syn-rift volcanism, volcanic activity continued following the onset of seafloor spreading and throughout the post-rift history of the margin. In the Pearl River Mouth Basin, post-rift basalts range in age from ~27 – 17 Ma (Yan et al., 2006). Near Taiwan and southeast China, post-rift basalts range in age from ~23 – 9 Ma (Angelier et al., 1990; Chung et al., 1995; Wang et al., 2012). Volcanism became active throughout the entire margin during Pliocene – Holocene, with basaltic volcanism being particularly strong near Hainan Island in the northwestern SCS (Flower et al., 1992) and the Dongsha Rise (Ludmann and Wong, 1999). Numerous other volcanic bodies have also been interpreted throughout COT based on geophysical studies (Clift et al., 2001a; Tsai et al., 2004; Wang et al., 2006; Yan et al., 2001b), though little information on their composition or timing has been previously documented.

3.3 TAIGER DATA ACQUISITION AND PROCESSING

We acquired new MCS reflection and wide-angle OBS data during the summer of 2009 (Figure 3-2) as part of the joint NSF and Taiwanese-funded TAIGER (TAiwan Integrated GEodynamics Research) program. The new network of 2D seismic reflection and refraction lines was acquired throughout the region of Taiwan to study the geodynamics of the Taiwan arc-continent collision, but numerous MCS profiles and OBS stations were acquired southwest of Taiwan to study the margin adjacent to Taiwan as an analog for the initial conditions of collision. The data acquired during the MGL0905 cruise provide new high-resolution constraints on the crustal structure of the northern SCS margin in the northeastern SCS. Here we present the MCS reflection lines 05, 04, 20 and coincident OBS profile T3 (Figure 3-2).

Data were acquired with the seismic vessel R/V Marcus G. Langseth using a source array consisting of 36 airguns on 4 strings with a total nominal volume of 6600 in^3 towed at 8 m depth. On MCS profiles, shots were spaced 50 m apart and recorded for 15 seconds at a 2 ms sample rate by a 468 channel, 6 km streamer. The streamer had a receiver interval of 12.5 m and CDP spacing was 6.25 m. We acquired coincident four-component (vertical, two horizontal, and one hydrophone component) OBS data separately using a shot interval of 150 m to minimize contamination from previous shot noise. 17 OBS stations were deployed with a nominal spacing of 15 km, but 3 of the instruments were recovered without usable data. OBS were supplied by the U.S. OBS instrument pool (OBSIP) and recorded continuously with a 5 ms sample rate.

MCS reflection data were processed with an emphasis on multiple attenuation and imaged using pre-stack time migration following the processing flow in Chapter 2. The reflection data provide high-resolution constraints on the sedimentary strata down to the

top of basement reflection. Crustal reflectivity and a Moho reflection are frequently imaged where multiples are successfully attenuated. The OBS data were minimally processed with gapped deconvolution, bandpass filtering, and offset-dependent gaining. The gapped deconvolution was used to collapse the seismic wave train to improve the accuracy in picking secondary arrivals at near offsets, such as reflections and sedimentary refractions. We chose a single operator for each OBS record using a 500 ms filter length and 100 ms prediction distance. Traces were subsequently band-pass filtered with a high-cut filter (4-14 Hz pass band, 4dB/octave roll-off) and then gained by offset to optimize picking at different offset ranges.

3.4 VELOCITY MODELING

3.4.1 Travel-time Picking

OBS were deployed along a 328 km profile spanning the continental shelf and distal margin of the northeastern SCS margin near Taiwan. Following instrument recovery, instruments were relocated using the direct arrival from source to instruments. Although the raw OBS records are contaminated by strong low frequency noise, the processed records contain high-quality data with usable signal typically out to ~60-80 km offset, with some records containing signal out to ~100 km offset (Figures 3-3, 3-4, and 3-5; see Appendix C for additional OBS records). First arrivals exhibit a range of apparent velocities, from ~2.0 km/s to over ~7.0-7.5 km/s, indicating that these data constrain the velocity structure of the whole crust and possibly upper mantle.

We recognize two refracted phases in these data: arrivals at near offsets with slow apparent velocities (less than ~5.0 km/s) that are consistent with seismic energy turning

through sedimentary strata, and arrivals with faster apparent velocities (over ~5.0 km/s) that we take to be from the crust and potentially upper mantle. Along the northern end of the profile, the cross-over point between sedimentary and crustal phases occurs at offsets of ~15-20 km, while sedimentary refractions are only observed as secondary arrivals at the southern end of the profile (Figure 3-5). We also interpret a top of basement reflection that may be observed as a wide-angle reflection at the northern end of the profile, but is observed at near offsets at the southern end of the profile. These initial observations are consistent with our new MCS reflection images (presented in a subsequent section) and earlier drilling and geophysical observations that show thicker (~4-6 km) post-rift strata in the rift basin along the continental shelf (Lee et al., 1993; Lin et al., 2003) and a much thinner sedimentary section (~1-2 km) in the deep basin (Li et al., 2007).

In total, we have picked 6476 refraction arrivals (1084 sedimentary arrivals, 5392 crustal arrivals) and 1590 reflection arrivals (1045 OBS top of basement reflections, and 545 MCS top of basement reflections) to be inverted by travel-time tomography for the margin velocity structure (Figure 3-6). Picks were assigned uncertainties ranging from 50 ms to 100 ms based on visual inspection. The uncertainties reflect varying S/N or data quality at different offsets and instruments, and are used to define the misfit tolerance for travel-time tomography.

3.4.2 Travel-time Tomography

We inverted the travel-time picks using the travel-time tomography scheme of Van Avendonk et al (2004b). Iterations of tomography consist of ray tracing (Moser, 1991; Moser et al., 1992) in an assumed seismic velocity model and then solving for model updates by linearized least-squares inversion of the misfits between observed and

calculated travel times. In this approach, the model space is over-parameterized and the inversion is regularized by damping, flattening (minimizing first-order spatial derivatives), and smoothing (minimizing spatial second-order derivatives). The objective is to solve for a minimum-structure velocity model that satisfies travel-time picks within the limits of the assigned uncertainties. Each iteration seeks to reduce χ^2, the normalized data misfit weighted by the corresponding uncertainties. The inversion progress from an assumed, but incorrect, starting model and incrementally reduces χ^2 until a geologically reasonable velocity model is achieved that produces a satisfactory fit between observed and calculated travel-times.

The phases we interpret in the OBS data, as well as newly acquired and previously published MCS data justify a layered model consisting of a water layer, sedimentary layer, and basement layer. We parameterize the model using these layers and discrete boundaries representing the seafloor and top of basement. We do not model the Moho and an upper mantle layer, as wide-angle Moho reflections and upper mantle refractions are not always apparent in OBS records. Instead, we include all potential upper mantle first arrivals in a basement layer that extends to the base of the model to avoid biasing the model with a potentially incorrect phase interpretation. Our model spans 328 km horizontally and 35 km vertically, and contains 657 x 141 = 92637 grid nodes, with a horizontal grid spacing of 0.5 km and a vertical grid spacing of 0.25 km.

We define the water layer of our starting model using seafloor bathymetry. The layer is assigned a velocity of 1500 m/s and is not updated throughout the inversion. The sedimentary layer is initially assigned a velocity of 2 km/s, while the basement layer is assigned a velocity gradient from 4.0 km/s at the top of the basement to 8.0 km/s at the

base of the model. Starting with this model, we performed 12 iterations of travel-time tomography, reducing the χ^2 to 1.0 and the RMS data misfit to 98 ms.

The final model (Figure 3-7) shows considerable lateral variation in layer thicknesses and velocities across the profile. The thickness of the sedimentary layer is ~4 km along the continental shelf, but it increases to ~6 km in a thick basin at the base of the continental slope. The sedimentary layer is thin (< 2 km) in the distal margin at the southern end of the profile, as suggested by examination of the cross-over points and MCS data. Sedimentary velocities are ~2.0 km/s in shallow strata and increase with burial depth, as would be expected for primarily compaction-driven velocities. Although we do not explicitly model the Moho, if we take velocities over 7.5 km/s to be indicative of the upper mantle, we observe the crustal thickness to vary dramatically across the model. Crust is thickest beneath the continental shelf (> 20 km), but rapidly thins to only ~4 km thick beneath the thick sedimentary basin at the base of the continental slope. The crust of the distal margin is thicker (~10-15 km) south of this zone, consistent with estimates from earlier gravity forward modeling (Yeh and Hsu, 2004).

3.4.3 Model Resolution

The ray paths calculated in the final model indicate that the crust and upper mantle is well-sampled across much of the profile (Figure 3-6). The ray coverage of the thin crust along the deep basin is excellent, but the lower crust and upper mantle beneath the continental shelf is poorly constrained. While the model provides useful constraints on the full crustal thickness and velocity structure of much of the margin, the model only provides a minimum crustal thickness for the continental shelf at the northern end of the profile.

We further assess the reliability of the model by computing a resolution matrix that gives a quantitative estimate of the model resolution directly from the inverse problem (Van Avendonk et al., 2004a). Averaging windows of various sizes may be applied to the resolution matrix to determine the resolvability of model features. We apply elliptical averaging windows of 8 km x 3 km and 16 km x 6 km to the resolution matrix to test the resolution limits of the velocity model (Figure 3-8). Considering resolution >0.5 as well-resolved, this analysis indicates that the relatively short wavelength velocity structure (Figure 3-8a) of much of the thin crust beneath the continental slope and distal margin is well resolved. The short wavelength velocity structure of the upper-middle crust of the continental shelf is also well-resolved, but as there is less ray coverage with depth beneath the shelf, the model only resolves longer wavelength features (Figure 3-8b).

3.5 Rifted Margin Structure in the Northeastern SCS

The velocity model and seismic reflection images provide new high-resolution constraints on the crustal structure and compositional nature of the margin from the continental shelf out to the distal margin of the COT. The T3 velocity model has been converted to time and displayed with the corresponding seismic reflection image along Line 20 to facilitate comparison between the datasets (Figure 3-9). We also present another dip-oriented seismic reflection profile, Line 05 (Figure 3-10) and strike-oriented seismic reflection profile, Line 04 (Figure 3-12), that demonstrate the primary features of the continental margin in the northeastern SCS. Here we discuss our observations and joint interpretation of seismic velocity and reflectivity.

3.5.1 Continental Shelf

Several TAIGER profiles cross Tainan basin, the outermost rift basin of the continental shelf near Taiwan. Industry drilling and reflection data have shown Tainan basin to consist of a half-graben rift basin and continental slope depocenter separated by a fault-bound basement high. The basin contains 2-6 km of Cenozoic post-rift and foreland basin strata, though this section may be as thick as 10 km immediately adjacent to Taiwan (Lee et al., 1993; Lin et al., 2003). Subsidence analyses from well data in Tainan basin indicate extension here continued beyond early Oligocene breakup, as rift faults in the basin were active throughout the Oligocene – early Miocene, and reactivated again in the late Miocene (Lin et al., 2003; Tensi et al., 2006). Late Cretaceous – Eocene syn-rift strata are missing in the basin, so that Oligocene strata were unconformably deposited on top of eroded Mesozoic basement strata (Lee et al., 1993; Lin et al., 2003).

The T3 velocity model similarly indicates a sedimentary section 2-4 km thick (Figure 3-7), consistent with these earlier studies. The basement reflection imaged in MCS profiles and used in the velocity modeling corresponds to the unconformity between Oligocene strata and pre-rift Mesozoic basement strata below (Lee et al., 1993). The Mesozoic strata are imaged along the reflection profile Line 20 as a weakly reflective package corresponding to seismic velocities of ~4.5 – 5.0 km/s in the upper ~3 km of the basement layer (Figure 3-9). The continental crust has seismic velocities over ~5.0 km/s, but the model does not constrain the full thickness of the crust. However, the coincident reflection image Line 20 (Figure 3-9) and parallel dip-line Line 05 (Figure 3-10) show a deep reflection at ~10.5 - 11 s two-way travel-time (TWT) that we interpret to be the Moho. The reflection occurs just ~0.5 - 1 s TWT beneath the constrained portion of the T3 velocity model, indicating the crust is ~25 km thick.

The seismic reflection data (Figures 3-9, 3-10) also image numerous normal faults throughout the continental shelf. The primary rift structures we image are predominately landward-dipping normal faults that penetrate into the middle crust. The major rift basin-bounding fault is particularly well-imaged on Line 05 (Figure 3-10), where it soles into a seismically reflective middle crust at ~7.0 seconds TWT or ~15 km depth. Many of these faults appear to be recently active, as faults cut shallow strata and in some cases extend to the seafloor. The recent activity may be due to flexure from loading at the Taiwan collision. The minor throw of these faults in the shallow subsurface, as well as flexural modeling of Taiwan (Lin and Watts, 2002), indicates that continental margin here experiences only minor effects from the collision.

3.5.2 Continental Slope

South of the continental shelf, the crust thins dramatically from ~25 km to ~4 km beneath a ~6 km thick sedimentary basin at the base of the continental slope (Figure 3-7). Upper mantle velocities and a strong Moho reflection (Figures 3-9, 3-10) shoal towards the thin crust and thick sedimentary section at the center of the basin. Crust gradually becomes thicker over a distance of ~100 km to the south (Figure 3-7), where faulted crustal blocks are evident in the seismic reflection images (Figures 3-9, 3-10). The fault blocks are bound by normal faults that are oriented towards the basin center and appear to sole into a weakly reflective low-angle detachment fault at ~8-9 sec TWT or ~15 km depth (Figure 3-11). These structures are typical of highly extended continental crust rather than oceanic crust as previously proposed for the northeastern SCS.

We interpret 3 unconformities in the post-rift sedimentary section that may be mapped throughout the region (Figures 3-9, 3-10). The deepest of these is limited to the

extent of the continental slope, suggesting the highly thinned rift basin was a local sediment sink through the early post-rift history. Drilling constraints are limited to Tainan basin on the continental shelf (Lin and Watts, 2003), and so we lack age control on these events in the distal margin. However, fanning growth strata may frequently be observed in deeper sedimentary packages on top of the normal-faulted crustal blocks that we interpret as evidence for syn-rift deposition (Figure 3-11). A high-amplitude reflection occurs at the top of the syn-rift strata that we take to be the early Oligocene breakup unconformity, since it marks the boundary between apparent syn-rift and post-rift strata.

The presence of syn-rift strata and breakup unconformity reinforces our interpretation of highly thinned continental crust rather than oceanic crust. We also identify possible volcanic features interspersed among the faulted crustal blocks. Two of the largest volcanic bodies identified in the TAIGER dataset are observed on Line 04 near the seaward edge of the highly thinned rift basin (Figure 3-12). The largest volcanic body penetrates through the seafloor and is observable in bathymetry (Figure 3-2). This feature has been sampled by dredging, which recovered ~22 Ma post-rift basalt samples (Wang et al., 2012). Several high-amplitude reflections we interpret as sills occur throughout the post-rift section near these volcanic bodies as well (Figures 3-9, 3-12), further indicating that much of the volcanism here post-dates rifting. Possible syn-rift volcanic material is imaged on a fault block beneath the continental slope on Line 05 (Figure 3-10). This block does not contain any apparent syn-rift strata, and the basement reflection is discontinuous and rugose in character. However, we find little other evidence for extensive syn-rift magmatism, despite the extreme crustal thinning here.

3.5.3 Continent-Ocean Transition

The COT is imaged at the seaward end of Line 20 and T3, where crust is ~12-15 km thick (Figure 3-7). In contrast to the highly thinned rift basin beneath the continental slope, few extensional structures are apparent in the seismic reflection images. The nature of the crust is ambiguous from seismic reflection data alone, although the deepest unconformity we interpret here may correspond to the breakup unconformity associated with the fault blocks along the continental slope. The presence of syn-rift strata and a breakup unconformity would imply the crust below must have a continental origin, though we identify several possible volcanic zones within the crust from the reflection images. These distinct zones are characterized by a rugose basement reflection with numerous diffractions and out of plane reflections (Figure 3-14). Despite this evidence for magmatism in the distal margin, we do not observe any seaward-dipping reflectors that would indicate extrusive volcanic material from extensive syn-rift magmatism as observed in magma-rich margins. Instead, the volcanic bodies we observe disrupt the breakup unconformity and frequently deform the overlying post-rift strata, consistent with a pulse of post-rift magmatism.

The T3 velocity model provides stronger constraints on the composition of the crust of the distal COT. The velocity structure we model is inconsistent with either normal or atypically thick ocean crust, which is characterized by a change in velocity gradient from oceanic layer 2 pillow basalts and sheeted dikes to oceanic layer 3 gabbros (Figure 3-9). However, figure 3-9 also demonstrates the velocity of the distal COT crust is faster than upper continental crust velocity of the continental shelf. This may be due to a component of mafic magmatic intrusions in the distal margin that increases the bulk velocity resolved in our model. This interpretation is consistent with the recent magnetic

modeling that suggests crust in the northeastern SCS may be magmatically intruded upper crust (Yeh et al., 2012). Magmatic intrusions could potentially obscure extensional structures that may have been involved in the rifting process, and may explain the paucity of extensional structures apparent in seismic reflection data.

Though the T3 velocity model precludes oceanic crust in our study area, the velocity structure we observe is strikingly similar to the velocity structure of the highly attenuated but magmatically-intruded continental crust that constitutes the COT of the western and central northern SCS margin (Figure 3-9). This includes a distinct lower crustal body with fast seismic velocities of ~6.9 km/s – 7.5 km/s (Figure 3-14) similar to the HVLC reported near the Pearl River Mouth Basin and Dongsha Rise (Nissen et al., 1995b; Wang et al., 2006; Yan et al., 2001a). Continuous reflections mark the top and base of the layer, and we observe intermittent internal reflectivity, though reflectivity is in places obscured by residual multiple energy (Figure 3-14). The HVLC occurs throughout the distal COT, but it pinches out against the Moho beneath the faulted blocks of the highly thinned rift basin (Figure 3-11).

Vp/Vs modeling suggests the HVLC is likely a mafic magmatic feature of the northern SCS margin (Zhao et al., 2010), rather than serpentinized upper mantle as observed in some margins (Funck et al., 2004). Other researchers have also interpreted the HVLC as a magmatic body by association with volcanic bodies in the overlying crust (Franke, 2012; Nissen et al., 1995b; Yan et al., 2001a). The reflectivity of the HVLC we observe is suggestive of magma intruded or underplated to continental crust (McBride et al., 2004). We also interpret the HVLC in the northeastern SCS margin as a mafic magmatic body, though we cannot distinguish between magma ponded at the base of the

crust or intruded into the lower crust. We discuss the possible timing of this body in the following section.

3.6 Discussion: Magmatism and Extension of the Northeastern SCS

Our observation of tilted fault blocks with syn-rift strata, volcanic zones, and HVLC are consistent with a wide rifted margin in the northeastern SCS that contains highly thinned and magmatically modified continental crust. Figure 3-15 summarizes these features in schematic diagram. We have identified two notable domains in the distal margin outboard of the continental shelf: a highly thinned rift basin consisting of normal-faulted crustal blocks and low-angle detachment fault beneath a wide continental slope, and a zone of thinned but more magmatically modified continental crust in the distal COT. These data do not encounter SCS oceanic crust, but the COT extends south towards a zone of seamounts or ridges near latitude 20° N that we assume to be the continent-ocean boundary for the northern SCS. This is in agreement with the continent-ocean boundary proposed by Briais et al. (1993) and Taylor and Hayes (1980) based on unequivocal magnetic lineations south of this latitude (Figure 3-2).

3.6.1 Crustal Thinning

Geophysical studies of the unstretched crust of South China report a crustal thickness of ~30-35 km (Li et al., 2006). Assuming this as an estimate for the initial crustal thickness, we can determine the stretching factor β ($\beta = \frac{\text{Initial Crustal Thickness}}{\text{Final Crustal Thickness}}$) based on our observations of crustal thickness. Crust is ~25 km thick at the continental shelf, and so we estimate β = ~1.2 – 1.4. Subsidence analyses on wells in Tainan basin

indicate β = 1.4-1.6 for the continental shelf (Lin et al., 2003). The difference between β determined from well data and the β we determine may reflect some amount of stretching in the upper mantle recorded by the basin stratigraphy that is not constrained in our crustal-scale data, but the difference may also include some degree of error in our estimate of crustal thicknesses.

The crust does not thin monotonically towards the COT, but reaches a minimum thickness of ~ 4 km beneath the continental slope, where we estimate a maximum β of ~7.5 – 8.5. Crust gradually becomes thicker towards the COT, where it maintains a uniform thickness of ~15 km. Our estimates of β in the distal COT depend on the nature of the HVLC. If the HVLC indicates magmatic material intruded into the lower crust, our observations of crustal thickness represent the final crustal thickness after rifting and β = ~2.0-2.3. However, if the ~3-5 km thick HVLC indicates magmatic material underplated to the base of the crust, the true thickness of rifted crust may be ~10 km and β = ~3.0 – 3.5.

3.6.2 Extensional Structures

In Tainan basin along the continental shelf, we have imaged listric normal faults that sole into a reflective middle crust at ~15-20 km depth, suggesting a weak mid-crustal detachment near the brittle-ductile transition with a top-to-the-north sense of shear. A weak zone in the middle crust has previously been inferred for the northern SCS margin from seismicity observations in Taiwan's foreland (Mouthereau and Petit, 2003), while a numerical model of the Taiwan collision invokes a weak middle crust to explain a pre-collisional phase of extension (presented in Chapter 5).

The evidence for a weak middle crust detachment contradicts the classical "christmas tree" profile of crustal strength, which presumes the middle crust near the brittle-ductile transition is the strongest part of the crust (Brace and Kohlstedt, 1980; Goetze and Evans, 1979). Such detachments may evolve naturally near the brittle-ductile transition during rifting (Bos and Spiers, 2002; Lavier and Manatschal, 2006; Mancktelow and Pennacchioni, 2005; Regenauer-Lieb et al., 2006), as detachments near the brittle-ductile transition have been documented in other extensional environments (i.e. Miller et al., 1983). However, studies of the unstretched continental crust in South China have suggested the possibility of a mid-crustal shear zone formed during the pre-rift Mesozoic tectonic history of South China (Zhang and Wang, 2007; Zhang et al., 2005; Zhou and Li, 2000). If this is the case, then the weak middle crust inferred for the northern SCS margin may be an inherited feature that is exploited during Cenozoic rifting.

The normal faults we image at the base of the continental slope indicate strain was localized here to a degree in a high-β rift basin, since the normal faults are generally oriented towards the thin crust at the basin center. On the seaward-side of the basin, we also interpret a low-angle intra-crustal detachment. We interpret a top-to-the north sense of shear for this detachment, primarily based on the presumption that the north-dipping normal faults sole into it. However it is also possible that the normal faults in the upper crust and detachment fault represent different generations of faulting, as studies of mamga-poor margins display complex polyphase faulting as crust progressively thins in the distal margin (Reston et al., 2007). If this is the case, the sense of shear on the detachment is much less certain.

Strain localization is not unique to the northeastern SCS, but appears to be a consistent feature of the continental slope along much of the northern SCS margin. The Baiyun sag (Hu et al., 2009) and Xisha trough (Qiu et al., 2001) are similar high- β basins beneath the continental slope, and Hayes et al. (1995) describe other similar local minima in crustal thickness associated with tilted fault blocks near the Dongsha Rise. Despite the strain localization and large amount of crustal thinning, continental breakup occurred ~100 km outboard of these basins.

At such high β, the entire crust and upper mantle may become brittle (Reston, 2009), potentially leading to serpentinization of the upper mantle via fluids from through-going faults, or extensive syn-rift magmatism may be generated by decompression melting. Serpentinization or magmatism can facilitate breakup where strain is localized (Pérez-Gussinyé et al., 2001). The intra-crustal low-angle detachment marks the deepest limit of apparent brittle deformation in these data, though nearby normal faults on the landward-side of the rift basin may penetrate into the upper mantle (Figure 2-11 in chapter 2; Li et al., 2007). However, the upper mantle seismic velocity (~8 km/s) is consistent with unaltered upper mantle, and as discussed above, we infer little – modest syn-rift magmatism here. Without serpentinite or extensive melt to weaken the upper mantle, the mantle advected in the high-β rift may have retained sufficient strength to prevent breakup here.

3.6.3 Magmatism in the COT

Our observations show surprisingly little evidence for significant syn-rift magmatism in the high-β failed rift basin, where we would expect the most decompression melting. We image large volcanic edifices nearby, but the ~22 Ma

dredged sample (Wang et al., 2012), occurrence of sills in the post-rift sedimentary section, and disruption of the possible breakup unconformity and post-rift strata indicate these are more likely associated with post-rift magmatism. These observations indicate the extreme crustal thinning here was not accompanied by voluminous syn-rift magmatism.

The COT exhibits more evidence for significant magmatism. This includes volcanic or intrusive zones at the top of the basement in seismic reflection images and relatively fast crustal velocities that we take to reflect some degree of magmatic intrusion, particularly in the HVLC at the base of the crust. As discussed above, the HVLC is consistent with mafic magmatism as observed in many magma-rich rifted margins. We take the ~3-5 km thick HVLC to be an approximate minimum thickness of melt in the distal COT, with the likelihood that more melt has been intruded into the crust above the HVLC as well.

While such lower crustal magmatic bodies are regarded as syn-rift features in magma-rich margins, the timing of the HVLC in northern SCS margin is uncertain, at best. Nissen et al. (1995b) argued that heat flow, margin subsidence and thickness of the HVLC (~3-7 km) are inconsistent with syn-rift underplating, and so the HVLC must be a pre-rift lower crustal body. Studies of Mesozoic granitoids and volcanic rocks have predicted mafic underplating in association with the predominately felsic magmatism in southeast China prior to Cenozoic rifting (Zhou and Li, 2000). However, recent velocity models of south China indicate continental crust is generally slower than 7.0 km/s. (Li et al., 2006; Zhang and Wang, 2007). It is therefore unlikely that the HVLC is a pre-rift feature of the crust.

Other studies have proposed the HVLC is associated with the Pliocene-Holocene magmatic event that post-dates seafloor spreading (Franke, 2012; Wang et al., 2006; Yan et al., 2001a; Zhao et al., 2010). The post-spreading interpretation has been favored based on the argument that the HVLC was mainly limited to the vicinity of the Dongsha Rise, which was strongly affected by the Pliocene-Holocene magmatic event. However, the HVLC is not strictly limited to the Dongsha Rise, but pinches out towards Hainan Island (Nissen et al., 1995b; Qiu et al., 2001), where Pliocene-Holocene magmatism is also particularly strong. Additionally, our new observations reveal the HVLC extends into the northeastern SCS, where little Pliocene-Holocene volcanism has been documented. We do not rule out a Pliocene – Holocene contribution to the HVLC, but the link between the HVLC and post-spreading volcanism may be tenuous.

Instead, we note that the HVLC spatially corresponds to the northwest and eastern sub-basins of the SCS. This would suggest the HVLC could be related to late Cretaceous – Oligocene rifting or Oligocene – Miocene seafloor spreading in these sub-basins. We compare our observations to melt production in the 1D thermal model of pure shear rifting from Bown and White (1995) to gain further insight into the possible relationship between crustal thinning and magmatism in the distal margin. Their model predicts melt generation from decompression melting in asthenosphere upwelling beneath uniformly stretching and thinning lithosphere based on assumed rift durations, stretching factors, asthenospheric mantle potential temperatures, mantle solidus, and initial conditions.

We assume a single rifting episode lasting ~20 – 35 m.y. for simplicity. The lower limit of 20 m.y. is the duration of syn-rift volcanism in the northeastern SCS (Wang et al., 2012a). The upper limit of 35 my reflects the general rift duration reported for the northern SCS margin (Clift et al., 2001b; Line et al., 2003; Ru and Pigott, 1986; Su et al.,

1989), though there may be multiple distinct episodes within that timeframe (Lee and Lawver, 1994; Ru and Pigott, 1986). For these rift durations, neither the high-β rift basin with β ~7.5 – 8.5 or the distal COT with β ~2.0 – 3.5 produce any melt for an asthenospheric mantle potential temperature of 1300° C (Figure 3-16). However, when the mantle potential temperature is increased to 1400° C, the predicted melt thickness equals or exceeds the minimum crustal thickness we observe with still little melt generated in the distal COT. Therefore, the distribution of magmatism we infer in the distal margin is inconsistent with uniform stretching during pure shear rifting.

3.6.4 Convective Removal of Continental Lithosphere

The distribution of magmatism we interpret in the northeastern SCS does not correlate well with the crustal thinning we estimate. It is also difficult to reconcile with melt predictions from a simple 1D model of uniform, pure shear rifting (Bown and White, 1995) over published rift durations for the northern SCS margin. The magmatic features of the distal margin may require the additional removal of the lithosphere, or a mantle plume source. We consider it unlikely that the magmatism was driven by a deep-seated mantle plume, as there is no current evidence for such a plume in the SCS. Though we interpret a number of magmatic features in the distal margin, the northern SCS margin does not have the large igneous province or seaward-dipping reflectors that are hallmarks of plume-influenced magmatic margins, such as the North Atlantic rifted margins.

The possibility of depth-dependent stretching, with preferentially greater extension in the mantle, has been raised in subsidence analyses of wells in the Pearl River Mouth Basin (Clift and Lin, 2001). 2D dynamic models of rifting also invoke preferential mantle stretching to explain similarly wide rifted margins offshore Angola and Brazil

(Huismans and Beaumont, 2011). In their models, lithospheric mantle stretches and breaks up prior to the crust, and is then convectively removed during the final stages of rifting, leaving the highly extended crust in contact with warm, asthenospheric mantle.

We lack the constraints to address the amount of stretching accommodated in the lithospheric mantle during rifting, but geochemical studies of Cenozoic mantle xenoliths and basalts along the southeast coast of China and the continental shelf near Taiwan support convective removal of continental lithosphere between the latest stages of rifting and subsequent seafloor spreading. These studies indicate Eocene (~56 – 38 Ma) syn-rift magmatism was generated in refractory, but metasomatized continental lithosphere that pre-dates rifting and may be as old as late-Archean – Proterozoic in age (Xu et al., 2000; Wang et al., 2012a, Wang et al., 2003). However, post-rift Miocene (~23 – 9 Ma) basalts exhibit an EM2 mantle signature that requires removal of the refractory mantle and influx of fertile asthenospheric mantle between the latest rifting stages at the end of the Eocene and early Miocene post-rift seafloor spreading (Xu et al., 2000; Wang et al., 2012a; Wang et al., 2012b; Chung et al., 1995).

The persistence of occasional Archean-Proterozoic mantle xenoliths within post-rift Miocene basalts (Wang et al., 2003) renders whole-sale lithospheric delamination unlikely. Chung et al. (1994) instead proposed convecting mantle could pluck away blocks of the continental lithosphere, allowing up-welling of warm asthenosphere that can induce magmatism. This model closely resembles the fate of lithospheric mantle in the late stage of rifting in the model of Huisman and Beaumont (2011). This may be particularly plausible for the South China Sea, as numerous geophysical and geochemical studies support a similar model of convective removal of Archean continental lithosphere

during Mesozoic – Cenozoic tectonic events in eastern China near the Yellow Sea (Gao et al., 2002; Griffin et al., 1998; Menzies et al., 1993).

The recently published dredge sample of ~22 Ma EM2 basalt from the large volcanic body imaged on Line 04 (Figure 3-2, Wang et al., 2012b) links the magmatic features we interpreted in the distal margin to magmatism induced by possible convective removal of lithosphere. Our observations indicate magmatism was strongest in the distal margin, where we have interpreted multiple volcanic or intrusive bodies and a HVLC. This may suggest that the convective removal process is more vigorous or effective in the distal margin. We postulate that such a process could be enhanced in the distal margin where mantle-upwelling is likely focused leading up to breakup and the onset of seafloor spreading.

3.7 CONCLUSIONS

The TAIGER seismic reflection and wide-angle OBS data provide new crustal-scale constraints on the structure of the northern SCS rifted margin in the northeastern SCS. These data image crust ~25 km thick and listric normal faults that sole into a weak middle crust at the continental shelf. In contrast to previous interpretations of the crustal nature in the northeastern SCS, these data provide evidence for highly extended continental crust with increasing magmatic modification in the distal COT. The data presented here do not image the COB, which places the COB south of latitude ~ 20°. Crust is thinnest beneath the continental slope, where it is characterized by tilted fault blocks and a low-angle intra-crustal detachment fault. Despite the extreme crustal thinning and apparent strain localization beneath the continental slope, breakup occurred over 100 km to the south.

The distal COT consists of thinned continental crust overprinted with what we interpret as possibly late stage syn-rift or post-rift magmatism. Magmatic features we identify include volcanic zones at the top of the basement and a ~3-5 km thick HVLC that represents either magmatic underplating or pervasive lower crustal intrusions. The crustal velocities of the distal COT are transitional between continental and oceanic crust, which we take to indicate some degree of magmatic intrusion into the extended continental crust. The spatial and temporal distribution of magmatism in the northern SCS margin may be explained by convective removal of pre-rift lithospheric mantle and influx of warm, fertile mantle between the latest stage of rifting and post-rift seafloor spreading. Breakup and the onset of seafloor spreading may have focused mantle convection and hence convective removal of the lithospheric mantle in the distal COT.

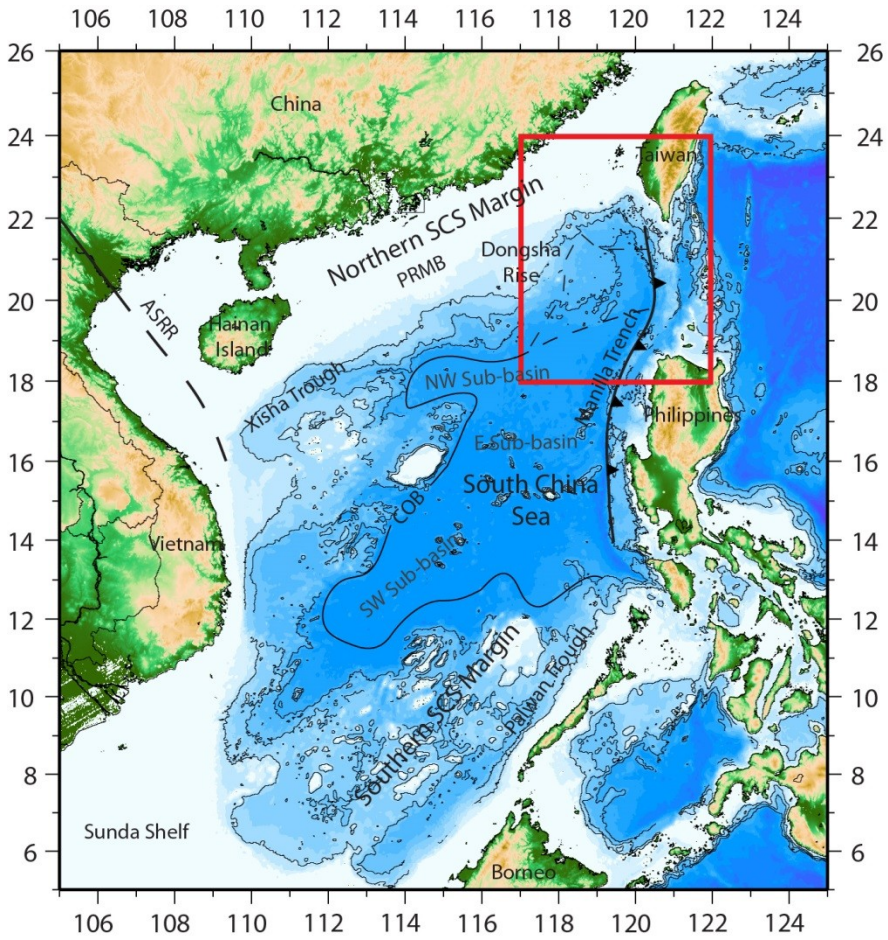

Figure 3-1: Regional tectonic map of the South China Sea (SCS) marginal basin. The SCS consists of Northwest, East, and Southwest sub-basins. Red box is study area (Figure 2). COB is continent-ocean boundary as defined by geophysical and drilling studies. Dashed COB lines area are two proposed COBs in study area (see Figure 2). ASRR = Ailao Shan-Red River fault system. PRMB = Pearl River Mouth Basin.

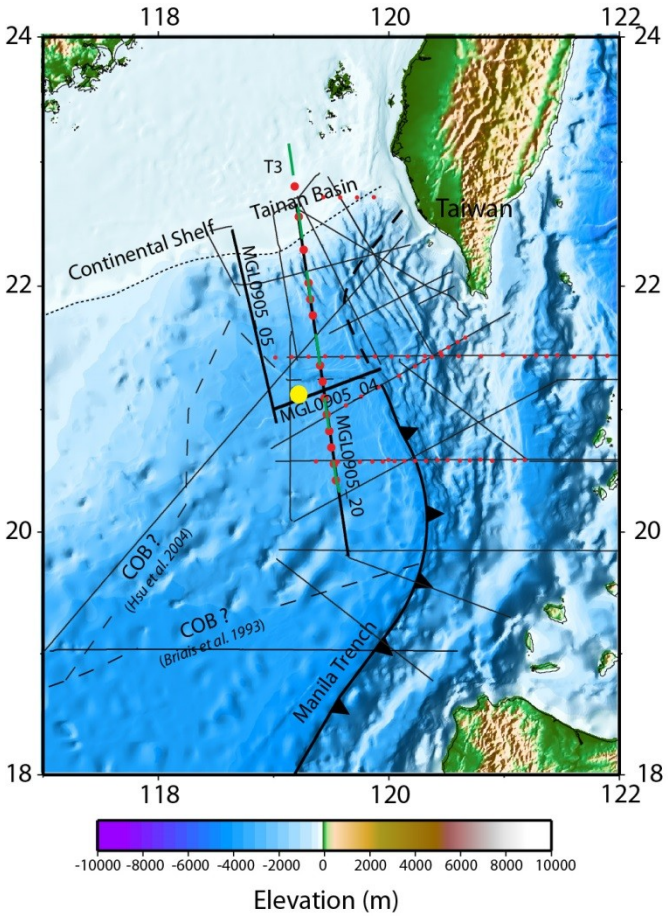

Figure 3-2: Study area (see red box on Figure 1). Dashed lines are COB proposed by (Briais et al., 1993) and (Hsu et al., 2004), dotted line is the continental shelf edge. Solid black lines are MCS reflection profiles, green line is T3 wide-angle seismic profile with OBS locations in red circles. Bold black lines are MCS reflection profiles presented here. Yellow circle is location of dredge samples in (Wang et al., 2012).

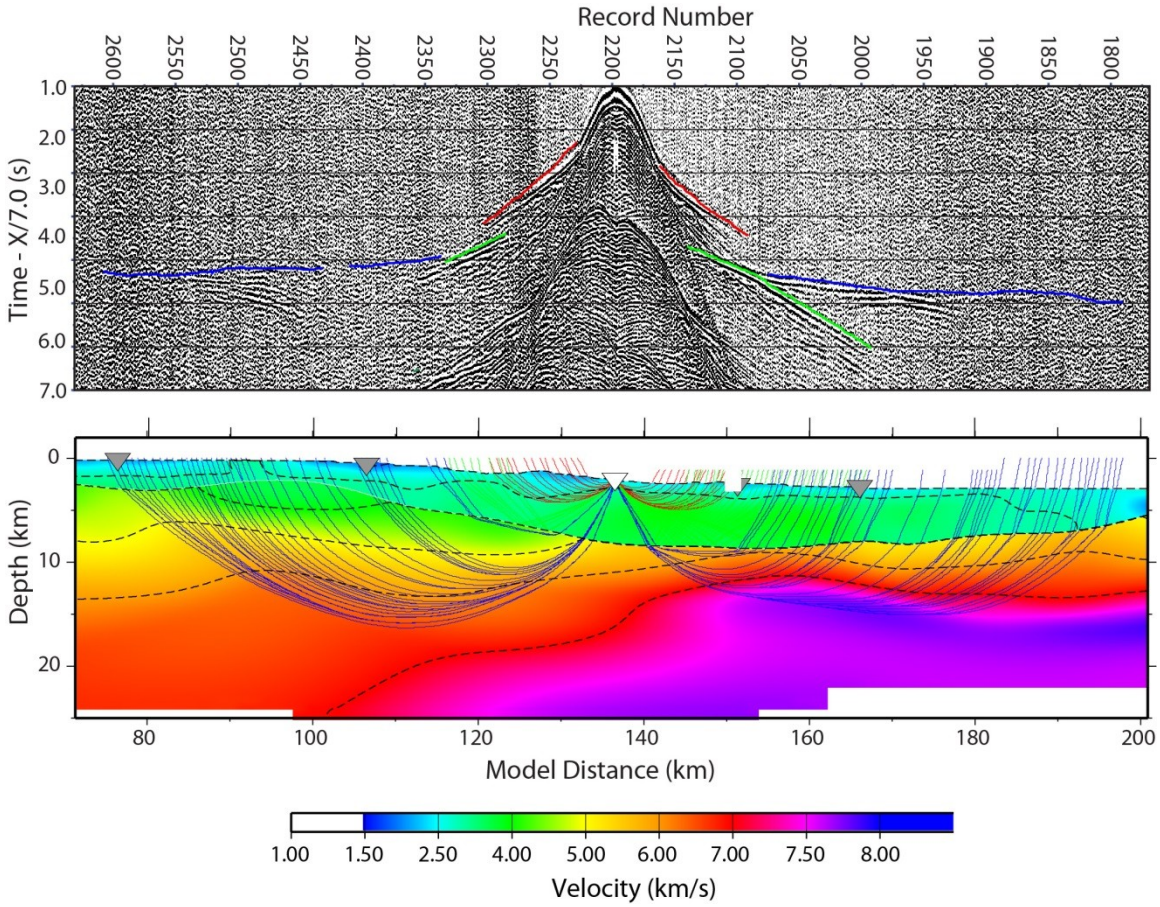

Figure 3-3: Top – OBS 10 hydrophone component with picked sedimentary layer refractions (red), crustal layer refractions (blue) and top of basement wide-angle reflections (green). Bottom – Ray coverage for OBS 10 in final velocity model.

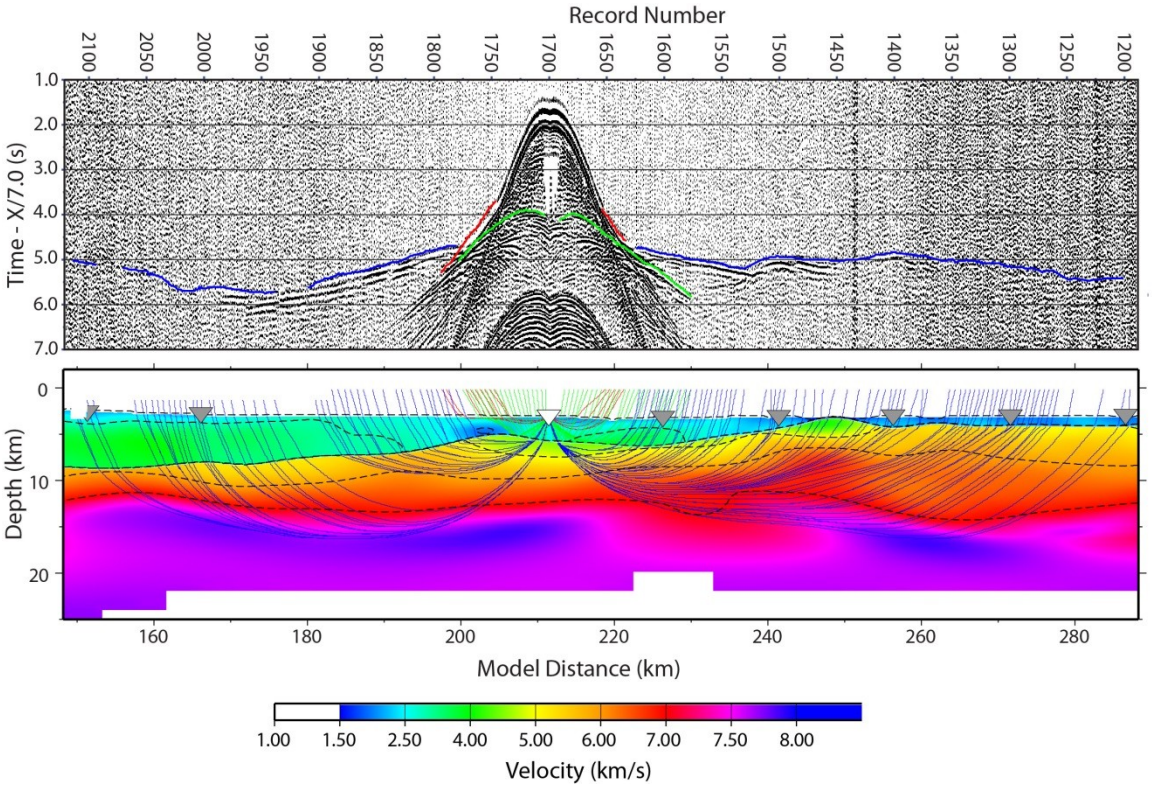

Figure 3-4: Top – OBS 15 hydrophone component with picked sedimentary layer refractions (red), crustal layer refractions (blue) and top of basement wide-angle reflections (green). Bottom – Ray coverage for OBS 15 in final velocity model.

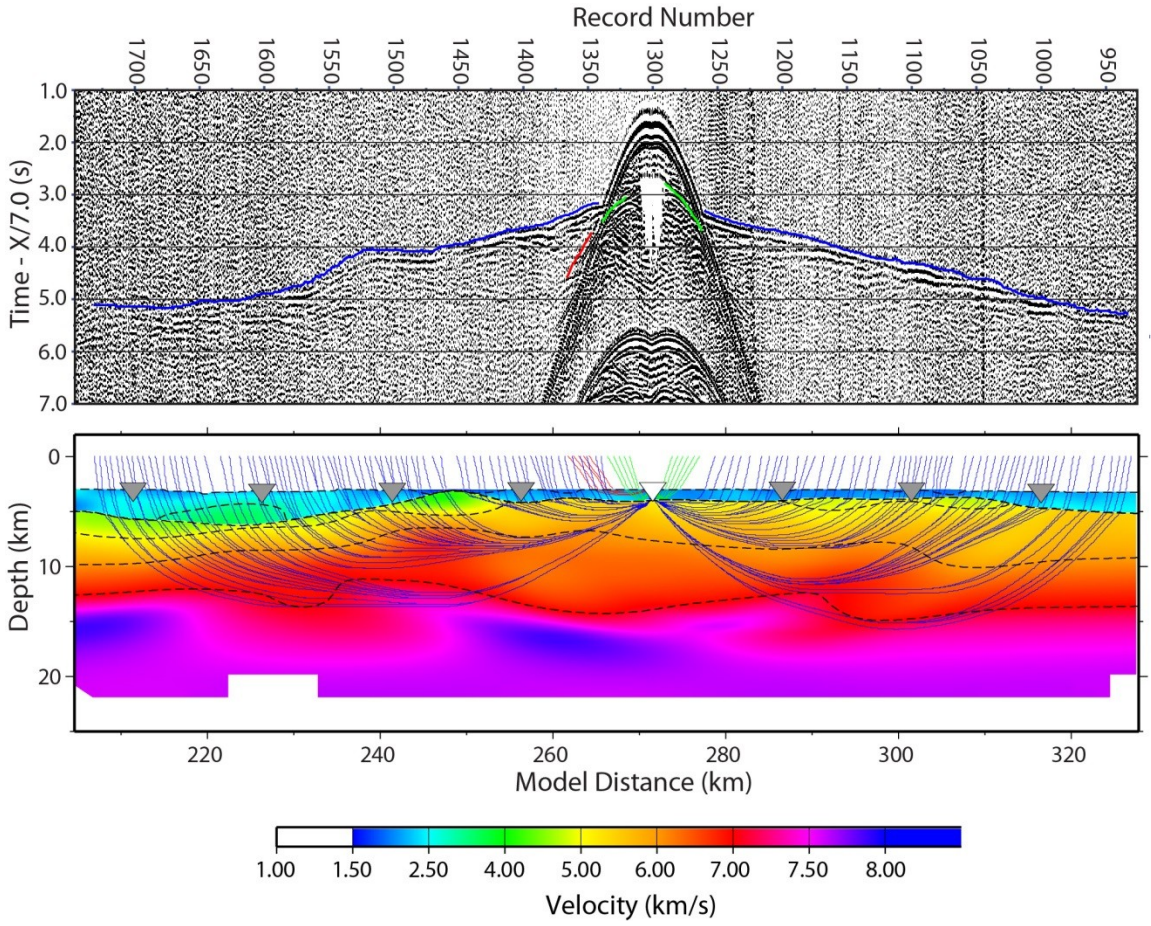

Figure 3-5: Top – OBS 19 hydrophone component with picked sedimentary layer refractions (red), crustal layer refractions (blue) and top of basement wide-angle reflections (green). Bottom – Ray coverage for OBS 19 in final velocity model.

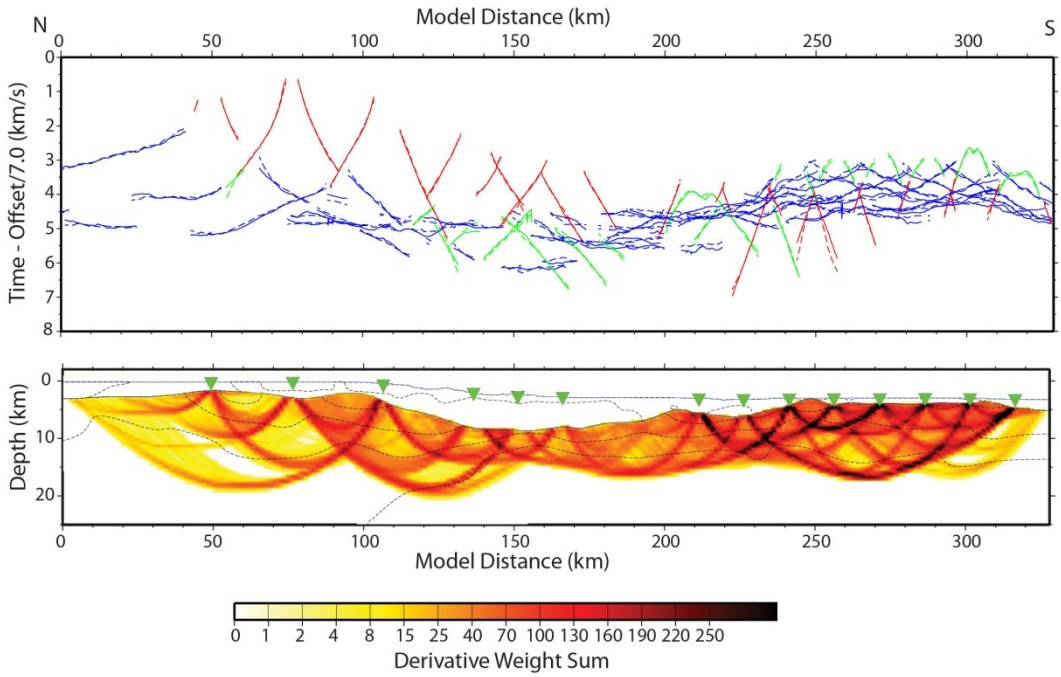

Figure 3-6: Top – all picked (solid lines) and calculated (dashed) arrival times. Red – sedimentary layer refractions, green – top of basement wide-angle reflection, blue – crustal layer refractions. Bottom – Derivative weight sum indicates ray coverage throughout crust. Green triangles are OBS locations. Ray coverage is excellent throughout the transitional crust outboard of the continental shelf (model distance ~120 km – 328 km), but only the lower crust of the continental shelf is unsampled.

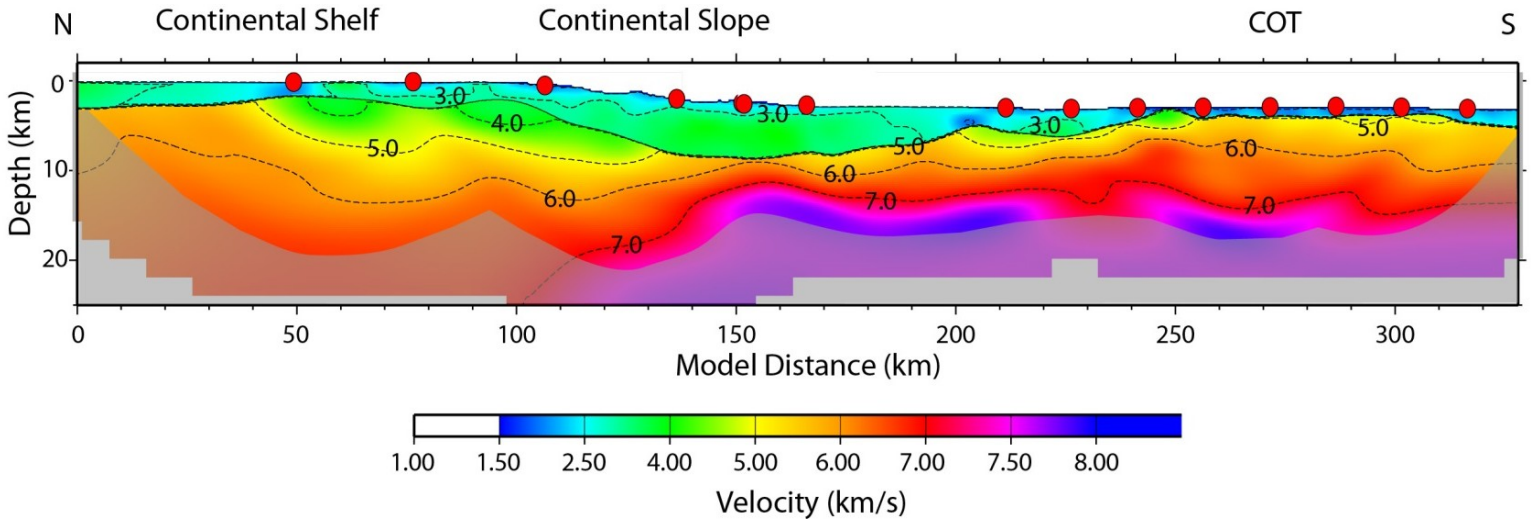

Figure 3-7: Travel-time tomography velocity model along T3. Red circles are OBS locations, gray mask indicates areas of poor ray coverage. Sedimentary layer is characterized by velocities of ~2.0-3.5 km/s, crustal layer by velocities over ~4.0 km/s – 7.5 km/s. Upper mantle velocities are > 7.5 km/s. The sedimentary layer is thickest (~6-7 km) from model distance ~130 km – 180 km, which overlies thin (>5 km) crust. Crust is thickest (> 20 km thick) at the north end of T3 along the continental shelf, crust at the south end of the line is ~15 km thick.

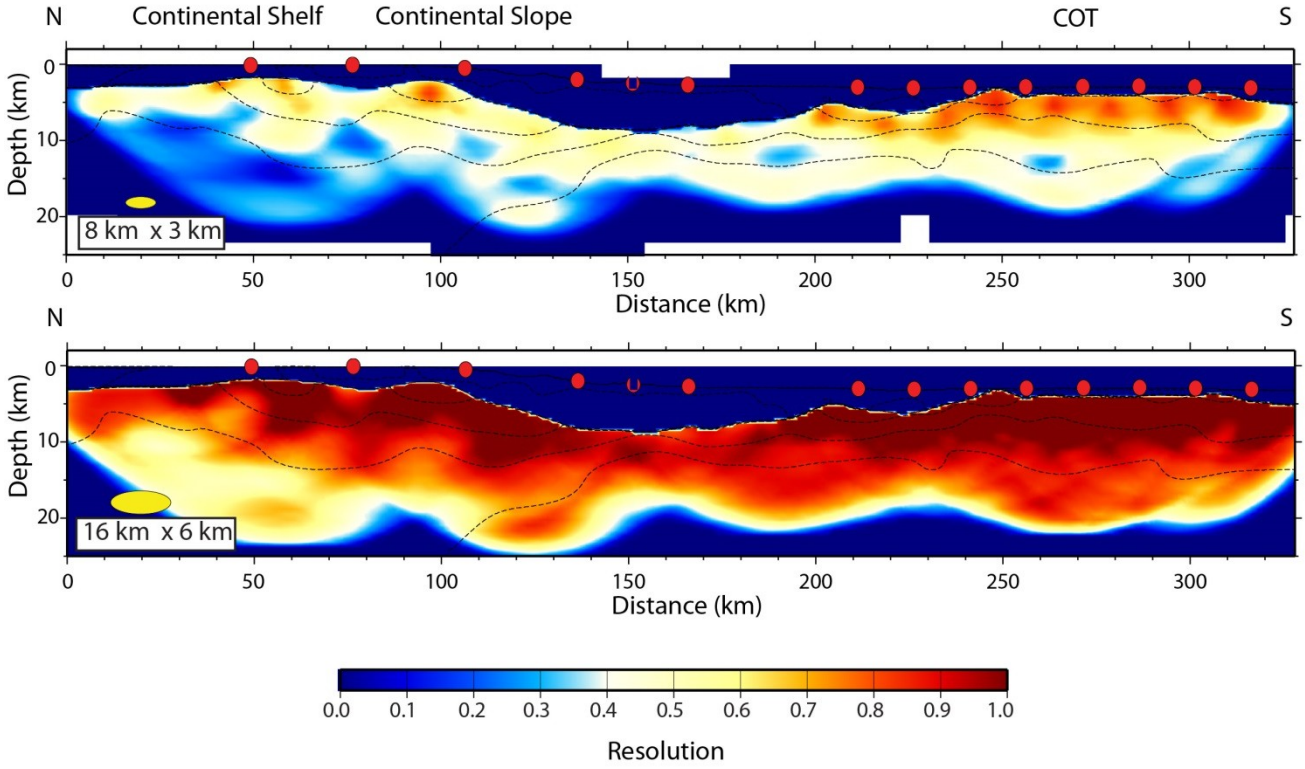

Figure 3-8: Resolution of crustal layer in T3 tomography model in figure 3-7. Features with resolution over 0.5 are considered well-resolved. Top – 8 x 3 km elliptical velocity perturbations are well-resolved in the upper crust of the continental shelf, but are well-resolved throughout the thinner crust south of the continental shelf. Bottom – 16 x 6 km elliptical velocity perturbations are well-resolved throughout the model where there is ray coverage.

Figure 3-9: Pre-stack time migrated seismic reflection image (top) and interpretation (bottom) along MGL0905_20 (see figure 3-2 for location), coincident with much of T3 velocity model (underlain in bottom interpreted panel – colors same as figure 3-8). These data image rift faults along the continental shelf and slope, but few major extensional features are apparent in the COT. Green horizon is basement. Four regional unconformities may be mapped throughout the region, including a possible breakup unconformity (blue horizon). A weakly reflective lower crustal layer is imaged along much of the line, though residual multiples contaminate much of the deep crustal section. Black box is zoom in figure 3-12.

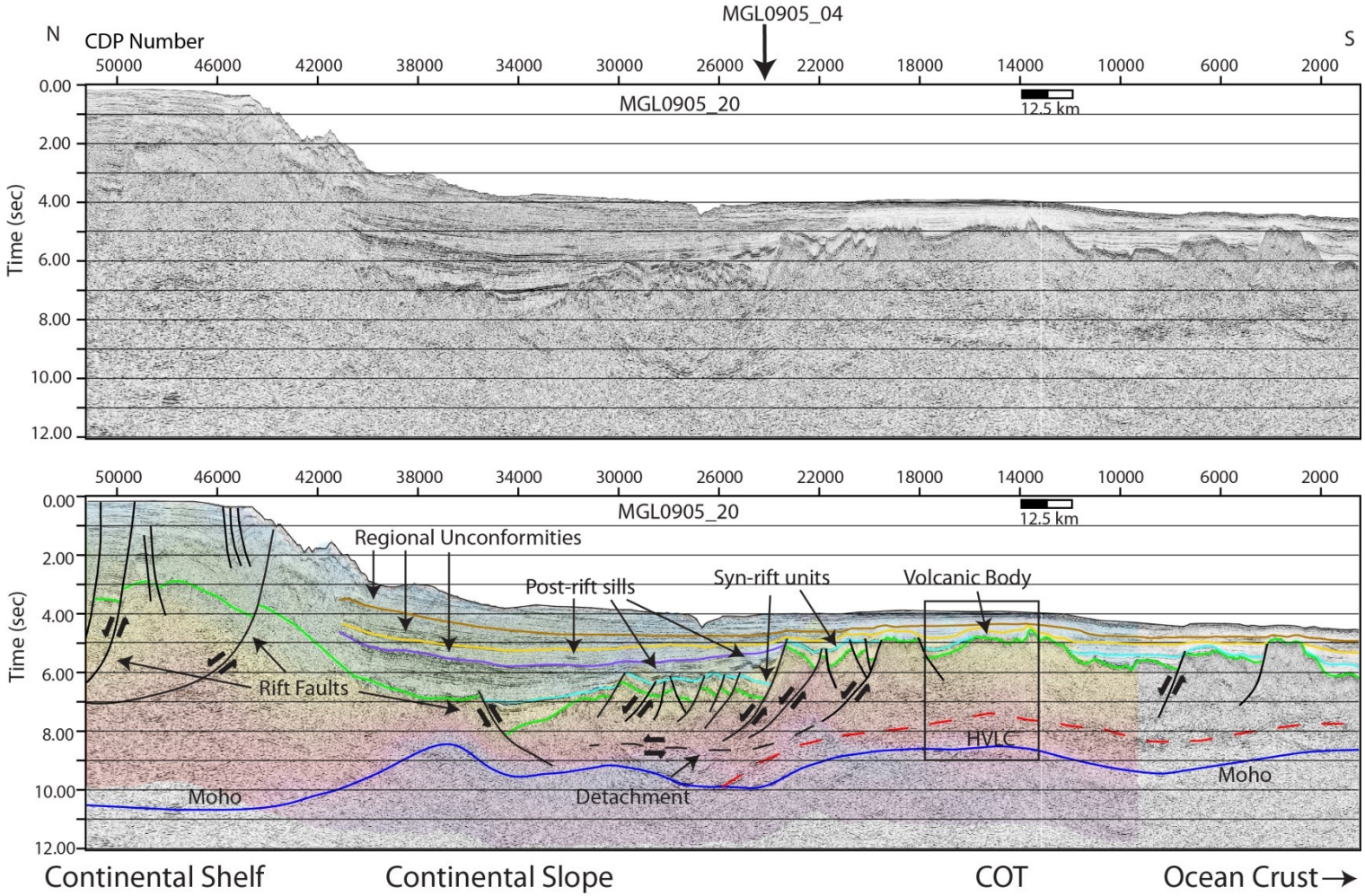

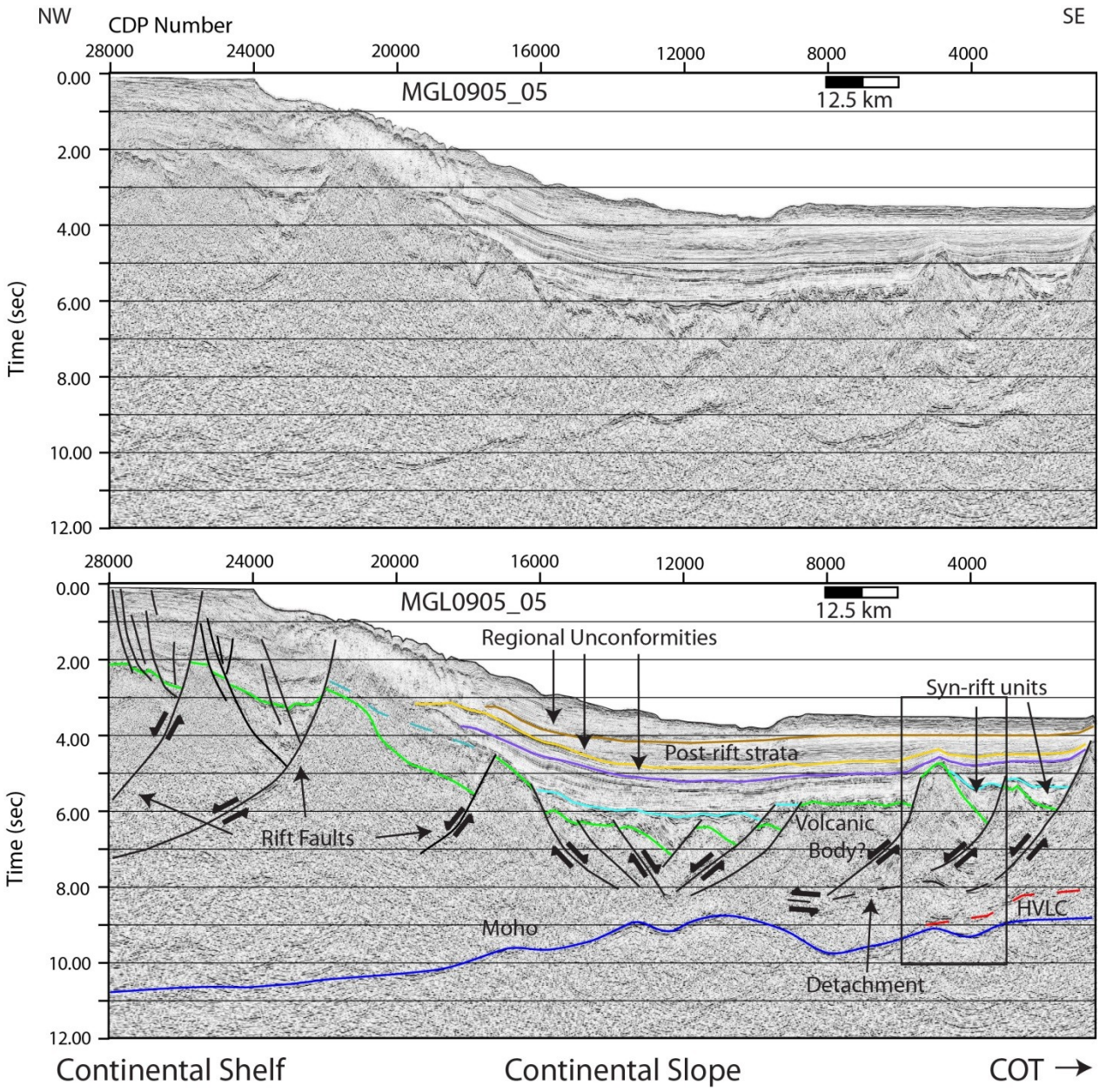

Figure 3-10: Pre-stack time migrated seismic reflection image along MGL0905_05 (see figure 3-1 for location). Along the continental shelf, listric rift faults sole into the middle crust. Faulted crustal blocks and syn-rift strata along the continental slope, with faults soling into a weakly reflective detachment. A strong Moho reflection may be observed across the profile. Black box is zoom in figure 3-14.

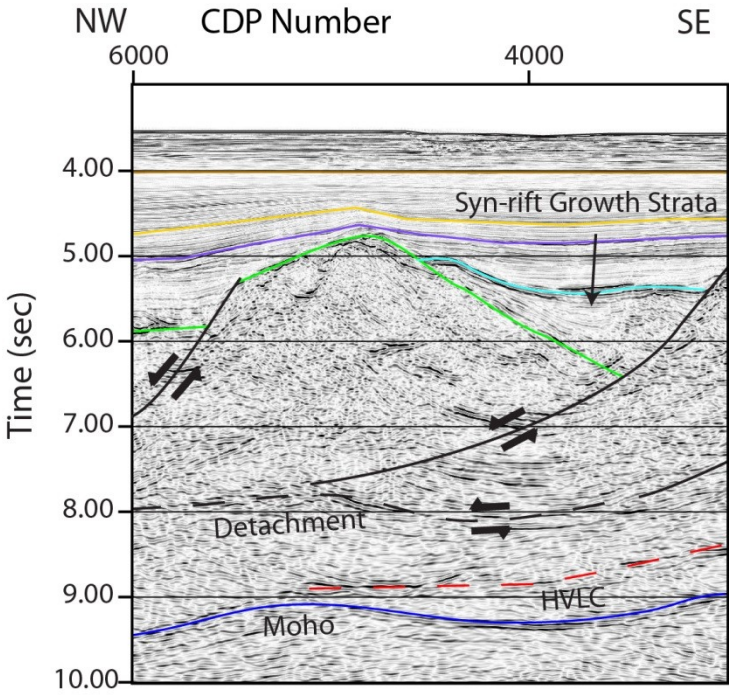

Figure 3-11: Detailed view of faulted crustal block along MGL0905_05 (see figure 3-10 for location). Faults sole into a weakly reflective detachment. Fanning reflections indicate syn-extension deposition. The syn-rift package is capped by a high-amplitude reflection that is likely the ~30 Ma breakup unconformity (blue). A lower crust reflection pinches out against the Moho reflection that we interpret as the top of a magmatically underplated layer.

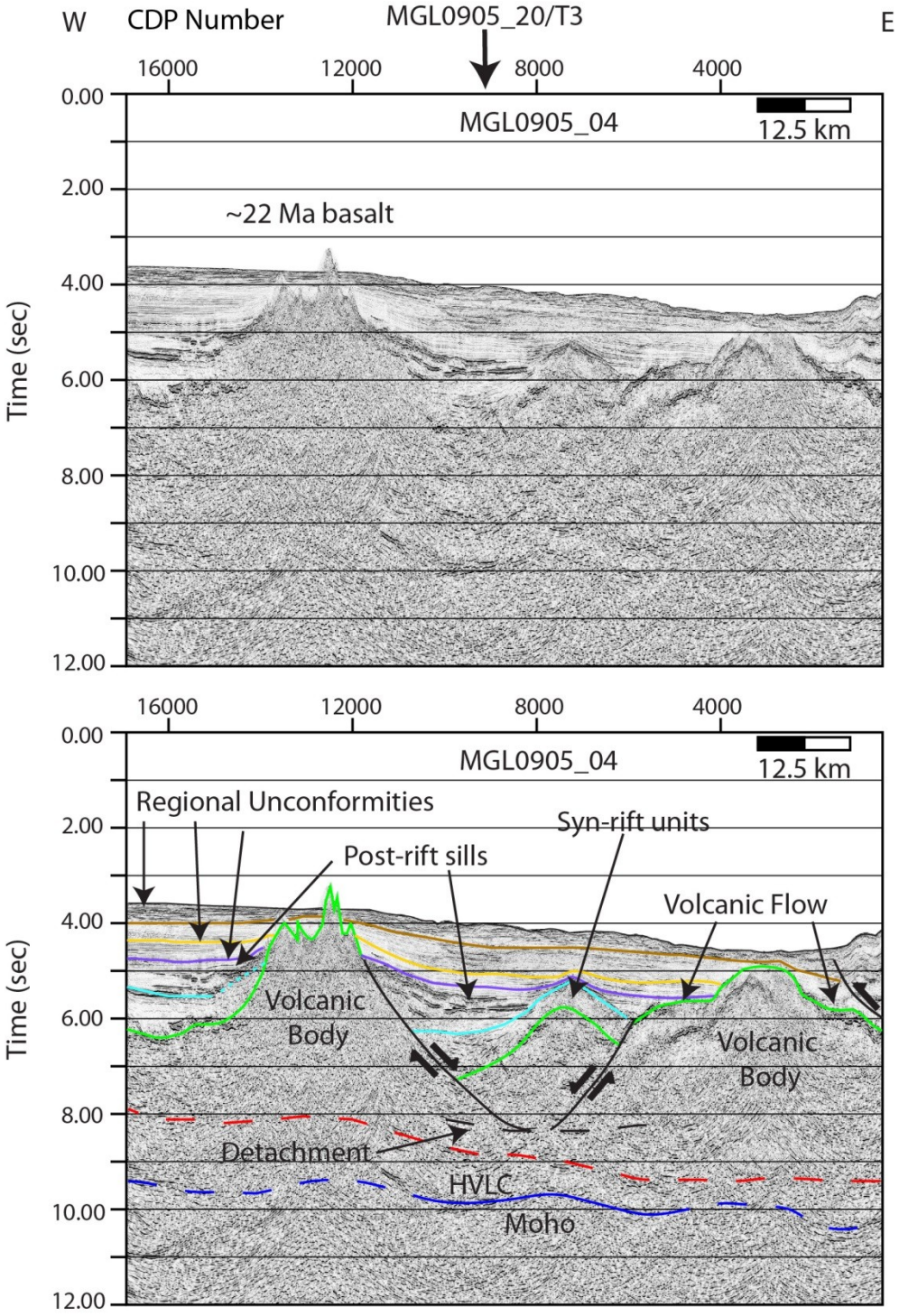

Figure 3-12: Pre-stack time migrated seismic reflection image along MGL0905_04 (see figure 3-1 for location). Large volcanic bodies are imaged at the southern edge of the failed rift basin, but a faulted crustal block lies between them. Abundant sills may be observed throughout the post-rift sedimentary section, indicating post-rift magmatism. The western volcanic body is sampled by dredging, which recovered a ~22 Ma enriched basalt (Wang et al., 2012).

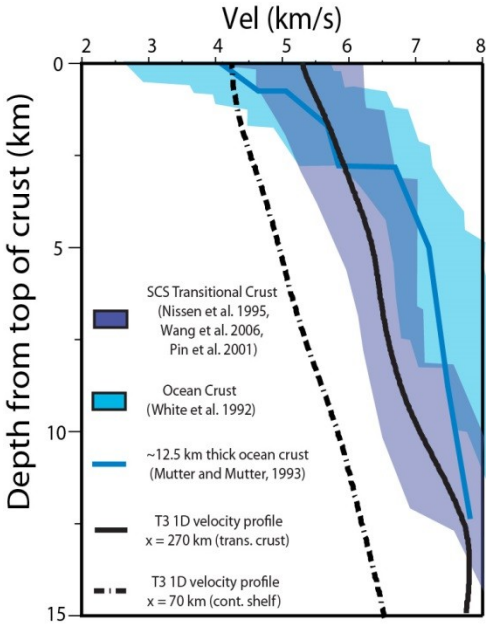

Figure 3-13: 1D velocity profiles from the transitional crust (model distance x=270 km, black solid line) and the continental shelf (model distance x=70 km, black dashed line). The transitional crust velocity structure is consistent with the magmatically-modified, hyper-extended continental crust observed in the northern SCS transitional crust (purple field), but inconsistent with average ocean crust (blue field) or atypically thick ocean crust (solid blue line). However, it is also much faster than the moderately extended continental crust observed at the continental shelf.

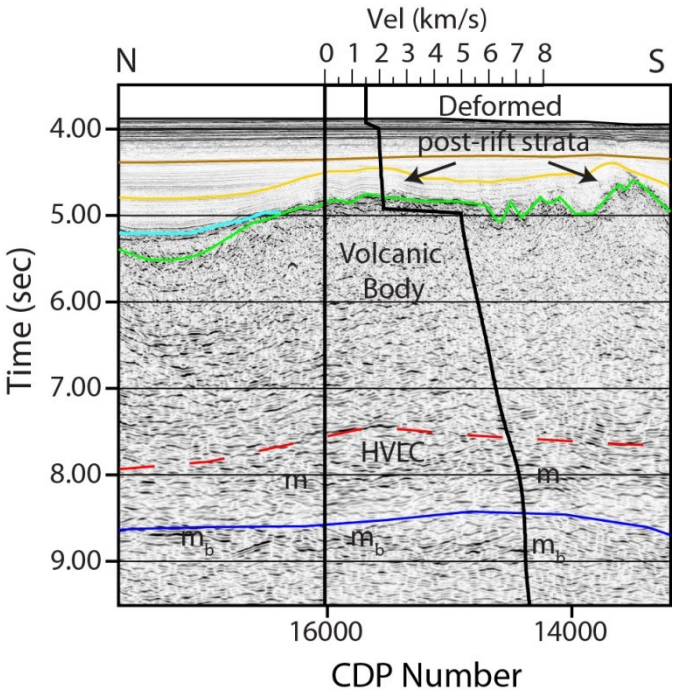

Figure 3-14: Detailed view of possible volcanic body in the COT imaged on MGL0905_20 with 1D time-velocity profile (model distance x = 270 km) overlain (see figure 3-11 for location). The volcanic body is characterized by rugose, diffractive seismic character. No breakup unconformity is observed overlying these features, and the later post-rift strata are deformed, indicating a phase of post-rift magmatism. Despite some residual multiple contamination (m = seafloor multiple, m_b = basement multiple), lower crustal reflectivity corresponds to a high-velocity (~6.7 – 7.2 km/s) lower crustal layer that may be due to magmatic underplating.

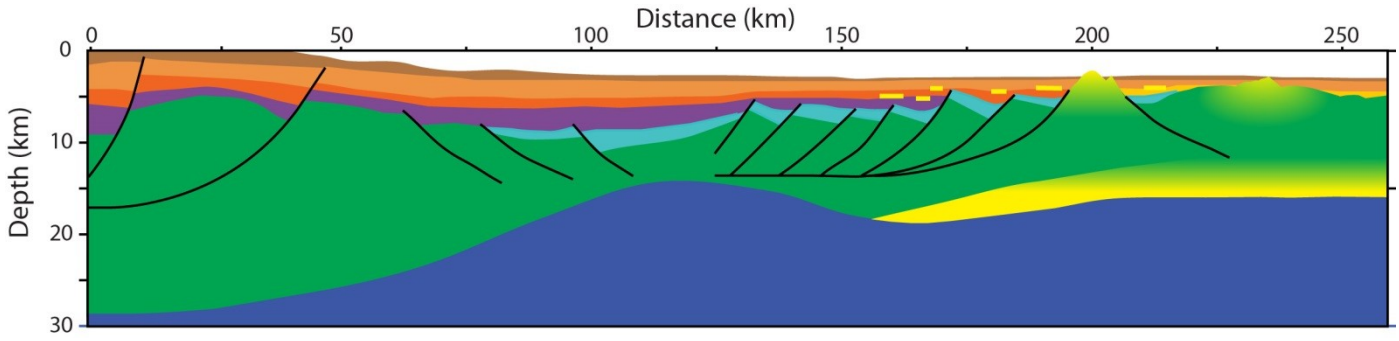

Figure 3-15: Summary rifted margin structure observed in the northeastern SCS. Green – continental crust, blue – syn-rift strata, purple and brown – post-rift strata, yellow – volcanic features including lower crustal magmatic underplating, post-rift sills, and volcanic bodies.

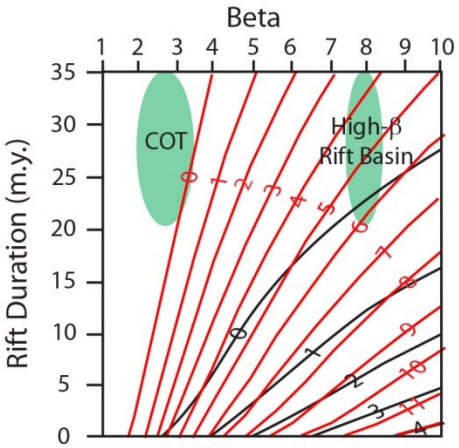

Figure 3-16: 1D thermal model after (Bown and White, 1995) compared to rift duration and crustal stretching factor beta inferred for highly extended crust beneath the continental slope and the COT. Black lines indicate melt produced (in km) from a 1300° C mantle, and red lines are melt production from a 1400° C mantle. For these inferred rift duration and beta, the model predicts no melt production in the COT where the magmatic activity is primarily observed, and up to ~ 6 km of melt production in the high- β rift basin along the continental slope, where little syn-rift magmatism is observed.

Chapter 4:Crustal Accretion in the Manila Trench Accretionary Wedge at the Transition from Subduction to Mountain-Building in Taiwan

4.1 INTRODUCTION

Arc-continent collisions are believed to be an important mechanism for growth of the continents throughout geologic time (Sengör et al., 1993). They mark the closing of an ocean basin at the end of a Wilson cycle, and may involve subduction or accretion of a significant amount of continental material. Yet there are few examples of arc-continent collision occurring in the present day to inform models of the collision process, and as such, there are many aspects of arc-continent collision that are poorly understood. In particular, the behavior of colliding continental crust and lithosphere during collision remains an outstanding issue during the mountain-building process.

This problem is drawn into particularly sharp focus at the Taiwan arc-continent collision, where there has been much debate over the importance of thin-skinned versus thick-skinned structural styles. Suppe (1981) used topographic profiles and the geometry of a basal décollement in the Western Foothills foreland fold-and-thrust belt to argue Taiwan behaves as a steady-state thin-skinned critical wedge. In this model, mountain belts, like accretionary wedges, are described as a deforming wedge of granular media separated by a basal décollement from crust passively subducting below (Davis et al., 1983). Many subsequent studies have expanded on this model by incorporating the effects of erosion, sedimentation, thermal effects and rheological heterogeneity (Morley, 2007; Willett et al., 1993; Willett, 1999) or sought to justify its application beyond the foreland fold-and-thrust belt of Taiwan (Carena et al., 2002; Willett et al., 2003).

However, there are a number of first-order observations that suggest that basement is involved to a significant degree in the mountain-building process in Taiwan, particularly in the Central Range metamorphic hinterland, where pre-Tertiary basement of the northern South China Sea (SCS) continental margin has been exhumed and exposed at the surface (Ho, 1986). Several studies have argued that Taiwan may be described as a thick-skinned wedge driven primarily by underplating rather than frontal accretion (Beyssac et al., 2007; Fuller et al., 2006; Simoes et al., 2007). This model explains the incorporation of crustal material as a down-stepping of the basal décollement into continental crust, shaving off slivers of crust into the overlying wedge as the thick, buoyant continental shelf attempts to subduct eastward beneath the Philippine Sea plate.

A fundamental implication of these models is that the exposed basement rocks of the Central Range are a consequence of steady-state subduction of the northern SCS continental shelf, a requirement not obviously supported by seismicity and regional tomography velocity models (Kuo-Chen et al., 2012). Additionally, numerous studies of rifted continental margins around the world have revealed a wide-range of complex structural and compositional styles (Menzies et al., 2002; Reston, 2009) that may influence the collision process in different ways (Afonso and Zlotnik, 2011; Beltrando et al., 2010; Manatschal, 2004; Reston and Manatschal, 2011). Recently, McIntosh et al. (2013) argued Taiwan is the result of a multi-stage collision in which thin, highly extended continental crust is subducted and structurally underplated to the accretionary prism in advance of the encroaching continental shelf, and then subsequently uplifted and exhumed to the surface during collision with the shelf.

The key drivers of this model include: 1) the identification of a wide zone of thin transitional crust outboard of the northern SCS continental shelf near Taiwan that

contains faulted blocks of highly extended continental crust of the northern SCS margin; and 2) identification of high-velocity material beneath the metamorphosed sediments of the Central Range near Hengchun Peninsula in southern Taiwan taken to be accreted and exhuming transitional crust. In this model, the exposed continental basement rocks of the Central Range originate from the transitional crust of the distal continental margin at the earliest stages of collision, rather than steady-state collision with the thick continental shelf.

We investigate this possibility with coincident multi-channel seismic (MCS) reflection data and wide-angle ocean-bottom seismometer (OBS) data from offshore southern Taiwan that constrain the crustal structure of the incipient mountain belt at the early stages of collision. These data reveal a fast seismic velocity anomaly that is suggestive of crustal material structurally underplating the accretionary prism at the early stages of mountain-building. Our new observations support a multi-stage collision in Taiwan and indicate the crustal accretion process is presently occurring at the Manila trench subduction zone south of Taiwan and southeast of the northern SCS continental shelf.

4-2 TECTONIC BACKGROUND

The Taiwan arc-continent collision is the culmination of a complete Wilson cycle that began by rifting of South China in the late Cretaceous, forming the northern SCS continental margin and conjugate margin (Ru and Pigott, 1986). Rifting eventually led to continental breakup in the early Oligocene followed by the opening of the SCS ocean basin by seafloor spreading from early Oligocene – mid-Miocene (Briais et al., 1993). SCS ocean crust began subducting eastward beneath the Philippine Sea plate at the

Manila trench starting in the early to mid-Miocene (Hall, 2002), consuming the ocean crust and in the northern SCS, bringing the Luzon arc of the Philippine Sea plate into collision with the southern Chinese continental margin of the Eurasia plate (Figure 4-1). Because of the oblique geometry of the collision, the Taiwan arc-continent collision began in central-northern Taiwan ~5-7 Ma (Huang et al., 2006) and has been actively propagating southward (Byrne and Liu, 2002; Lee et al., 2006; Suppe, 1984).

Previous researchers have exploited this geometry by interpreting different spatial transects across Taiwan as different temporal stages in the collision process. In northern Taiwan, post-collisional processes dominate, but may be complicated by the opening of the Okinawa trough and roll-back of the Ryukyu trench east and north of Taiwan (Clift et al., 2008; Teng, 1996). Southern Taiwan and immediately offshore southern Taiwan is in the early stage of mountain building (Huang et al., 2000), while further offshore south and southwest of Taiwan likely represents the 'pre-collision' conditions of the northern SCS margin and Manila trench subduction system (Byrne and Liu, 2002).

The Taiwan orogen is frequently discussed in terms of five tectono-stratigraphic domains (Huang et al., 1997). From west to east, they are the Coastal Plain foreland basin; Western Foothills foreland fold-and-thrust belt; Hsuehshan Range in northern Taiwan, an inverted Paleocene rift basin of the northern SCS margin; the Central Range metamorphic hinterland; and the Coastal Range accreted Luzon arc complex. While much of the Central Range is metamorphosed and highly deformed sedimentary strata from the northern SCS passive margin, the eastern Central Range also contains exhumed blocks of pre-Tertiary passive margin metamorphic and igneous basement (Beyssac et al., 2007; Ho, 1986). The Central Range extends south towards Hengchun peninsula and its offshore equivalent, the Hengchun ridge. Morphologically, the Hengchun ridge continues

southward into the accretionary prism along the Manila trench, suggesting a genetic link between the Central Range and the Manila trench accretionary wedge.

Numerous geophysical studies have focused on the Manila trench south of Taiwan in the context of arc-continent collision dynamics as well as seismic hazard potential. These studies describe the accretionary wedge as a doubly-vergent prism consisting of a lower slope domain consisting of imbricate folds and thrusts, and an upper slope domain characterized by a lack of seismic reflectivity and change in bathymetry from the thrust fault ridges of the lower slope (Lin et al., 2008; Liu et al., 1997). The transition from lower slope to upper slope is marked by a sharp change in bathymetric relief, but Lin et al. (2009) infer the transition may be controlled by one or more out-of-sequence thrusts (OOSTs). In the area of incipient collision near Taiwan, the wedge grows significantly, likely in response to early collisional processes, as well as the proximity of sediment sources of the northern SCS margin and onshore Taiwan mountain belt (Huang et al., 2006). The Manila trench loses its sharp bathymetric character in the early collision zone and becomes a less well-defined deformation front (Liu et al., 1997). Shortening offshore southern Taiwan is also accommodated by back-thrusting in the rear of the wedge (Lundberg et al., 1997; Reed et al., 1992) and in the forearc block, which may be subducting (Cheng, 2008; Malavieille et al., 2002; McIntosh et al., 2005).

Near Taiwan, the nature of crust subducting at the Manila trench has been a matter of debate that is critical for our understanding of the Taiwan collision. Distinct linear magnetic anomalies indicate normal ocean crust of the SCS is currently subducting along the Manila trench south of a prominent bend in the trench near latitude 20° N (Briais et al., 1993). Hsu et al. (2004) interpreted potentially older (late Eocene) ocean crust subducting north of here from magnetic data, but this crust is much thicker – up to

~12 km – than typical ocean crust (Yeh and Hsu, 2004). Such thick ocean crust may comprise the continent-ocean transition (COT) at magma-rich margins under the influence of hot spots (Menzies et al., 2002), but no seaward-dipping reflectors or large igneous provinces have been identified that are diagnostic of a magma-rich rifting episode. Instead, recent MCS reflection profiles have identified tilted fault blocks typical of highly extended continental crust rather than atypically thick ocean crust (chapter2, 3; McIntosh et al, 2013).

Similar extended continental crust has been identified by geophysical studies elsewhere along the northern SCS margin (Hu et al., 2009; Nissen et al., 1995b). These studies show the western and central northern SCS margin to consist of moderately extended continental crust overlain by passive margin strata along the continental shelf and a wide distal margin consisting of highly extended continental crust with sporadic volcanic bodies. ODP drilling recovered syn-rift strata in the distal margin, further suggesting rifted continental crust is present ~150-200 km outboard of the continental shelf (Wang et al., 2000). Crust is ~10-20 km thick in the distal margin, but may be locally as thin as <5 km in failed rift basins at the base of the continental slope with several km or more of post-rift passive margin sediments (Hu et al., 2009; Qiu et al., 2001; Yan et al., 2001).

The northern SCS continental margin may represent an intermediately magmatic rifted margin, as the COT in the distal margin also contains some amount of magmatism (Clift et al., 2001). This includes interspersed zones of volcanic bodies and a high-velocity lower crust (HVLC) with velocities of ~6.9-7.5 km/s that has been attributed to either magmatic underplating (Wang et al., 2006; Yan et al., 2001; Zhao et al., 2010), lower crustal intrusions (Franke, 2012) or pre-rift crustal structure of south China (Nissen

et al., 1995b). The timing and spatial extent of magmatic activity and the nature of the lower crustal body are not well understood throughout the margin, particularly in the vicinity of Taiwan. To date, only moderate amounts of syn-rift volcanism has been found, despite the numerous intrusive volcanic bodies distributed throughout the COT. Instead, much of the volcanic activity appears to occur mainly during the Miocene and later, concurrent with the seafloor spreading that opened the SCS ocean basin after the main rifting episodes (Yan et al., 2006; Yeh et al., 2010; Wang et al 2012a; Wang et al., 2012b).

4-3 DATA AND PROCESSING

New MCS reflection and wide-angle OBS data were acquired during the summer of 2009 as part of the joint US and Taiwanese-funded TAIGER (Taiwan Integrated Geodynamics Research) program. We present a coincident OBS and MCS reflection profile (MGL0905-27) from this program acquired across the southern Chinese continental margin and Manila trench south of Taiwan that constrains the crustal structure of the subducting crust and overlying accretionary wedge in the initial stages of arc-continent collision (Figure 4-1). Data were acquired using the seismic vessel *R/V Marcus G. Langseth* with a source array that consisted of 36 airguns with a total nominal volume of ~6600 in^3 towed at 8 m depth. Shots were spaced every 50 m and recorded simultaneously by a 468 channel, 6 km-long streamer and 11 OBS from National Taiwan Ocean University with 2 horizontal, 1 vertical, and 1 hydrophone component. The streamer receiver spacing was 12.5 m and CDP spacing was 6.25 m. OBS spacing was variable, but ranged from ~15-20 km at the southwest end of the profile to ~10 km at the

northeast end. MCS data were recorded for 15 seconds at a 2 ms sample rate, and wide-angle data were continuously recorded at a 4 ms sample rate.

4.3.1 MCS Data

MCS data were processed through pre-stack time migration following the processing flow outlined in chapter 2, including gap deconvolution, 2D surface-related multiple elimination (SRME), radon filtering, offset-weighting, and high-cut bandpass filtering with the purpose of attenuating multiples. The final pre-stack time migrated image (Figure 4-2) provides high-resolution constraints on the sedimentary and crustal structure across much of the profile. The MCS data image sedimentary strata and structure across the continental margin southwest of the Manila trench and throughout the accretionary wedge. The top of basement reflection and strong Moho reflection are well-imaged across the Manila trench and into the lower slope of the accretionary wedge, but are not apparent beneath the upper slope. We also observe a continuous reflection in the lower crust across much of the profile southwest of the trench. Deep, sporadic reflectivity is also imaged within the upper slope of the accretionary wedge, but much of this energy may be residual multiple energy or out of plane reflectivity.

4.3.2 OBS Data

Wide-angle OBS data are generally of high quality at the near to middle offsets, though it varies considerably from instrument to instrument. Unfortunately, the 50 m shot spacing was chosen for optimal MCS data imaging, so the OBS data quality suffers at offsets beyond ~40 km (Figure 4-3), where noise from previous shots obscures

signal (Christeson et al., 1996). This was particularly problematic with arrivals from within the accretionary wedge, which are of weak amplitude and reflect the significant topography of the seafloor. Minimal processing was required to pick first arrivals at near to middle offsets, including bandpass filtering, automatic gain control (AGC) and offset gaining. However, at far offsets where random noise may dominate weak signal, we apply several processing steps that are generally successful at attenuating the previous shot noise, and boost the signal-to-noise ratio (Figures 4-3 and 4-4, additional OBS records in Appendix D). Following OBS relocation, we applied a bandpass filter, gap deconvolution, coherency filtering (dip-based coherency filter and FX-deconvolution), stacking of adjacent traces, and AGC or offset gaining.

The combination of coherency filtering and stacking was particularly successful at attenuating noise at far offsets. Arrivals at far offsets (> ~40 km) are deep crustal or upper mantle arrivals with apparent velocities of ~6.5 – 8.0 km/s. The dip-based coherency filter was designed to emphasize energy with dips within this range, excluding any coherent noise from previous shots that would have a much slower apparent velocity. While the smaller shot spacing causes severe previous shot noise problems, we take advantage of the larger number of traces by stacking adjacent traces to further mitigate S/N issues. This level of processing was required to identify deep crustal and upper mantle arrivals at far offsets that are critical in constraining the full crustal thickness. However, this also introduces added uncertainty in first arrival picks compared to first arrivals picked at near offsets, as processing artifacts such as wavelet side-lobes or spurious coherent noise may be present. Picks at these offsets were made with careful comparison to raw and minimally processed data and in some cases were aided by strong multiples and reciprocal picks from neighboring OBS locations. In total, we picked

15,758 first-arrivals out to offsets of ~70 km to be inverted using travel-time tomography for crustal-scale velocity structure. We assign pick uncertainties ranging from 50 ms at near offsets to 150 ms at far offsets that reflect varying S/N, frequency content, and potential processing artifacts that may reduce our picking confidence (Figures 4-3 and 4-4).

4-4 VELOCITY STRUCTURE

We inverted first arrivals using the minimum structure travel-time tomography scheme of Van Avendonk et al. (2004a) . In this scheme, ray tracing is performed in a reference velocity model that is then updated by model perturbations solved for by a linearized inversion. The inversion seeks to reduce χ^2, the L2-norm of a cost function defined by travel-time misfits weighted by pick uncertainties. The inversion is regularized by damping, flattening (minimizing first-order spatial derivatives) and smoothing (minimizing second-order spatial derivatives) as preferred. The target χ^2 of each subsequent iteration is reduced incrementally to produce robust, geologically reasonable velocity model. The iterations of ray tracing and linearized inversion are terminated when they achieve a satisfactory fit between observed and calculated arrival times within the tolerance of pick uncertainties.

We parameterize our model as a simple two-layer model containing a water layer on top of a subsurface layer. The layer boundary is constrained by bathymetry, and the top layer is assigned a water velocity of 1500 m/s. The MCS image (Figure 4-2) shows how the earth layer may be further divided into sedimentary, crustal, and upper mantle layers, but reflections from layer boundaries are not consistently observed across the entire profile, particularly within the upper slope of the accretionary prism. We therefore

limit our inversion to first arrivals, which are known to produce smooth, but robust results (Zelt et al., 2003).

4.4.1. First-Arrival Tomography Velocity Model

Our model spans 250 km in the horizontal direction and 30 km in the vertical direction, and contains 501 x 201 = 100701 grid nodes. Grid spacing is 0.5 km in the horizontal direction, and 0.15 km in the vertical direction. To construct the initial velocity model, stacking velocities from the MCS reflection data were converted to interval velocities using the Dix equation, then depth converted and smoothed. To add the water layer of the model, we used bathymetry to define the depth to the seafloor and set velocities above the seafloor to 1500 m/s. We performed 14 iterations of travel-time tomography to update the earth layer, reducing the $\chi 2$ from 122 in the initial model to 1.2 in our final model. The final velocity model (Figure 4-5) has an RMS misfit of 73 ms.

The velocity model shows a laterally smooth velocity structure along the continental margin southwest of the Manila trench, but exhibits stronger spatial variation throughout the Manila trench accretionary wedge. Along the southwest end of the profile, velocities vary smoothly from slow velocities consistent with sedimentary rock velocities (less than ~4.0 km/s) near the seafloor to seismic velocities consistent with upper mantle velocities (greater than ~7.5 km/s) ~15 km beneath the seafloor. Across the accretionary wedge lower slope (model distance 115 km – 165 km), the model includes a ~10 km thick section of relatively slow velocity (less than ~5.0 km/s) material consistent with a thick wedge of sediments. Beneath the wedge, seismic velocities are over ~5.0 km/s, consistent with subducting crust. Upper mantle seismic velocities shoal, however, indicating thinner crust beneath the thick accretionary wedge than outboard of the trench.

At the transition from lower to upper slope (model distance 170 km), our model shows evidence for high velocity material within the upper slope wedge not observed in the lower slope wedge, as seismic velocities greater than ~5.0 km/s begin to rise towards the northeast end of the profile, rather than continuing to dive below the accretionary wedge.

4.4.2. Model Resolution

Velocity contours generally parallel seismic reflectivity observed in the MCS data, suggesting our velocity model is a reliable representation of the geology offshore southern Taiwan where constrained. In general, the upper and lower crust are well sampled, but upper mantle velocities are poorly sampled across much of the profile, particularly beneath the upper slope of the wedge in the northeast end of the profile (Figure 4-6). Figure 4-6 also emphasizes that portions of the model southwest of the first OBS and northeast of the last OBS do not have reversed ray coverage, and so the model velocity may not accurately reflect the true propagation velocity. For example, the shallow sedimentary section at the southwest end of the line has a higher velocity of ~4.0 km/s here compared to ~2.0-2.5 km/s where the model is well sampled.

The reliability of the model can be quantitatively assessed by computation of a resolution matrix (Van Avendonk et al., 2004b). The resolution matrix can be interrogated to test how well bodies of a specified dimension are resolved in the model, analogous to the more traditional checkerboard tests. Figure 4-7 demonstrates that 8 km by 3 km elliptical velocity anomalies in the crust are well resolved from model distance 40 km – 200 km. Upper mantle velocities are well-resolved in the center of the profile (model distance 100 km – 160 km), but where ray coverage is poor, we lack strong constraints on the upper mantle velocities so that only the very large wavelength velocity

structure is resolved. Resolution also suffers at profile distances 0 km – 40 km and 220 km – 250 km where we lack reversed ray paths, although large-wavelength features of the crust may still be adequately resolved. Our resolution analysis indicates that crustal thickness beneath the continental margin and lower slope of the accretionary wedge is generally well-resolved, but that we do not adequately resolve upper mantle velocities or subducting crust beneath the upper slope beyond model distance 190 km.

4-5 Crustal Structure of the Incipient Arc-Continent Collision

The OBS and MCS data provide new, high-resolution constraints on the crustal structure at an early stage of arc-continent collision south of Taiwan. The pre-stack time migrated MCS image was converted to depth using the tomography velocity model for the sake of comparison (Figure 4-8). These images show a strike-oriented view of the rifted margin that is obliquely converging with the Manila trench subduction zone, but a dip-oriented view of the accretionary prism that is developing into an incipient mountain belt. Our results yield new insights into the nature of the crust along the continental margin outboard of the Manila trench, the subducting crust beneath the Manila trench accretionary wedge, and the structure and dynamics of the wedge during the onset of collision.

4.5.1. Continental Margin (Model Distance 0 – 115 km)

Southwest of the Manila trench we image post-rift sedimentary strata less than 2 km thick, overlying crust ~10-14 km thick (Figure 4-8a), similar to previous estimates of crustal thickness (Yeh and Hsu, 2004). The sedimentary strata are highly reflective, and

generally have slow seismic velocities of ~2.0 – 3.0 km/s, except where we lack reversed ray coverage at the southwest end of the profile. A high-amplitude reflection occurs at the base of the post-rift section along much of the continental margin (Figure 4-8a) that we interpret as a regional unconformity. The unconformity caps a weakly reflective sedimentary package with seismic velocities of 3.0 – 5.0 km/s that is distinct from the relatively flat-lying, reflective post-rift strata above (Figure 4-8a).

We observe this unit and unconformity across much of the margin along this profile, but it is absent from profile distance ~25 km – 45 km, where the reflective post-rift strata directly overlie the top of basement reflection (Figures 4-2a and 4-8a). Here the basement reflection is rugose and diffractive in character, similar to volcanic bodies imaged in the SCS near the Pearl River mouth basin (Clift et al., 2001). The volcanic body disrupts the unconformity and deforms the overlying post-rift strata, consistent with a pulse of post-rift magmatic activity. Post-rift volcanism throughout the SCS produced predominately basaltic intrusions (Li and Rao, 1994; Yan et al., 2006). A basaltic dredge sample, dated at 22 Ma, was recovered from a nearby post-rift seamount (Wang et al., 2012). We speculate that the volcanic body we observe is likely basaltic as well.

The nature of the underlying crust is ambiguous from the MCS reflection image, due in large part to its strike-parallel orientation, but recent work documents the nearby presence of tilted fault blocks typical of highly extended continental crust (presented in chapters 2 and 3). These fault blocks are associated with a similar unconformity and underlying sedimentary unit as we interpret here. In these dip sections, strata in this sedimentary package are frequently fanning towards normal faults, suggestive of syn-rift deposition. Along the profile presented here, this deep sedimentary package also has relatively fast seismic velocities that are indicative of older, well-lithified sedimentary

strata. We interpret this unit as syn-rift, and the regional unconformity that separates these strata from post-rift strata above as a possible breakup unconformity.

The presence of crustal fault blocks, possible syn-rift strata and volcanic bodies is suggestive of the highly attenuated and magmatically-intruded continental crust that constitutes the wide distal margin along the western and central southern Chinese margin (Hayes et al., 1995; Nissen et al., 1995b; Wang et al., 2006). A detailed examination of the crustal velocities (Figure 4-9) demonstrates that the model velocity structure compares favorably with the velocity structure of this style of transitional crust (Nissen et al., 1995b; Wang et al., 2006; Yan et al., 2001), but is incompatible with average or atypically thick ocean crust, which is characterized by distinct velocity gradients in oceanic crust layer 2 and layer 3 (Mutter and Mutter, 1993). These observations further support the interpretation of the crust in this area of the SCS as highly thinned, but magmatically intruded continental crust.

We also observe a lower crustal body similar to the HVLC observed by Nissen et al. (1995b), Wang et al. (2006) and Yan et al. (2001) in the distal margin of the central northern SCS margin. Recent Vp/Vs modeling indicates the HVLC may be a magmatic feature of the COT (Zhao et al., 2010). Crustal velocities in south China are also generally less than 7.0 km/s (Zhang and Wang, 2007), further suggesting the HVLC is a magmatic feature emplaced either during or after rifting, rather than a pre-rift crustal body. The HVLC layer is less than 5 km thick, and is characterized by seismic velocities of 6.7 km/s – 7.5 km/s, consistent with the HVLC seismic velocities observed elsewhere along the margin. The top of the body is also associated with a strong, continuous reflection (Figures 4-2 and 4-8). A reflection we interpret as Moho occurs at the base of

the HVLC across much of the profile, although the reflection becomes weak near the Manila trench.

4.5.2. Accretionary Wedge Lower Slope (Model Distance 115 – 165 km)

The lower slope of the accretionary wedge extends from the Manila trench (model distance 115 km), where the toe of the wedge is ~2 km thick, to a sharp change in bathymetry at the accretionary wedge upper slope (model distance 165 km), where the wedge is ~10 km thick. Seismic velocities generally vary smoothly from ~2 km/s at the seafloor to ~5.5 km/s at the reflection from the top of subducting basement. At the toe of the wedge, we image ~2 km of flat-lying sediments on the incoming distal continental margin, while sedimentary strata are folded and faulted by a thrust at the deformation front (Figure 4-8b). Several discrete westward-verging imbricate thrust faults are clearly imaged that penetrate up to the seafloor or near the seafloor.

At the toe of the wedge, imbricate faults sole into a décollement near the top of the subducting basement (Figure 4-8b). The basement here is not overlain by the possible syn-rift package and breakup unconformity, and it is more rugose in reflection character, suggesting this may be another post-rift volcanic body intruded into the crust. Deeper into the wedge, thrust faults sole into a high-amplitude décollement that on-laps the volcanic body. The high-amplitude décollement caps a weakly reflective package of subducting sediments up to ~1 km thick that we interpret as the same possible syn-rift unit imaged along the continental margin (Figure 4-8b). A nearby seismic reflection profile previously acquired by Chinese researchers (Line 973) also documents a similar thickness of possible syn-rift sediments on top of normal-faulted basement subducting beneath a laterally continuous, high-amplitude décollement (Lin et al., 2009). The

décollement in this part of the accretionary wedge may be exploiting the breakup unconformity as a possible mechanical boundary between the older, more indurated weakly reflective syn-rift strata below and the relatively weak post-rift strata above. Where present, such a stratigraphic boundary may function as a décollement separating deforming post-rift strata above and subducting syn-rift strata and highly extended continental crust below.

Beneath the wedge, crust thins from ~10 km beneath the toe to ~6 km near the accretionary wedge lower slope – upper slope boundary (Figure 4-8). The seismic velocity of the crust is faster than crust outboard of the trench, ranging from ~5.5 km/s at the top of the basement to ~7.7 km/s at the Moho reflection at the base of crust. One possible interpretation is that this is the subducted continent-ocean boundary, as the crustal thickness approaches that of typical oceanic crust and the seismic velocity structure is faster here than in the thicker crust west of the trench. Another possible interpretation is that this is the along-strike view of a failed rift basin within the distal continental margin. Similar zones have been observed throughout the northern SCS continental margin such as the Xisha trough in southwestern corner of the margin (Qiu et al., 2001), Baiyun sag near the Pearl River Mouth basin in the central margin (Huang et al., 2005) and in similar basins near Dongsha Rise (Hayes et al., 1995; Nissen et al., 1995a). The crust in these highly extended zones may be very thin (~5-10 km). Our interpretation of underthrust syn-rift strata would also support this possibility rather than the possibility of a subducted continent-ocean boundary.

4.5.3. Accretionary Wedge Upper Slope (Model Distance 165 – 250 km)

The reflection image shows the shallow sedimentary features of the upper slope accretionary wedge, but reveals little of the deeper wedge structure. This may be due in part to poor signal penetration, or strata and thrust faults may have been deformed and rotated to steep dips not imaged by our acquisition geometry. The wedge strata that are imaged beneath the seafloor along the upper slope appear folded and rotated to steep dips, suggesting intense deformation and suggest the likelihood of steeply-dipping thrust faults (Figure 4-8c). Unfortunately, neither MCS reflection nor the wide-angle OBS data constrain the forearc backstop at the northeastern limit of the profile. We instead adopt the forearc limit east of Hengchun ridge (Figure 4-1) proposed in regional earthquake tomography studies (Cheng, 2008; Kuo-Chen et al., 2012).

We do not image an obvious OOST at the transition from lower slope to upper slope (Figure 4-8c), as interpreted in previous studies of the Manila trench (Lin et al., 2009; Liu et al., 1997) and frequently observed at major slope changes in other accretionary prisms (i.e. Kopp and Kukowski, 2003; Moore et al., 2007). However, the seismic velocities of the upper slope reveal another possible mechanism for the change from lower to upper slope (Figures 4-5 and 4-8). The velocity model shows an increase in seismic velocities at a shallower level compared to the lower slope. Seismic velocity has been seen to increase towards the rear of accretionary wedges due to increasing compaction, dewatering, underplating of subducted sediments, diagenesis, and even low-grade metamorphism. However, the velocity model shows seismic velocities over 6.0 km/s in the wedge, in excess of sedimentary velocities observed in other prisms (Christeson et al., 1999 and references therein). Instead, these fast velocities suggest the presence of structurally underplated crustal material. Subducting crust should continue to

descend beneath the prism, steepening to the east, and so crustal velocities would be expected to be deeper beneath the upper slope than lower slope. We take these high seismic velocities to be evidence for crustal material structurally underplated to the accretionary wedge. Such underplating could thicken the wedge and may explain the change in bathymetry at the lower – upper slope transition, although it does not necessarily preclude any OOST or associated faulting.

4-6 CRUSTAL ACCRETION AND MOUNTAIN-BUILDING IN TAIWAN

While there is a clear morphologic link between the Taiwan orogen and the offshore accretionary wedge (Huang et al., 1997), our observations highlight a number of structural similarities. For instance, both the lower slope wedge and Western Foothills are characterized by primarily west-vergent imbricate thrusts that sole into a thin-skinned décollement as well as folded sheets of northern SCS margin and foreland basin strata. One of the surprising features of our data is the high-velocity crustal material within the deformed margin strata of the accretionary wedge upper slope, similar to the deformed margin strata and crustal material that makes up the Central Range. Unfortunately, our data do not provide unambiguous constraints on the affinity of accreted crust within the wedge. However, we can gain insight into its nature by considering our interpretation of the crust beneath the lower slope and the distribution of crustal rocks in the Central Range.

If we have imaged the continent-ocean boundary beneath the lower slope, then it is likely that the high seismic velocities in the upper slope represent accreted ocean crust. A small distribution of partial ophiolite sequences are scattered throughout the Lichi mélange between the Central Range and the Coastal Range in southern Taiwan (Chung

and Sun, 1992), while the Yuli belt along the eastern flank of the Central Range contains mafic material as well (Beyssac et al., 2007). The Kenting mélange, a large shear zone in Hengchun Peninsula, also contains occasional blocks of mafic material, though it predominantly consists of massive mudstone (Chang et al., 2003). It could be that our data show evidence for emplacement of ocean crust, but we consider this interpretation unlikely, as ophiolitic material represents a small volumetric component of the mountain belt, and the high seismic velocities extend across much of the upper slope. Additionally, we consider it unlikely that such a volume of SCS oceanic crust should be accreted rather than continue to subduct.

Alternatively, we interpret the crust beneath the lower slope to be a failed rift similar to the Xisha trough or Baiyun sag. These failed rift basins are imbedded within the wide distal margin of the northern SCS margin, where crust consists of a mix of highly extended continental crust and mafic volcanic intrusions. It is therefore likely that fast seismic velocities in the accretionary prism upper slope are indicative of structurally underplated transitional crust. This interpretation is consistent with a multi-stage collision model of collision in which faulted blocks of highly extended continental crust are subducted and structurally underplated to the wedge, then subsequently uplifted and exhumed to the surface during collision with the continental shelf. This view is also supported by a high-velocity body beneath the Hengchun peninsula modeled along an onshore-offshore wide-angle profiles (McIntosh et al. 2005; McIntosh et al. 2013) and the tracts of exposed pre-Tertiary northern SCS continental margin basement rocks in the Central Range (Beyssac et al., 2007; Ho, 1986). The distribution of mafic material throughout the Central Range may also be explained by the subduction, underplating, uplift and eventual exhumation of the distal continental margin, as mafic volcanic bodies

are interspersed throughout the COT that may be subducted and entrained in the wedge as well.

4-7 CONCLUSION

The new MCS reflection image and seismic velocity model for MGL0905-27 provide constraints on the crustal structure of the southern Chinese margin and Manila trench accretionary prism at the early stage of collision occurring offshore southern Taiwan. Our data reveal transitional crust ~10-14 km thick outboard of the Manila trench and subducting beneath the accretionary wedge. The distal margin consists of highly extended continental crust with interspersed volcanic bodies and a < 5 km thick HVLC that may be indicative of magmatic underplating, similar to some of the major structural features observed in the western and central northern SCS continental margin. We image discrete imbricate thrusts throughout the accretionary wedge lower slope, but faults throughout the upper slope are not well-imaged. We do not image an OOST at the transition from lower slope to upper slope accretionary wedge, but instead, we observe a high-velocity body that we interpret as structurally underplated distal margin crust that can account for the change from lower slope to upper slope. Our observations support a model of arc-continent collision in Taiwan where such thin crust is subducted and underplated to the accretionary wedge at an early stage of collision then is subsequently uplifted and exhumed to the surface during collision with the continental shelf.

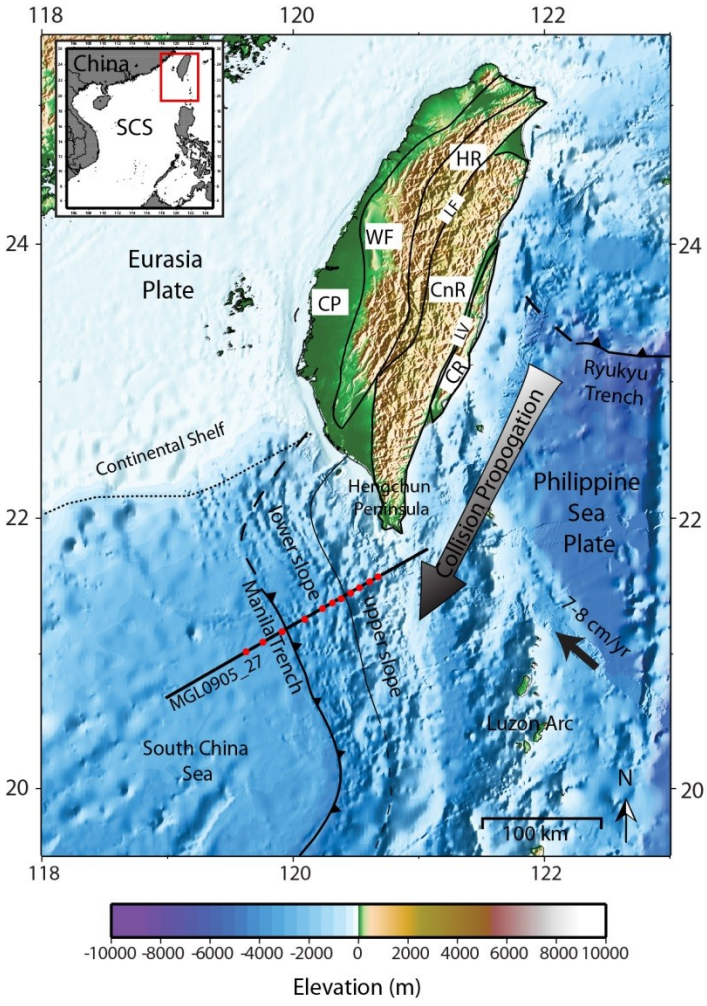

Figure 4-1: Onshore Taiwan consists of 5 tectonostratigraphic terranes: CP – Coastal Plain foreland basin; WF – Western Foothills fold-and-thrust belt; HR – Hsuehshan Range inverted Tertiary rift basin; CnR – Central Range metamorphic hinterland; CR – Coastal Range accreted arc complex. LF – Lishan fault; LV – Longitudinal Valley. Although the plate convergence is NW-SE at 7-8 cm/yr, the collision is propagating to the southwest due to the obliquely oriented continental shelf and subduction zone. The collision is older in central-northern Taiwan, but just beginning offshore southern Taiwan. MCS reflection data (solid black line) and wide-angle OBS data (red circles) were acquired along MGL0905-27 across the Manila Trench and accretionary wedge to constrain crustal structure of the early stage arc-continent collision.

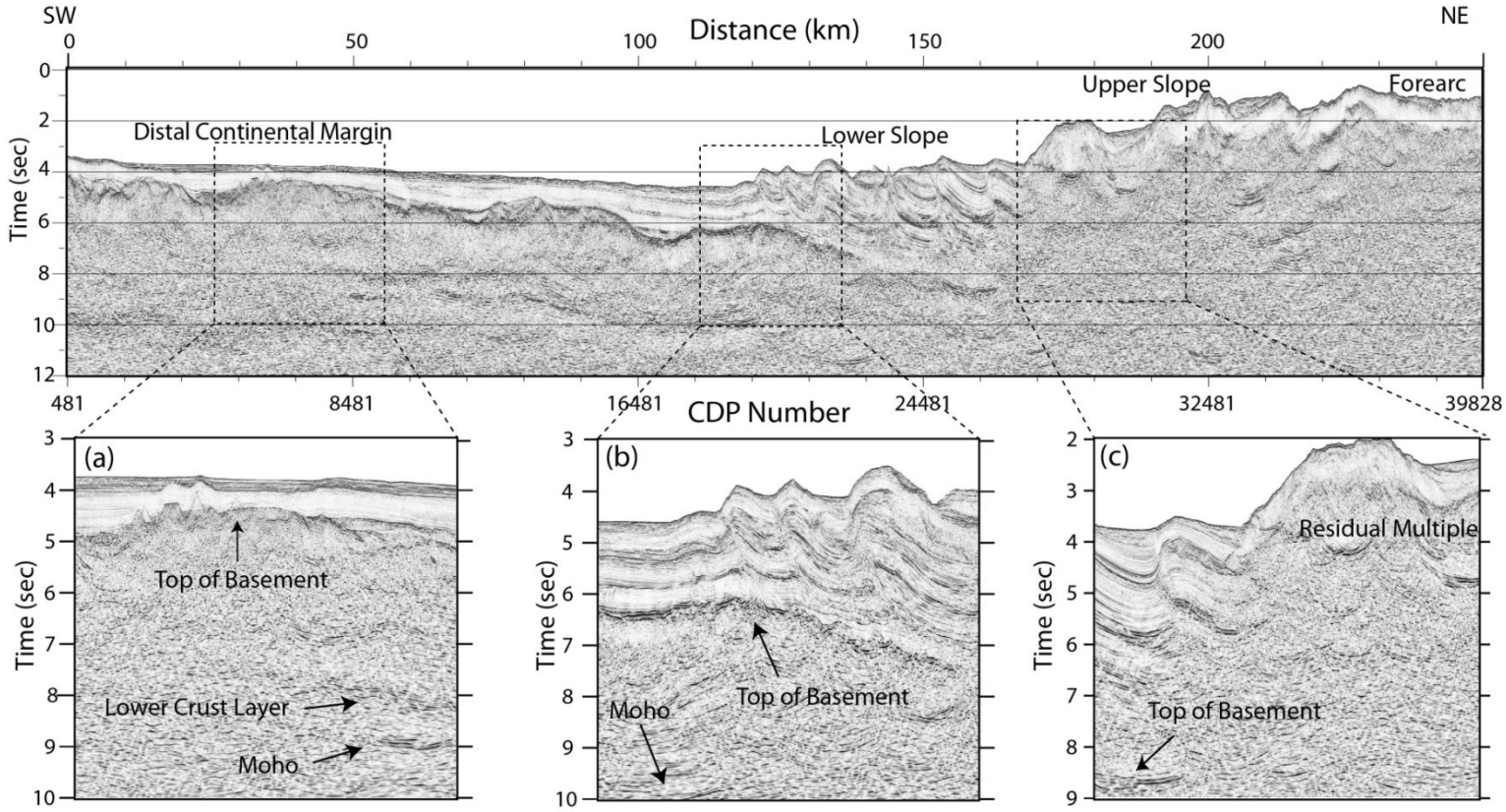

Figure 4-2: Pre-stack time migrated reflection data from MGL0905-27 image sediment and crustal structures along the incoming continental margin (a), lower slope (b) and upper slope (c) of the accretionary prism.

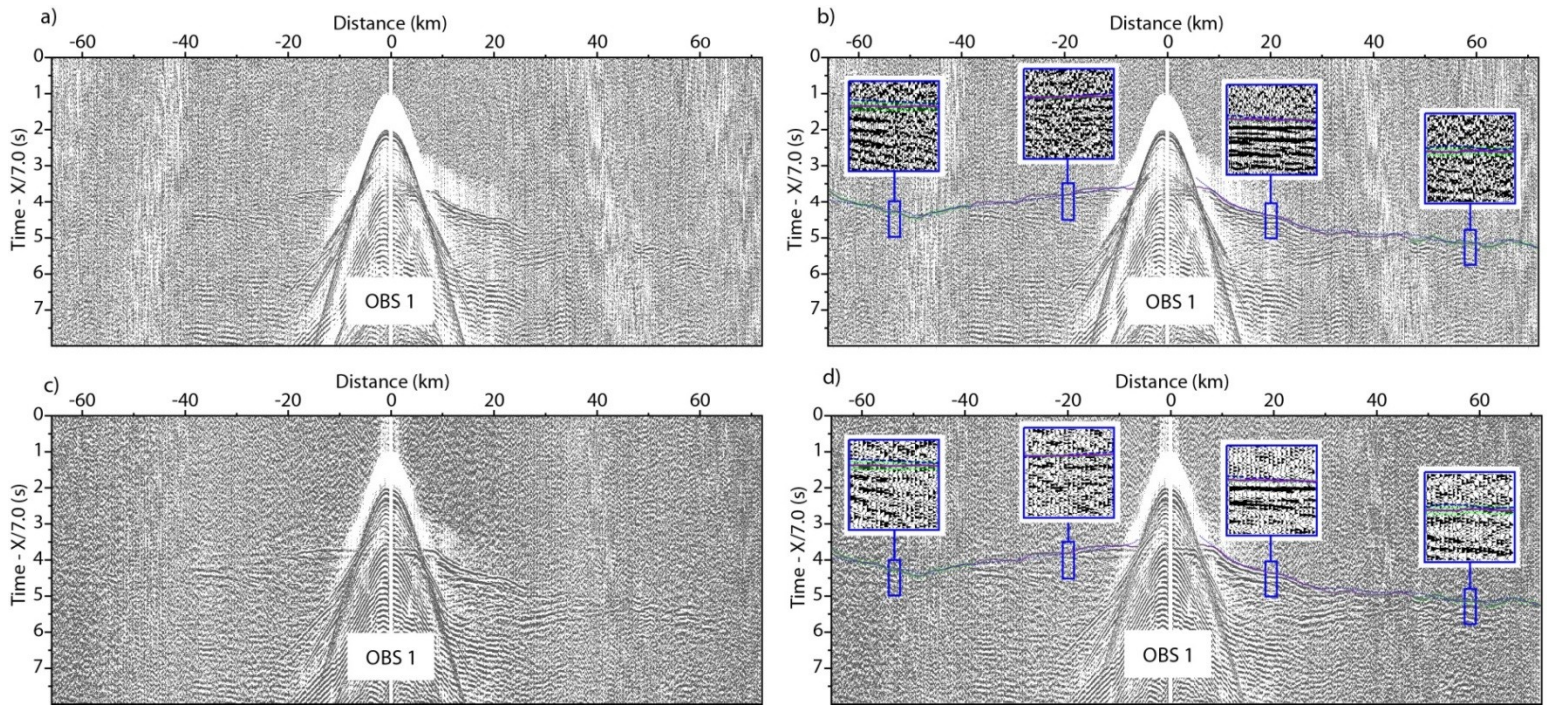

Figure 4-3: OBS 01 from the southwest end of MGL0905-27. (a) and (b) are with minimal processing (bandpass filter, AGC, and gaining with offset), but previous shot noise contaminates the record at offsets beyond ~40 km. Coherency filtering and trace stacking mitigate the noise and enhance S/N at far offset ((c), (d)). (b) and (d) show picked first arrivals (solid red line), pick uncertainties (green window), and calculated first arrivals (red dashed line).

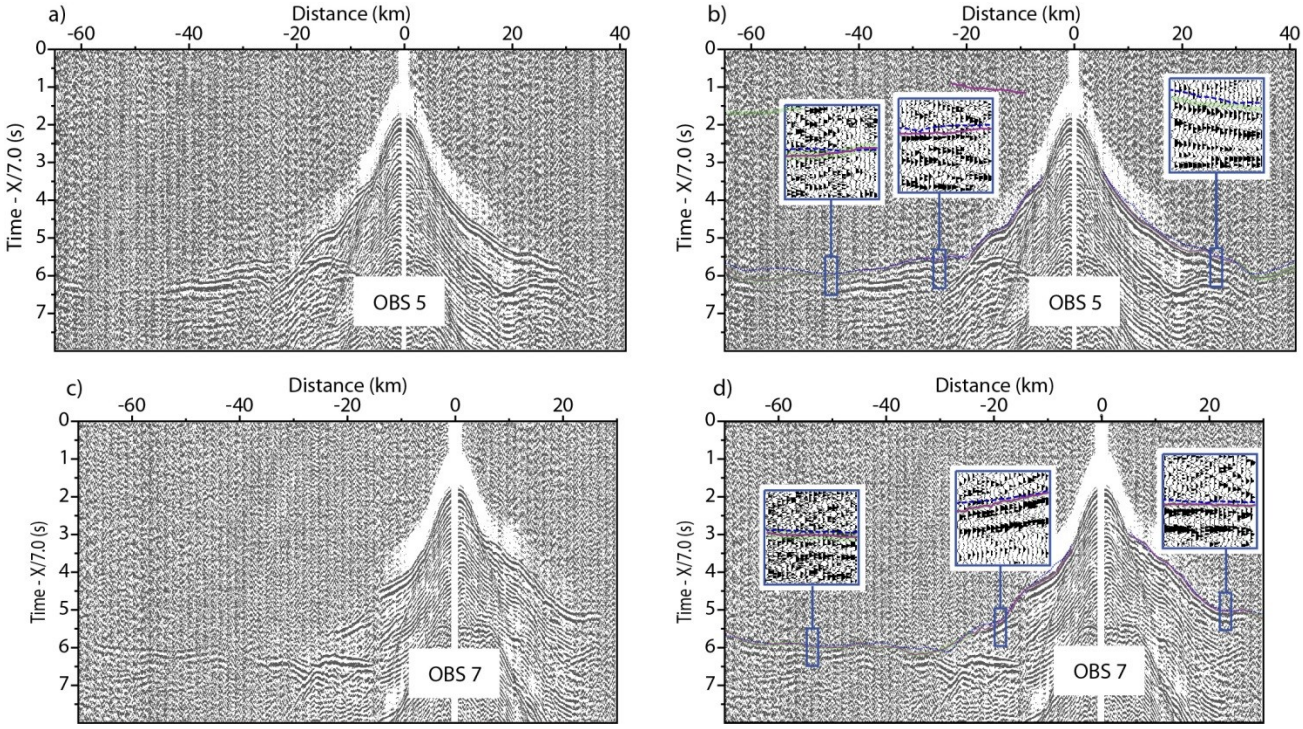

Figure 4-4: Examples of wide-angle OBS data with processing described in text. OBS 05 without (a) and with (b) picks (red solid line), pick uncertainties (green window) and calculated arrivals (red dashed line); OBS 07 without (c) and with (d) picks, uncertainties and calculated arrivals.

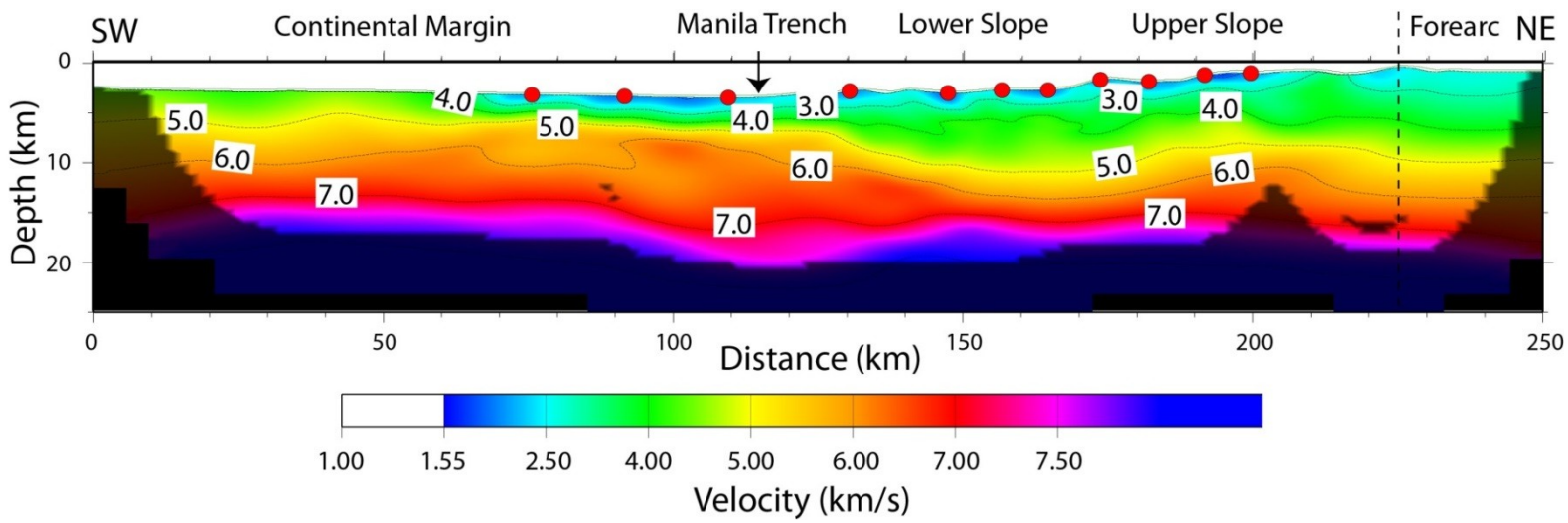

Figure 4-5: First-arrival travel-time tomography model along MGL0905-27 across the continental margin and Manila Trench subduction zone at an early stage of arc-continent collision. Red circles are OBS locations; dark mask indicates limits of ray coverage.

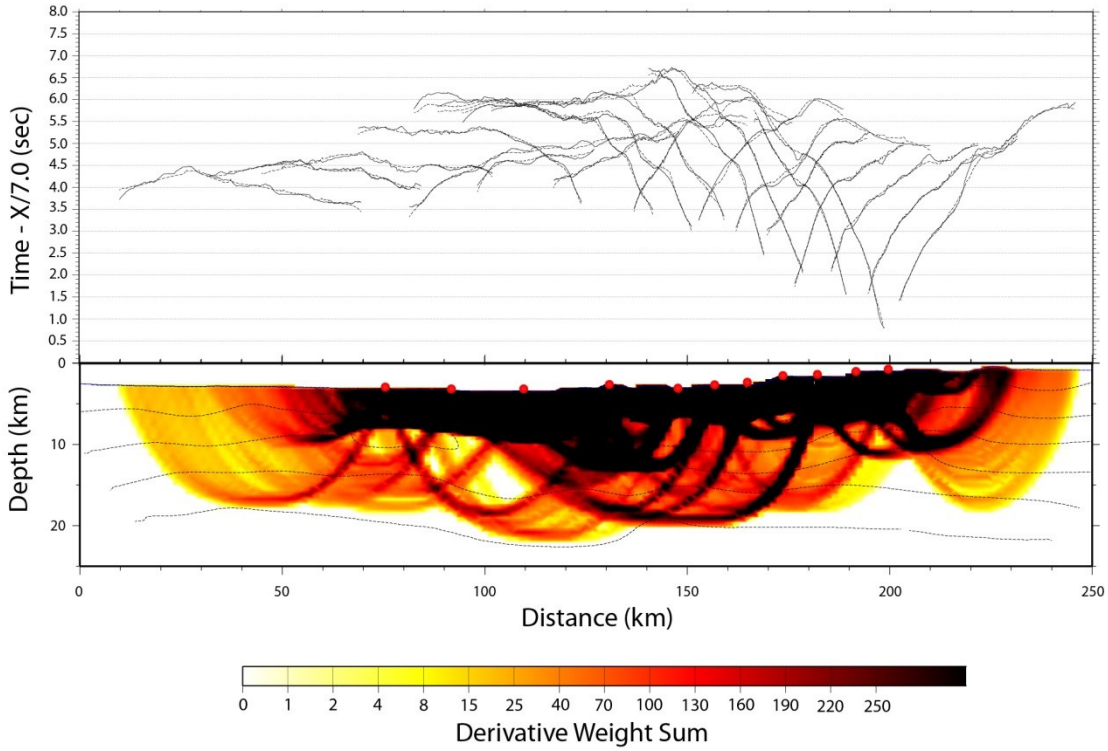

Figure 4-6: Top panel – picked (solid lines) and calculated (dotted lines) arrival times used in travel-time tomography. Bottom panel – derivative weight sum (DWS) indicate ray coverage throughout the model. Ray coverage is excellent in the crust between first and last OBS locations (red circles).

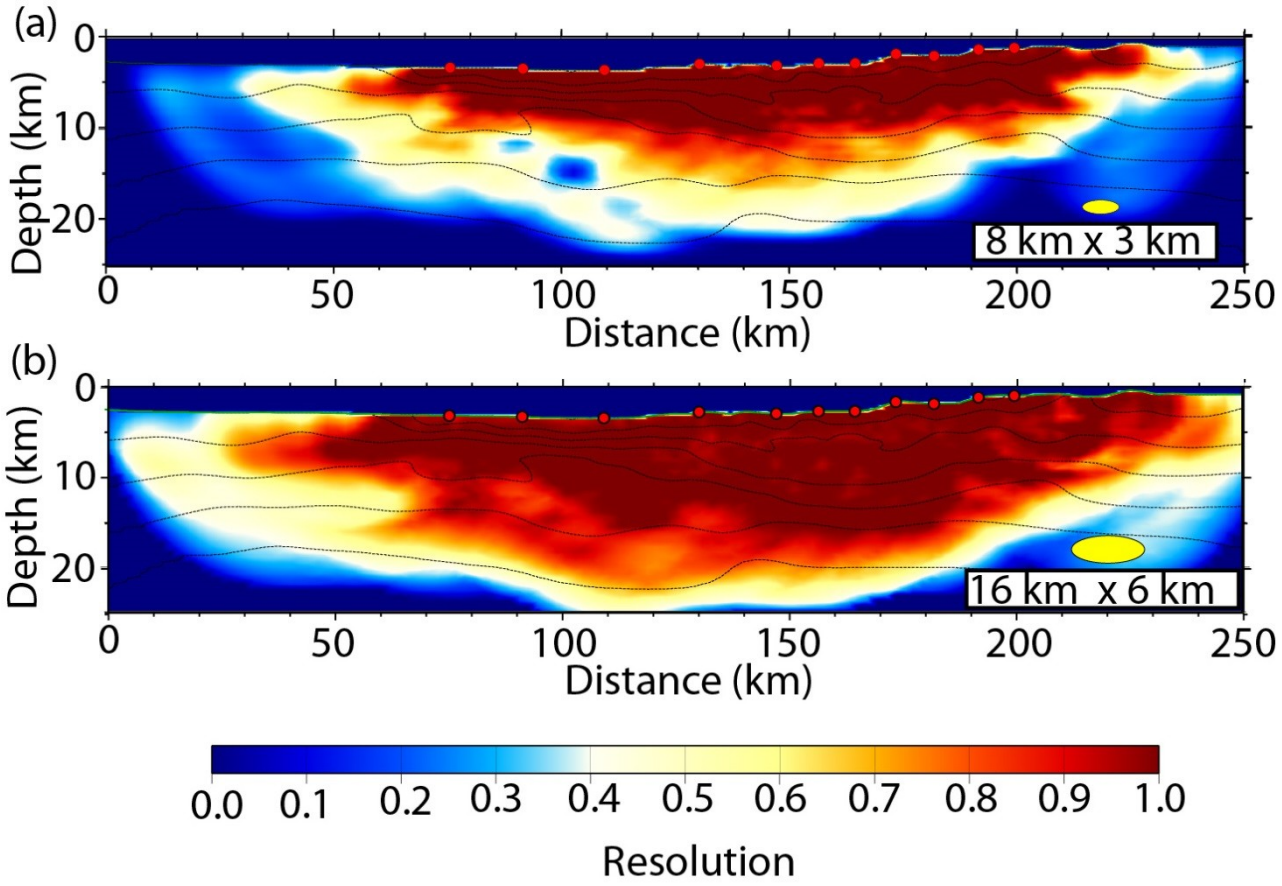

Figure 4-7: Resolution matrix for first-arrival tomography model. Areas with resolution values > 0.5 are considered well-resolved. This analysis shows that features in the crust are well resolved between the first and last OBS location (red circles). Outside the OBS locations, resolution suffers, although large-wavelength features are still adequately resolved.

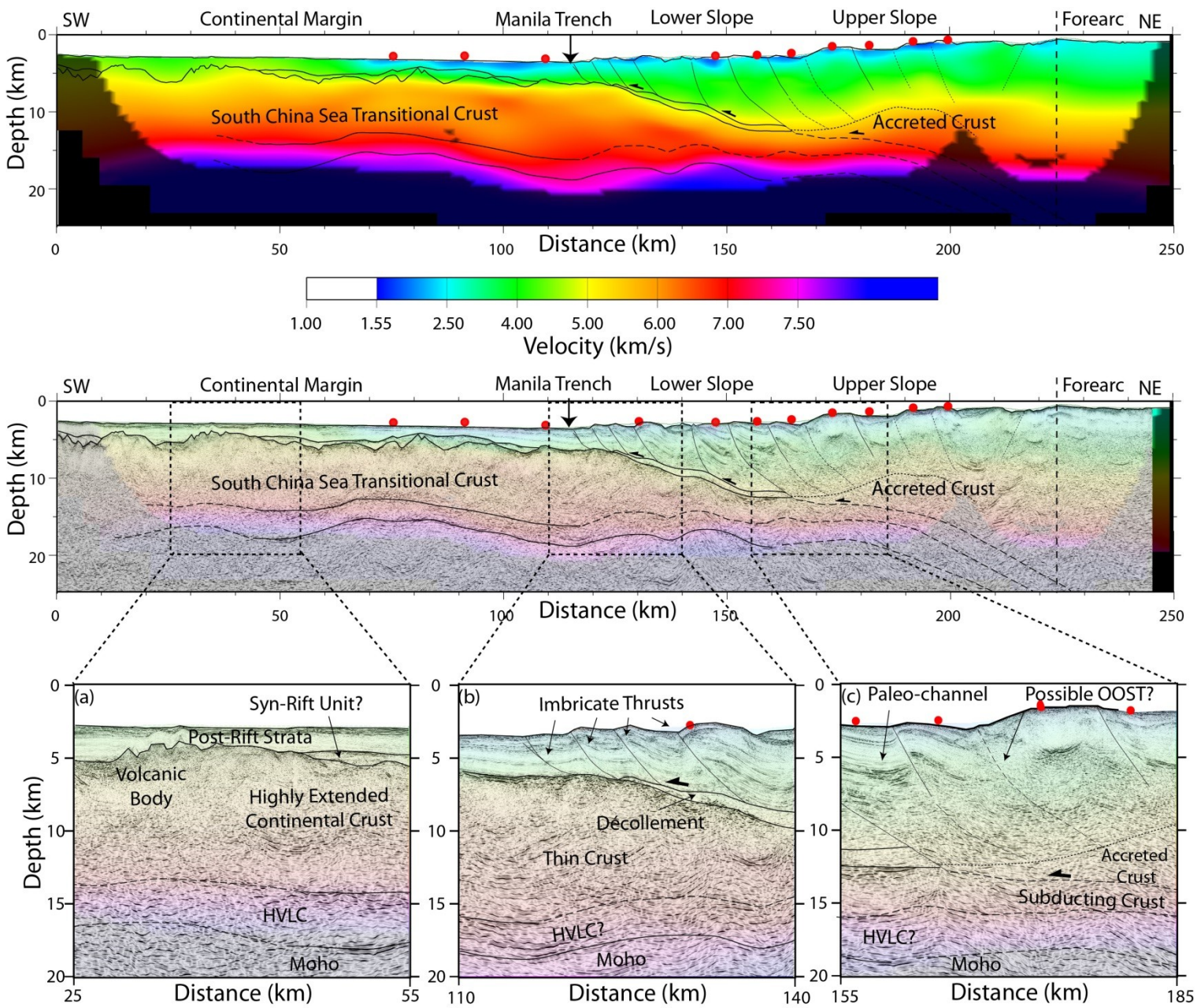
SW
Continental Margin
Manila Trench
Lower Slope
Upper Slope
Forearc
NE
Depth (km)
South China Sea Transitional Crust
Accreted Crust
Distance (km)
1.00
1.55
2.50
4.00
5.00
6.00
7.00
7.50
Velocity (km/s)
(a)
Syn-Rift Unit?
Post-Rift Strata
Volcanic Body
Highly Extended Continental Crust
HVLC
Moho
(b)
Imbricate Thrusts
Décollement
Thin Crust
HVLC?
Moho
(c) Paleo-channel
Possible OOST?
Accreted Crust
Subducting Crust
HVLC?
Moho

Figure 4-8 (above): First-arrival tomography velocity model with depth-converted MCS image overlain. Crust is ~10-14 km thick at the southwest end of the line, but thins to ~6 km beneath the accretionary wedge lower slope. (a) Major features along continental margin are consistent with SCS transitional crust including post-rift strata < 2 km thick (<4 km/s); possible syn-rift strata bound on top by a breakup unconformity; crust ~10 -14 km thick including a HVLC (6.7 – 7.5 km/s) < 5 km thick (b) Major features of the lower slope wedge include imbricate thrusts; reflective folded strata from the incoming southern Chinese margin); thinner, faster velocity crust (5.5 – 7.8 km/s) (c) High-velocities (> 6 km/s) likely indicate crustal material underplated to the accretionary wedge upper slope.

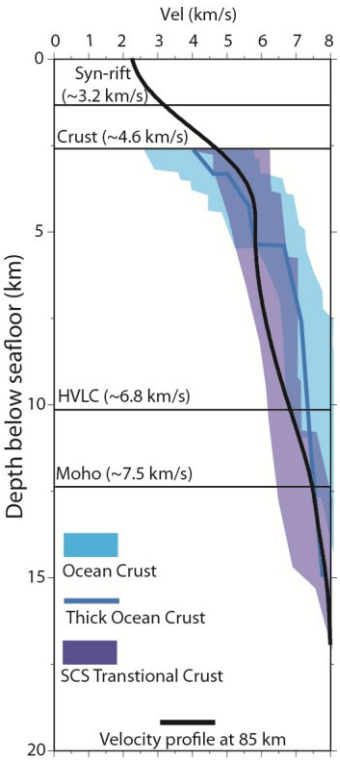

Figure 4- 9: 1D velocity profile from x = 85 km (black line) shows the velocity structure of crust is consistent with velocity structure of SCS transitional crust (Nissen et al., 1995b; Qiu et al., 2001; Wang et al., 2006; Yan et al., 2001) that consists of highly-extended but magmatically intruded continental crust. The velocity structure is also incompatible with the faster, two-layer velocity structure of typical ocean crust (White et al., 1992) and thick ocean crust (Mutter and Mutter, 1993).

Chapter 5: Active Extension in Taiwan's Pre-Collision Zone: A New Model of Plate-Bending in Continental Crust

5-1 INTRODUCTION

Extensional features have been observed in convergent settings around the world, such as the Himalaya (Burchfield et al., 1992), the Apennines (Cavinato and De Celles, 1999; Wallis et al., 1993), the Alps (Mancktelow, 1992; Ratschbacher et al., 1989), and Costa Rica (McIntosh et al., 1993; Ranero et al., 2003). Extension during subduction and collision has been explained by a variety of mechanisms, including gravitational collapse or flexure due to topographic loads, slab rollback, and bending of subducting oceanic plates near trenches. Numerous extensional structures observed in the Taiwan arc-continent collision have been attributed to several such mechanisms. Flexural normal faults from orogenic loading permeate the Taiwan foreland, offsetting shallow foreland strata and in places penetrating the underlying basement (Lin and Watts, 2002). Extension has been recorded in the Central Range metamorphic hinterland, even as it is uplifting (Crespi et al., 1996). Northern Taiwan is in a state of tension, due to post-collisional collapse and the encroaching Okinawa back-arc spreading center (Clift et al., 2008). Recently acquired multichannel seismic (MCS) reflection data in the South China Sea along the pre-collision zone southwest of Taiwan (Figure 5-1) suggest that extension may also occur in convergent settings by bending at the hinge of the continental margin before the onset of collision.

5-2 GEOLOGIC BACKGROUND

Taiwan is the site of active collision between the northern SCS rifted margin of the Eurasia plate and the Luzon arc of the Philippine Sea plate (Figure 5-1). The obliquity of convergence between the northeast-trending margin and north-trending arc led to the onset of collision ~6.7 Ma in northern Taiwan, while collision is just beginning in southern Taiwan (Lin and Watts, 2002). The southwestern propagation of collision has prompted many researchers to interpret different spatial transects as representing different temporal stages of the collision process (Byrne and Liu, 2002). In particular, much attention has been given to understanding the area of incipient collision in southern Taiwan and the pre-collision northern SCS margin immediately southwest of Taiwan.

The northern SCS margin formed by rifting during the Late Cretaceous–Oligocene near the arc of a Mesozoic subduction zone (Li and Li, 2007). Previous studies have revealed the margin to be an intermediate magmatic rifted margin (Clift et al., 2001), consisting of passive margin sediments overlying moderately extended rift basins along the continental shelf (Ru and Pigott, 1986), and a wide distal margin consisting of thinned and volcanically intruded continental crust (Nissen et al., 1995; Wang et al., 2006). In the vicinity of Taiwan, Hsu et al. (2004) interpreted much of the continental slope in Taiwan's pre-collision zone as volcanically thickened oceanic crust, rather than thinned continental crust. This ~12–15-km-thick body of crust in the distal margin (Yen and Yeh, 1998), whether thick ocean crust or thin continental crust, is subducted at the Manila Trench at the eastern extent of the South China Sea, north of a prominent bend in the Manila Trench at ~latitude 20°N.

One of the enigmatic features of the northern SCS margin is the amount of post-rift extension that occurred after seafloor spreading began ~30 Ma (Briais et al., 1993).

For example, most of the rifting history of the Tainan Basin may have been concurrent with Oligocene– early Miocene seafloor spreading (Lin et al., 2003). Exploration data from rift basins near Taiwan have identified a more recent episode of post-rift extension during the mid-Late Miocene that postdated the primary rifting and thermal subsidence, but predated the onset of collision (Angelier et al., 1990; Lin et al., 2003; Tensi et al., 2006).

Recently acquired MCS reflection data along the northern SCS margin reveal active extension on a deep-seated rift basin–bounding normal fault near the shelf break in Taiwan's pre-collision zone along strike of the mid-Late Miocene post-rift extension. We present a new seismic reflection image of the active fault, and introduce a new model of plate bending in continental crust due to subduction of transitional crust at the Manila Trench to explain this extension and the latest episode of post-rift extension observed in the Taiwan region. We also discuss the role these faults may have played in the Taiwan arc-continent collision.

5-3 Active Crustal Extension in the Pre-Collision Setting of Taiwan

MCS data were acquired in the vicinity of Taiwan as part of the joint U.S. National Science Foundation and Taiwan-funded TAIGER (Taiwan integrated geodynamics research) program, designed to study the geodynamics of arc-continent collision in Taiwan. Data were acquired during the summer of 2009 with the R/V Marcus G. Langseth using a source array of ~6600 in3 towed at a depth of 8 m with a 6 km streamer. Shot spacing was 50 m, hydrophone spacing was 12.5 m, and common depth point spacing was 6.25 m. Processing was performed using Paradigm's Focus software, and depth migrated using Paradigm's Geodepth software.

Several of these seismic profiles cross the Tainan Basin (Figure 5-1). Previous studies have shown the Tainan Basin to contain as much as ~2 km of foreland basin strata overlying ~4 km of post-rift strata, although these sequences may be even thicker immediately adjacent to Taiwan (Lin et al., 2003). Oligocene strata unconformably overlie eroded Mesozoic basement, so that Late Cretaceous–Eocene syn-rift strata are not present in the basin (Lin et al., 2003). A fault-bound basement high (Central uplift) separates the Tainan Basin into a half-graben rift basin (northern depression) and a continental slope depocenter (southern depression). The Central uplift served as a rift flank during Oligocene– Early Miocene extension and, along with other rift faults near Taiwan, was reactivated in the mid-Late Miocene. This extensional episode has previously been attributed to either renewed thermal activity (Angelier et al., 1990; Lin et al., 2003) or as flexure due to obduction of South China Sea oceanic crust (Tensi et al., 2006).

Figure 5-2 shows a new MCS profile from the southwestern extent of the Tainan Basin. The most striking features of this profile are a deep-seated, landward-dipping listric normal fault and a strong Moho reflection. This rift basin–bounding fault is imaged down to depths of 16–18 km, where it soles out in the mid-crust. At the seafloor, the fault forms a spectacular scarp with ~850 m of relief, indicating recent extensional activity ahead of the southward-propagating collision. Below the fault, the Moho rises abruptly from >25 km to ~20 km depth. North of the fault, we image ~4–6 km of foreland basin and post-rift margin strata, consistent with previous studies of the Tainan Basin. These sediments are offset by a number of normal faults that extend to the seafloor, and in some cases, penetrate the basement.

A bathymetric low near the continental shelf break (Figure 5-1) corresponds to the fault scarp and indicates that the active extension abates towards Taiwan. In addition, the relief of the fault scarp is much greater than the offsets typically observed on flexural faults in Taiwan's foreland (Chou and Yu, 2002). These observations suggest that the active extension is not caused by orogenic loading at Taiwan, but requires another mechanism. One possible mechanism is loading of the subducting distal continental margin at the Manila Trench south of the collision zone. We explore this possibility with numerical modeling.

5-4 New Model of Plate-Bending in Continental Crust

We conducted a set of thermo-mechanical numerical experiments simulating convergence between a subduction zone and a continental margin (Figure 5-3) that produce extensional episodes along the continental shelf similar to those observed in our seismic data and in rift basins near Taiwan during the mid-Late Miocene (for a complete discussion of the numerical modeling, see Appendix A). Figure 5-2 demonstrates that the major rift fault soles into the middle crust, suggesting a weak middle crust. Such a weak middle crust has also been inferred based on the distribution of seismicity in Taiwan's foreland (Mouthereau and Petit, 2003). Figure 5-3 illustrates the evolution of a numerical model in which we made use of an evolving weak middle crust that weakens the margin as a function of strain (Lavier and Manatschal, 2006; Jammes et al., 2010). To simulate such a process in the models, we assume that the entire crust is weakened by replacing plagioclase with wet quartz in shear zones. These weak mineral phases accumulate during the tectonic history of the basin and provide the mechanism to form a weak semi-brittle middle crustal layer (Lavier and Manatschal, 2006; Jammes et al., 2010). Such a

layer plays the role of a deep-seated décollement in the crust that both weakens the crust and localizes deformation.

Figure 5-3A shows the initial conditions of the model with a passive margin formed by rifting and subsequent thermal subsidence. Figure 5-3B shows the model after 7 m.y. of convergence, where thin crust of the distal margin has entered the subduction zone. Loading of the crust by the accretionary prism in the far field is sufficient to generate extension on landward-dipping normal faults rooted in the weak middle crust near the shelf break of the continental margin. During this stage, the crust is also locally thinned to <25 km, similar to the Moho in our seismic observations (Figure 5-2). Our models demonstrate that normal faults near the hinge of the margin are zones of weakness that may be exploited by plate bending when the distal margin is subducted prior to collision. This extensional event pre-dates more proximal orogenic loading and associated flexure, just as the mid-Late Miocene extension in Taiwan pre-dates the arc-continent collision.

5-5 Rift Faults in the Taiwan Collision

Observations from our seismic imaging and numerical models provide strong evidence for extension and crustal thinning by plate bending prior to collision. However, the numerical models also demonstrate that these faults may be compressionally reactivated during collision (Figure 5-3C) in a style of thick-skinned tectonics observed in Taiwan's foreland (Hung et al., 1999; Lee et al., 2002; Mouthereau and Lacombe, 2006) and in collisional belts elsewhere. The subsequent stage of this process may be exemplified by the Hsuehshan Range, an inverted rift basin that supports some of Taiwan's highest topography (Clark et al., 1993; Tillman and Byrne, 1995). The

Hsuehshan Range is bound on the east by the Lishan fault, a major structural and morphologic boundary that separates lightly metamorphosed continental shelf strata of the Hsuehshan Range on the west from metamorphosed and highly deformed marine sediments and pre-Tertiary basement blocks of the Central Range to the east.

Although the tectonic history of the Lishan fault has been controversial in the past, most recent work suggests that the Lishan fault is a reactivated extensional fault of the northern SCS continental margin (Fisher et al., 2002; Lee et al., 1997; Simoes et al., 2007). Recent magnetotelluric data have also identified the Lishan fault as a listric, northwestward-dipping structure penetrating to mid-crustal levels (Bertrand et al., 2009), similar to the rift basin–bounding fault observed in our seismic reflection profile. Although the Tainan Basin does not contain the Eocene syn-rift section exposed in the Hsuehshan Range (Fisher et al., 2002), the similar history as a rift fault, similar geometry, and orientation of the Lishan fault to our new observations suggests that the rift fault along the Central uplift may serve as a pre-collision analogue for the Lishan fault system. This fault occurs close to the continental shelf break, which further suggests that the Lishan fault may divide Taiwan into an eastern domain representing subduction and collision of the distal margin, and a domain west of the Lishan fault representing collision of the continental shelf (Figure 5-3C). The Hsuehshan Range and Lishan fault extend toward southern Taiwan, where margin strata are not yet uplifted. Here, either the Lishan fault may exist in the subsurface as a continuation of the rift basin–bounding fault along the Central uplift, or southern Taiwan may be situated at the transition between the younger Tainan Basin and the older, now uplifted basin of the Hsuehshan Range.

5-6 CONCLUSIONS

New seismic imaging reveals active extension on a major rift fault near the continental shelf break along Taiwan's pre-collision margin. This extensional episode is similar to extension identified in other rift basins in Taiwan's foreland prior to arc-continent collision. The observed active faulting may be caused by bending of the continental crust due to subduction of the distal continental margin at the Manila Trench. In addition, prior to compressional reactivation the Lishan fault may have been a rift basin– bounding fault similar to the fault observed near the continental shelf break along the Central uplift in the Tainan Basin. The Lishan fault may divide Taiwan into a collisional domain involving the continental slope and distal margin in the Central Range to the east, and a collisional domain involving thicker continental crust and continental shelf strata in the Hsuehshan Range and Western Foothills to the west.

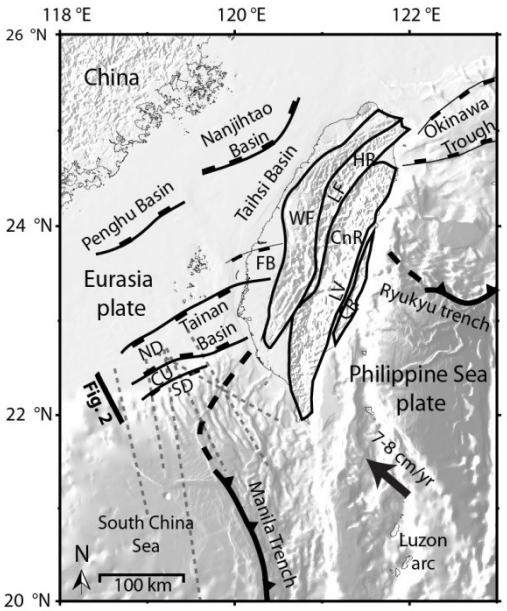

Figure 5-1: Regional bathymetry and tectonic map of study area. Tainan Basin consists of northern and southern depression sub-basins (ND, SD) separated by Central uplift (CU) basement high. Tectonic terranes in Taiwan include foreland basin (FB), Western Foothills fold-and-thrust belt (WF), Hsuehshan Range (HR), Central Range (CnR), and Coastal Range (CR). Hsuehshan Range and Central Range are separated by Lishan fault (LF), a major structural and morphologic boundary. Longitudinal Valley (LV) is Eurasia–Philippine Sea plate suture. Dashed lines are Taiwan TAIGER (Taiwan integrated geodynamics research) program multichannel seismic reflection profiles crossing Tainan Basin (not presented here).

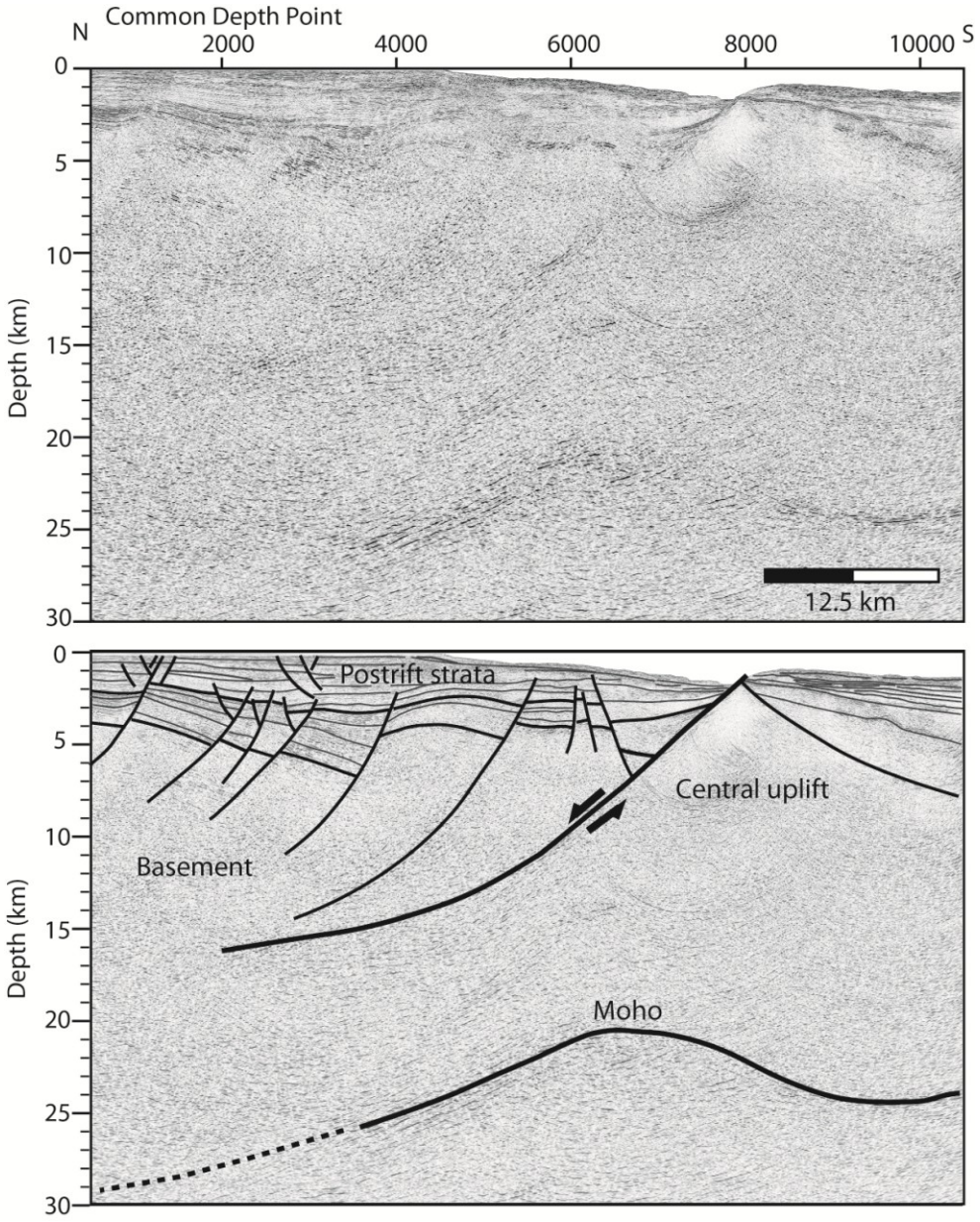

Figure 5-2: Depth-migrated seismic line MGL0905_07 (for a large-scale image, see the Data Repository [see footnote 1]) from the Taiwan TAIGER (Taiwan integrated geodynamics research) program (see Fig. 1 for location). Seismic data image as much as ~6 km of post-rift and foreland basin strata. Several faults are imaged, including rift basin–bounding fault along Central uplift. Fault creates significant fault scarp at seafloor, indicating recent activity. Moho shoals abruptly beneath Central uplift rift fault. CDP— common depth point.

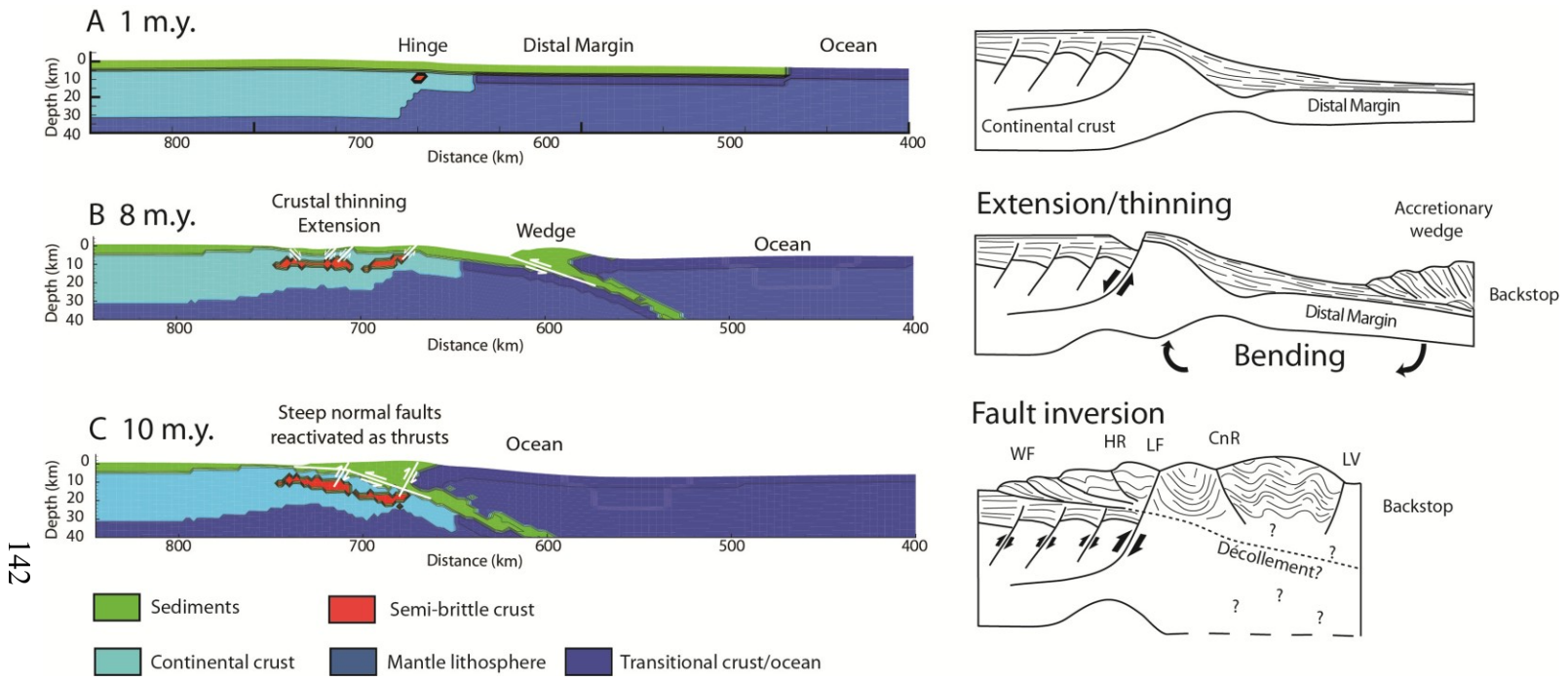

Figure 5-3: Evolutionary model of rifted margin during collision. A: Initial conditions of rifted margin. B: The subducting distal continental margin levers under vertical load of accretionary prism, causing extensional reactivation of rift basin–bounding fault near hinge of margin rooted into semi-brittle middle crust. C: Normal faults of continental margin are reversed in compression and interact with a growing thin-skinned wedge, similar to Western Foothills and Hsuehshan Range in Taiwan west of Lishan fault.

Chapter 6: Summary

The crustal-scale geophysical observations presented in this dissertation provide new insights into the tectonic history of the northeastern SCS, where the northern SCS rifted margin is actively growing into a mountain belt over the course of ~7 m.y. of collision with the Luzon arc at the Manila trench. The new observations shed new light on the evolution of the northern SCS margin from rifting at the start of a Wilson Cycle to mountain-building during arc-continent collision at the end of the Wilson Cycle. In particular, these studies address the behavior of the continental crust during collision and demonstrate the importance on the style of rifted margin in the collision process. The findings of this dissertation are summarized in figures 6-1 and 6-2.

As described in chapter 3, the new seismic reflection images and a wide-angle travel-time tomography velocity model depict a wide rifted margin in the northeastern SCS similar to the "intermediate magmatic" style of rifted margin reported in the western and central northern SCS margin (Clift et al., 2001). However, much of the evidence for syn-rift magmatism comes from volcanic rocks recovered from wells in rift basins (Yan et al., 2006; Wang et al., 2012a) along the continental shelf rather than geophysical observations, which suggest predominately post-rift magmatic bodies in the continent-ocean transition of the distal margin. These include a high-velocity lower crustal layer that likely represents mafic magmatic underplating or lower crustal intrusions, volcanic bodies intruded into near the top of the basement, and post-rift sills injected into the post-rift sedimentary section.

Rifting in the distal margin is instead accompanied by little to modest magmatism, despite the extreme crustal thinning that occurred beneath the continental slope (Figure 6-1a, 6-1b). Crust here is as thin as ~4 km in a highly-stretched rift basin.

The crust of the basin is characterized by faulted blocks that sole into an intra-crustal low-angle detachment fault. The orientation of faults toward the basin center suggests strain was localized in the basin during rifting, but failed to proceed to breakup and seafloor spreading.

In other rifted margins, this amount of thinning and strain localization can lead to serpentinization of an embrittled upper mantle or abundant magmatism, processes which can weaken the lithosphere and facilitate breakup (Pérez-Gussinyé 2001b). It is likely that the margin is too warm for serpentinization due to the initial conditions of the thermally un-equilibrated lithosphere. This requires temperatures over ~600° C for the mantle depths in the distal margin (Ulmer and Trommsdorff, 1995). However, the relatively long rift duration may have also allowed the advecting mantle to cool, suppressing decompression melting. Without these, the mantle may have retained much of its strength as it advected to crustal levels and ultimately prevented breakup in this rift basin.

The magmatic bodies imaged in the distal margin were likely emplaced contemporaneously with Miocene post-rift seafloor spreading, as dredging of a volcanic edifice imaged in the TAIGER data recovered a ~22 Ma post-rift basalt sample (Wang et al., 2012b). The post-rift magmatism may have been triggered by thermal erosion of old, depleted continental lithosphere (Figure 6-1c, 6-1d). This possibility has been raised in previous geochemical studies of depleted Eocene syn-rift basalts and enriched Miocene post-rift basalts in the Taiwan region (Chung et al., 1994; Chung et al., 1995; Xu et al., 2000; Wang et al., 2012a). It may be that thermal erosion is enhanced in the distal margin where mantle convection may be focused following breakup and the start of seafloor spreading around ~30 Ma.

A new coincident seismic reflection and wide-angle OBS profile is presented in chapter 4 that tracks the highly extended continental crust of the thin, distal margin into the Manila trench subduction zone offshore southern Taiwan. Here the Manila trench accretionary wedge is growing into an incipient mountain belt during the early stage of mountain-building. A first-arrival travel-time tomography model reveals a fast seismic velocity anomaly beneath the Hengchun Ridge that suggests this growth is at least in part driven by structural underplating of the subducting distal margin crust at the base of the wedge.

The Hengchun Ridge is the morphologic extension of the onshore Central Range, where basement blocks of the northern SCS margin are exposed. Recent tomography studies across southern Taiwan also associate the Central Range with a similar high-velocity anomaly (McIntosh et al., 2013). These observations all suggest a link between the Central Range and the highly extended continental crust in the distal northern SCS margin. This also reinforces the assumption of offshore southern Taiwan as a direct analog for the early stage collision in Taiwan. In this case, the Central Range is not a result of steady-state subduction of the continental shelf as described by critical wedge models of Taiwan, but is instead formed by subduction and structural underplating to the wedge at the onset of collision, then uplifted and exhumed to the surface when the continental shelf collides.

Rift faults at the continental shelf may reactivate in a flexural response to subduction of the distal margin, as argued in chapter 5. A seismic reflection profile across the ‘pre-collision’ continental shelf edge southwest of Taiwan images a major rift basin-bounding fault that has been recently active ahead of the southward-propagating collision. The reflection image and bathymetry show a substantial fault scarp with ~850

m of relief at the seafloor. The fault penetrates ~16-18 km deep where it soles out into a possibly weak middle crust. A geodynamic model of collision suggests this can happen if the colliding crust is sufficiently weak. A similar extensional event has been documented in Taiwan's foreland during the mid-Miocene (~12.5 Ma – 6.5 Ma) prior to the onset of collision at ~7 Ma (Lin et al., 2003; Tensi et al., 2006) that may be further evidence that rift faults may be extensionally reactivated as the distal margin subducts at the early stage of collision. The structurally underplated crust in the accretionary wedge could possibly exaggerate this effect by increasing the vertical load in the subduction zone compared to the load from a purely sedimentary wedge.

In the geodynamic model, the weak rift faults are inverted as collision progresses to include the continental shelf. The Lishan fault may be an example of such a rift fault near the continental shelf break that was compressionally reactivated in the Taiwan collision. The Lishan fault may then approximate the limit of the continental shelf in the Taiwan mountain belt, with the Western Foothills and Hsuehshan Range west of Taiwan representing the continental shelf in collision and the Central Range east of the Lishan fault representing the subducted and collided continental slope and distal margin. This interpretation is compatible with the conclusions of chapter 4, which explores a possible relationship between the Central Range and the distal rifted margin.

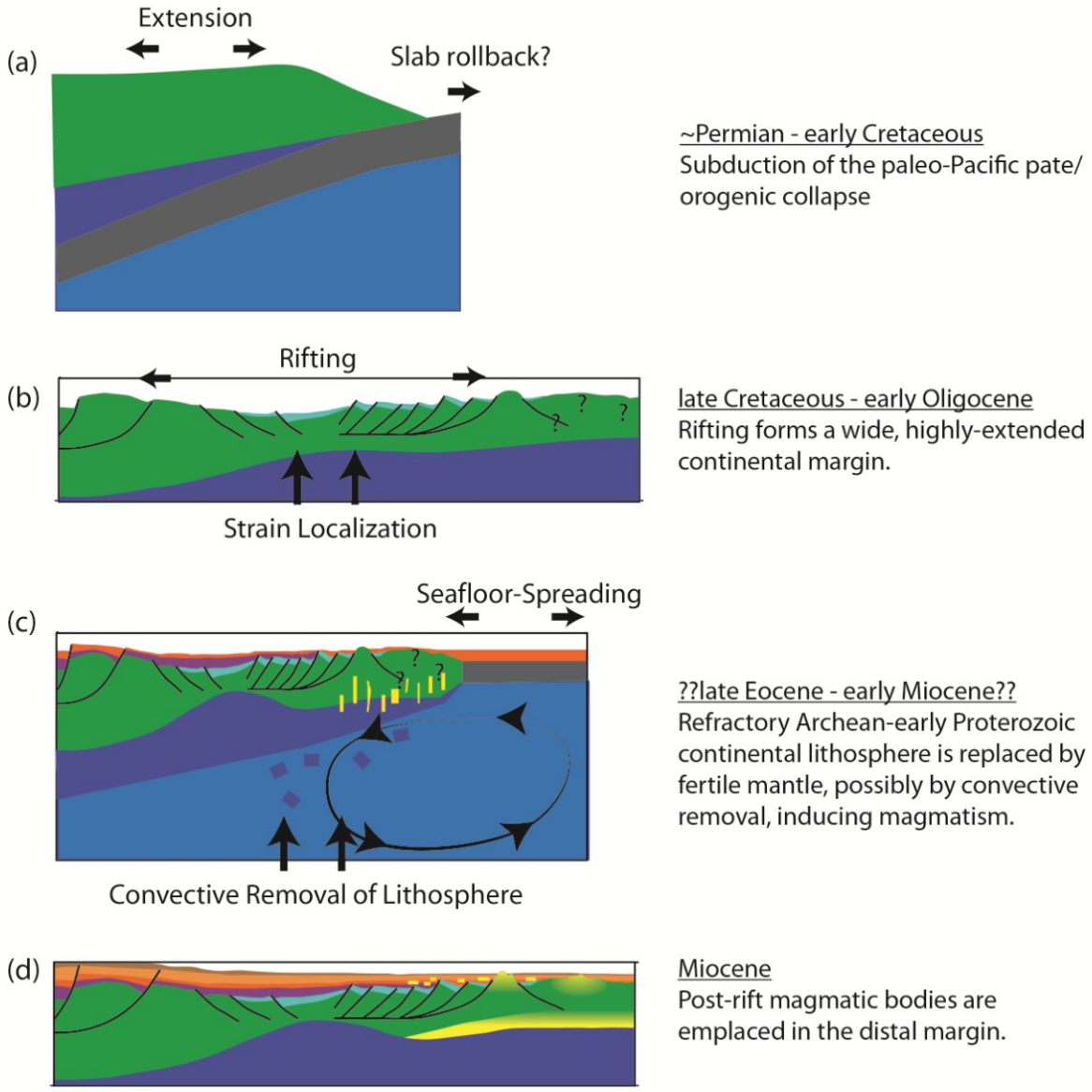

Figure 6-1: Summary of pre-collision tectonic history of the northern SCS rifted margin as inferred from geophysical observations near Taiwan.

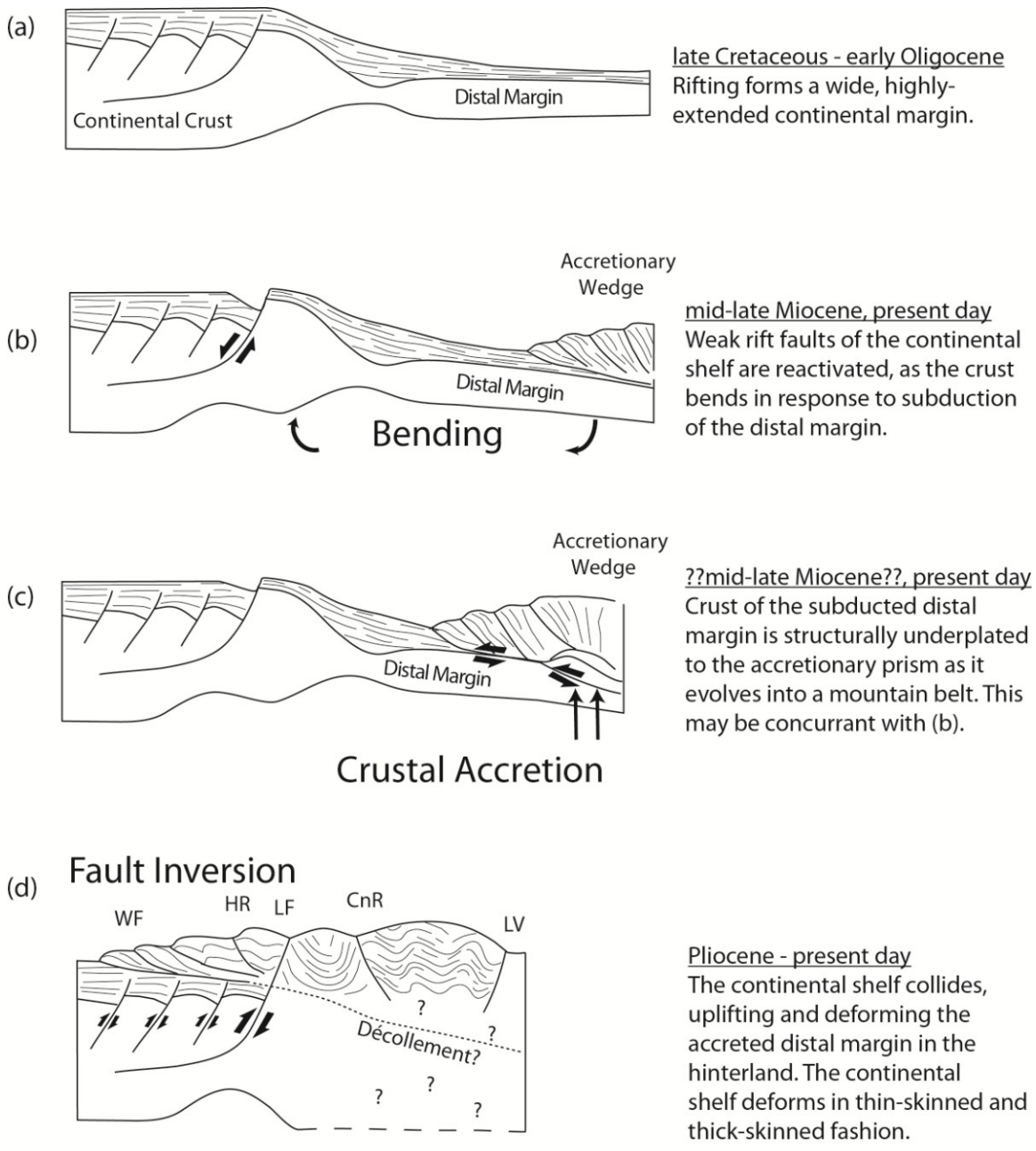

Figure 6-2: Summary of arc-continent collision between the northern SCS margin and the Luzon arc of the Manila trench subduction zone discussed in the dissertation.

Appendix A: Seismic Reflection Images

This appendix contains seismic reflection images used to inform the interpretations throughout the main body of the dissertation, but not presented in the submitted manuscripts. Seismic images were produced using the processing flow discussed in chapter 2.

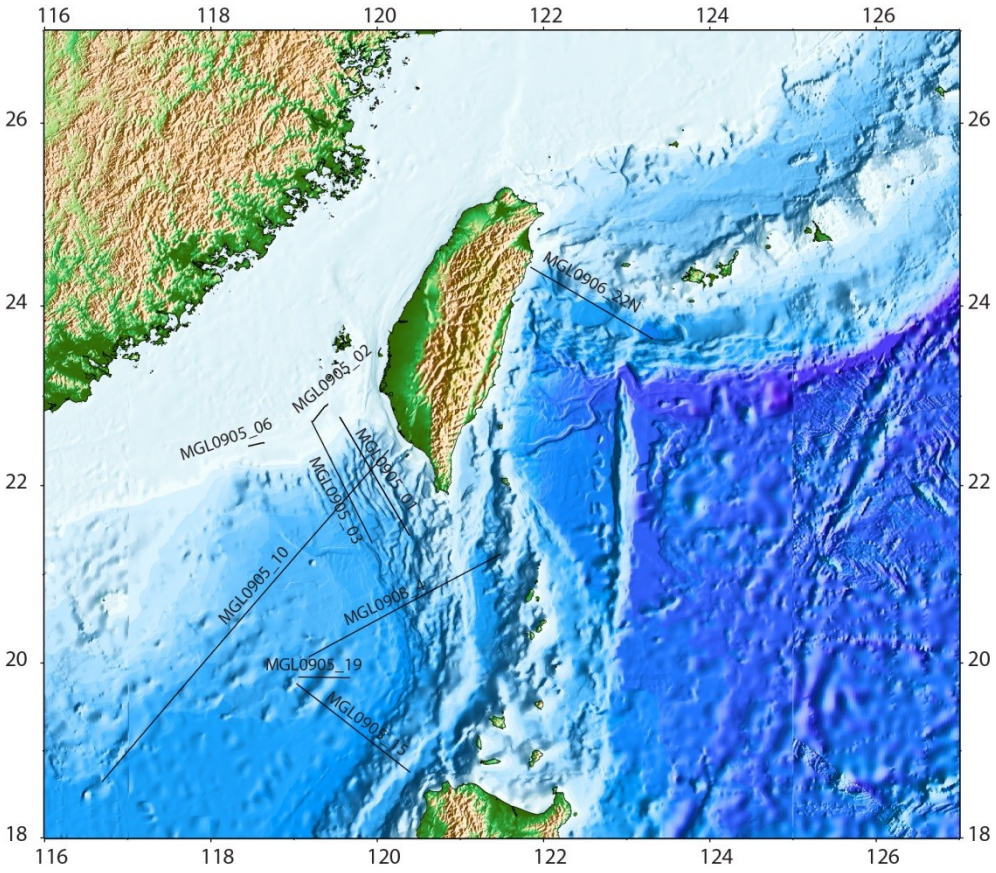

Figure A-1: Location of seismic profiles in Appendix A.

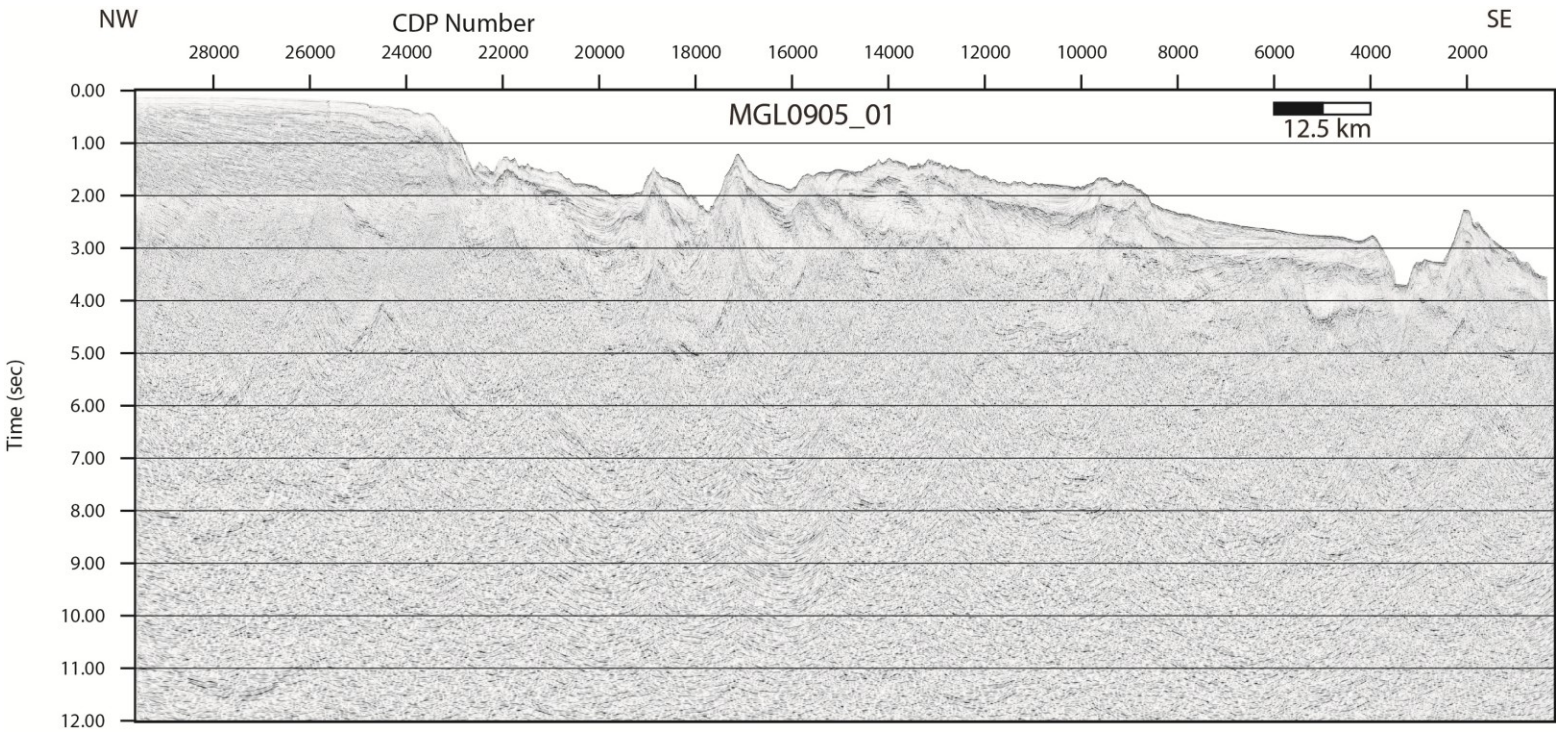

Figure A-2: Reflection profile
MGL0905_01

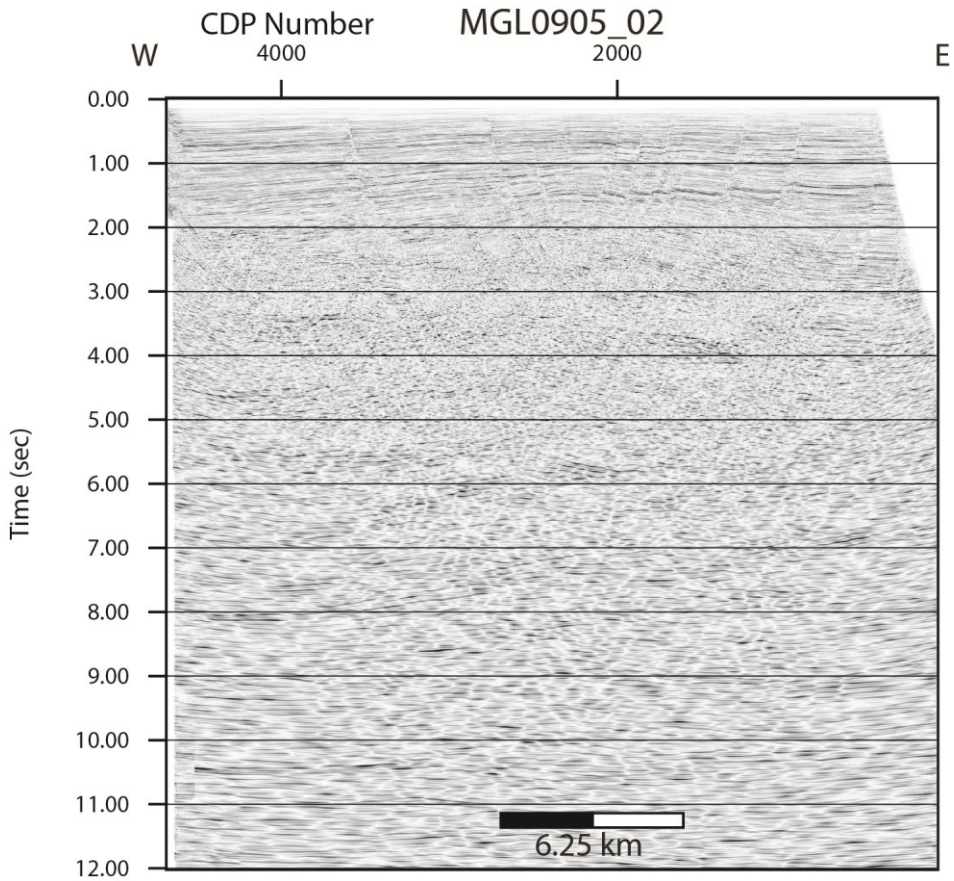

Figure A-3: Reflection profile MGL0905_02.

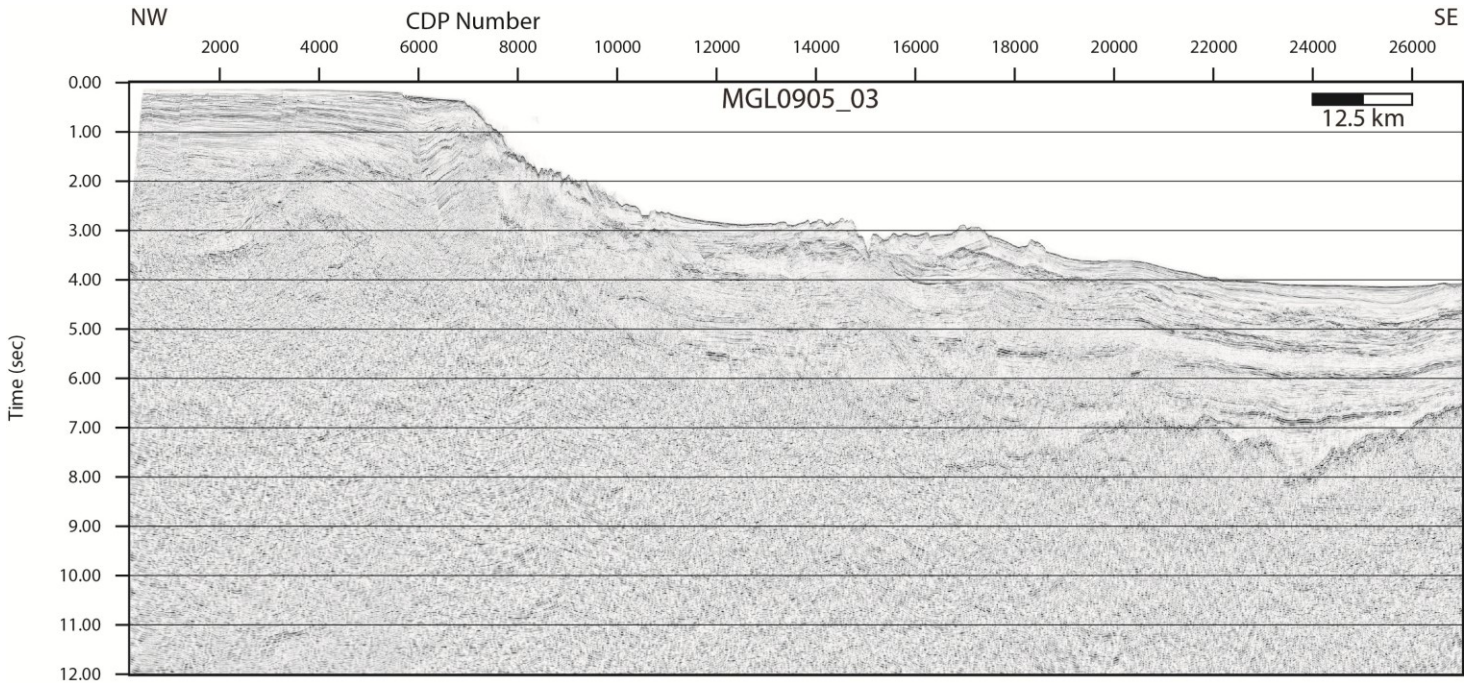

Figure A-4: Reflection profile MGL0905_03

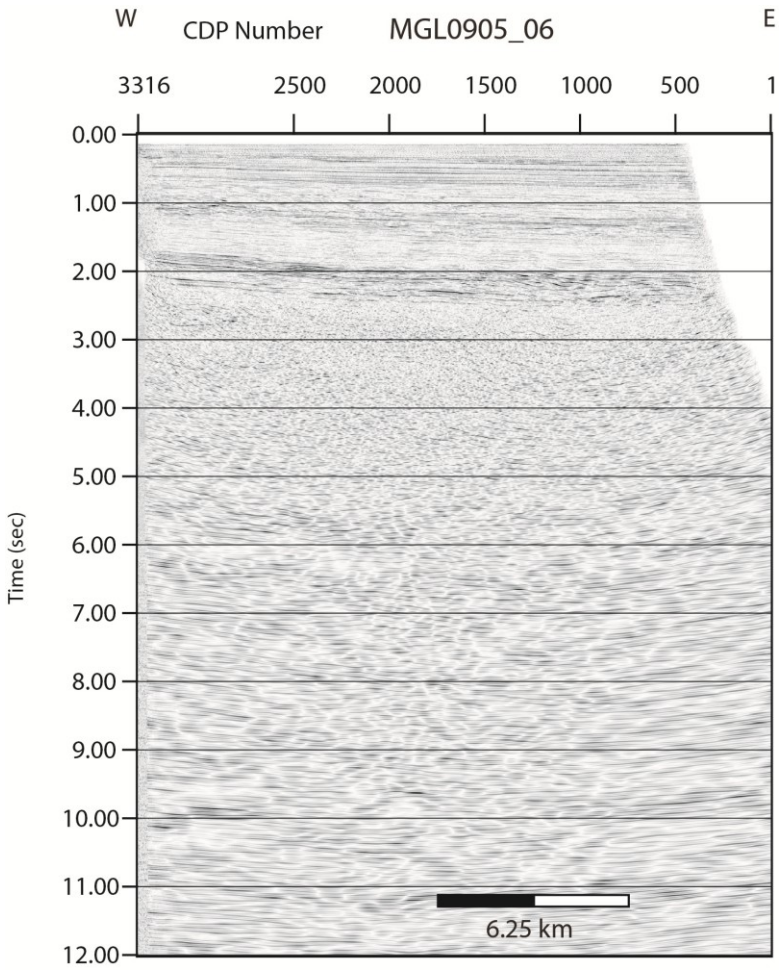

Figure A-5: Reflection profile MGL0905_06

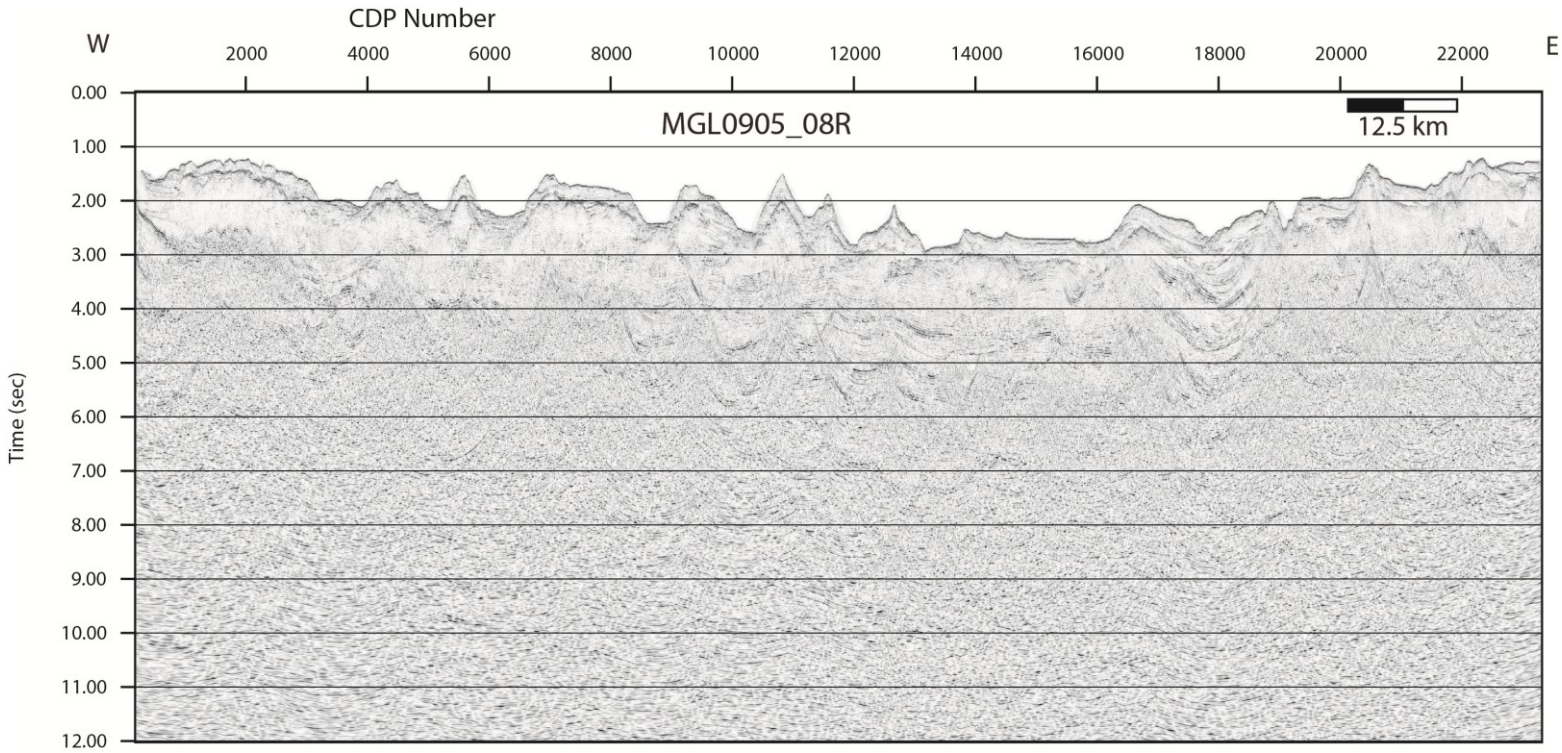

Figure A-6: Reflection profile
MGL0905_08R

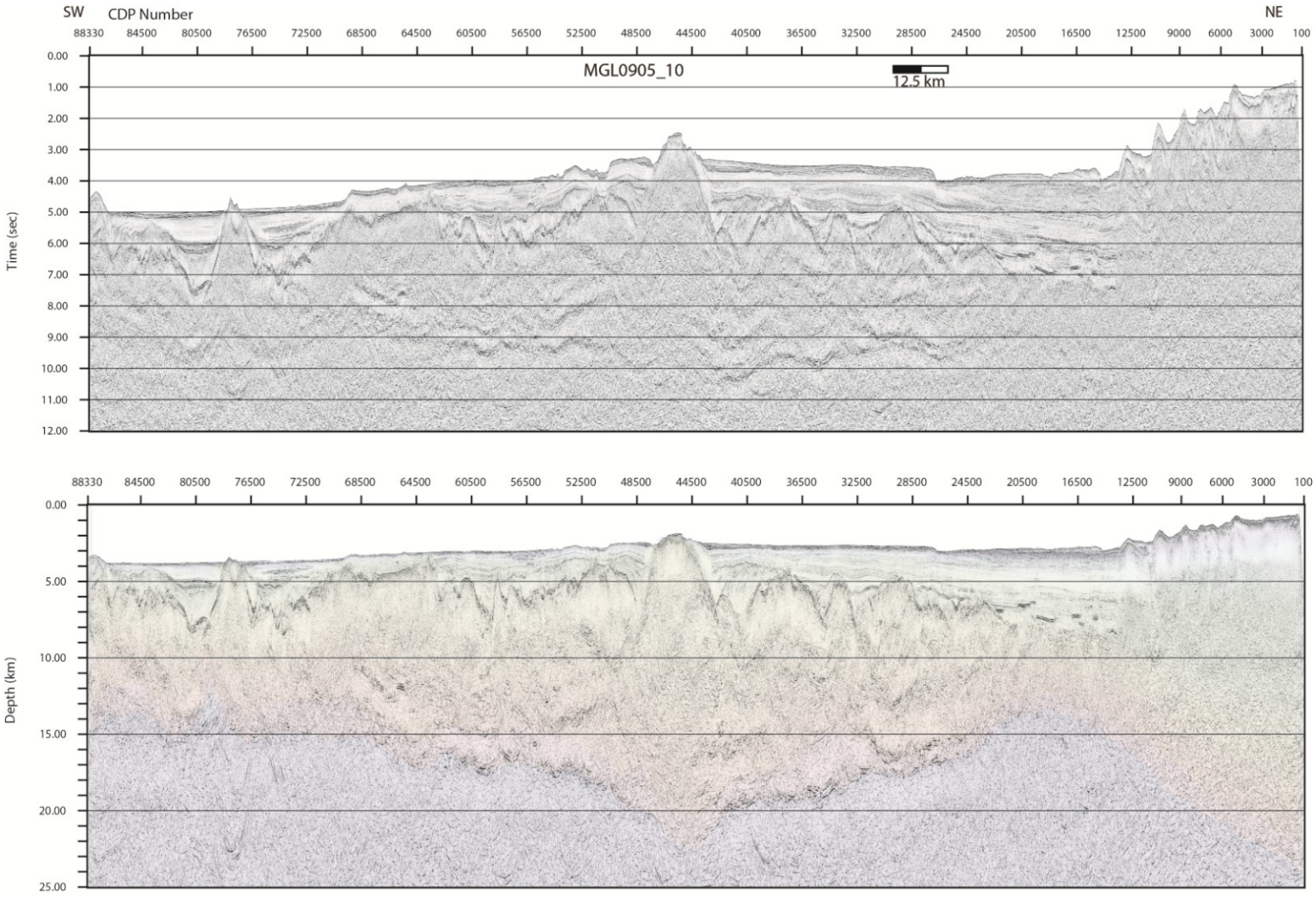

Figure A-7: Reflection profile MGL0905_10 in time (top) and (depth_). Velocity model is overlain on the depth section

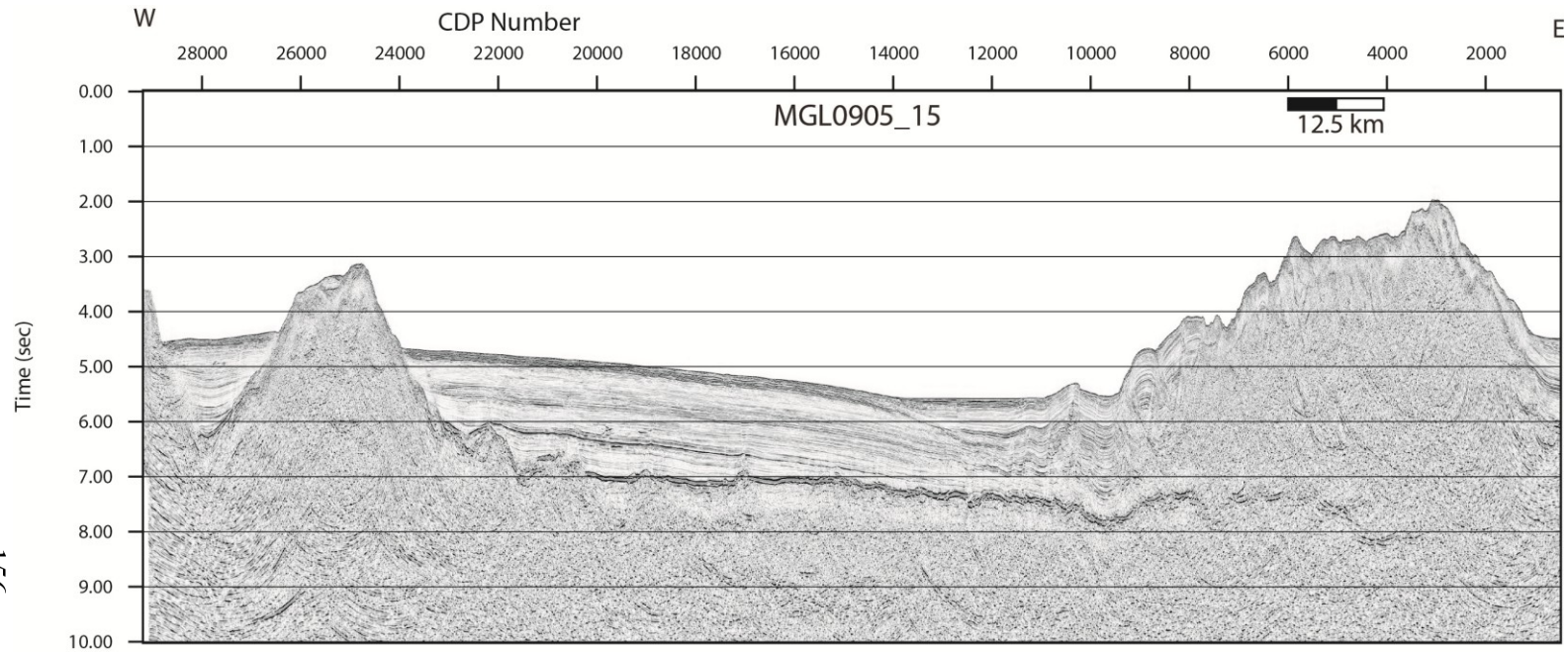

Figure A-8: Reflection profile
MGL0905_15

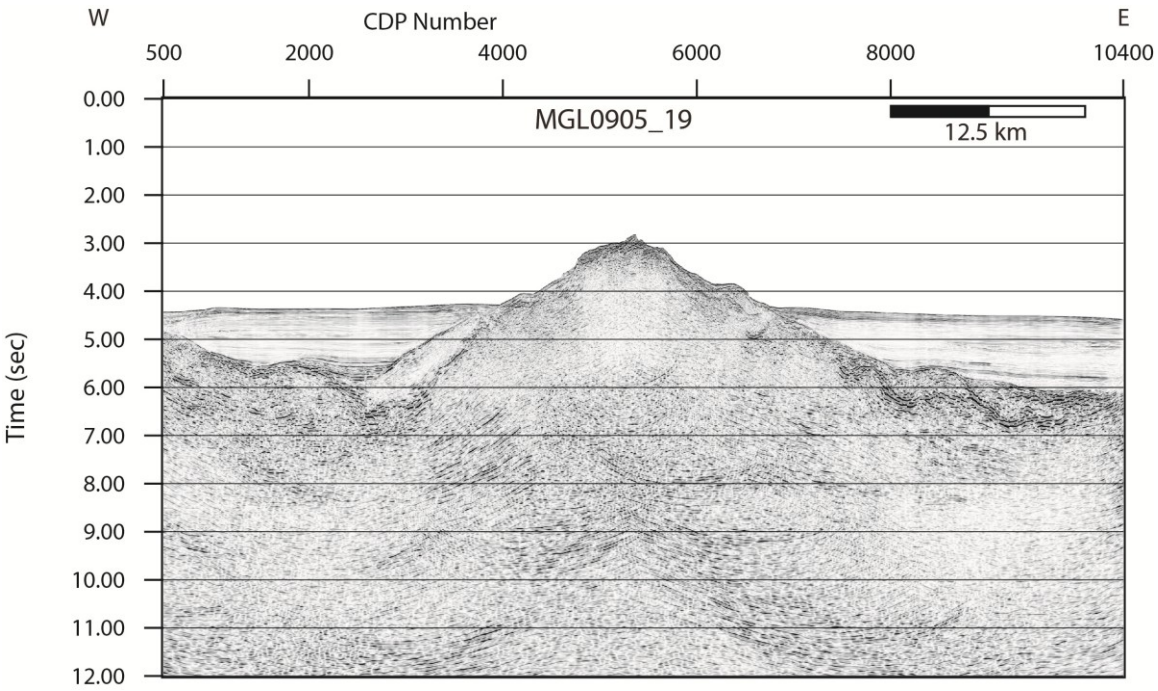

Figure A-9: Reflection profile MGL0905_19

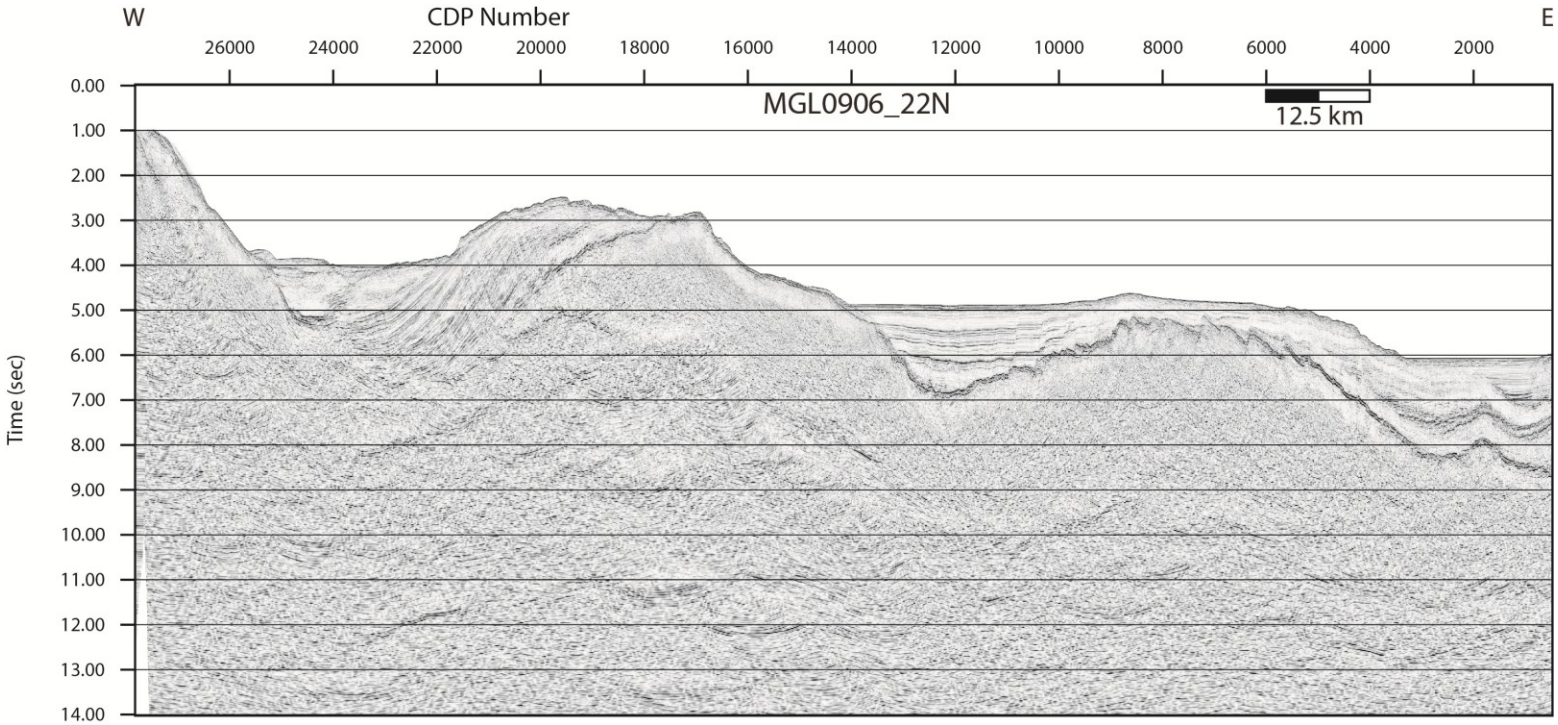

Figure A-10: Reflection profile
MGL0906_22N

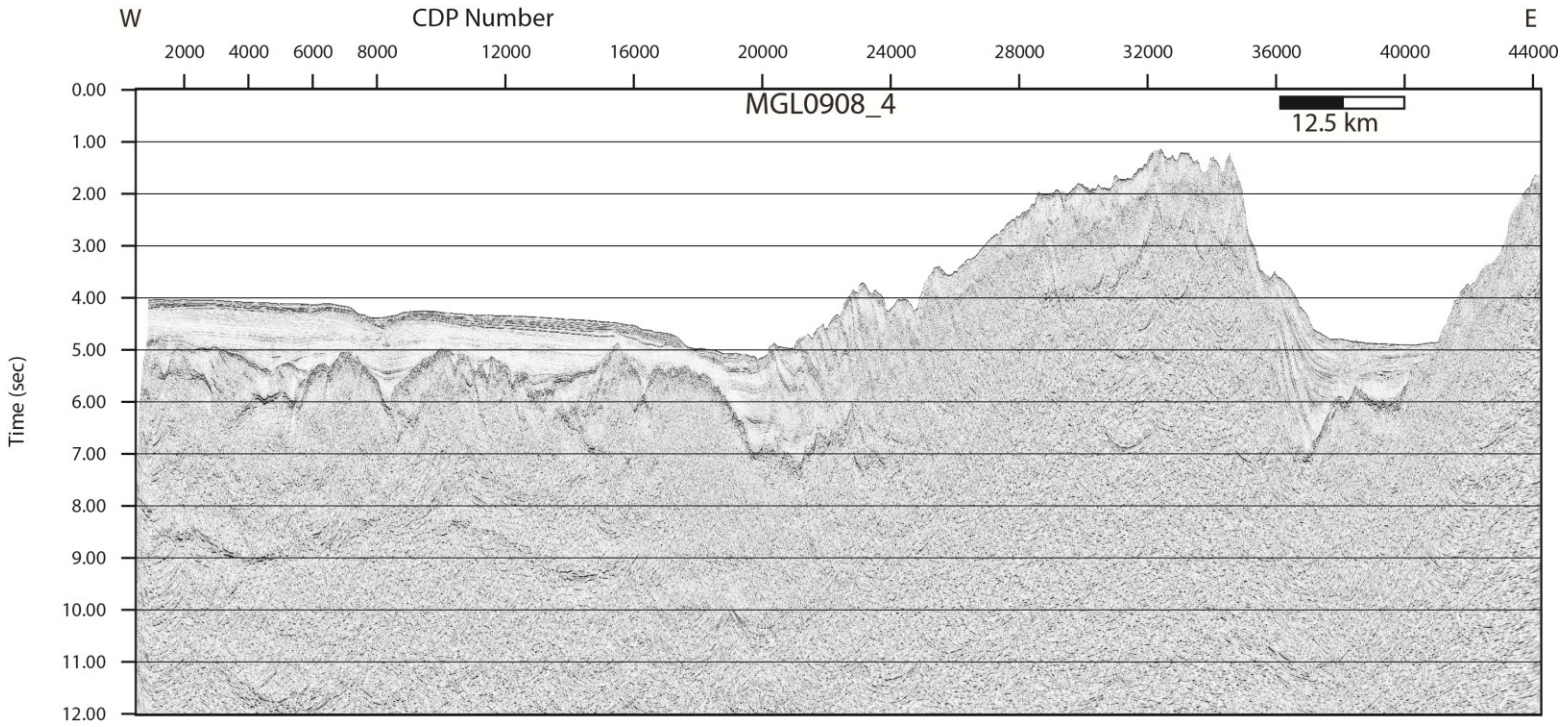

Figure A-11: Reflection profile MGL0908_4

Appendix B: T3 OBS

Appendix B contains the ocean bottom seismometer (OBS) records acquired along T3. Three instruments (OBS 10, OBS 15, and OBS 19) are presented in the chapter 3 manuscript, and the other records are presented here. Each has been minimally processed with similar parameters as described in chapter three including gapped deconvolution and a bandpass filter.

OBS	Long.	Lat.
3	119.185	22.8041
6	119.221	22.5614
8	119.263	22.2939
10	119.304	22.0269
11	119.32	21.8947
12	119.342	21.7633
15	119.405	21.3598
16	119.426	21.2274
17	119.442	21.0924
18	119.463	20.9599
19	119.484	20.8241
20	119.503	20.6902
21	119.524	20.5574
22	119.543	20.4238

Table B-1: T3 OBS locations after relocation using the water wave.

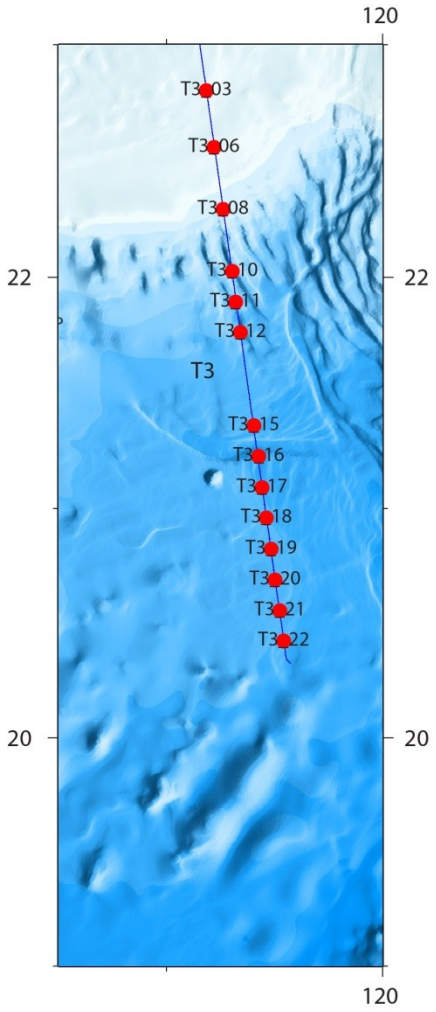

Figure B-1: T3 wide-angle profile with OBS locations.

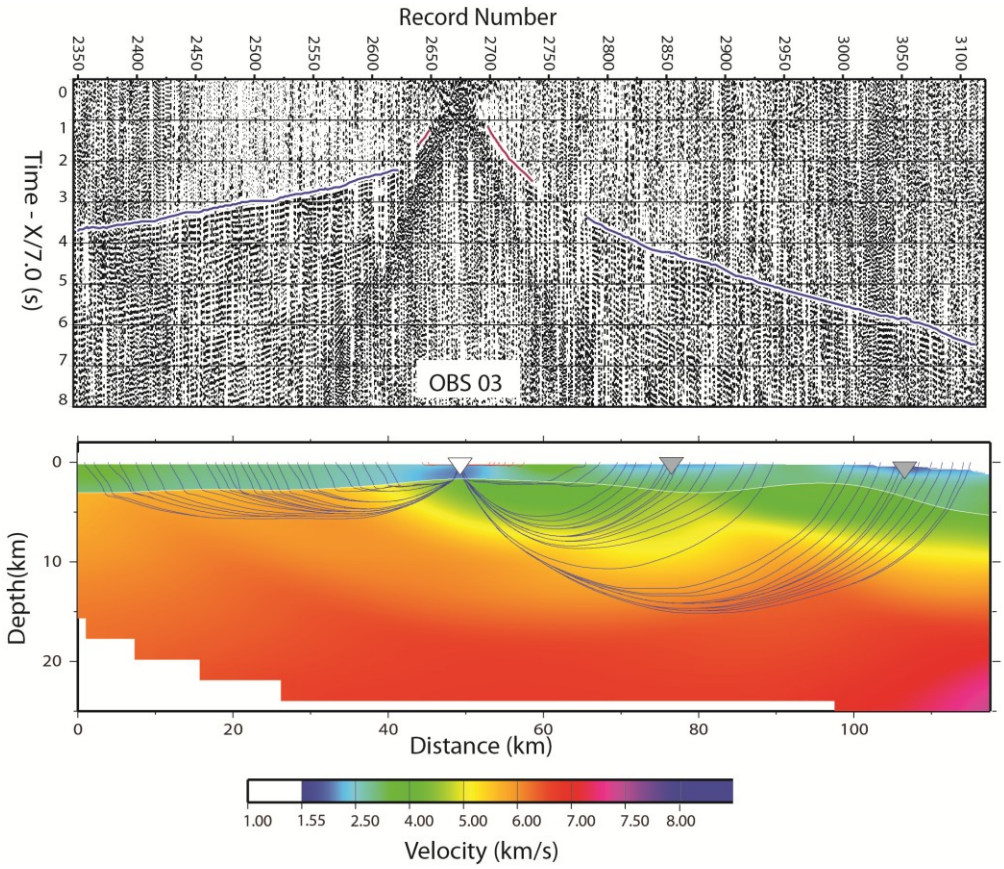

Figure B-2: OBS 03 travel-time picks and ray coverage in the T3 final velocity model presented in chapter 3. Blue picks are refractions in the basement layer, green picks are top of basement reflection picks, and red picks are refractions in the sedimentary layer.

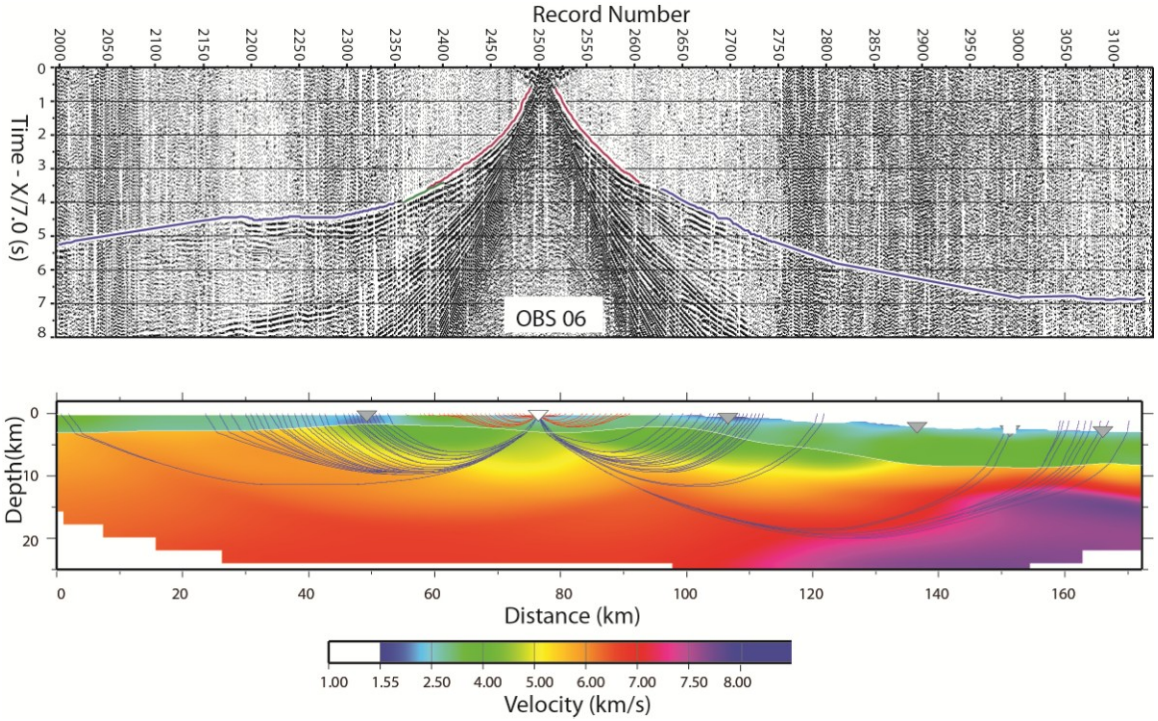

Figure B-3: OBS 06 travel-time picks and ray coverage in the T3 final velocity model presented in chapter 3. Blue picks are refractions in the basement layer, green picks are top of basement reflection picks, and red picks are refractions in the sedimentary layer.

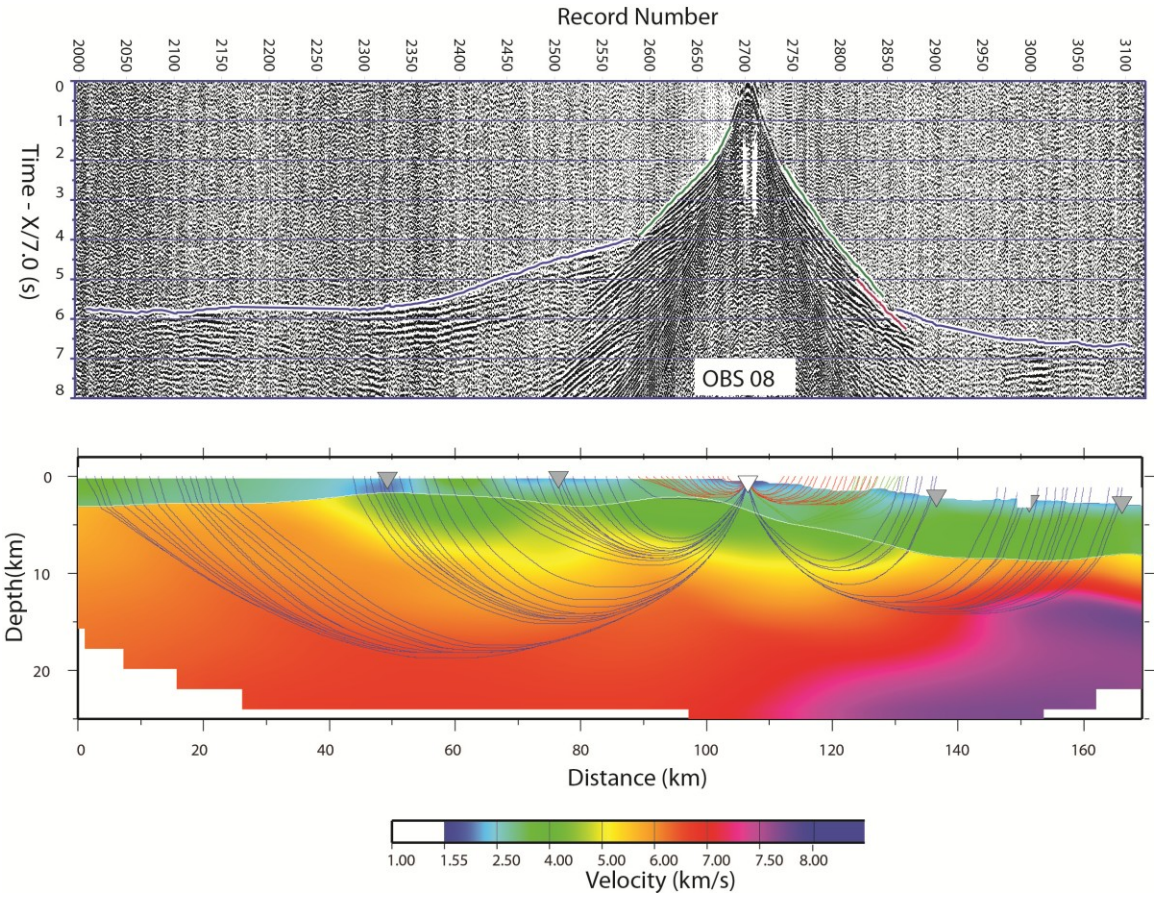

Figure B-4: OBS 08 travel-time picks and ray coverage in the T3 final velocity model presented in chapter 3. Blue picks are refractions in the basement layer, green picks are top of basement reflection picks, and red picks are refractions in the sedimentary layer.

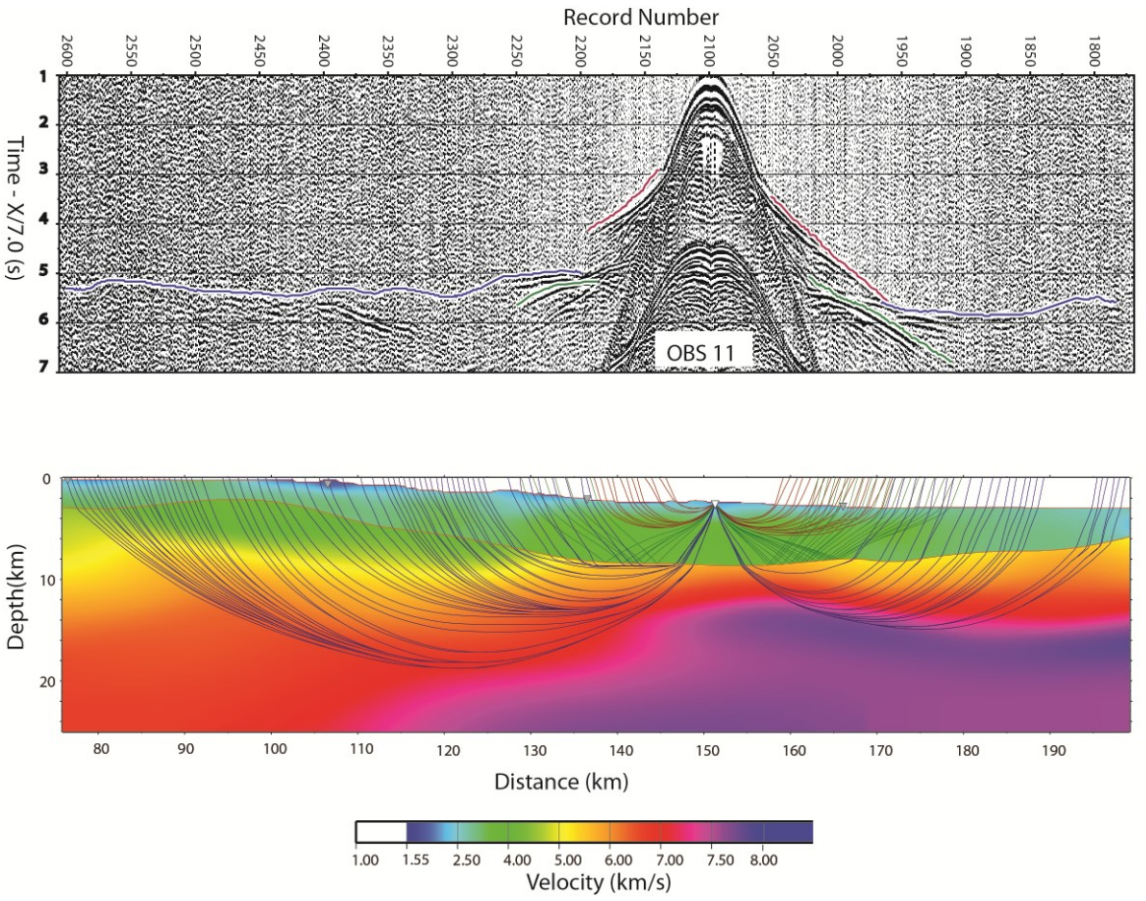

Figure B-5: OBS 11 travel-time picks and ray coverage in the T3 final velocity model presented in chapter 3. Blue picks are refractions in the basement layer, green picks are top of basement reflection picks, and red picks are refractions in the sedimentary layer.

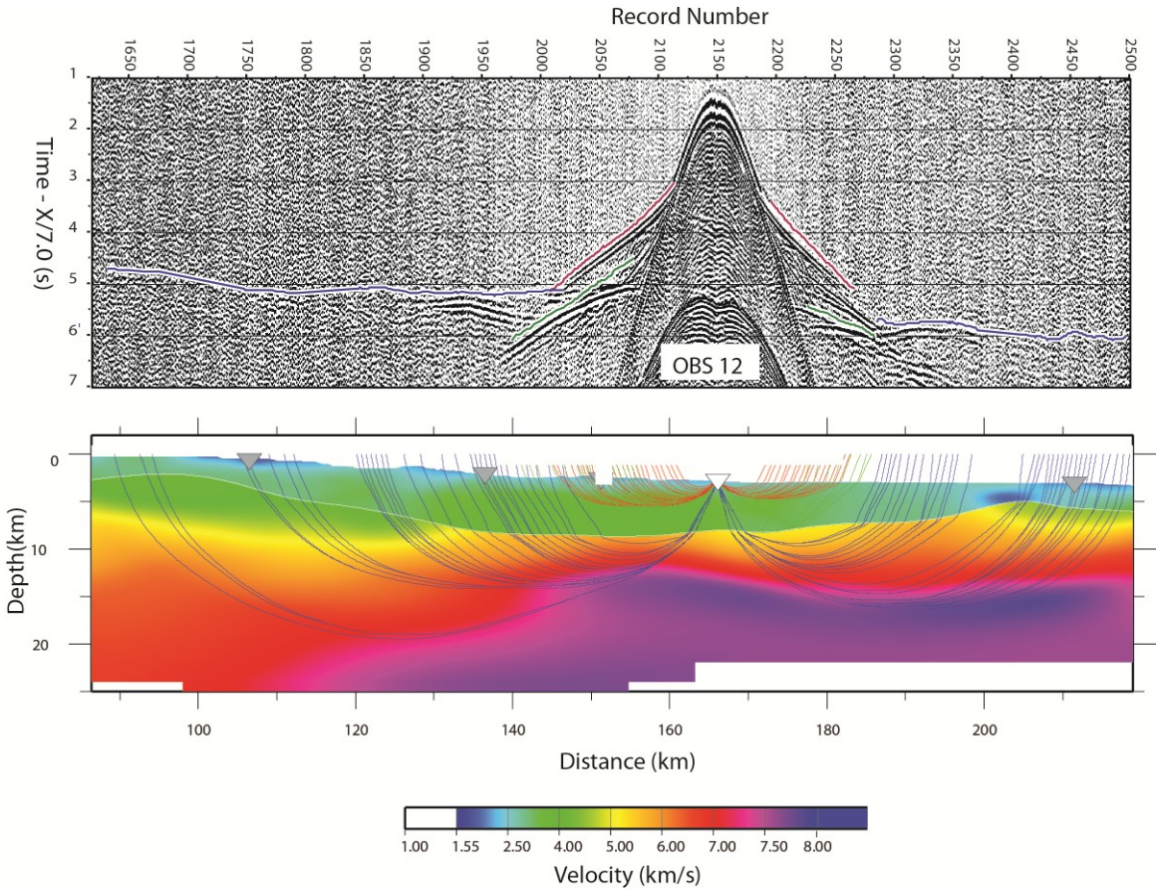

Figure B-6: OBS 12 travel-time picks and ray coverage in the T3 final velocity model presented in chapter 3. Blue picks are refractions in the basement layer, green picks are top of basement reflection picks, and red picks are refractions in the sedimentary layer.

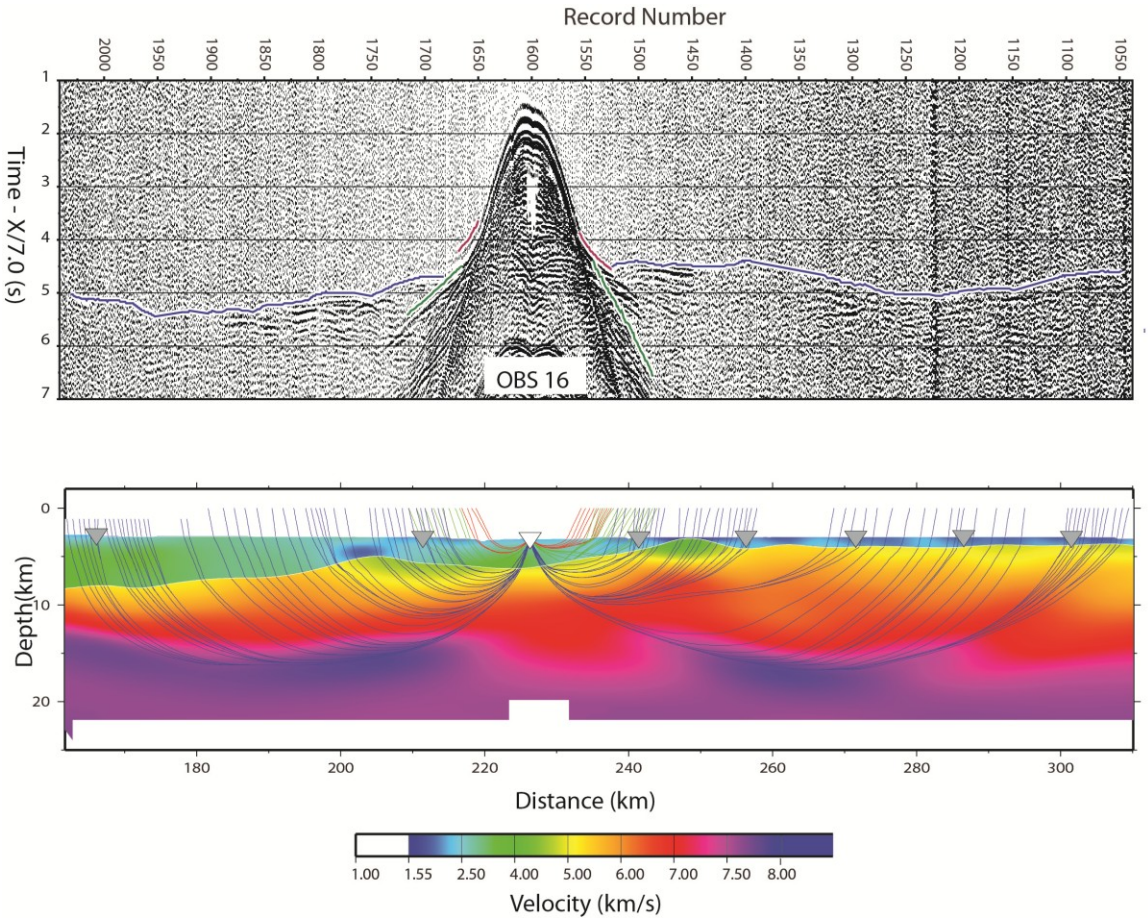

Figure B-7: OBS 16 travel-time picks and ray coverage in the T3 final velocity model presented in chapter 3. Blue picks are refractions in the basement layer, green picks are top of basement reflection picks, and red picks are refractions in the sedimentary layer.

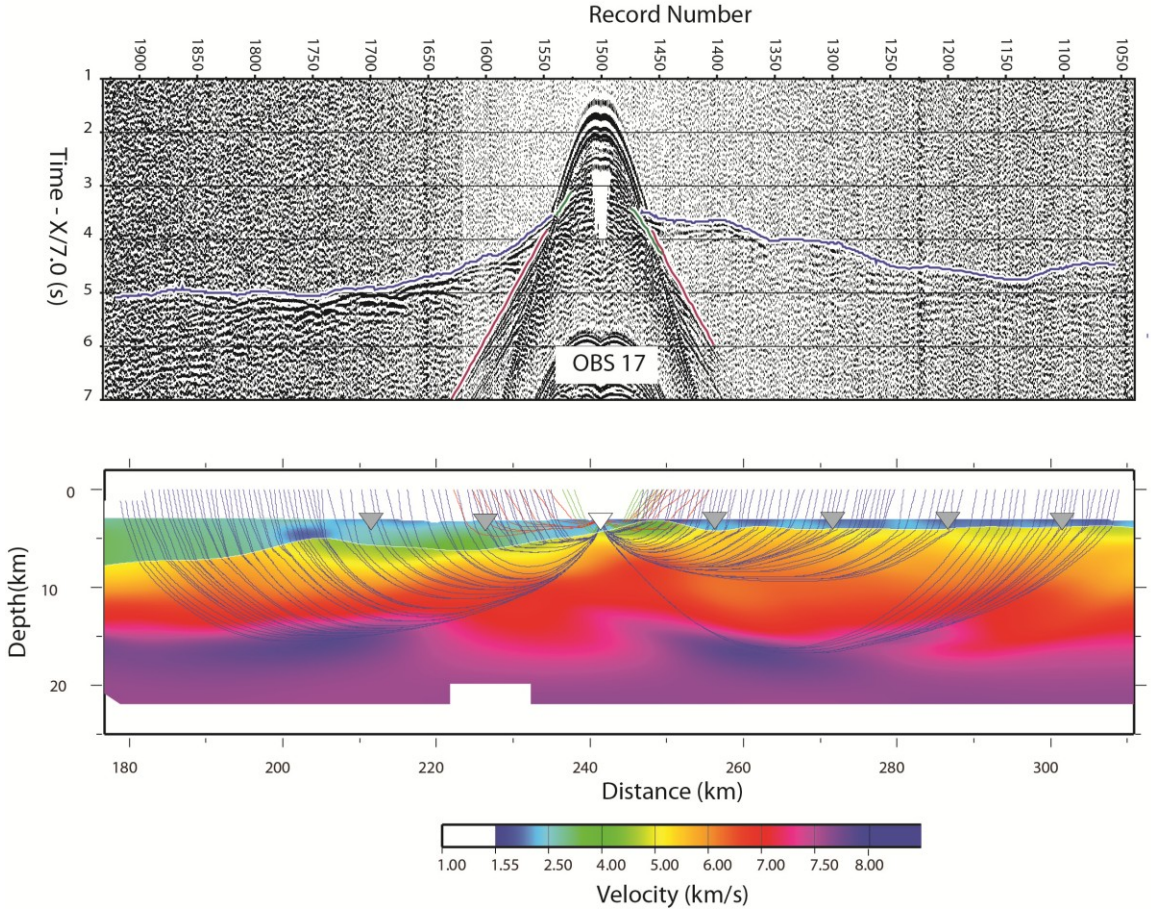

Figure B-8: OBS 17 travel-time picks and ray coverage in the T3 final velocity model presented in chapter 3. Blue picks are refractions in the basement layer, green picks are top of basement reflection picks, and red picks are refractions in the sedimentary layer.

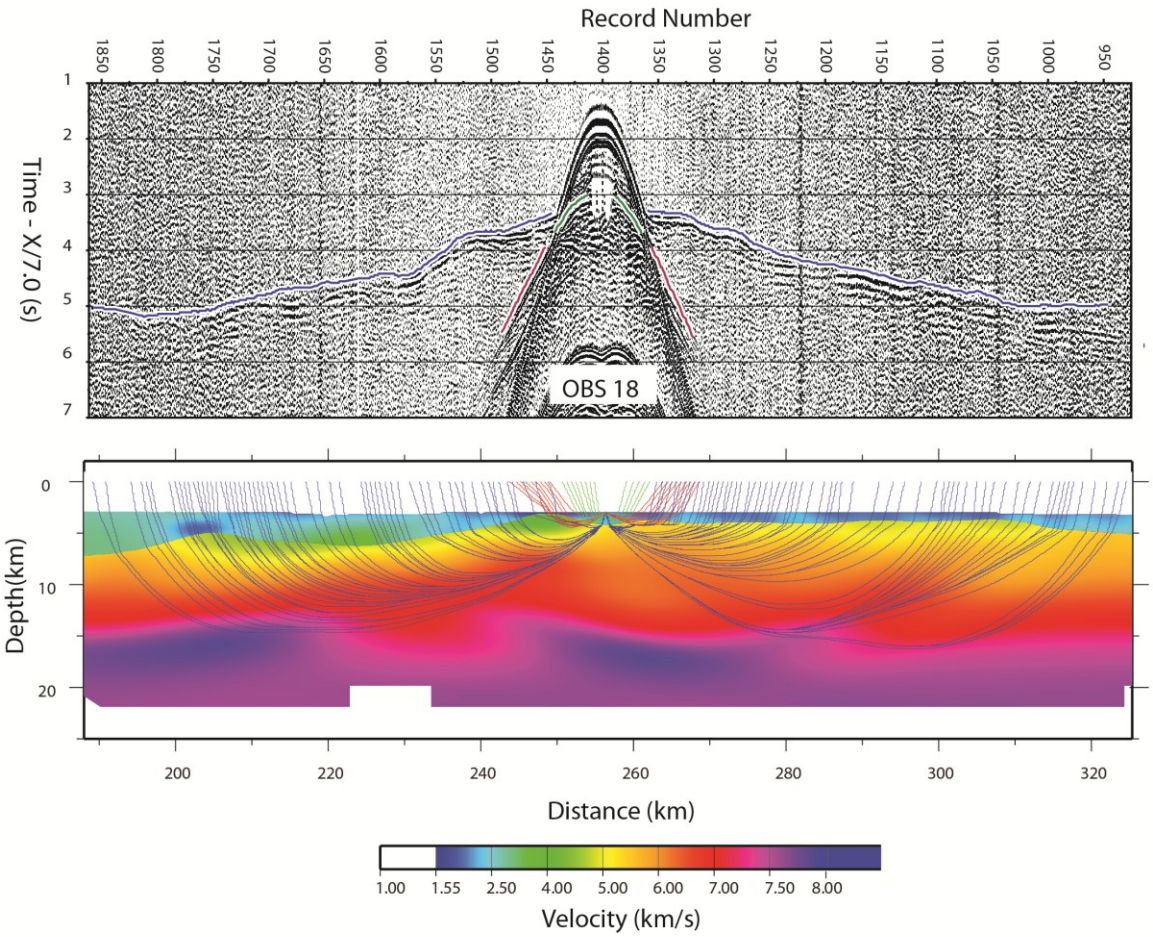

Figure B-9: OBS 18 travel-time picks and ray coverage in the T3 final velocity model presented in chapter 3. Blue picks are refractions in the basement layer, green picks are top of basement reflection picks, and red picks are refractions in the sedimentary layer.

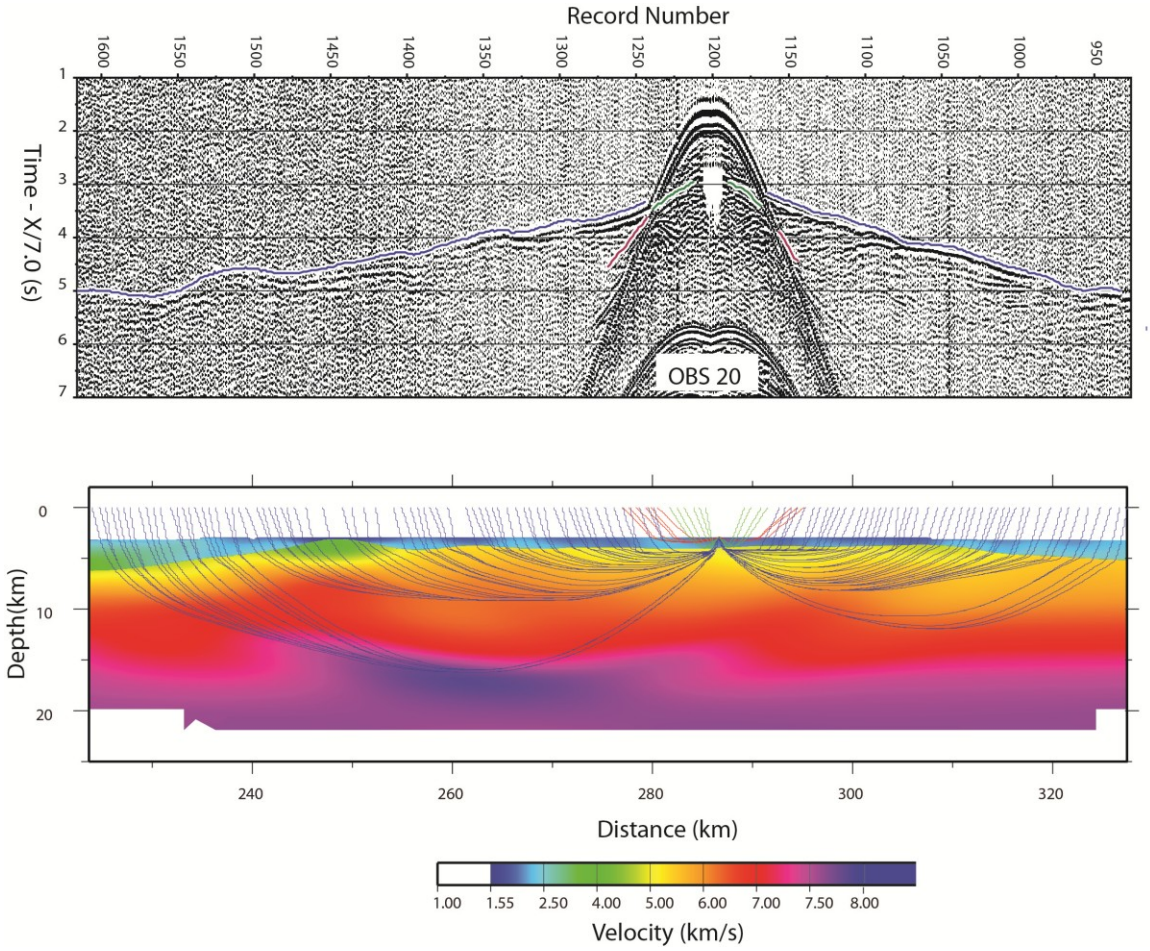

Figure B-10: OBS 20 travel-time picks and ray coverage in the T3 final velocity model presented in chapter 3. Blue picks are refractions in the basement layer, green picks are top of basement reflection picks, and red picks are refractions in the sedimentary layer.

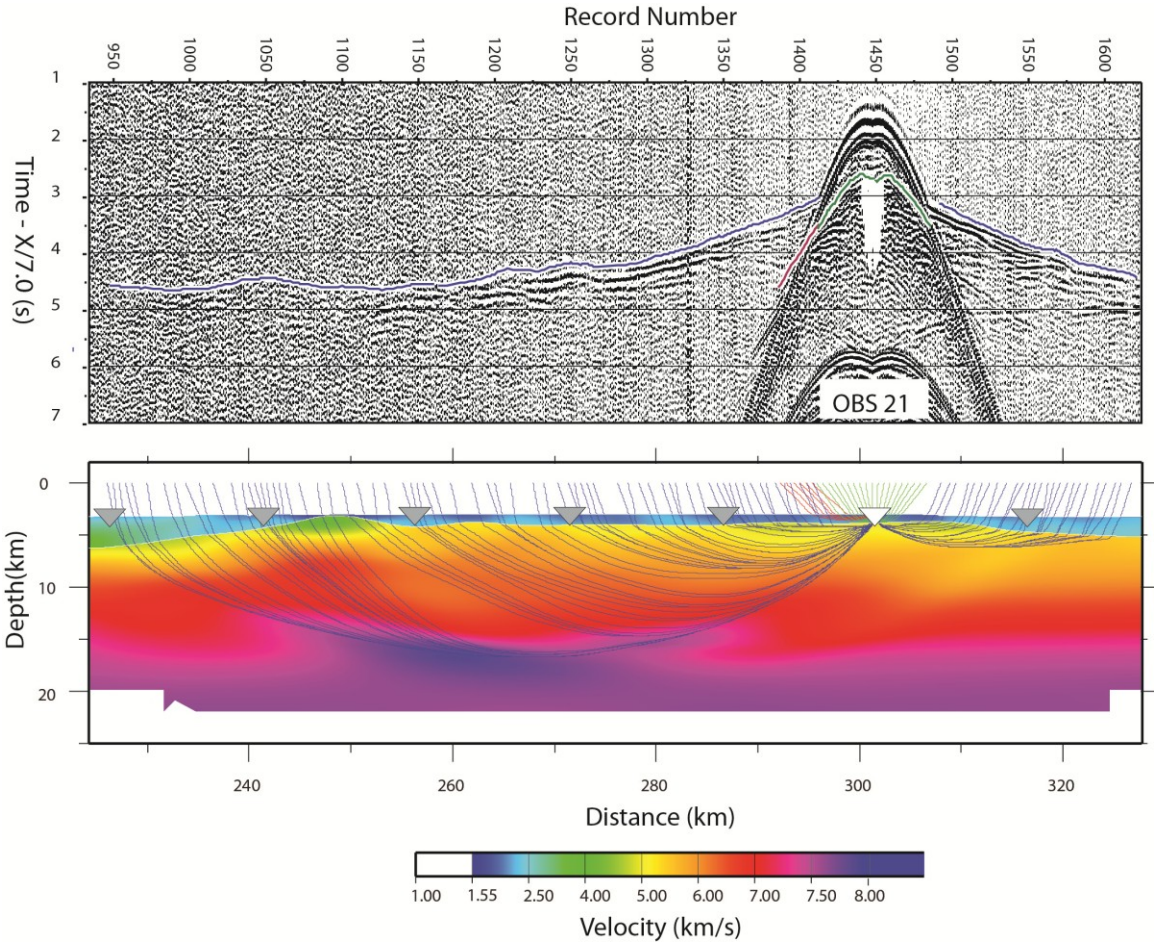

Figure B-11: OBS 21 travel-time picks and ray coverage in the T3 final velocity model presented in chapter 3. Blue picks are refractions in the basement layer, green picks are top of basement reflection picks, and red picks are refractions in the sedimentary layer.

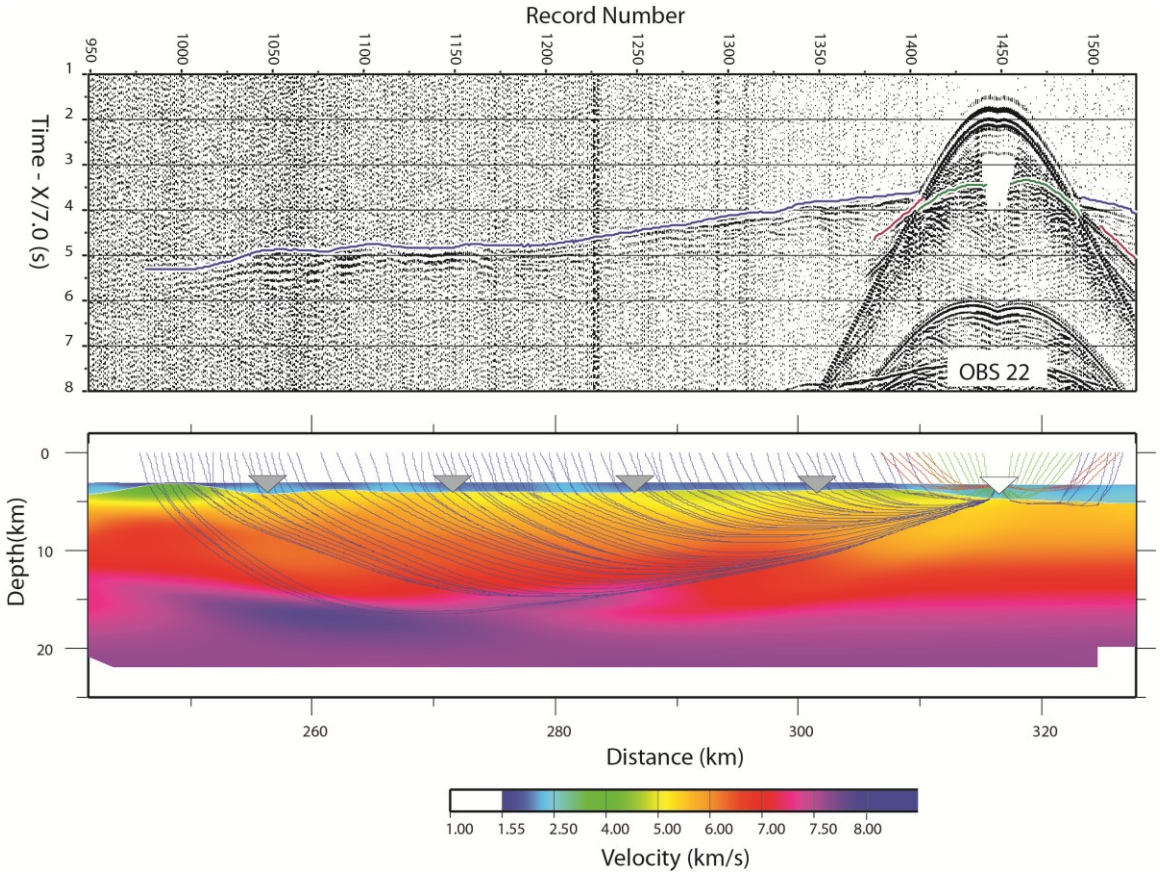

Figure B-12: OBS 22 travel-time picks and ray coverage in the T3 final velocity model presented in chapter 3. Blue picks are refractions in the basement layer, green picks are top of basement reflection picks, and red picks are refractions in the sedimentary layer.

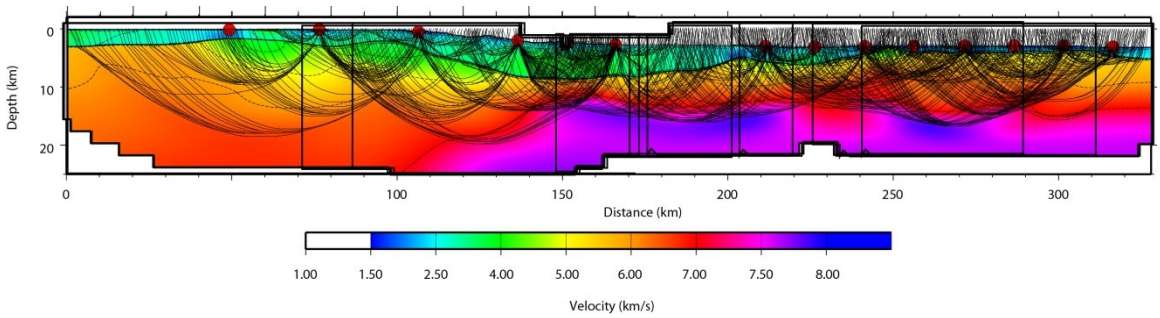

Figure B-13: Ray coverage in T3 velocity model.

Appendix C: MGL0905_27 OBS

This section of the appendix contains the ocean bottom seismometer (OBS) records acquired along MGL0905_27 not included in chapter 4. OBS 1, OBS 5, and OBS 7 are presented in chapter 4. Each has been minimally processed and fully processed with similar processing as described in chapter 4.

OBS	Long	Lat
1	119.636	21.0241
2	119.77	21.0953
3	119.921	21.1737
4	120.097	21.2652
5	120.237	21.3444
6	120.315	21.3859
7	120.384	21.4173
8	120.459	21.4586
9	120.528	21.4977
10	120.61	21.5415
11	120.675	21.578

Table C-1: MGL0905_27 OBS locations.

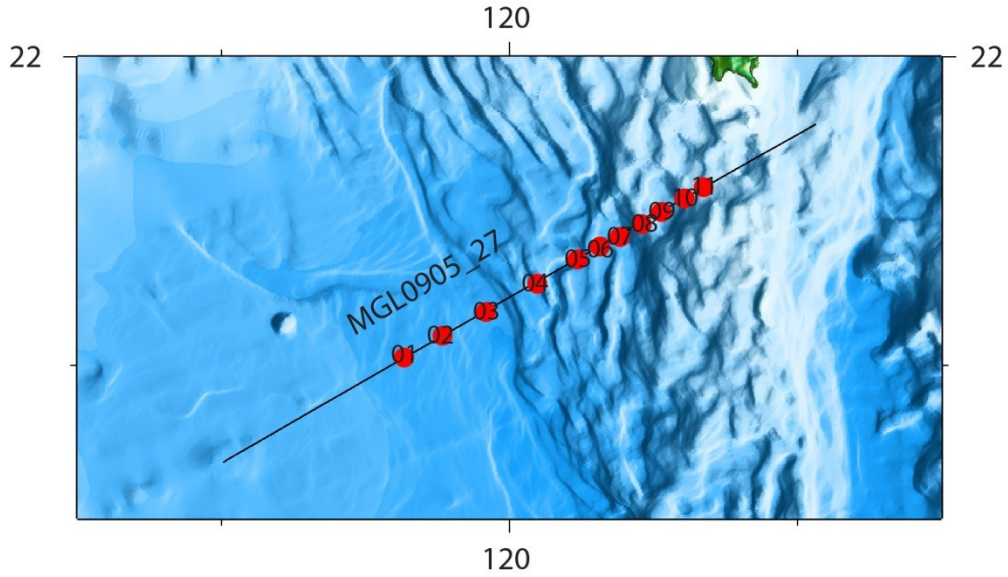

Figure C-1. Location map of MGL0905_27 coincident reflection and wide-angle refraction profile.

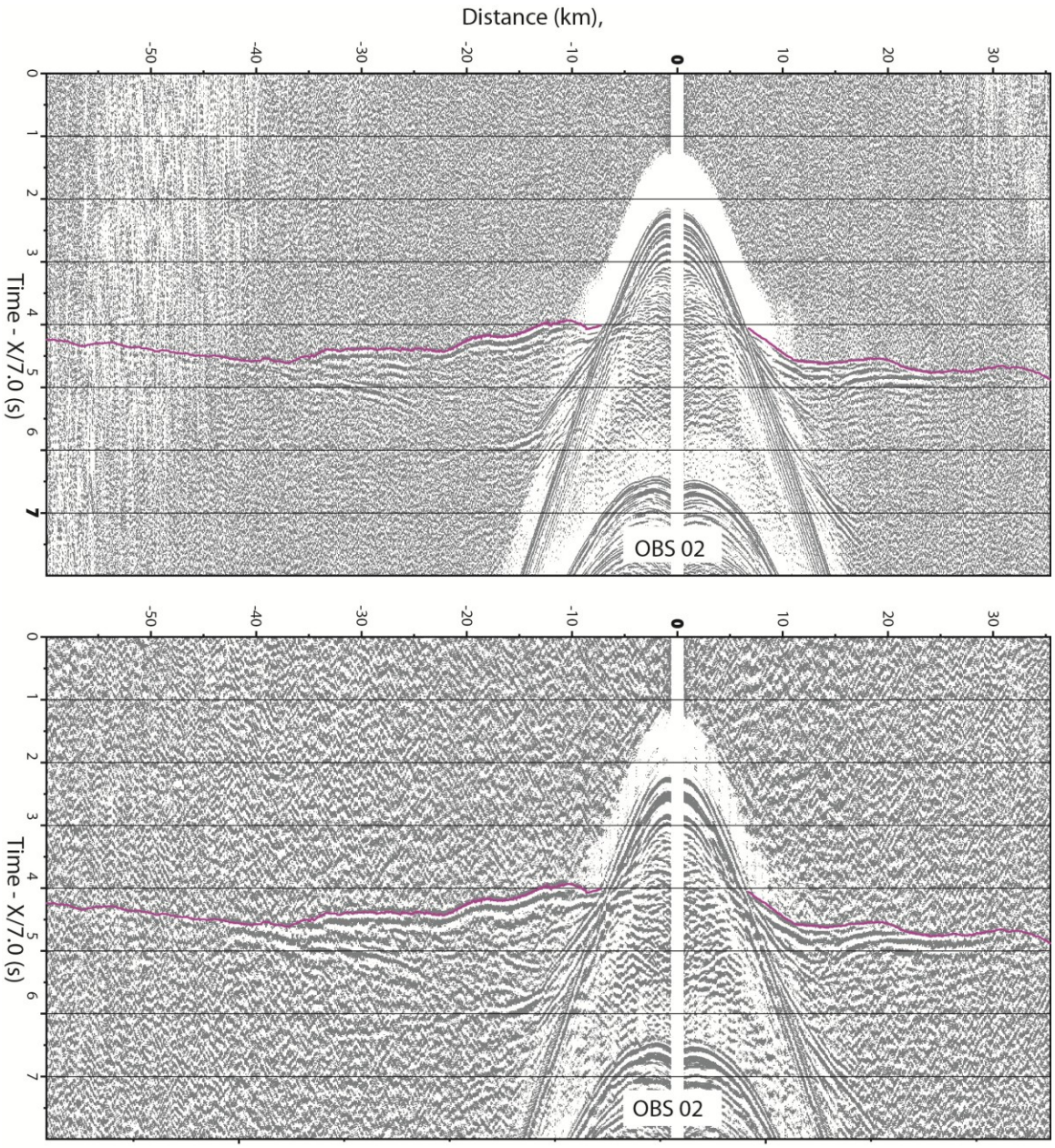

Figure C-2: OBS 02 vertical component with first-arrival travel-time picks. Top is processed with only a bandpass filter, AGC and gaining with offset; bottom is processed to suppress the previous shot noise using gapped deconvolution, coherency filtering, fx deconvolution, trace stacking, bandpass filtering, AGC and gaining with offset.

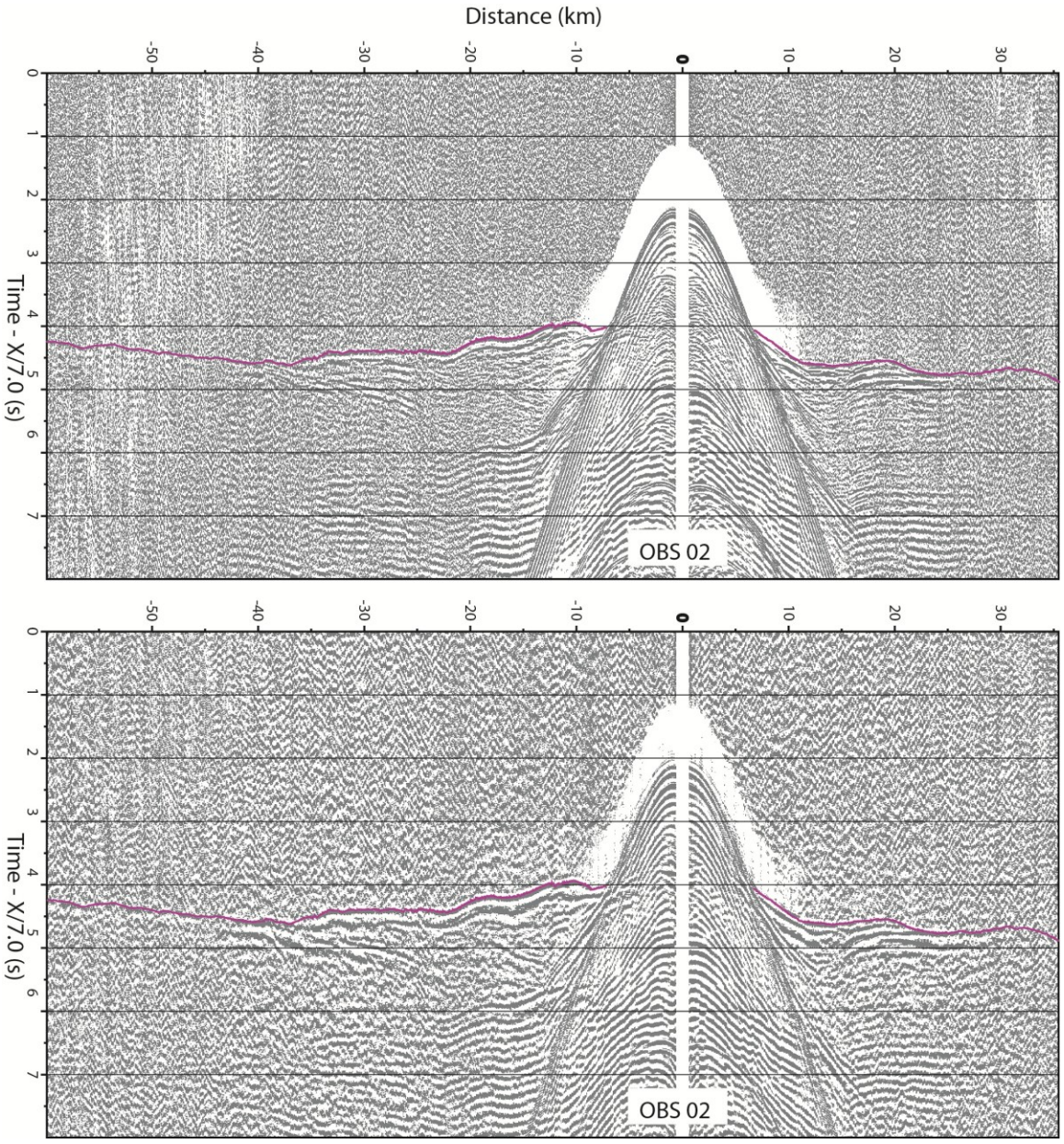

Figure C-3: OBS 02 hydrophone component with first-arrival travel-time picks. Top is processed with only a bandpass filter, AGC and gaining with offset; bottom is processed to suppress the previous shot noise using gapped deconvolution, coherency filtering, fx deconvolution, trace stacking, bandpass filtering, AGC and gaining with offset.

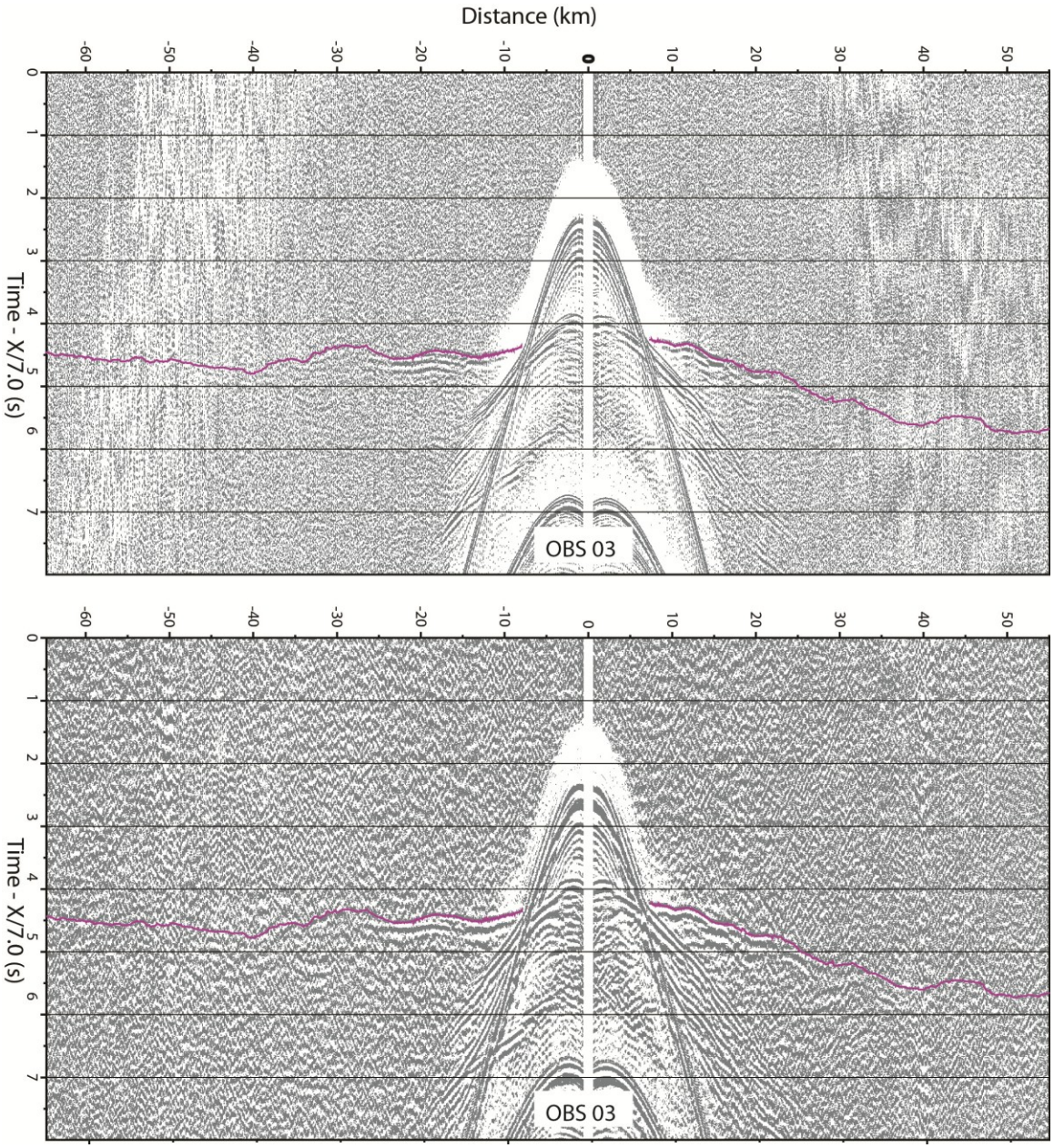

Figure C-4: OBS 03 vertical component with first-arrival travel-time picks. Top is processed with only a bandpass filter, AGC and gaining with offset; bottom is processed to suppress the previous shot noise using gapped deconvolution, coherency filtering, fx deconvolution, trace stacking, bandpass filtering, AGC and gaining with offset

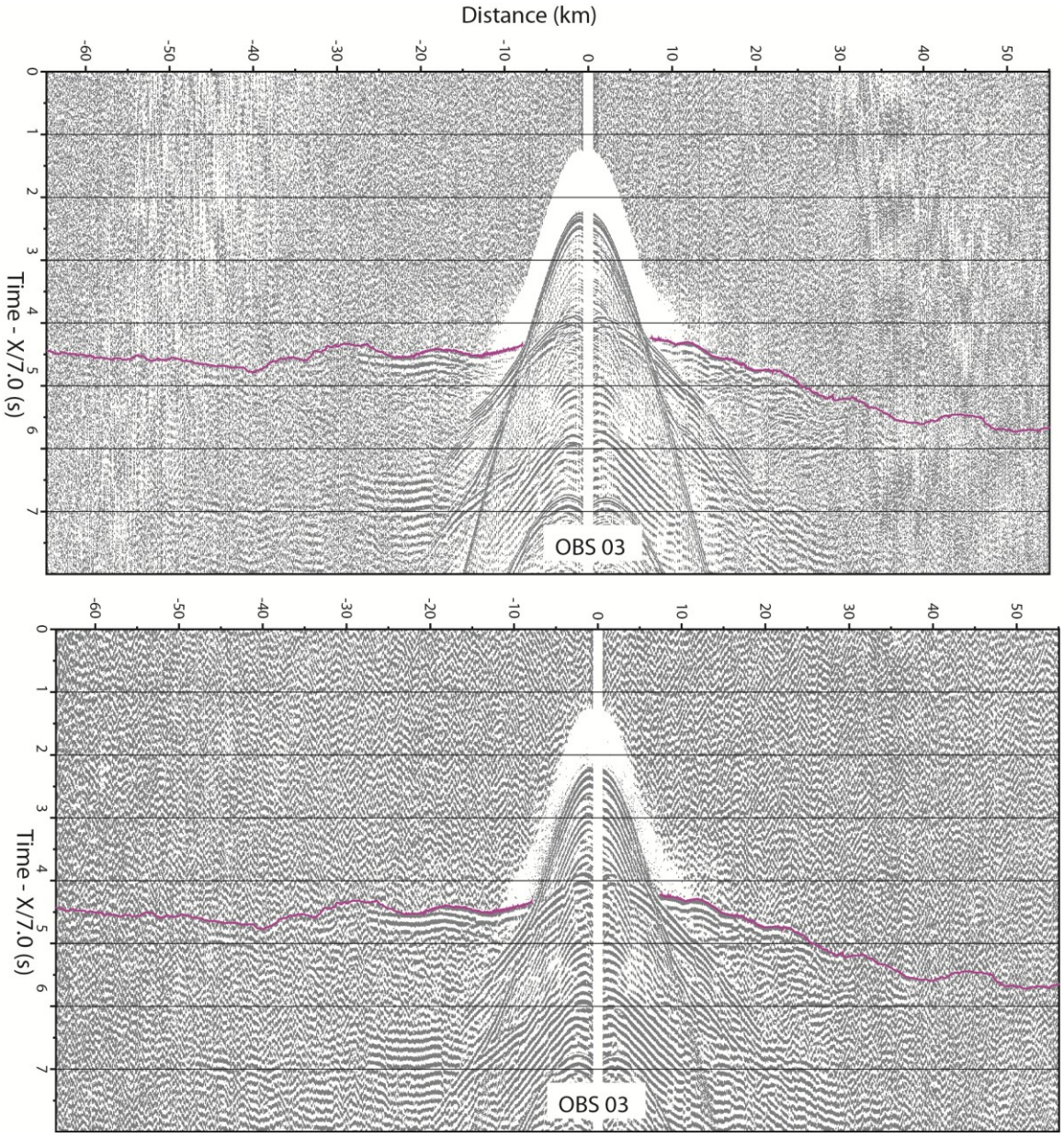

Figure C-5: OBS 03 hydrophone component with first-arrival travel-time picks. Top is processed with only a bandpass filter, AGC and gaining with offset; bottom is processed to suppress the previous shot noise using gapped deconvolution, coherency filtering, fx deconvolution, trace stacking, bandpass filtering, AGC and gaining with offset.

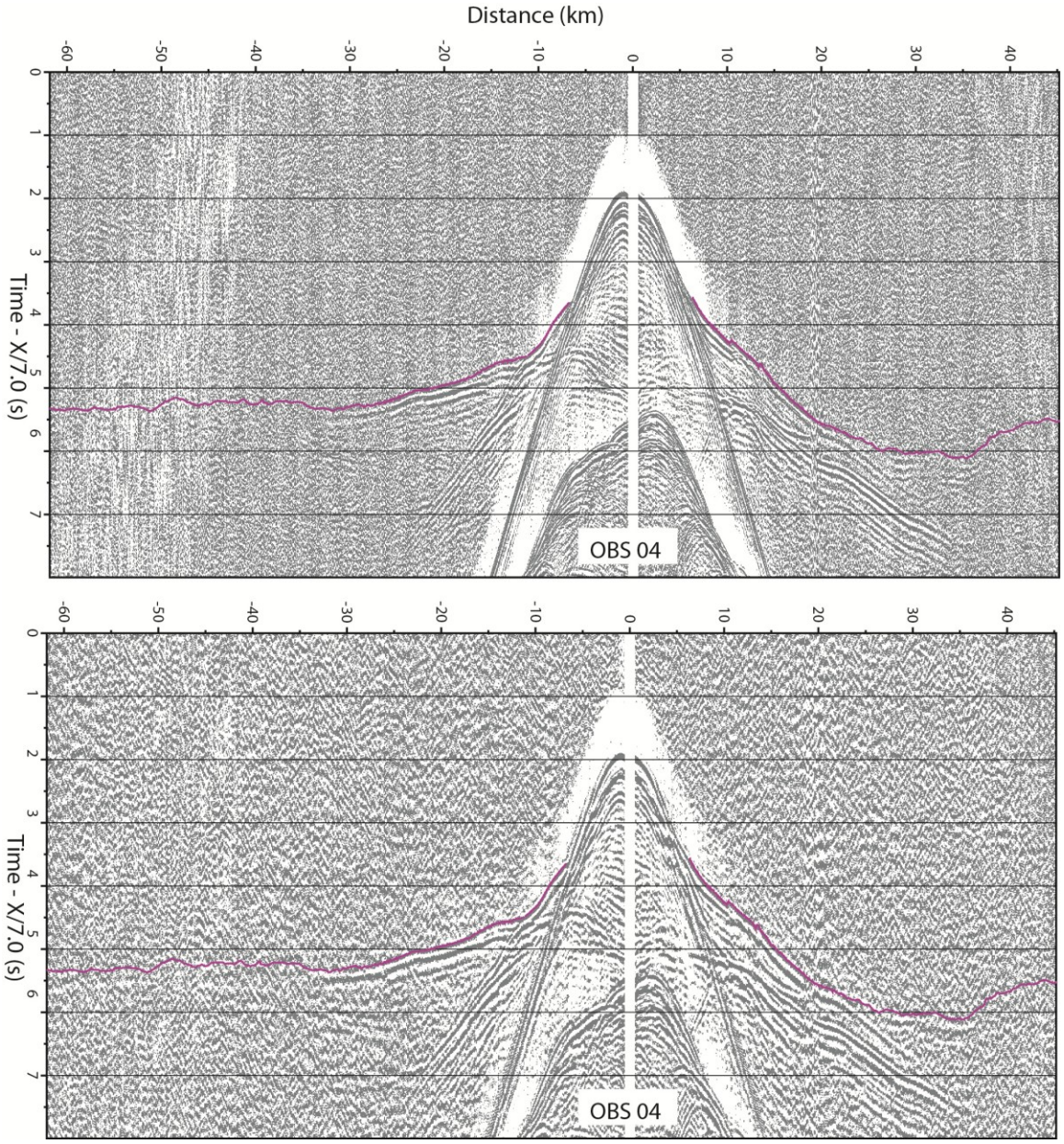

Figure C-6: OBS 04 vertical component with first-arrival travel-time picks. Top is processed with only a bandpass filter, AGC and gaining with offset; bottom is processed to suppress the previous shot noise using gapped deconvolution, coherency filtering, fx deconvolution, trace stacking, bandpass filtering, AGC and gaining with offset.

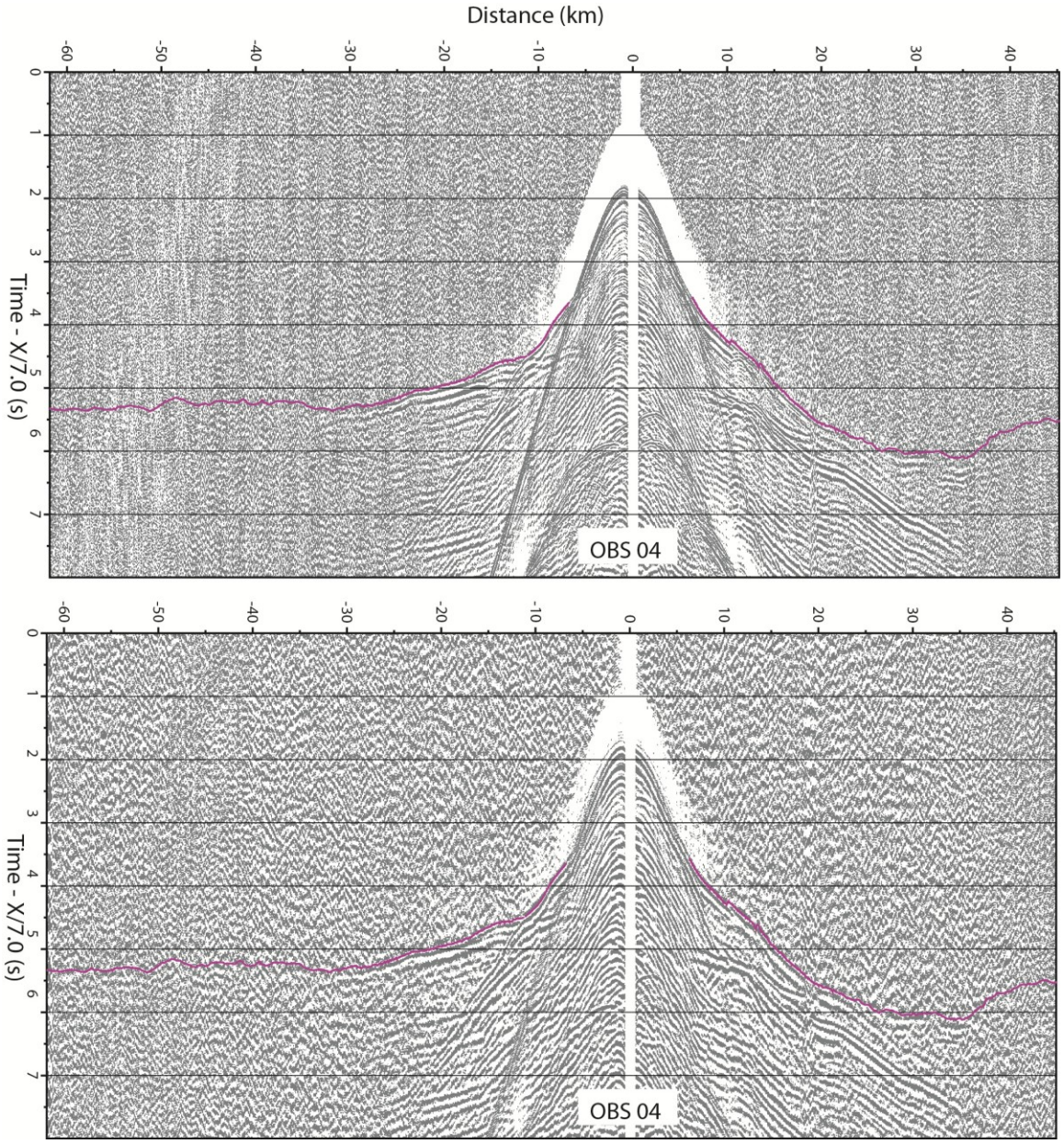

Figure C-7: OBS 04 hydrophone component with first-arrival travel-time picks. Top is processed with only a bandpass filter, AGC and gaining with offset; bottom is processed to suppress the previous shot noise using gapped deconvolution, coherency filtering, fx deconvolution, trace stacking, bandpass filtering, AGC and gaining with offset.

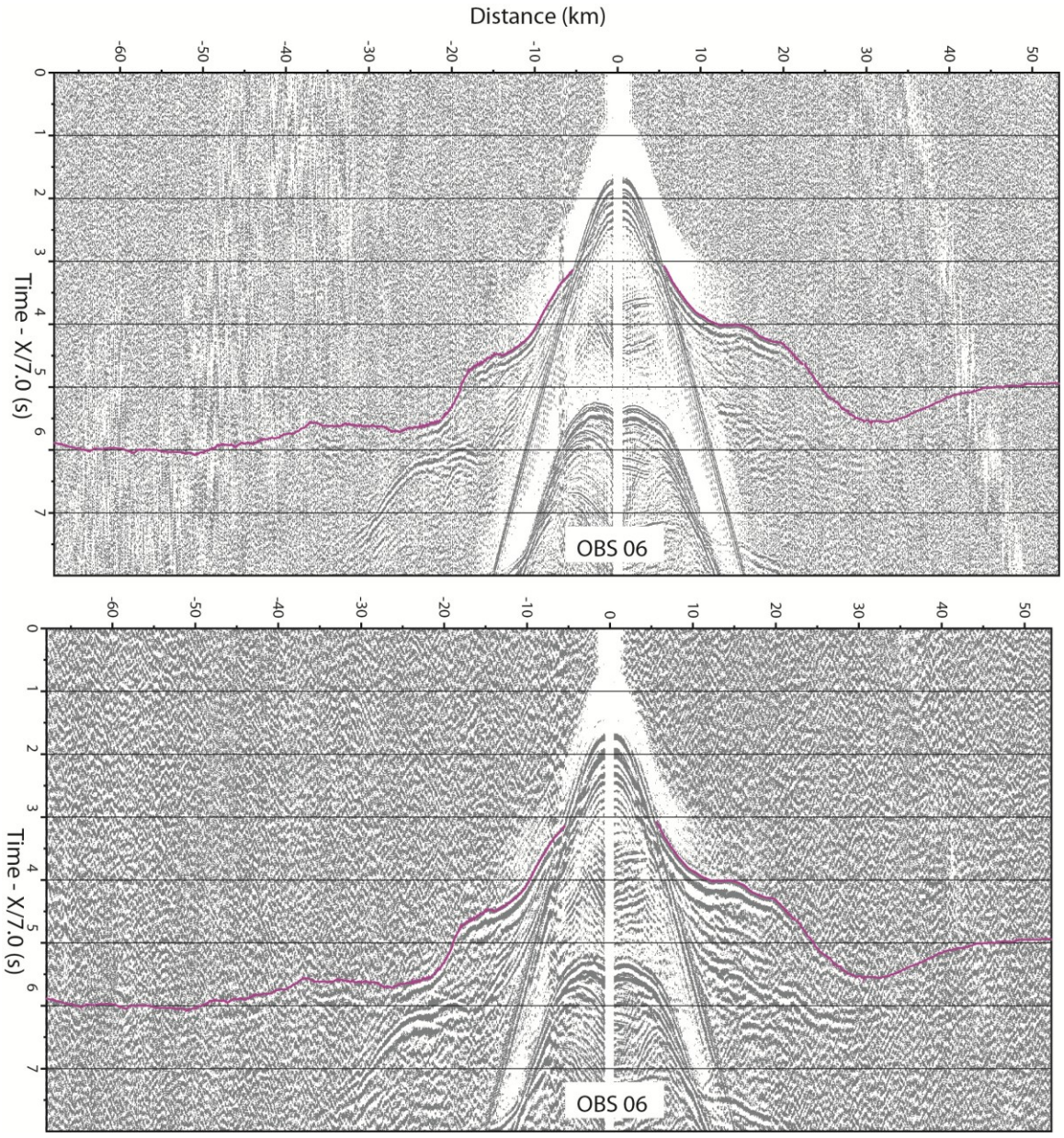

Figure C-8: OBS 06 vertical component with first-arrival travel-time picks. Top is processed with only a bandpass filter, AGC and gaining with offset; bottom is processed to suppress the previous shot noise using gapped deconvolution, coherency filtering, fx deconvolution, trace stacking, bandpass filtering, AGC and gaining with offset.

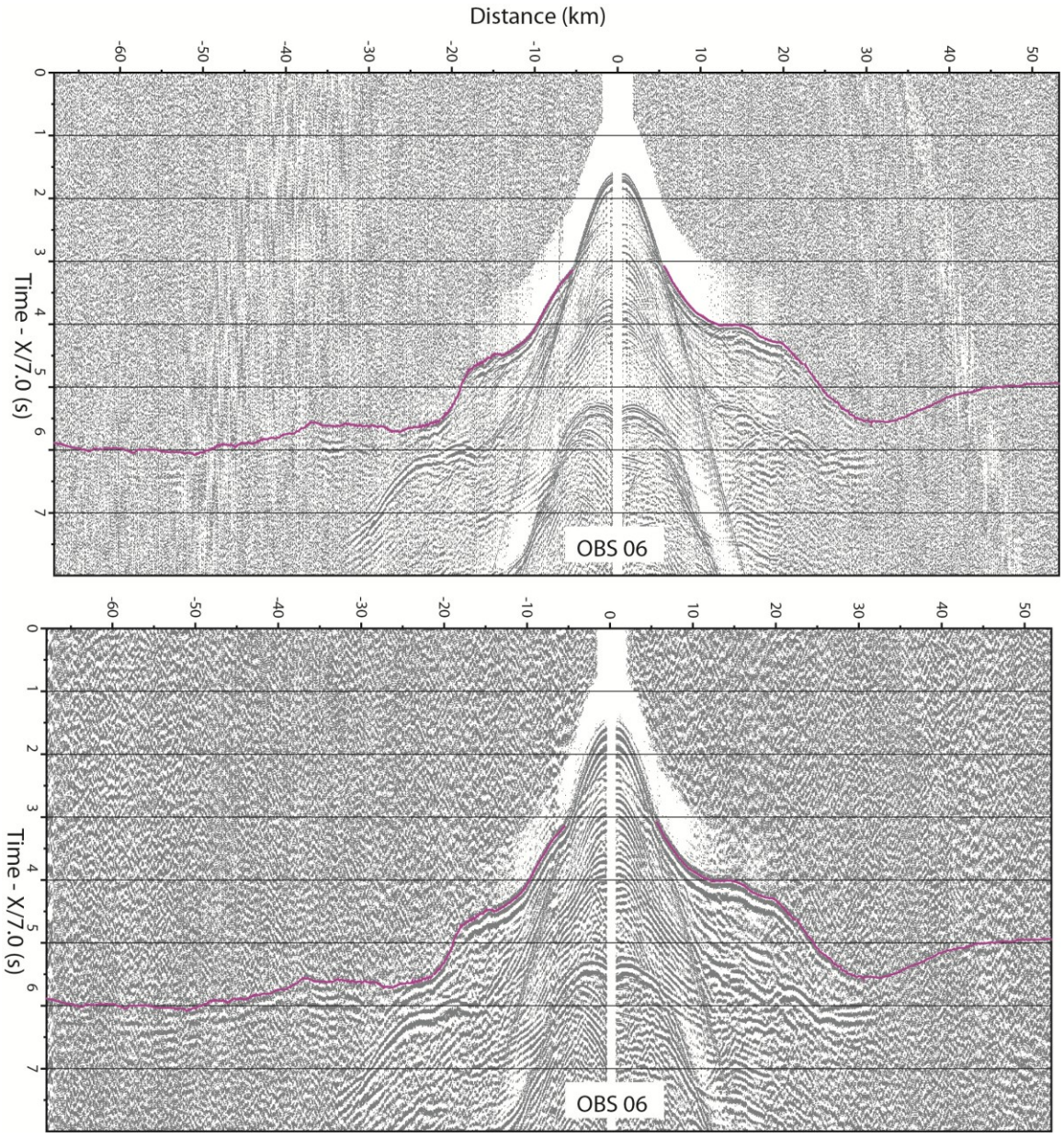

Figure C-9: OBS 06 hydrophone component with first-arrival travel-time picks. Top is processed with only a bandpass filter, AGC and gaining with offset; bottom is processed to suppress the previous shot noise using gapped deconvolution, coherency filtering, fx deconvolution, trace stacking, bandpass filtering, AGC and gaining with offset.

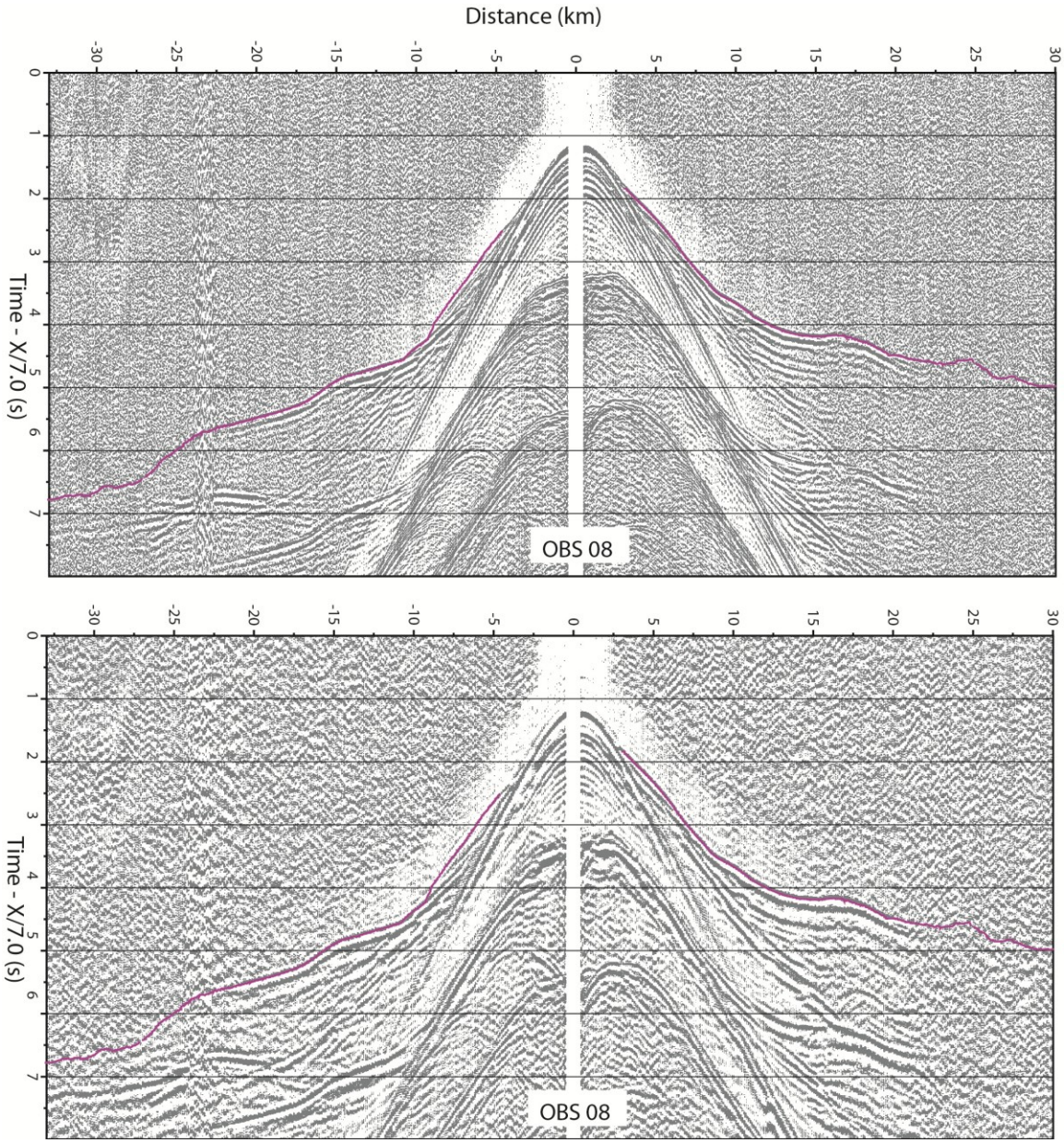

Figure C-10: OBS 08 vertical component with first-arrival travel-time picks. Top is processed with only a bandpass filter, AGC and gaining with offset; bottom is processed to suppress the previous shot noise using gapped deconvolution, coherency filtering, fx deconvolution, trace stacking, bandpass filtering, AGC and gaining with offset.

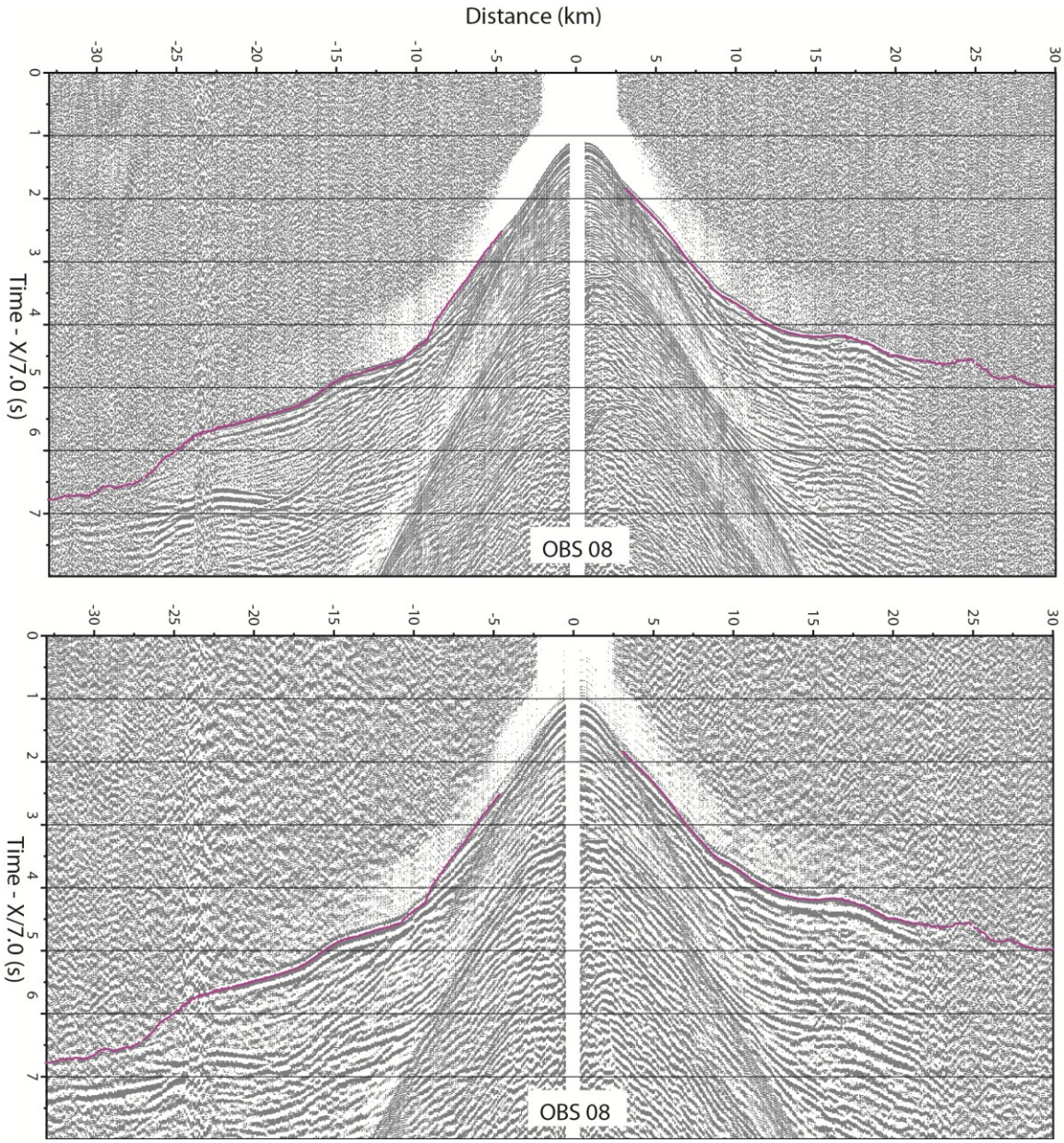

Figure C-11: OBS 08 hydrophone component with first-arrival travel-time picks. Top is processed with only a bandpass filter, AGC and gaining with offset; bottom is processed to suppress the previous shot noise using gapped deconvolution, coherency filtering, fx deconvolution, trace stacking, bandpass filtering, AGC and gaining with offset.

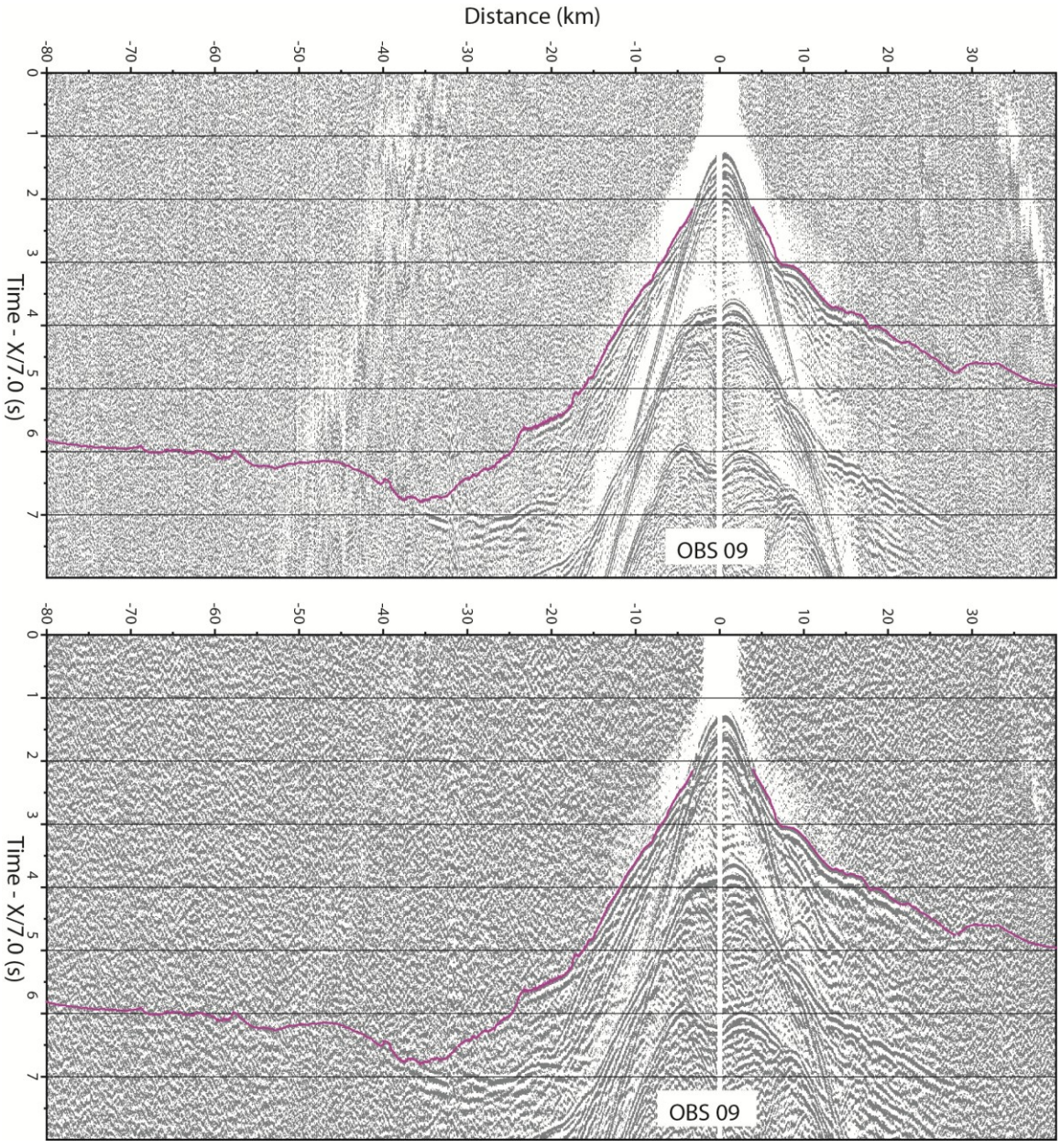

Figure C-12: OBS 09 vertical component with first-arrival travel-time picks. Top is processed with only a bandpass filter, AGC and gaining with offset; bottom is processed to suppress the previous shot noise using gapped deconvolution, coherency filtering, fx deconvolution, trace stacking, bandpass filtering, AGC and gaining with offset

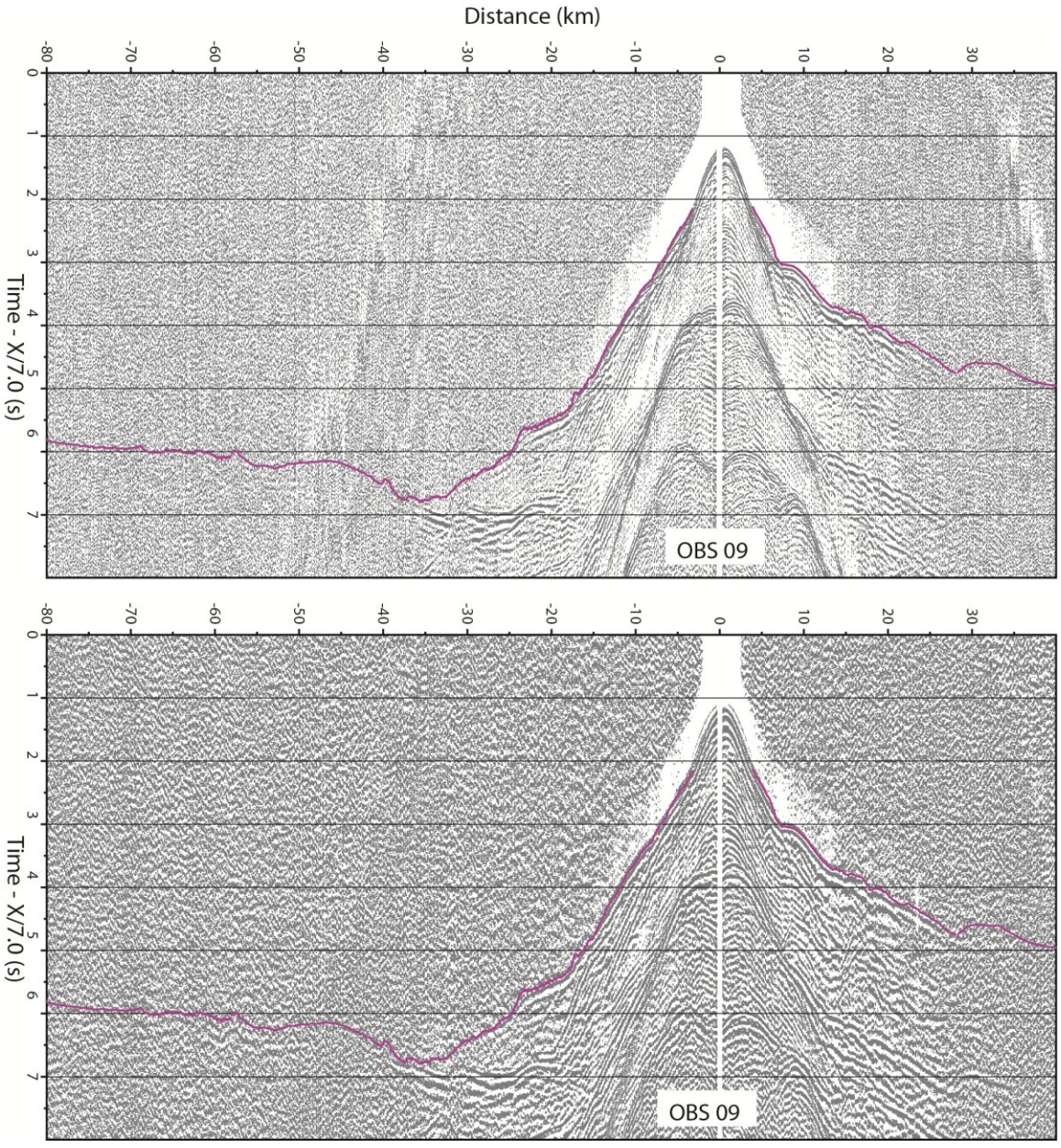

Figure C-13: OBS 09 hydrophone component with first-arrival travel-time picks. Top is processed with only a bandpass filter, AGC and gaining with offset; bottom is processed to suppress the previous shot noise using gapped deconvolution, coherency filtering, fx deconvolution, trace stacking, bandpass filtering, AGC and gaining with offset

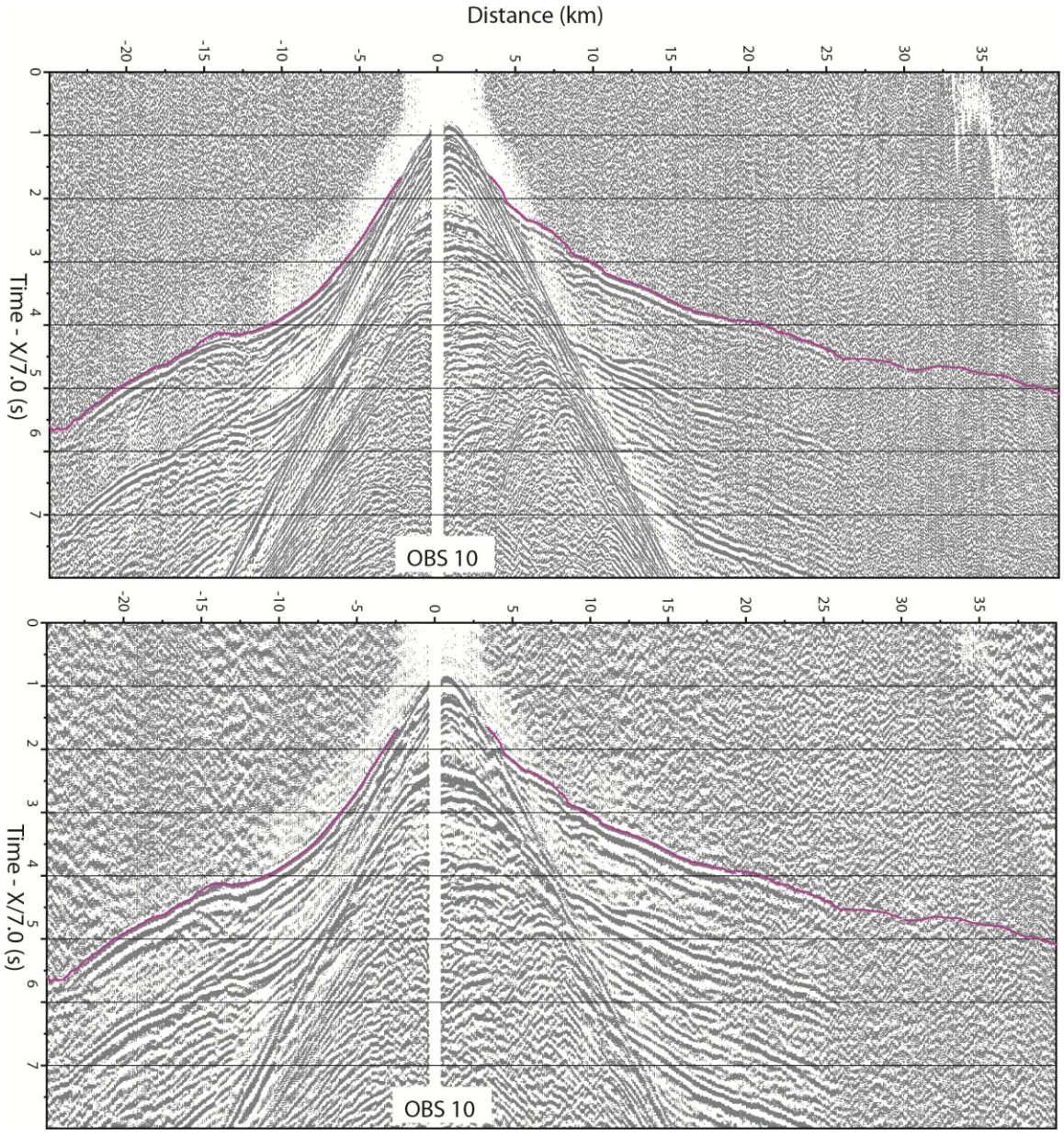

Figure D-14: OBS 10 vertical component with first-arrival travel-time picks. Top is processed with only a bandpass filter, AGC and gaining with offset; bottom is processed to suppress the previous shot noise using gapped deconvolution, coherency filtering, fx deconvolution, trace stacking, bandpass filtering, AGC and gaining with offset

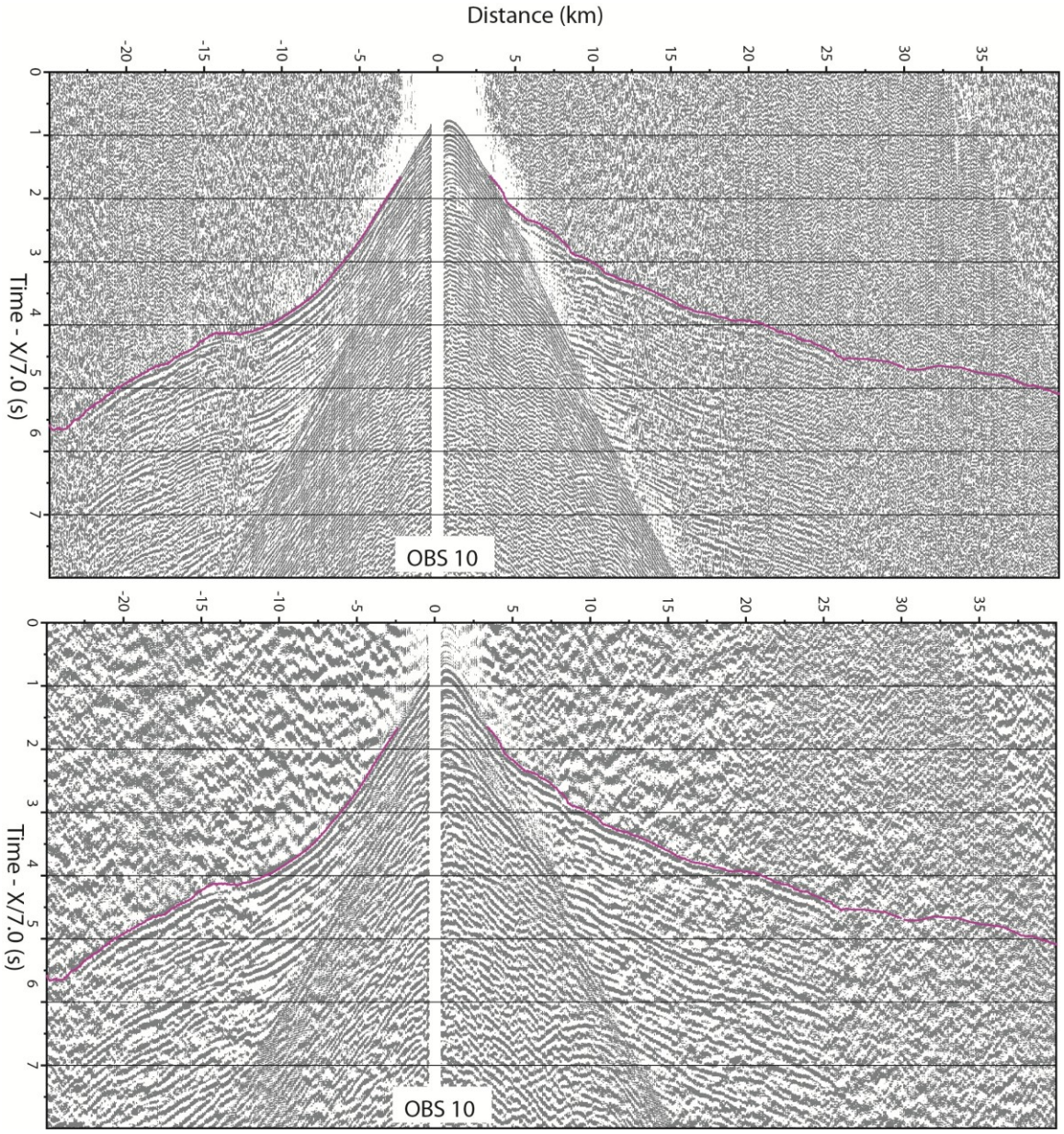

Figure D-15: OBS 10 hydrophone component with first-arrival travel-time picks. Top is processed with only a bandpass filter, AGC and gaining with offset; bottom is processed to suppress the previous shot noise using gapped deconvolution, coherency filtering, fx deconvolution, trace stacking, bandpass filtering, AGC and gaining with offset

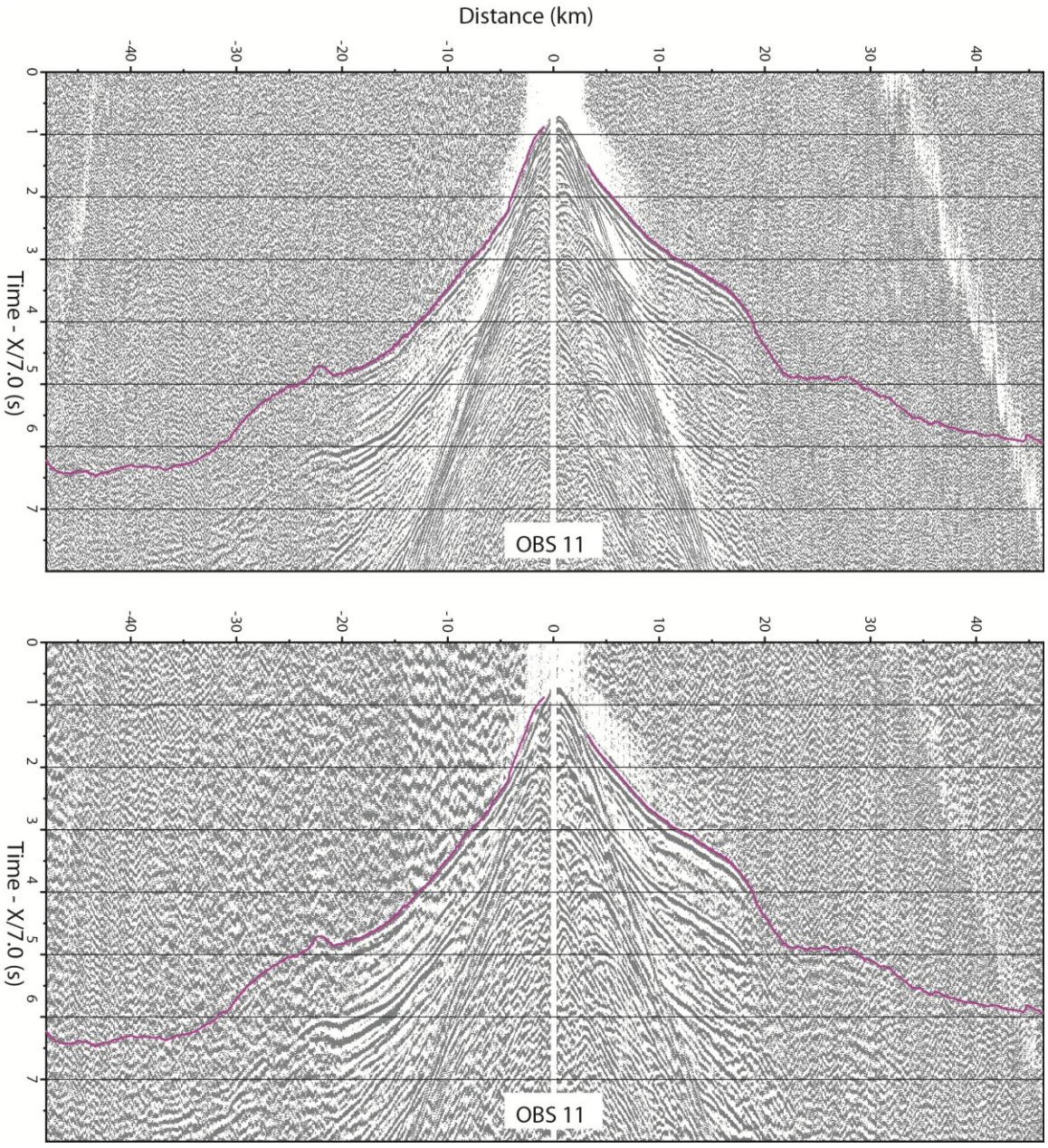

Figure C-16: OBS 11 vertical component with first-arrival travel-time picks. Top is processed with only a bandpass filter, AGC and gaining with offset; bottom is processed to suppress the previous shot noise using gapped deconvolution, coherency filtering, fx deconvolution, trace stacking, bandpass filtering, AGC and gaining with offset.

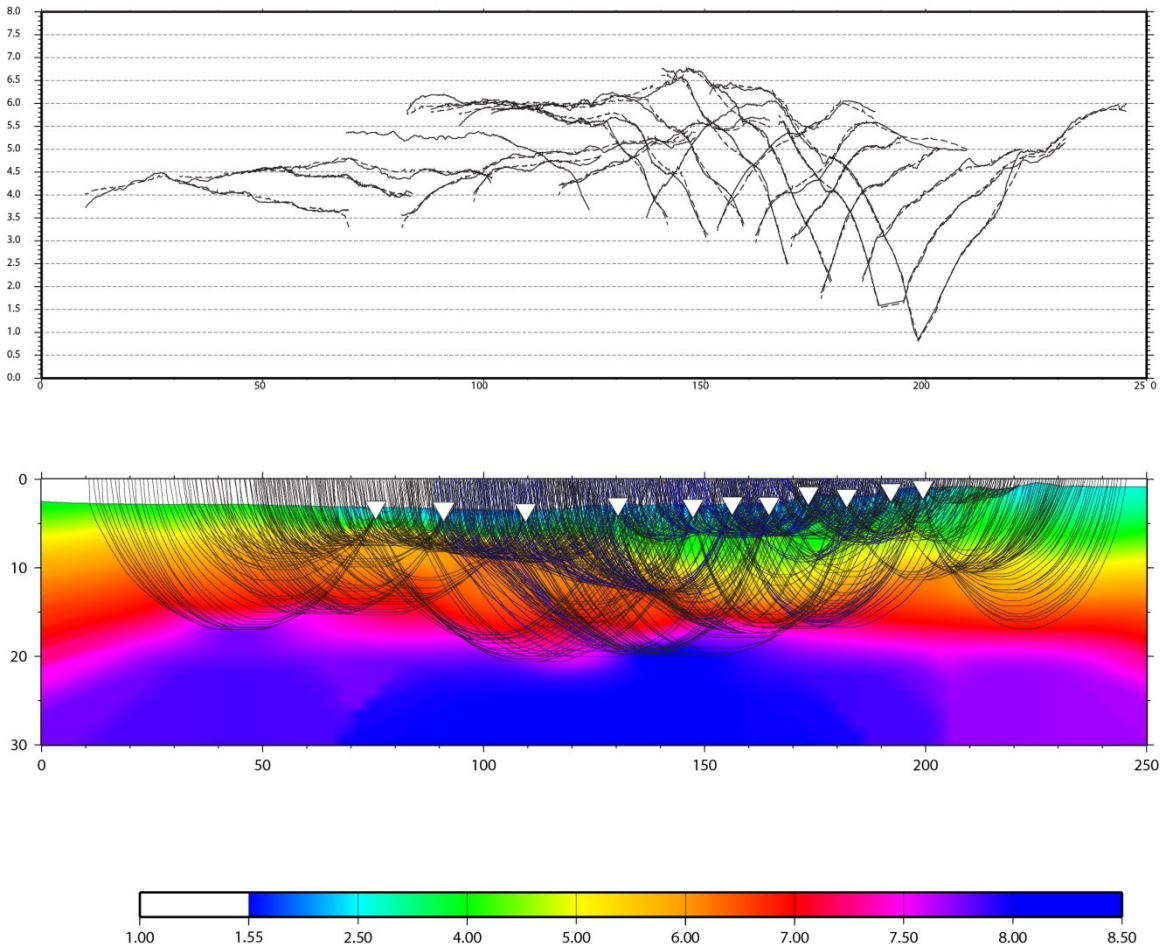

Figure C-17: Ray coverage of MGL0905_27 velocity model.

Appendix D: Numerical Modeling

A-1: Mechanical and Thermal Equilibrium

For each numerical time step, the modelling involves direct solution of the equation of motion for every grid point including the effects of inertia:

$$\frac{\partial \sigma_{ij}}{\partial x_j} - \rho g_i = \rho \frac{\partial v_i}{\partial t} \qquad (1)$$

where v_i is the velocity at each grid point, g_i is the acceleration due to gravity, ρ is the mass density and σ_{ij} is the stress in each grid element. In order to approximate quasi-static processes, the effects of inertia must be damped in a way akin to oscillations in a damped oscillator. Starting from a non-equilibrium state, the forces present at each grid point are summed ($f_i = \rho \delta v_i / \delta t$). The corresponding out-of-balance forces and the mass at the grid point give rise to acceleration. The accelerations are integrated to calculate the new velocities that are used to determine the incremental strain, ε_{ij} at each grid point. During a single time step, finite rotations also change the stress tensor, which is defined with respect to a fixed frame of reference. Before the incremental strains are determined, the stress tensor is updated to take these rotations into consideration as follows.

$$\sigma_{ij}^{new} = \sigma_{ij}^{old} + \left(\omega_{ik} \sigma_{kj} - \sigma_{ik} \omega_{kj} \right) \Delta t \qquad (2)$$

where Δt is the time step and ω_{ij} , the rotation per unit time, is given in terms of the velocity derivatives by

$$\omega_{ij} = \frac{1}{2}\left(\frac{\partial v_i}{\partial x_j} - \frac{\partial v_j}{\partial x_i} \right) \qquad (3)$$

By using the constitutive law for elastic, viscous and plastic rheologies, the corresponding stress increments are determined from the strain increments and the forces that they produce on the surrounding grid points are summed to determine the new out-of-balance forces and velocities. This dynamic response is then damped to approach a quasi-static equilibrium. FLAC is a very powerful technique for simulating non-linear rheological behaviour at relatively high resolution (the grid size is 1 km) because the explicit time-marching scheme does not require the storage of the large matrices that are needed for implicit methods. The time step of the calculation scales with the elastic-plastic property of our model. If the problem is purely elastic, the time step of the dynamic response scales with the velocity of the elastic wave propagating through the elements. This time step is of the order of a few hundredths of a second. Therefore, the resolution of the domains studied and the timescale needed for our numerical experiments would yield very long run times. In order to decrease the CPU time needed to perform the numerical experiments, we increase the speed of calculation by setting the boundary displacement per time step to a fraction of the grid spacing. To set the boundary displacement, we choose a ratio of boundary velocity to sound velocity of $10^{-6} – 10^{-5}$. We find that this ratio allows for fast enough runs and at the same time minimizes the error in the strain calculation.

This scheme models the evolution of the temperature as the model material deforms by using a Lagrangian formulation of the explicit finite difference method used in FLAC. For each time step, the flow of heat through each element is calculated using

Fourier's law. The corresponding energy is then summed and the temperature is calculated at each grid points using the energy equation:

$$\rho C_p \frac{\partial T}{\partial t} - \nabla.(kT) = H \qquad (4)$$

where T is the temperature, ρ is the density of the material, C_p is capacity calorific, k is the thermal conductivity tensor, and H is the heat production per unit volume.

A-2: RE-MESHING

The initial mesh of the model is made of quadrilaterals subdivided into two pairs of superimposed constant-strain triangular zones. The use of triangular zones eliminates the problem of "hour-glassing" deformation sometimes experienced in finite differences. Since this method is Lagrangian (i.e., the numerical grid follows the deformations), the simulation of large deformation (locally more than 50%) involves re-meshing to overcome the problem of degradation of numerical precision when elements are distorted. Re-meshing is triggered when one of the triangles in the grid elements are distorted enough that one of its angles becomes smaller than a given value. Every time re-meshing occurs, strains at each grid point are interpolated between the old deformed mesh and the new undeformed mesh using the barycentric coordinates of the nodes and Gauss points of the new elements in the old deformed mesh. The new state of strain is then used with the rheological laws to calculate the stress and resulting out-of-balance forces to start the time step cycle again. When re-meshing occurs, errors in the interpolation of the state variables result in an increase in the out-of-balance force, and artificial accelerations and oscillations may occur. For this reason the solution may not be in equilibrium

immediately after re-meshing. After testing different criteria to trigger re-meshing in order to reduce the oscillations, and a minimum angle of 15° was chosen before re-meshing of the grid.

A-3: PARTICLE TRACKING

Particles are distributed in the grid elements to guarantee that the boundary between the different physical phases in the model (i.e., quartz, plagioclase, olivine) do not diffuse at the time of re-meshing. These particles have both Eulerian and Lagrangian coordinates attached to the elements. When re-meshing occurs, their Eulerian and barycentric (Lagrangian) coordinates and their physical properties are registered in the old grid. When the new regular grid is formed the Eulerian coordinate of the particles are used to calculate the new barycentric coordinates of the particles in the new grid elements. Then the physical properties are then properly assigned with no spatial diffusion. These particles are also used to track the pressure, strain and temperature history of the different phased through the deformation history. New particles are added or destroyed when needed (i.e. when few particles populate one given grid element or when a particle falls out of the new mesh boundaries after re-meshing). Similar re-meshing techniques have been developed in previous work showing the efficiency of this method (*Babeyko and Sobolev*, 2008; *Burov and Yamato*, 2008; *Popov and Sobolev*, 2008)

A-4: RHEOLOGY

For ductile material, we use the Maxwell viscoelastic constitutive equations relating the deviatoric stresses to the deviatoric strains. In this formulation τ_M, the Maxwell time at which viscous deformation starts after a period of elastic strain accumulation, is defined as $t_M = 2\eta/E$ where E is the Young's modulus, η being the effective viscosity. The semi-brittle part of the crust is defined as a bi-mineralic rock with a strong phase (anorthosite) and a weak phase (quartz) (*Lavier and Manatschal*, 2006). We model semi-brittle fractures by the accumulation of strain (damage) in the middle crust. Where plastic strain accumulation occurs over a certain threshold, we assume that the shear zones become ductile by changing the rheology from that of anorthosite to quartz. Yield is initiated for an amount of work corresponding to 4.e6 J between temperatures of 300ºC and 450ºC corresponding to the onset of plasticity for quartz and the onset of plasticity for plagioclase (*Lavier and Manatschal*, 2006).

Since anorthosite is brittle for a temperature as high as 450°C, the middle crust is brittle at greenschist to amphibole facies condition, which corresponds to the initial temperature conditions in the crust in the Pyrenean-Bay of Biscay system. When strain (elasto-plastic or visco-elastic deformation) accumulates in the middle crust, we assume that a weak phase, chosen as wet quartz, replaces anorthosite in the shear fracture. Also, after the initiation of the fracture, for a small amount of elasto-plastic or ductile strain (3 %), we accumulate weak quartz in the fractured zone that will then flow in a visco-elastic (ductile) manner. This leads to the progressive formation of ductile shear zones in the models that act as semi-brittle fracture. This process is similar to what is described in the field for the formation and evolution of ductile shear zones (*Manktelow and Pennachioni, 2005*).

The main assumption of our models is that the type of fracture observed in the semi-brittle crust is resulting from the accumulation of plastic work (i.e. any inelastic work accumulated in the semi-brittle media). This can be brittle plastic or viscous strain accumulation. A simple yield criterion based on Freudhental's critical plastic work criterion (*Freudhental*, 1950) was used that depends on both the square root of the second invariant of stress, σ^{II} and strain, ε^{II} (also called Mises stress and strain) to simulate the formation of fracture as a function of plastic and viscous work (i.e. semi-brittle fracture):

$$\int_0^{\varepsilon_c} \sigma^{II} \varepsilon^{II} d\varepsilon = C \qquad (5)$$

Where ε_c is the critical strain at which fracture occurs and C is a constant set at 4.10^6 J to initiate semi-brittle fracture at high stresses, $\sigma^{II} = 4.10^8$ Pa for low strains (ε_c = 0.01) and at low stresses $\sigma^{II} = 4.10^6$ Pa for high strains (ε_c = 1). For this range of parameters, fracture can both initiate in the brittle crust for high stress environments and in the ductile crust for low stress environments. The goal of modeling here is to lend new insight into the evolution of deformation over thousands to millions of year. At this time scale nucleation of the shear zones is instantaneous and it can be assumed that the stresses are constant over the time of damage and nucleation. The yield criterion becomes:

$$\sigma^{II} \varepsilon_c = C$$
with
$$\varepsilon_c = \varepsilon_c^{elastoplastic} + \varepsilon_c^{viscoelastic} \qquad (6)$$

$\varepsilon^{elastoplastic} \approx \sigma^{II}_{Mohr} / E$ where σ^{II}_{Mohr} is the square root of second invariant of stress at the Mohr-Coulomb failure criteria and E is Young´s modulus. $\varepsilon^{viscoelastic} \approx \sigma^{II}_{creep} / C$ where

σ_{creep}^{II} is the square root of the second invariant of the dislocation creep yield stress and C the viscosity at the yield strength.

When assuming pressure dependent Mohr-Coulomb plastic behaviour for the brittle crust and viscous creep for the ductile crust, one can plot the yield stress envelope as a function of depth for a given geotherm in the classical Christmas tree shape (e.g., *Kholstedt, et al.,* 1995). The yield stress for semi-brittle fractures is dependent on critical work and accumulated strain. This principle of the yield stress envelope can be extended by plotting the ductile fracture criterion as yield stress as a function of total strain (Figure D-1). To have a consistent yield stress between Mohr-Coulomb, viscous creep and ductile fracture, the Mises stress, σ^{II} is calculated for Mohr Coulomb and viscous creep at yield. Mohr Coulomb shear stress, τ at yield is defined as:

$$\tau = \mu \sigma_n \tag{7}$$

Where σ_n is the normal stress, μ the friction coefficient. In 2D the second invariant of the stress at yield is defined as a function of the principal stresses as:

$$\sigma_{yield}^{II} = \sqrt{\sigma_1^{yield} \sigma_3^{yield}} \tag{8}$$

or as a function of shear stress at yield, with $\sigma_n = \frac{\sigma_1 + \sigma_3}{2}$ and $\tau = \frac{\sigma_1 - \sigma_3}{2}$.

$$\sigma_{yield}^{II} = \sqrt{\tau^2 \left(\frac{1-\mu}{\mu} \right)} \tag{9}$$

For viscous creep the second invariant at yield is defined as follow:

$$\sigma_{yield}^{II} = A^{\frac{1}{n}} \left(\dot{\varepsilon}^{II} \right)^{-\frac{1}{n}} e^{\frac{Q}{nRT}} \tag{10}$$

where A is the creep law pre-exponent, Q the activation energy, $\dot{\varepsilon}^{II}$ the square root of the second invariant of the strain rate, n the creep law exponent, R the gas constant and T the temperature. Finally, the yield for semi-brittle fracture is defined as:

$$\sigma^{II} = \frac{C}{\varepsilon^{II}} \qquad (11)$$

Figure D-1 is a plot of yield stresses as a function of depth for a friction coefficient of 0.6 and a dislocation creep law for plagioclase for a constant strain rate of $\dot{\varepsilon}^{II} = 10^{-14}$ s^{-1}, a linear geotherm of 13.3 °C/km (400 °C at 30 km depth) and $C = 4.10^6$ J, a value that corresponds to a yield at a stress of 400 MPa for a strain of 1%. The defined rheology develops quasi-static fractures or veins at or near the brittle ductile transition that coalesce into ductile shear zones. In the brittle part of the crust these zones form as shear fractures following the Mohr-Coulomb orientation for localization. In the ductile crust the fractures form in the direction of the minimum principal stress. Both types of fractures are then deforming in a ductile manner after a time, t_M corresponding to the initial elastic response of a Maxwell body.

A-5: MODELS

The PARAVOZ code (*Poliakov et al.*, 1993) was used for the modelling. This version is extended to account for energy conservation and particle phase and properties tracking to reduce phase boundary diffusion in between re-meshings after large amounts of deformation (*Lavier and Buck*, 2002; *Lavier and Manatschal*, 2006). Figure D-2 illustrates the model set-up. The model box size is 300 km deep and 1200 km wide. The grid size is 2x4 km in the low resolution parts of the models and set at 2x2 km in the area

where collision occurs. The initial geometry of the model is that of a low-resolution passive margin (to the left) and an oceanic plate (to the right). The continent (equivalent to Eurasia) is 400 km wide with a 30 km thick crust thinning to 12 km over 50 km. The transition from continent to ocean is defined as a zone of thin transitional crust (200 km x 8 km thick). A 400 m thick layer of sediments is covering the oceanic crust and a 4 km thick layer of sediments covers the margin.

A zone of pre-deformed and pre-weakened oceanic crust and mantle is set to the left of the arc to initiate subduction there. The thermal age is initially set by calculating a continental geotherm over the thickness of the lithosphere corresponding to a given age after the end of the last tectonic event (Lavier and Steckler, 1997). Eclogite transformation of the oceanic crust occurs when oceanic crust reaches the depth of 50 km. The density at 273°C of the oceanic crust is increased by 350 $Kg.m^{-3}$. Serpentinization of the mantle occurs when the subducting oceanic crust is in contact with the mantle at a depth lower than 50 km. The density at 273°C is then decreased by 300 $Kg.m^{-3}$. An algorithm then transforms 2 to 3 elements above the subducting oceanic crust to serpentinized mantle with a weak olivine rheology (we decrease the activation energy of dry olivine by one order of magnitude) and a lower density (Table D-1).

The collision is imposed kinematically by allowing flux of oceanic lithosphere at 5 cm yr-1 on the right side of the box. The flux at the bottom boundary is controlled by a Winkler foundation that simulates isostatic equilibrium. Table D-1 gathers the physical properties used to model the lithosphere. To localize deformation in the crust the friction coefficient is decrease from 0.6 to 0.1 and the cohesion from 44 to 4 MPa. The creep viscosities of the continental, oceanic crust and the lithospheric mantle are controlled by dislocation creep laws (equation 10).

Figures D-3 to D-5 show a more detailed evolution of the model presented in chapter 5. In addition to the phase field, the square root of the second invariant of the strain rate and the viscosity in the model are shown (Figures D-3 – D-5). Each field is overlaid by a contour-plot of the boundaries between the phases. The strain rate shows the evolution of the active fault during the formation of the rift and the wedge. The viscosity shows areas of elasto-plastic behavior (from red to green 10^{23} Pa.s) and visco-elastic behavior (from green to blue 10^{20} Pa.s). The bottom plot is the density in the whole models with the corresponding topography on top. Following the models of subduction previously developed with the same numerical technique (Gurnis et al., 2004), subduction is initiated and maintained by the presence of a very weak slab interface with a coefficient of friction less the 0.02.

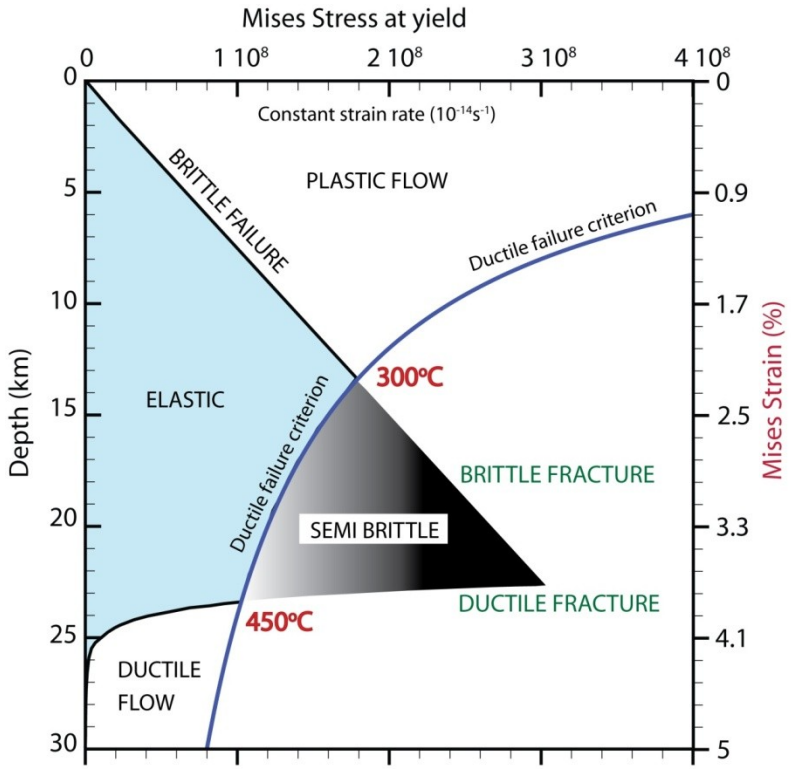

Figure D-1: The square root of the second invariant of the yield stress for Mohr-Coulomb, dislocation creep and semi-brittle fracture. The yield stress of the crust is not only dependent on the normal stress, temperature and strain rate but also on the second invariant of the strain at yield (elasto-plastic and visco-elastic) that is equivalent to a measure of damage in the rocks. The resulting deformation in the lithosphere is therefore dependent on the amount of damage accumulated in the middle to lower crust. This process must be facilitated by hydro-fracturing in the presence of aqueous fluid in the crust and lithosphere.

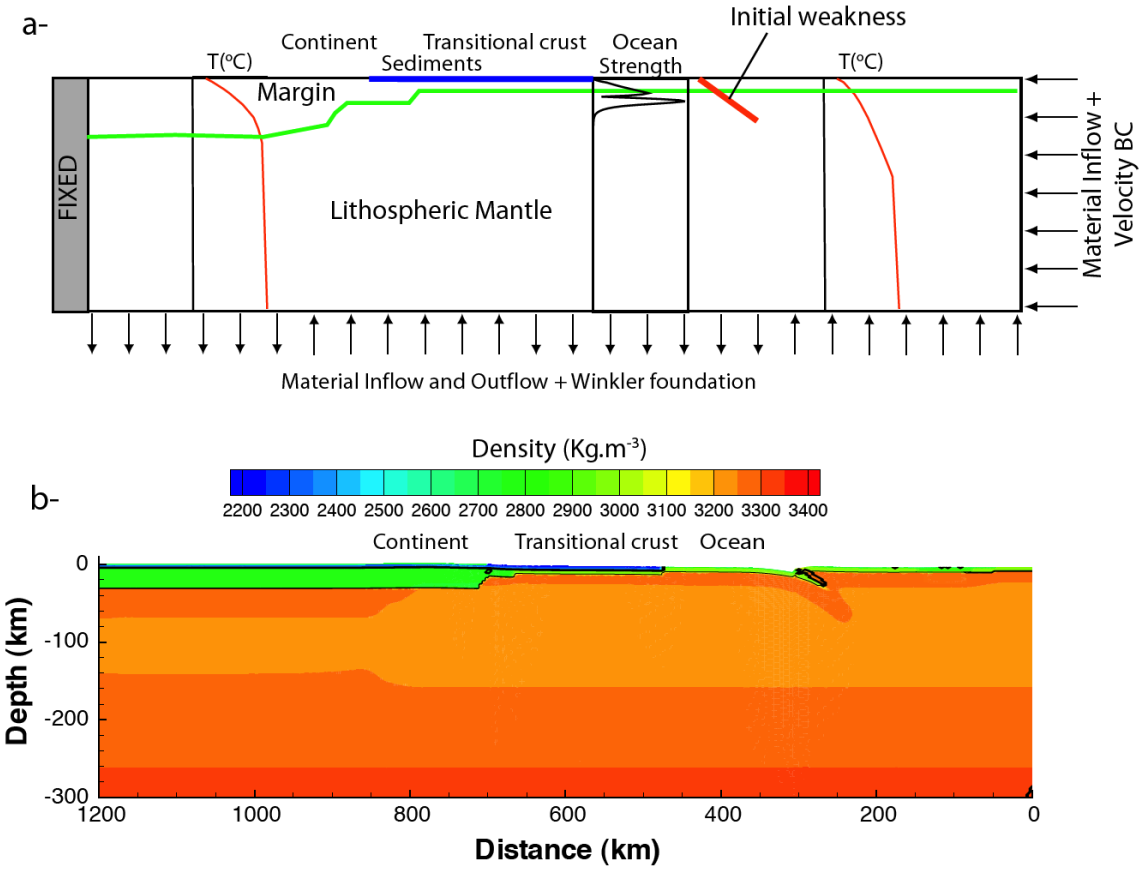

Figure D-2: The numerical code is an extended version of the model PARAVOZ (Yuri Podlatchikov, Alexei Poliakov) (Poliakov et al., 1993; Lavier and Buck, 2002; Lavier and Manatschal, 2006; Jammes et al, 2010) that contains Eulerian-Lagrangian particles to track phase boundaries of the material transported during the brittle and ductile processes simulated in the model.

Parameter	Symbol	Value			
Rheological parameters					
Friction coefficient	μ	0.6-0.3			
Cohesion		44MPa-4MPa			
Power-law exponent	A	*Crust: Quartz*[1] $5\ 10^{2}\ MPa^{-n}.s^{-1}$	*Crust:Plagioclase*[2] $3.3\ 10^{-4}\ MPa^{-n}.s^{-1}$	*Gabbroic lower crust*[1] $1.25\ 10^{-1}\ MPa^{-n}.s^{-1}$	*Mantle: Dry olivine*[1] $7\ 10^{4}\ MPa^{-n}.s^{-1}$
Activation energy	Q	$2\ 10^{5}\ J.mol^{-1}$	$2.38\ 10^{5}\ J.mol^{-1}$	$3.5\ 10^{5}\ J.mol^{-1}$	$5.2\ 10^{5}\ J.mol^{-1}$
Initial constant	n	3	3.2	3.05	3
Universal gas constant	R	$8.3144\ J.mol^{-1}.°C^{-1}$			
Thermal parameters					
Crustal conductivity		$2\ W^{-1}K^{-1}$			
Mantle conductivity		$3.3\ W^{-1}K^{-1}$			
Heat production crust		$10^{-9}W.Kg^{-1}$			
Moho temperature		500°C			
Asthenosphere temperature		1330°C			
Thermal expansion coefficient		$3.10^{-5}K^{-1}$			
Surface temperature		10°C			
Densities					
Crustal density at 273°C		$2800\ kg.m^{3}$			
Mantle lithosphere density at 273°C		$3300\ kg.m^{3}$			

[1](*Kirby and Kronenberg, 1987*)
[2](*Ranalli, 1995*)

Table D-1: Modeling parameters.

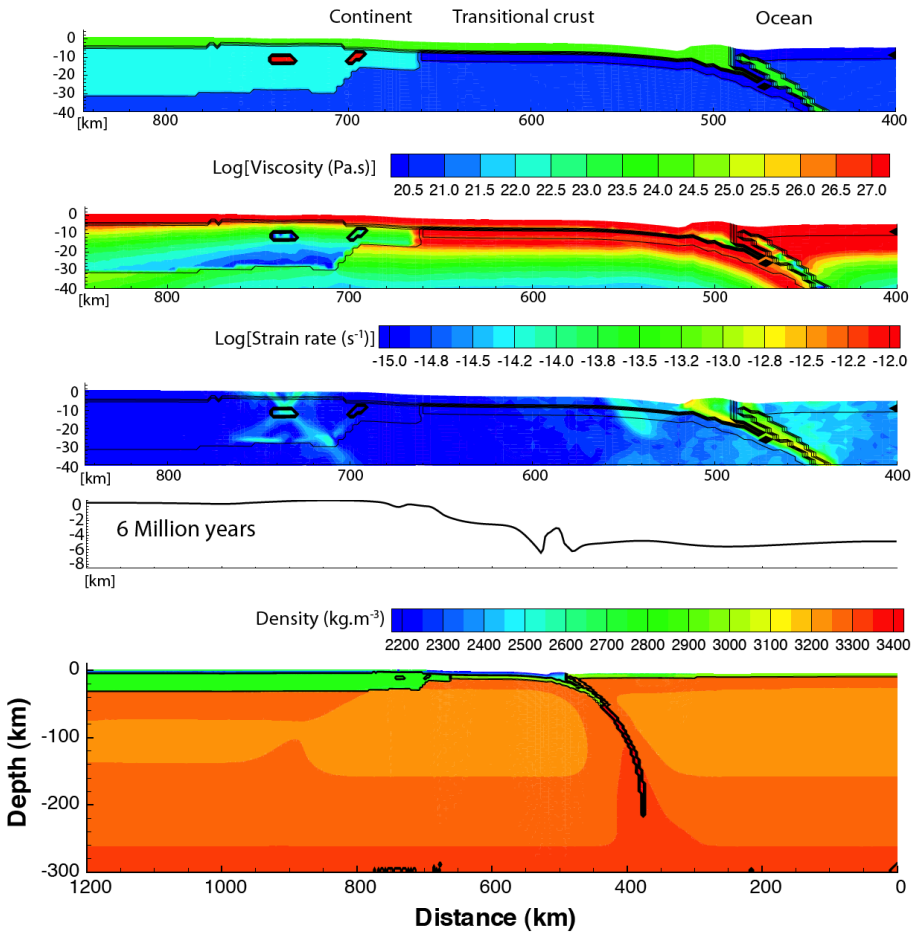

Figure D-3: Evolution of the subduction to collision after 6 million years.

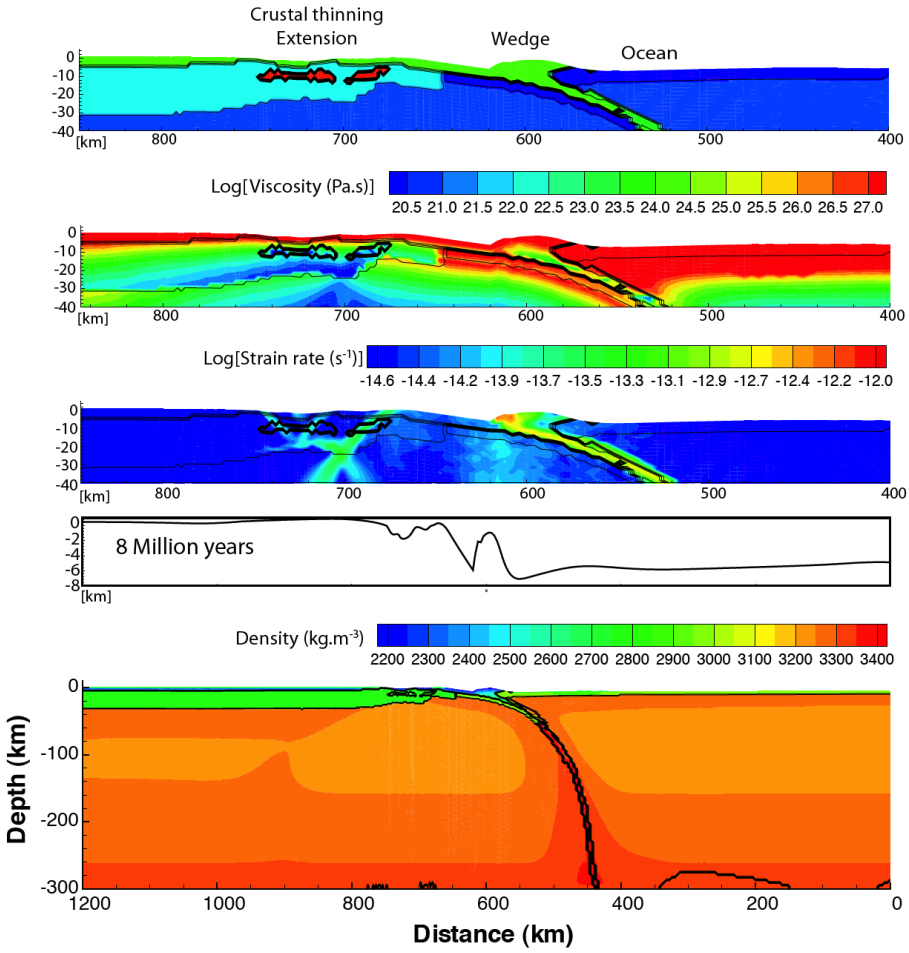

Figure D-4: Evolution of the subduction to collision after 8 million years.

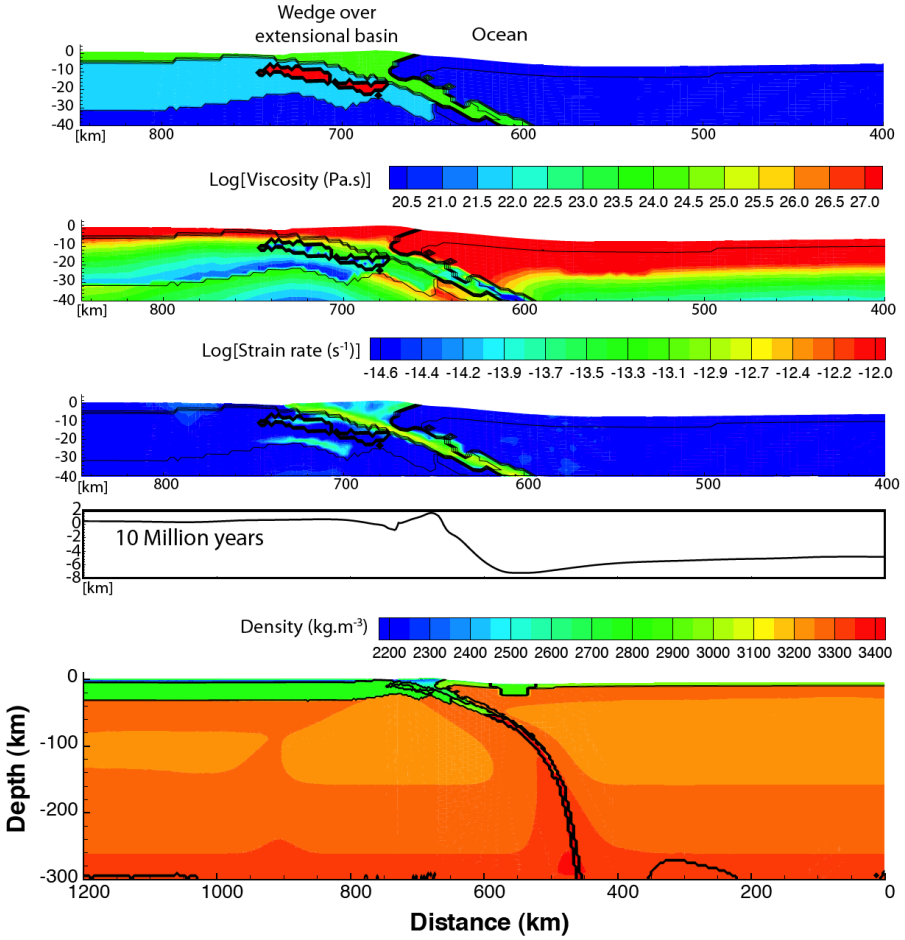

Figure D-5: Evolution of the subduction to collision after 10 million years.

References

Afonso, J. C., and S. Zlotnik (2011), The Subductability of Continental Lithosphere: The Before and After Story, in *Arc-Continent Collision*, edited, pp. 53-86, Springer Berlin Heidelberg.

Angelier, J., H.-T. Chu, and J.-C. Lee (1996), Shear concentration in a collision zone: kinematics of the Chihshang Fault as revealed by outcrop-scale quantification of active faulting, Longitudinal Valley, eastern Taiwan, *Tectonophysics*, *274*, 117-143.

Angelier, J., F. Bergerat, H. T. Chu, W. S. Juang, and C. Y. Lu (1990), Paleostress analysis as a key to margin extension: The Penghu Islands, South China Sea, *Tectonophysics*, *183*(1-4), 161-176.

Babeyko, A.Y. and S.V. Sobolev (2008), High-resolution numerical modeling of stress distribution in visco-elasto-plastic subducting slabs, *Lithos*, 103, 205-216.

Barckhausen, U., and H. A. Roeser (2004), Seafloor spreading anomalies in the South China Sea revisited, *Geophysical Monograph Series*, *149*, 121-125.

Beltrando, M., D. Rubatto, and G. Manatschal (2010), From passive margins to orogens: The link between ocean-continent transition zones and (ultra)high-pressure metamorphism, *Geology*, *38*(6), 559-562.

Berndt, C., and G. F. Moore (1999), Dependence of multiple-attenuation techniques on the geologic setting: A case study from offshore Taiwan, *The Leading Edge*, *18*, 74-80.

Bertrand, E., M. Unsworth, C.-W. Chiang, C.-S. Chen, C.-C. Chen, F. Wu, E. Turkoglu, H.-L. Hsu, and G. Hill (2009), Magnetotelluric evidence for thick-skinned tectonics in central Taiwan, *Geology*, *37*(8), 711-714.

Beyssac, O., M. Simoes, J. P. Avouac, K. A. Farley, Y.-G. Chen, Y.-C. Chan, and B. Goffé (2007), Late Cenozoic metamorphic evolution and exhumation of Taiwan, *Tectonics*, *26*(6), TC6001.

Bos, B., and C. J. Spiers (2002), Frictional-viscous flow of phyllosilicate-bearing fault rock: Microphysical model and implications for crustal strength profiles, *Journal of Geophysical Research: Solid Earth*, *107*(B2), ECV 1-1-ECV 1-13.

Boutilier, R. R., and C. E. Keen (1999), Small-scale convection and divergent plate boundaries, *Journal of Geophysical Research: Solid Earth*, *104*(B4), 7389-7403.

Bown, J. W., and R. S. White (1995), Effect of finite extension rate on melt generation at rifted continental margins, *Journal of Geophysical Research*, *100*, 18011-18029.

Brace, W. F., and D. L. Kohlstedt (1980), Limits on lithospheric stress imposed by laboratory experiments, *Journal of Geophysical Research: Solid Earth*, *85*(B11), 6248-6252.

Briais, A., P. Patriat, and P. tapponnierr (1993), Updated Interpretation of Magnetic Anomalies and Seafloor Spreading Stages in the South China Sea: Implications for the Tertiary Tectonics of Southeast Asia, *Journal of Geophysical Research*, *98*(B4), 6299-6328.

Burchfiel, B. C., Z. Chen, K. V. Hodges, Y. Liu, L. H. Royden, C. Deng, and J. Xu (1992), The South Tibetan detachment system, Himalayan Orogen; extension contemporaneous with and parallel to shortening in a collisional mountain belt, *Geological Society of America Special Papers*, *269*.

Burov E. and P. Yamato (2008), Continental plate collision, P-T-t-z conditions and unstable vs. stable plate dynamics: Insights from thermo-mechanical modelling, *Lithos* 103, 178-204.

Byrne, T. B., and C.-S. Liu (2002), Preface: Introduction to the geology and geophysics of Taiwan, in *Geology and Geophysics of an Arc-Continent Collision, Taiwan*, edited by T. B. Byrne and C.-S. Liu, pp. i-iv, The Geological Society of America.

Carena, S., J. Suppe, and H. Kao (2002), Active detachment of Taiwan illuminated by small earthquakes and its control of first-order topography, *Geology*, *30*(10), 935-938.

Cavinato, G. P., and P. G. De Celles (1999), Extensional basin in the tectonically bimodal central Apennines fold-thrust belt, Italy: Response to corner flow above a subducting slab in retrograde motion, *Geology*, *27*, 955-958.

Chamot-Rooke, N., and X. Le Pichon (1999), GPS determined eastward Sundaland motion with respect to Eurasia, confirmed by earthquakes slip vectors at Sunda and Philippine trenches, *Earth and Planetary Science Letters*, *173*, 439-455.

Chang, C.-P., J. Angelier, T.-Q. Lee, and C.-Y. Huang (2003), From continental margin extension to collision orogen: structural development and tectonic rotation of the Hengchun peninsula, southern Taiwan, *Tectonophysics*, *361*, 61-82.

Chemenda, A. I., R. K. Yang, C.-H. Hsieh, and A. L. Groholsky (1997), Evolutionary model for the Taiwan collision based on physical modelling, *Tectonophysics*, *274*, 253-274.

Cheng, W. B. (2008), Tomographic imaging of the convergent zone in Eastern Taiwan - A subducting forearc sliver revealed?, *Tectonophysics*.

Chi, W.-C., D. L. Reed, G. Moore, T. Nguyen, C.-S. Liu, and N. Lundberg (2003), Tectonic wedging along the rear of the offshore Taiwan accretionary prism, *Tectonophysics*, *374*, 199-217.

Chou, Y.-W., and H.-S. Yu (2002), Structural expressions of flexural extension in the arc-continent collisional foredeep of western Taiwan, in *Geology and Geophysics of an Arc-Continent Collision, Taiwan*, edited by T. B. Byrne and C.-S. Liu, pp. 1-12, Geological Society of London Special Publication.

Christeson, G. L., Y. Nakamura, K. D. McIntosh, and P. L. Stoffa (1996), Effect of shot interval on ocean bottom seismograph and hydrophone data, *Geophys. Res. Lett.*, *23*(25), 3783-3786.

Christeson, G. L., K. D. McIntosh, T. H. Shipley, E. R. Flueh, and H. Goedde (1999), Structure of the Costa Rica convergent margin, offshore Nicoya Peninsula, *J. Geophys. Res.*, *104*(B11), 25443-25468.

Chung, S.-L., and S.-s. Sun (1992), A new genetic model for the East Taiwan Ophiolite and its implications for Dupal domains in the Northern Hemisphere, *Earth and Planetary Science Letters*, *109*, 133-145.

Chung, S.-L., S.-s. Sun, K. Tu, C.-H. Chen, and C.-y. Lee (1994), Late Cenozoic basaltic volcanism around the Taiwan Strait, SE China: Product of lithosphere-asthenosphere interaction during continental extension, *Chemical Geology*, *112*(1), 1-20.

Chung, S.-L., B.-M. Jahn, S.-J. Chen, T. Lee, and C.-H. Chen (1995), Miocene basalts in northwestern Taiwan: Evidence for EM-type mantle sources in the continental lithosphere, *Geochimica et Cosmochimica Acta*, *59*(3), 549-555.

Clark, M. B., D. M. Fisher, C.-Y. Lu, and C.-H. Chen (1993), Kinematic analyses of the Hsuehshan Range, Taiwan: A large-scale pop-up structure, *Tectonics*, *12*(1), 205-217.

Clift, P., and J. Lin (2001), Preferential mantle lithospheric extension under the South China margin, *Marine and Petroleum Geology*, *18*, 929-945.

Clift, P., G. H. Lee, N. Anh Duc, U. Barckhausen, H. Van Long, and S. Zhen (2008a), Seismic reflection evidence for a Dangerous Grounds miniplate: No extrusion origin for the South China Sea, *Tectonics*, *27*(3), TC3008.

Clift, P., A. T. S. Lin, A. Carter, F. Wu, A. E. Draut, T.-H. Lai, L.-Y. Fei, H. Schouten, and L. Teng (2008b), Post-collisional collapse in the wake of migrating arc-continent collision in the Ilan Basin, Taiwan, in *SPE436: Formation and Applications of the Sedimentary Record in Arc Continent Collision Zones*, edited by A. E. Draut, P. D. Clift and D. W. Scholl, Geological Society of America.

Clift, P. D., J. Lin, and P. Odp Leg 184 Scientific (2001), Patterns of extension and magmatism along the continent-ocean boundary, South China margin, *Geological Society, London, Special Publications*, *187*(1), 489-510.

Crespi, J. M., Y.-C. Chan, and M. S. Swaim (1996), Synorogenic extension and exhumation of the Taiwan hinterland, *Geology*, *24*, 247-250.

Dadson, S. J., et al. (2003), Links between erosion, runoff variability and seismicity in the Taiwan orogen, *Nature*, *426*, 648-651.

Davis, D., J. Suppe, and F. A. Dahlen (1983), Mechanics of Fold-and-Thrust Belts and Accretionary Wedges, *Journal of Geophysical Research*, *88*(B2), 1153-1172.

Deschamps, A. E., S. E. Lallemand, and J.-Y. Collot (1998), A detailed study of the Gagua Ridge: A fracture zone uplifted during a plate reorganisation in the Mid-Eocene, *Marine Geophysical Researches*, *20*, 403-423.

Fisher, D. M., C.-Y. Lu, and H.-T. Chu (2002), Taiwan Slate Belt: Insights into the ductile interior of an arc-continent collision, in *Geology and Geophysics of an Arc-Continent Collision, Taiwan*, edited by T. B. Byrne and C.-S. Liu, Geological Society of America.

Flower, M. F. J., M. Zhang, C.-Y. Chen, K. Tu, and G. Xie (1992), Magmatism in the South China Basin: 2. Post-spreading Quaternary basalts from Hainan Island, south China, *Chemical Geology*, *97*(1–2), 65-87.

Font, Y., C.-S. Liu, P. Schnurle, and S. Lallemand (2000), Constraints on backstop geometry of the southwest Ryukyu subduction based on reflection seismic data, *Tectonophysics*, *333*, 135-158.

Franke, D. (2012), Rifting, lithosphere breakup and volcanism: Comparison of magma-poor and volcanic rifted margins, *Marine and Petroleum Geology*.

Franke, D., U. Barckhausen, N. Baristeas, M. Engels, S. Ladage, R. Lutz, J. Montano, N. Pellejera, E. G. Ramos, and M. Schnabel (2011), The continent-ocean transition at the southeastern margin of the South China Sea, *Marine and Petroleum Geology*, *28*(6), 1187-1204.

Freudenthal, A.M. (1950), The inelastic behaviour of engineering materials and structures, in *Journal of the Franklin Institute*, edited by John Wiley, pp. 584-585.

Fuller, C. W., S. D. Willett, D. Fisher, and C. Y. Lu (2006), A thermomechanical wedge model of Taiwan constrained by fission-track thermochronometry, *Tectonophysics*(425), 1-24.

Funck, T., H. R. Jackson, K. E. Louden, S. A. Dehler, and Y. Wu (2004), Crustal structure of the northern Nova Scotia rifted continental margin (eastern Canada), *Journal of Geophysical Research: Solid Earth*, *109*(B9), B09102.

Gao, S., R. L. Rudnick, R. W. Carlson, W. F. McDonough, and Y.-S. Liu (2002), Re–Os evidence for replacement of ancient mantle lithosphere beneath the North China craton, *Earth and Planetary Science Letters*, *198*(3), 307-322.

Goetze, C., and B. Evans (1979), Stress and temperature in the bending lithosphere as constrained by experimental rock mechanics, *Geophysical Journal of the Royal Astronomical Society*, *59*(3), 463-478.

Griffin, W. L., Z. Andi, S. Y. O'Reilly, and C. G. Ryan (1998), Phanerozoic evolution of the lithosphere beneath the Sino-Korean Craton, *Geodynamics Series*, *27*, 107-126.

Gurnis, M., Lavier, L.L. and C. Hall, Evolving force balance during incipient subduction, *Geochem., Geophys., Geosys*., 5(7).

Hall, R. (2002), Cenozoic geological and plate tectonic evolution of SE Asia and the SW Pacific: computer-based reconstructions, model and animations, *Journal of Asian Earth Sciences*, *20*, 353-431.

Hamilton, W. (1979), *Tectonics of the Indonesian region*, 345 pp., U.S. Geological Survey Professional Paper.

Hayes, D. E., S. S. Nissen, P. Buhl, J. Diebold, Y. Bochu, Z. Weijun, and C. Yongqin (1995), Throughgoing crustal faults along the northern margin of the South China Sea and their role in crustal extension, *Journal of Geophysical Research*, *100*(B11), 22,435-422,446.

Ho, C.-S. (1988), *An introduction to the geology of Taiwan: explanatory text of the geologic map of Taiwan*, Central Geological Survey, Ministry of Economic Affairs.

Ho, C. S. (1986), A Synthesis of the Geologic Evolution of Taiwan, *Tectonophysics*, *125*, 1 -16.

Holloway, N. H. (1982), North Palawan Block, Philippines - Its Relation to Asian Mainland and Role in Evolution of South China Sea, *AAPG Bulletin*, *66*, 1355-1383.

Hopper, J. R., T. Dahl-Jensen, W. S. Holbrook, H. C. Larsen, D. Lizarralde, J. Korenaga, G. M. Kent, and P. B. Kelemen (2003), Structure of the SE Greenland margin from seismic reflection and refraction data: Implications for nascent spreading center subsidence and asymmetric crustal accretion during North Atlantic opening, *Journal of Geophysical Research: Solid Earth*, *108*(B5), 2269.

Hsu, S.-K., J.-C. Sibuet, and C.-T. Shyu (2001), Magnetic inversion in the East China Sea and Okinawa Trough: tectonic implications, *Tectonophysics*, *333*, 111-122.

Hsu, S.-K., Y.-C. Yeh, W.-B. Doo, and C.-H. Tsai (2004), New bathymetry and magnetic lineations identifications in the northernmost South China Sea and their tectonic implications, *Marine Geophysical Researches*, *25*, 29-44.

Hu, D., D. Zhou, X. Wu, M. He, X. Pang, and Y. Wang (2009), Crustal structure and extension from slope to deepsea basin in the northern South China Sea, *Journal of Earth Science*, *20*(1), 27-37.

Huang, C.-Y., P. B. Yuan, and S.-J. Tsao (2006), Temporal and spatial records of active arc-continent collision in Taiwan: A synthesis, *Geological Society of America Bulletin*, *118*(3-4), 274-288.

Huang, C.-Y., P. B. Yuan, C.-W. Lin, T. K. Wang, and C.-P. Chang (2000), Geodynamic processes of Taiwan arc-continent collision and comparison with analogs in Timor, Papua New Guinea, Urals and Corsica, *Tectonophysics*, *325*, 1-21.

Huang, C.-Y., W.-Y. Wu, C.-P. Chang, S. Tsao, P. B. Yuan, C.-W. Lin, and X. Kuan-Yuan (1997), Tectonic evolution of accretionary prism in the arc-continent collision terrane of Taiwan, *Tectonophysics*, *281*, 31-51.

Huang, C., D. Zhou, Z. Sun, C. Chen, and H. Hao (2005), Deep crustal structure of Baiyun Sag, northern South China Sea revealed from deep seismic reflection profile, *Chinese Science Bulletin*, *50*(11), 1131-1138.

Huang, Z., W. Su, Y. Peng, Y. Zheng, and H. Li (2003), Rayleigh wave tomography of China and adjacent regions, *Journal of Geophysical Research: Solid Earth*, *108*(B2), 2073.

Huismans, R., and C. Beaumont (2011), Depth-dependent extension, two-stage breakup and cratonic underplating at rifted margins, *Nature*, 473(7345), 74-78.

Hung, J.-H., D. V. Wiltschko, H.-C. Lin, J. B. Hickman, P. Fang, and Y. Bock (1999), Structure and Motion of the Southwestern Taiwan Fold and Thrust Belt, *TAO*, *10*(3), 543-568.

Jammes, S., G. Manatschal, L. Lavier, and E. Masini (2009), Tectonosedimentary evolution related to extreme crustal thinning ahead of a propagating ocean: Example of the western Pyrenees, *Tectonics*, *28*(4).

Jammes, S., L. Lavier, G. Manatschal., Extreme crustal thinning of the Bay of Biscay and Western Pyrenees: From observations to modeling, *Geochem., Geophys., Geosys,* 11(10).

Johnson, K. M., P. Segall, and S. B. Yu (2005), A viscoelastic earthquake cycle model for Taiwan, *Journal of Geophysical Research*, *110*(B10).

Kao, H., Sern-su, J. Shen, and K.-F. Ma (1998), Transition from oblique subduction to collision: Earthquakes in the southernmost Ryukyu arc-Taiwan region, *Journal of Geophysical Research*, *103*(B4), 7211-7229.

Kirby, S.H. and A.K. Kronenberg (1987), Rheology of the lithosphere: Selected topics, *Rev. Geophys.*, 25, 1219-1244.

Klingelhoefer, F., T. Berthet, S. Lallemand, P. Schnurle, C.-S. Lee, C.-S. Liu, K. McIntosh, and T. Theunissen (2011), P-wave Velocity structure of the southern Ryukyu margin east of Taiwan: results from the ACTS wide-angle seismic experiment, *Tectonophysic*.

Kohlstedt, D.L., B. Evans, and S.J. Mackwell (1995), Strength of the lithosphere: Constraints imposed by laboratory experiments, *Journal of Geophysical Research*, 100(B9)

Kopp, H., and N. Kukowski (2003), Backstop geometry and accretionary mechanics of the Sunda margin, *Tectonics*, *22*(6), 1072.

Korenaga, J., W. S. Holbrook, G. M. Kent, P. B. Kelemen, R. S. Detrick, H. C. Larsen, J. R. Hopper, and T. Dahl-Jensen (2000), Crustal structure of the southeast Greenland margin from joint refraction and reflection seismic tomography, *Journal of Geophysical Research: Solid Earth*, *105*(B9), 21591-21614.

Kuo-Chen, H., F. T. Wu, and S. W. Roecker (2012), Three-dimensional P velocity structures of the lithosphere beneath Taiwan from the analysis of TAIGER and related seismic data sets, *J. Geophys. Res.*, *117*(B6), B06306.

Lacombe, O., and F. Mouthereau (2002), Basement-involved shortening and deep detachment tectonics in forelands of orogens: Insights from recent collision belts (Taiwan, Western Alps, Pyrenees), *Tectonics*, *21*(4), 1030.

Lallemand, S., Y. Font, H. Bijwaard, and H. Kao (2001), New insights on 3-D plates interaction near Taiwan from tomography and tectonic implications, *Tectonophysics*, *335*, 229-253.

Lavier, Luc L., Michael S. Steckler, and Frederic Brigaud, Climatic and tectonic control on the Cenozoic evolution of the West African margin, *Marine Geology*, 178)1_, 63-80.

Lavier, L.L. and W.R. Buck (2002), Half graben versus large-offset low-angle normal fault: Importance of keeping cool during normal faulting, *Journal of Geophysical Research*, 107(B6).

Lavier, L. L., and G. Manatschal (2006), A Mechanism to Thin the Continental Lithosphere at Magma-Poor Margins, *Nature*, *440*(16), 324-328.

Lee, C.-I., Y.-L. Chang, and M. P. Coward (2002), Inversion tectonics of the fold-and-thrust belt, western Taiwan, in *Geology and Geophysics of an Arc-Continent Collision, Taiwan*, edited by T. B. Byrne and C.-S. Liu, pp. 13-30, Geological Society of America.

Lee, J.-C., J. Angelier, and H.-T. Chu (1997), Polyphase history and kinematics of a complex major fault zone in the northern Taiwan mountain belt: the Lishan Fault, *Tectonophysics*, *274*, 97-115.

Lee, T.-Y., and L. A. Lawver (1994), Cenozoic Plate Reconstruction of the South China Sea Region, *Tectonophysics*, *235*(1-2), 149-180.

Lee, T.-Y., C.-H. Tang, J.-S. Ting, and Y.-Y. Hsu (1993), Sequence stratigraphy of the Tainan Basin, offshore southwestern Taiwan, *Petroleum Geology of Taiwan*, *28*, 119-158.

Lee, Y.-H., C.-C. Chen, T.-K. Liu, H.-C. Ho, H.-Y. Lu, and W. Lo (2006), Mountain building mechanisms in the Southern Central Range of the Taiwan Orogenic Belt - From accretionary wedge deformation to arc-continental collision, *Earth and Planetary Science Letters*, *252*, 413-422.

Lester, R., and K. McIntosh (2012), Multiple attenuation in crustal-scale imaging: examples from the TAIGER marine reflection data set, *Marine Geophysical Research*, 1-17.

Lester, R., L. L. Lavier, K. McIntosh, H. J. A. Van Avendonk, and F. Wu (2012), Active extension in Taiwan's precollision zone: A new model of plate bending in continental crust, *Geology*, *40*(9), 831-834.

Li, C.-F., Z. Zhou, J. Li, H. Hao, and J. Geng (2007), Structures of the northeasternmost South China Sea continental margin and ocean basin: geophysical constraints and tectonic implications, *Marine Geophysical Researches*, *28*(1), 59-79.

Li, P., and C. Rao (1994), Tectonic characteristics and evolution history of the Pearl river mouth basin, *Tectonophysics*, *235*(1), 13-25.

Li, S., W. D. Mooney, and J. Fan (2006), Crustal structure of mainland China from deep seismic sounding data, *Tectonophysics*, *420*(1) 239-252.

Li, Z.-X., and X.-H. Li (2007), Formation of the 1300-km-wide intracontinental orogen and postorogenic magmatic province in Mesozoic South China: A flat-slab subduction model, *Geology*, *35*(2), 179-182.

Lin, A. T., and A. B. Watts (2002), Origin of the West Taiwan basin by orogenic loading and flexure of a rifted continental margin, *Journal of Geophysical Research*, *107*(B9).

Lin, A. T., A. B. Watts, and S. P. Hesselbo (2003), Cenozoic stratigraphy and subsidence history of the South China Sea margin in the Taiwan region, *Basin Research*, *15*, 453-478.

Lin, A. T., B. Yao, S.-K. Hsu, C.-S. Liu, and C.-Y. Huang (2009), Tectonic features of the incipient arc-continent collision zone of Taiwan: Implications for seismicity, *Tectonophysics*, *479*(1), 28-42.

Lin, A. T., C.-S. Liu, C.-C. Lin, P. Schnurle, G.-Y. Chen, W.-Z. Liao, L. S. Teng, H.-J. Chuang, and M.-S. Wu (2008), Tectonic features associated with the overriding of an accretionary wedge on top of a rifted continental margin: An example from Taiwan, *Marine Geology*, *255*(3), 186-203.

Lin, J.-Y., J.-C. Sibuet, C.-S. Lee, S.-K. Hsu, and F. Klingelhoefer (2007), Origina of the southern Okinawa Trough volcanism from detailed seismic tomography, *Journal of Geophysical Research*, *112*(B08).

Liu, C.-S., I. L. Huang, and L. S. Teng (1997), Structural features off southwestern Taiwan, *Marine Geology*, *137*, 305-319.

Liu, M., X. Cui, and F. Liu (2004), Cenozoic rifting and volcanism in eastern China: a mantle dynamic link to the Indo-Asian collision?, *Tectonophysics*, *393*(1), 29-42.

Liu, T.-K., S. Hsieh, Y.-G. Chen, and W.-S. Chen (2001), Thermo-kinematic evolution of the Taiwan oblique-collision mountain belt as revealed by zircon fission track dating, *Earth and Planetary Science Letters*, *186*, 45-56.

Louden, K. E. (1980), The Crustal and Lithospheric Thicknesses of the Philippine Sea as Compared to the Pacific, *Earth and Planetary Science Letters*, *50*, 275-288.

Ludmann, T., and H. K. Wong (1999), Neotectonic Regime on the Passive Continental Margin of the Northern South China Sea, *Tectonophysics*, *311*(1-4), 113-138.

Lundberg, N., and R. J. Dorsey (1990), Rapid Quaternary emergence, uplift, and denudation of the Coastal Range, eastern Taiwan, *Geology*, *18*, 638-641.

Lundberg, N., D. L. Reed, C.-S. Liu, and J. Jay Lieske (1997), Forearc-basin closure and arc accretion in the submarine suture zone south of Taiwan, *Tectonophysics*, *274*, 5-23.

Malavieille, J., and G. Trullenque (2009), Consequences of continental subduction on forearc basin and accretionary wedge deformation in SE Taiwan: Insights from analogue modeling, *Tectonophysics*, *466*, 377-394.

Malavieille, J., S. E. Lallemand, S. Dominguez, A. Deschamps, C.-Y. Lu, C.-S. Liu, P. Schnurle, and A. S. Crew (2002), Arc-continent collision in Taiwan: New marine observations and tectonic evolution, in *Geology and Geophysics of an Arc-Continent Collision, Taiwan*, edited by T. B. Byrne and C.-S. Liu, pp. 187-211, Geological Society of America.

Manatschal, G. (2004), New models for evolution of magma-poor rifted margins based on a review of data and concepts from West Iberia and the Alps, *Int J Earth Sci (Geol Rundsch)*, *93*(3), 432-466.

Mancktelow, N. S. (1992), Neogene lateral extension during convergence in the Central Alps: Evidence from interrelated faulting and backfolding around the Simplonpass (Switzerland), *Tectonophysics*, *215*, 295-317.

Mancktelow, N. S., and G. Pennacchioni (2005), The control of precursor brittle fracture and fluid–rock interaction on the development of single and paired ductile shear zones, *Journal of Structural Geology*, *27*(4), 645-661.

McBride, J. H., R. S. White, J. R. Smallwood, and R. W. England (2004), Must magmatic intrusion in the lower crust produce reflectivity?, *Tectonophysics*, *388*(1–4), 271-297.

McIntosh, K., e. Silver, and T. Shipley (1993), Evidence and mechanisms for forearc extension at the accretionary Costa Rica Convergent Margin, *Tectonics*, *12*(6), 1380-1392.

McIntosh, K., Y. Nakamura, T.-K. Wang, R.-C. Shih, A. Chen, and C.-S. Liu (2005), Crustal-scale seismic profiles across Taiwan and western Philippine Sea, *Tectonophysics*, *401*, 23-54.

McIntosh, Kirk; Harm Van Avendonk; Luc Lavier; Ryan Lester; Daniel Eakin; Francis Wu; Char-Shine Liu; Chao-Shing Lee (accepted 2013), Inversion of a hyper-extended rifted margin in the southern Central Range of Taiwan, *Geology*.

Menzies, M. A., S. L. Klemperer, C. J. Ebinger, and J. Baker (2002), Characteristics of volcanic rifted margins, in *Volcanic Rifted Margins*, edited by M. A. Menzies, S. L. Klemperer, C. J. Ebinger and J. Baker, pp. 1-14, Geological Society of America Special Paper, Boulder, Colorado.

Miller, E. L., P. B. Gans, and J. Garing (1983), The Snake Range Décollement: An exhumed Mid-Tertiary ductile-brittle transition, *Tectonics*, *2*(3), 239-263.

Moore, G. F., N. L. Bangs, A. Taira, S. Kuramoto, E. Pangborn, and H. J. Tobin (2007), Three-Dimensional Splay Fault Geometry and Implications for Tsunami Generation, *Science*, *318*(5853), 1128-1131.

Morley, C. K. (2007), Interaction between critical wedge geometry and sediment supply in a deep-water fold belt, *Geology*, *35*(2), 139-142.

Mosner, T.J. (1991) Shortest path calculation of seismic rays, *Geophysics*, 56, 59-67.

Mosner, T.J., G. Nolet, and R. Snider (1992), Ray Bending Revisited, *Bulletin of the Seismological Society of America*, 82, 259-288.

Mouthereau, F., and C. Petit (2003), Rheology and strength of the Eurasian continental lithosphere in the foreland of the Taiwan collision belt: Constraints from seismicity, flexure, and structural styles, *J. Geophys. Res.*, *108*(B11), 2512.

Mouthereau, F., and O. Lacombe (2006), Inversion of the Paleogene Chinese continental margin and thick-skinned deformation in the Western Foreland of Taiwan, *Journal of Structural Geology*, *28*, 1977-1993.

Mouthereau, F., B. Deffontaines, O. Lacombe, and J. Angelier (2002), Variations along the strike of the Taiwan thrust belt: Basement control on structural style, wedge geometry, and kinematics, in *Geology and Geophysics of an Arc-Continent Collision, Taiwan*, edited by T. B. Byrne and C.-S. Liu, pp. 31-54, Geological Society of America.

Mouthereau, F., O. Lacombe, B. Deffontaines, J. Angelier, and S. Brusset (2001), Deformation history of the southwestern Taiwan foreland thrust belt: insights from tectono-sedimentary analyses and balanced cross-sections, *Tectonophysics*, *333*(1), 293-318.

Murauchi, S., et al. (1968), Crustal Structure of the Philippine Sea, *Journal of Geophysical Research*, *73*(10), 3143-3171.

Mutter, C. Z., and J. C. Mutter (1993), Variations in thickness of layer 3 dominate oceanic crustal structure, *Earth and Planetary Science Letters*, *117*(1), 295-317.

Mutter, J. C., M. Talwani, and P. L. Stoffa (1984), Evidence for a thick oceanic crust adjacent to the Norwegian margin, *Journal of Geophysical Research*, *89*(B1), 483-502.

Nissen, S. S., D. E. Hayes, Y. Bochu, Z. Weijun, C. Yongqin, and N. Xiaupin (1995a), Gravity, heat flow, and seismic constraints on the processes of crustal extension: Northern margin of the South China Sea, *Journal of Geophysical Research*, *100*(B11), 22,447-422,483.

Nissen, S. S., D. E. Hayes, P. Buhl, J. Diebold, Y. Bochu, Z. Weijun, and C. Yongqin (1995b), Deep penetration seismic soundings across the northern margin of the South China Sea, *Journal of Geophysical Research*, *100*(B11), 22,407-422,433.

Northrup, C. J., L. H. Royden, and B. C. Burchfiel (1995), Motion of the Pacific plate relative to Eurasia and its potential relation to Cenozoic extension along the eastern margin of Eurasia, *Geology*, *23*(8), 719-722.

Pérez-Gussinyé, M., and T. J. Reston (2001a), Rheological evolution during extension at nonvolcanic rifted margins: Onset of serpentinization and development of detachments leading to continental breakup, *Journal of Geophysical Research: Solid Earth*, *106*(B3), 3961-3975.

Pérez-Gussinyé, M., T. J. Reston, and J. Phipps Morgan (2001b), Serpentinization and magmatism during extension at non-volcanic margins: the effect of initial lithospheric structure, *Geological Society, London, Special Publications*, *187*(1), 551-576.

Poliakov, A.N.B., Yu Podladchikov and C. Talbot (1993), Initiation of salt diapirs with frictional overburdens: numerical experiments, *Tectonophysics*, 228 (3-4), 199-201.

Popov, A. A., S. V. Sobolev (2008), SLIM3D: A tool for three-dimensional thermomechanical modeling of lithospheric deformation with elasto-visco-plastic rheology, *Physics of Earth and Planetary Interiors*, 171 (1-4), 55-75.

Pubellier, M., C. Monnier, R. Maury, and R. Tamayo (2004), Plate kinematics, origin and tectonic emplacement of supra-subduction ophiolites in SE Asia, *Tectonophysics*, *392*(1-4), 9-36.

Qiu, X., S. Ye, S. Wu, X. Shi, Z. Di, K. Xia, and E. R. Flueh (2001a), Crustal Structure Across the Xisha Trough, Northwestern South China Sea, *Tectonophysics*, *341*(1-4), 179-193.

Ranero, C. R., J. P. Morgan, K. McIntosh, and C. Reichert (2003), Bending-related faulting and mantle serpentinization at the Middle America trench, *Nature*, *425*, 367-373.

Ranalli, G., (1995),Rheology of the Earth, 2nd ed., 436 pp., Chapman and Hall, London.

Ratschbacher, L., W. Frisch, F. Neubauer, S. M. Schmid, and J. Neugebauer (1989), Extension in compressional orogenic belts: The eastern Alps, *Geology*, *17*(5), 404-407.

Rau, R.-J., and F. T. Wu (1995), Tomographic imaging of lithospheric structures under Taiwan, *Earth and Planetary Science Letters*, *133*(3-4), 517-532.

Reed, D. L., N. Lundberg, C.-S. Liu, and B.-Y. Kuo (1992), Structural relations along the margins of the offshore Taiwan accretionary wedge: implication for accretion and crustal kinematics, *Acta Geologica Taiwanica*, *30*, 105-122.

Regenauer-Lieb, K., R. F. Weinberg, and G. Rosenbaum (2006), The effect of energy feedbacks on continental strength, *Nature*, *442*(7098), 67-70.

Reston, T., and G. Manatschal (2011), Rifted Margins: Building Blocks of Later Collision, in *Arc-Continent Collision*, edited, pp. 3-21, Springer Berlin Heidelberg.

Reston, T. J. (2009), The structure, evolution and symmetry of the magma-poor rifted margins of the North and Central Atlantic: A synthesis, *Tectonophysics*, *468*(1–4), 6-27.

Reston, T.J. (2007), The formation of non-volcanic rifted margins by the progressive extension of the lithosphere: the example of the West Iberian margin, *Geological Society of London Special Publications,* 282(1), 77-110.

Reston, T. J., C. M. Krawczyk, and D. Klaeschen (1996), The S reflector west of Galicia (Spain): Evidence from prestack depth migration for detachment faulting during continental breakup, *Journal of Geophysical Research: Solid Earth*, *101*(B4), 8075-8091.

Ru, K., and J. D. Pigott (1986), Episodic rifting and subsidence in the South China Sea, *AAPG Bulletin*, *70*(9), 1136-1155.

Ruppel, C. (1995), Extensional processes in continental lithosphere, *Journal of Geophysical Research: Solid Earth*, *100*(B12), 24187-24215.
Schoenberger, M. (1996), Optimum weighted staack for multiple suppresion, *Geophysics*, *61*(3), 891-901.
Sengör, A. M. C., B. A. Natal'in, and V. S. Burtman (1993), Evolution of the Altaid tectonic collage and Palaeozoic crustal growth in Eurasia, *Nature*, *364*(6435), 299-307.
Shi, X., E. Burov, S. Leroy, X. Qiu, and B. Xia (2005), Intrusion and its implication for subsidence: A case from the Baiyun Sag, on the northern margin of the South China Sea, *Tectonophysics*, *407*(1-2), 117-134.
Shinjo, R. (1999), Geochemistry of high Mg andesites and the tectonic evolution of the Okinawa Trough-Ryukyu arc system, *Chemical Geology*, *157*, 69-88.
Shluter, H. U., K. Hinz, and M. Block (1996), Tectono-stratigraphic terranes and detachment faulting of the South China Sea and Sulu Sea, *Marine Geology*, *130*(1-2), 39-51.
Simoes, M., J. P. Avouac, O. Beyssac, B. Goffe, K. A. Farley, and Y.-G. Chen (2007), Mountain building in Taiwan: A thermokinematic model, *Journal of Geophysical Research*, *112*(B11405).
Su, D., N. White, and D. McKenzie (1989), Extension and subsidence of the Pearl River Mouth Basin, northern South China Sea, *Basin Research*, *2*(4), 205-222.
Suppe, J. (1980), Imbricated structure of western foothills belt, southcentral Taiwan, *Petroleum Geology of Taiwan,* 17, 1-16.
Suppe, J. (1981), Mechanics of mountain building and metamorphism in Taiwan, *Memoir of the Geological Society of China*, *4*, 67-89.
Suppe, J. (1984), Kinematics of arc-continent collision, flipping of subduction, and back-arc spreading near Taiwan, *Memoir of the Geological Society of China*, *6*, 21-33.
Tang, J.-C., A. I. Chemenda, J. Chery, S. Lallemand, and R. Hassani (2002), Compressional subduction regime and initial arc-continent collision: Numerical modeling, in *Geology and Geophysics of an Arc-Continent Collision, Taiwan*, edited by T. B. Byrne and C.-S. Liu, pp. 177-186, Geological Society of America.
Tapponnier, P., G. Peltzer, A. Y. Le Dain, R. Armijo, and P. Cobbold (1982), Propagating extrusion tectonics in Asia: New insights from simple experiments with plasticine, *Geology*, *10*(12), 611-616.
Taylor, B., and D. E. Hayes (1980), The tectonic evolution of the South China Basin, *Geophysical Monograph Series*, *23*, 89-104.
Taylor, B., and D. Hayes (1983), Origin and History of the South China Sea Basin, in *The Tectonic and Geologic Evolution of Southeast Asian Seas and Islands, Part 2*, edited, pp. 23-56.
Teng, L. S. (1996), Extensional collapse of the northern Taiwan mountain belt, *Geology*, *24*(10), 949-952.

Tensi, J., F. Mouthereau, and O. Lacombe (2006), Lithospheric bulge in the West Taiwan Basin, *Basin Research*, *18*, 277-299.

Tillman, K. S., and T. B. Byrne (1995), Kinematic analysis of the Taiwan Slate Belt, *Tectonics*, *14*(2), 322-341.

Tsai, C.-H., S.-K. Hsu, Y.-C. Yeh, C.-S. Lee, and K. Xia (2004), Crustal Thinning of the Northern Continental Margin of the South China Sea, *Marine Geophysical Researches*, *25*(1-2), 63-78.

Ulmer, Peter, Voklmar Trommsdorff (1995), Serpentine stability to mantle depths and subduction-related magmatism, *Science*, 268(5212), 858-861.

Van Avendonk, H. J. A., D. J. Shillington, W. S. Holbrook, and M. J. Hornbach (2004a), Inferring crustal structure in the Aleutian island arc from a sparse wide-angle seismic data set, *Geochem. Geophys. Geosyst.*, *5*(8), Q08008.

Van Avendonk, H. J. A., W. S. Holbrook, D. Okaya, J. K. Austin, F. Davey, and T. Stern (2004b), Continental crust under compression: A seismic refraction study of South Island Geophysical Transect I, South Island, New Zealand, *J. Geophys. Res.*, *109*(B6), B06302.

Verschuur, D. J., A. J. Berkhoust, and C. P. A. Wapenaar (1992), Adaptive surface-related multiple elimination, *Geophysics*, *57*(9), 1166-1177.

Wallis, S. R., J. P. Platt, and S. D. Knott (1993), Recognition of Syn-Convergence Extension in Accretionary Wedges with Examples from the Calabriab Arc and the Eastern Alps, *American Journal of Science*, *293*, 463-495.

Wang, K.-L., S. Y. O'Reilly, W. L. Griffin, S.-L. Chung, and N. J. Pearson (2003), Proterozoic mantle lithosphere beneath the extended margin of the South China block: In situ Re-Os evidence, *Geology*, *31*(8), 709-712.

Wang, K.-L., S.-L. Chung, C.-H. Chen, R. Shinjo, T. F. Yang, and C.-H. Chen (1999), Post-collisional magmatism around northern Taiwan and its relation with opening of the Okinawa Trough, *Tectonophysics*, *308*, 363-376.

Wang, K.-L., S.-L. Chung, Y.-M. Lo, C.-H. Lo, H.-J. Yang, R. Shinjo, T.-Y. Lee, J.-C. Wu, and S.-T. Huang (2012a), Age and geochemical characteristics of Paleogene basalts drilled from western Taiwan: Records of initial rifting at the southeastern Eurasian continental margin, *Lithos*, *155*(0), 426-441.

Wang, K. L., Y. M. Lo, S. L. Chung, C. H. Lo, S. K. Hsu, H. J. Yang, and R. Shinjo (2012b), Age and geochemical features of dredged basalts from offshore SW Taiwan: The coincidence of intra-plate magmatism with the spreading South China Sea, *Terrestrial Atmospheric and Oceanic Science*, *23*(6), 657-669.

Wang, P., W. Prell, and P. Blum (2000), Proceedings of the Ocean Drilling Program, Initial Reports, 184, in *Ocean Drilling Program*, edited, College Station, Tx.

Wang, T. K., S.-F. Lin, C.-S. Liu, and C.-S. Wang (2004), Crustal structure of the southernmost Ryukyu subduction zone: OBS, MCS, and gravity modelling, *Geophysical Journal International*, *157*, 147-163.

Wang, T. K., M.-K. Chen, C.-S. Lee, and K. Xia (2006), Seismic imaging of the transitional crust across the northeastern margin of the South China Sea, *Tectonophysics*, *412*, 237-254.

Wang, W.-H. (2001), Lithospheric flexure under a critically tapered mountain belt: a new technique to study the evolution of the Tertiary Taiwan orogeny, *Earth and Planetary Science Letters*, *192*, 571-581.

Whipple, K. X. (2009), The influence of climate on the tectonic evolution of mountain belts, *Nature Geoscience*, *2*(2), 97-104.

Whipple, K. X., and B. J. Meade (2004), Controls on the strength of coupling among climate, erosion, and deformation in two-sided, frictional orogenic wedges at steady state, *Journal of Geophysical Research: Earth Surface*, *109*(F1), F01011.

White, R. S., D. McKenzie, and R. K. O'Nions (1992), Oceanic Crustal Thickness From Seismic Measurements and Rare Earth Element Inversions, *J. Geophys. Res.*, *97*(B13), 19683-19715.

White, R. S., L. K. Smith, A. W. Roberts, P. A. F. Christie, and N. J. Kusznir (2008), Lower-crustal intrusion on the North Atlantic continental margin, *Nature*, *452*(7186), 460-464.

White, R. S., G. D. Spence, S. R. Fowler, D. P. McKenzie, G. K. Westbrook, and A. N. Bowen (1987), Magmatism at rifted continental margins, *Nature*, *330*(6147), 439-444.

Whitmarsh, R. B., G. Manatschal, and T. A. Minshull (2001), Evolution of magma-poor continental margins from rifting to seafloor spreading, *Nature*, *413*, 150-154.

Willett, S., C. Beaumont, and P. Fullsack (1993), Mechanical model for the tectonics of doubly vergent compressional orogens, *Geology*, *21*(4), 371-374.

Willett, S. D. (1999a), Rheological dependence of extension in wedge models of convergent orogens, *Tectonophysics*, *305*(4), 419-435.

Willett, S. D. (1999b), Orogeny and orography: The effects of erosion on the structure of mountain belts, *Journal of Geophysical Research: Solid Earth (1978–2012)*, *104*(B12), 28957-28981.

Willett, S. D., D. Fisher, C. Fuller, Y. En-Chao, and L. Chia-Yu (2003), Erosion rates and orogenic-wedge kinematics in Taiwan inferred from fission-track thermochronometry, *Geology*, *31*(11), 945-948.

Wu, F. T., R.-J. Rau, and D. Salzberg (1997), Taiwan orogeny: thin-skinned or lithospheric collision?, *Tectonophysics*, *274*, 191-220.

Wu, F. T., C. S. Chang, and Y. M. Wu (2004), Precisely relocated hypcentres, focal mechanisms and active orogeny in Central Taiwan, *Geological Society of London Special Publication*, *226*(1), 333-353.

Xu, X., S. Y. O'Reilly, W. L. Griffin, and X. Zhou (2000), Genesis of Young Lithospheric Mantle in Southeastern China: an LAM–ICPMS Trace Element Study, *Journal of Petrology*, *41*(1), 111-148.

Yamato, P., F. Mouthereau, and E. Burov (2009), Taiwan mountain building: insights from 2-D thermomechanical modelling of a rheologically stratified lithosphere, *Geophysical Journal International*, *176*(1), 307-326.

Yan, P., Z. Di, and L. Zhaoshu (2001), A crustal structure profile across the northern continental margin of the South China Sea, *Tectonophysics*, *338*(1), 1-21.

Yan, P., H. Deng, H. Liu, Z. Zhang, and Y. Jiang (2006), The temporal and spatial distribution of volcanism in the South China Sea region, *Journal of Asian Earth Sciences*, *27*, 647-659.

Yeh, Y.-C., and S.-K. Hsu (2004), Crustal structures of the northernmost South China Sea: Seismic reflection and gravity modeling, *Marine Geophysical Researches*, *25*, 45-61.

Yeh, Y.-C., J.-C. Sibuet, S.-K. Hsu, and C.-S. Liu (2010), Tectonic evolution of the Northeastern South China Sea from seismic interpretation, *Journal of Geophysical Research*, *115*.

Yeh, Y.-C., S.-K. Hsu, W.-B. Doo, J.-C. Sibuet, C.-S. Liu, and C.-S. Lee (2012), Crustal features of the northeastern South China Sea: insights from seismic and magnetic interpretations, *Marine Geophysical Research*, 1-20.

Yen, H.-Y., and Y.-H. Yeh (1998), Two-dimensional crustal structures of Taiwan from gravity data, *Tectonics*, *17*(1), 104-111.

Yilmaz, O. (2001), *Seismic Data Analysis*, 2nd ed., Society of Exploration Geophysics, Tulsa.

Yu, S.-B., H.-Y. Chen, and L.-C. Kuo (1997), Velocity field of GPS stations in the Taiwan area, *Tectonophysics*, *274*, 41-59.

Zelt, C. A., K. Sain, J. V. Naumenko, and D. S. Sawyer (2003), Assessment of crustal velocity models using seismic refraction and reflection tomography, *Geophysical Journal International*, *153*(3), 609-626.

Zhang, Z., and Y. Wang (2007), Crustal structure and contact relationship revealed from deep seismic sounding data in South China, *Physics of the Earth and Planetary Interiors*, *165*(1–2), 114-126.

Zhao, M., X. Qiu, S. Xia, H. Xu, P. Wang, T. K. Wang, C.-S. Lee, and K. Xia (2010), Seismic structure in the northeastern South China Sea: S-wave velocity and Vp/Vs ratios derived from three-component OBS data, *Tectonophysics*, *480*(1), 183-197.

Zhou, X. M., and W. X. Li (2000), Origin of Late Mesozoic igneous rocks in Southeastern China: implications for lithosphere subduction and underplating of mafic magmas, *Tectonophysics*, *326*(3–4), 269-287.

Zhu, J., X. Qiu, H. Kopp, H. Xu, Z. Sun, A. Ruan, J. Sun, and X. Wei (2012), Shallow anatomy of a continental ocean transition zone in the northern South China Sea from multichannel seismic data, *Tectonophysics*, *554-557*(0), 18-29.

Zhu, M., S. Graham, and T. McHargue (2009), The Red River Fault zone in the Yinggehai Basin, South China Sea, *Tectonophysics*, *476*(3), 397-417.